TABLE OF CONTENTS

LIST OF TABLES

CHAPTER 1

CHAPTER 2

CHAPTER 3

CHAPTER 4

CHAPTER 5

LIST OF FIGURES

CHAPTER 2

CHAPTER 3

CHAPTER 4

LIST OF APPENDICES

CHAPTER 2

CHAPTER 3

CHAPTER 4

Note:

No permission required for the usage of Figures, Tables and Appendices in Chapter 2. Permission for usage of Figures, Tables and Appendices in Chapter 4 obtained (Springer Nature License) and can be presented by the thesis author upon request.

LIST OF ABBREVIATIONS

n. b. - nota bene

n. p. – not present

n. o. – no observed

vs. - versus

CT – computed tomography

microCT – micro computed tomography

nanoCT – nano computed tomography

SR – synchrotron radiation

HPHT – high pressure and high temperature

SEM-EDS – scanning electron microscope energy dispersive X-ray spectroscopy

BSE – backscattered electron

BND – bubble number density

BSD – bubble size distribution

NNO – nickel-nickel-oxide oxygen buffer

2D – two-dimensional

3D - three-dimensional

4D – four-dimensional (3D + time)

plag - plagioclase

cpx – clinopyroxene

amph – amphibole

mgt - magnetite

μm – micron or micrometer

MPa – mega Pascal

GPa – giga Pascal

kV – kilovolt

keV – kilo electron-volt

mA - milliampere

wt. % - weight percent

vol. % - volume percent

LIST OF SYMBOLS

$D_i^{s/l}$ – partition coefficient of element i between a solid (crystal) and a liquid (melt)
ΔF – Helmholtz free energy
σ_{AB} – surface energy or surface tension between phases A and B (solid, liquid, vapour)
$\Delta\sigma$ – a change in surface energy between two states (e.g. between fully separated bubble and crystal to fully attached)
θ – outer contact angle, measured within the melt/glass
ψ – inner contact angle, measured within the bubble
Φ, m, S, F – geometrical factor
B – factor
J – bubble nucleation rate
α – angle between two 2D planes that intersect each other, and a sphere, through its center
T – temperature
t – time
p – pressure
Δp_{sat} – supersaturation pressure
Δp_{dec} – decompression drop
$\alpha_{298\ K}$ – coefficient of thermal expansion at 298 K
π – 3.14159
fO_2 – oxygen fugacity
FeO_{TOT} – the concentration of total Fe expressed as FeO wt. %
μ - viscosity
ρ - density
R_a – arithmetic mean roughness value
r_{bubble} – bubble radius
$r^{critical}_{bubble}$ – critical bubble radius at the point of neutral buoyancy
$r_{plagioclase}$ – radius of a sphere with volume equivalent to the volume of a plagioclase crystal
$r_{eqv\ sphere}$ – radius of an equivalent sphere
V – volume
$V^{critical}_{\Sigma\ bubbles}$ – critical volume of the sum of all bubbles on a crystal
$V^{measured}_{\Sigma\ bubbles}$ – measured volume of all bubbles on a crystal
A_{oxide} – bubble surface area in contact with oxides
$S_{cap\ w/o\ base}$ – surface area of a spherical cap without its base
h – height of the spherical cap
S_{lune} – surface area of a spherical lune
v_t – terminal velocity
g – gravitational constant
F_G – gravitational force
$F^{buoyancy}$ – buoyancy force
$F^{buoyancy}_{net}$ – summation of buoyancy forces of a crystal and a bubble on its surface
$F^{buoyancy}_{difference}$ – difference of buoyancy forces of a crystal and a bubble on its surface
$F^{attachment}$ –attachment force between a crystal and a bubble on its surface
$F^{detachment}$ – detachment force between a crystal and a bubble on its surface

AKNOWLEDGEMENTS

There are many people who contributed to this PhD and to whom I am grateful.

I would like to first and foremost thank prof. Michael Higgins, my supervisor, for his guidance, patience, understanding and support. I feel very fortunate to have been your student!

Thank you prof. Don Baker, my co-supervisor, for opening the door for me at McGill and introducing me to experimental petrology. I am grateful to all the members of my PhD committee for agreeing to evaluate this thesis and my work: prof. Sarah-Jane Barnes, prof. Sarah Dare and prof. William Minarik.

A special thank you goes to Lucia Mancini and Gabriele Lanzafame from the Elettra Sincrotrone in Trieste. Thank you, Lucia, for opening the door for me and thank you, Gabriele, for all that you've taught me! Regarding the many aspects of tomography, I am additionally grateful to Mark Rivers, Francesco Brun, Julie Fife and Jake Casselman for their help and contribution.

I would like to thank Nelson Eby and Chris Ballhaus, the editors of Lithos and Contributions to Mineralogy and Petrology, respectively, at the publishing time of my articles, and all the reviewers, Matteo Masotta, Fabio Arzilli and anonymous, for their work.

I am appreciative to the University of Quebec in Chicoutimi and the Department of Applied Sciences for awarding me the Lucien Bouchard and Denis W. Roy grants.

I am grateful to my family back home, Ester, Sara, Dunja, Đurđa, Manja, Miro, Katja, for their love and support. Also, a thank you to all my friends, Croatian and Canadian! Thank you Judit and Michael, for your continuous help and support and for making me feel at home away from home.

And finally, the biggest thank you goes to my beloved husband Marko – you are at the center and the reason for everything and nothing would be possible without your unwavering love, patience, support and sacrifice. This PhD is for you and our family.

FUNDING

This work was mainly supported by a NSERC (Canada) Discovery grant to Michael D. Higgins (RGPIN 2012-25137), and additionally by another awarded to Don R. Baker (RGPIN-2015-06355).

The cost of travel and accommodation to Advanced Photon Source synchrotron in Illinois (U.S.A.) and the Swiss Light Source (Switzerland), in addition to the NSERC grants was supported also by a Student Travel/Research Grant awarded to Pia Pleše in 2014 by the Mineralogical Association of Canada. Additionally, the EXTREMA COST Action MP 1207 provided networking support for the travel to Switzerland.

This research used resources of the Advanced Photon Source, a U.S. Department of Energy (DOE) Office of Science User Facility operated for the DOE Office of Science by Argonne National Laboratory under Contract No. DE-AC02-06CH11357. Synchrotron imaging was performed at GeoSoilEnviroCARS (University of Chicago, Sector 13), Advanced Photon Source (APS), Argonne National Laboratory. GeoSoilEnviroCARS is supported by the National Science Foundation - Earth Sciences (EAR-1128799) and Department of Energy - GeoSciences (DE-FG02-94ER14466).

CHAPTER 1

Introduction, Hypotheses, Objectives, Methodology

1.1 Introduction

Modern volcanology explores all aspects of volcanic eruptions, and processes occurring on micron to kilometre scales. One of the most important micro-scale processes is the formation and development of bubbles in magmas, which can have a major effect on the explosivity and progress of volcanic eruptions (Hurwitz and Navon, 1994; Mangan and Sisson, 2000). The solubility of volatiles, the nucleation of bubbles and the efficiency of volatile transfer from melt to bubble control a magma's degassing efficiency (Gardner et al., 1999). The nucleation, growth and coalescence of bubbles can lead to the subsequent fragmentation of the magmatic foam or the formation of deep-rooted permeable paths and so govern volcanic eruption styles (Giachetti et al., 2010). One branch of volcanology aims to interpret all bubble-related processes in order to constrain and understand the conditions under which a volcano could erupt violently and thus help monitor and diminish eruption hazards. Most studies focus on natural volcanic rock textures that contain information on the processes of degassing and crystallization (e.g. Cichy et al., 2011). Experimental petrology can also be used to explore these same processes, with the added benefit of controlling pressure, temperature and compositions. The goal is to create samples that mimic natural environments under known and narrow conditions and to combat textural overprinting in post-process samples. In melts, bubbles are displaced more easily than other phases (e.g. crystals), so textural overprinting is especially problematic in bubble related studies (e.g. Shea et al., 2010).

A bubble is defined as a droplet of one substance surrounded by another, usually a gas in a liquid (Clift et al., 1978). When, due to change in pressure and temperature

conditions, volatile solubility in magma decreases, supersaturation ensues, and the volatile components segregate into gas bubbles. Although natural systems contain many different volatile species, such as H_2O, CO_2, S, F, Cl, most studies have focused on H_2O since its concentration in magmas is several orders of magnitude greater than that of other volatiles.

The focus of this research has been the experimental formation of H_2O gas bubbles within magmas of andesitic composition, in order to study their interactions with crystals (pre-existing or newly formed) of different compositions. Interactions here encompass heterogeneous nucleation (nucleation on a pre-existing surface) of bubble on crystals, heterogeneous nucleation of crystals on bubbles, their detachment and attachment.

1.2 Problem: What is the influence of crystals on bubbles in magmas?

1.2.1 Bubble nucleation

Bubble nucleation is strongly dependent on the content of volatiles in the melt, the decompression rate, temperature and surface tension (Hirth et al., 1970; Shea, 2017 and references therein). Henceforth, I will restrict discussion to the case of water vapour bubbles in magmas, as this is the focus of this thesis. Classical nucleation theory states that because of local fluctuations in the concentration of molecular water in the melt, small clusters (critical sized nuclei) of water molecules form, which can grow or shrink depending on the addition or loss of new molecules by diffusion (Volmer and Webber, 1926; Blander and Katz, 1975). Once a critical nucleus has formed, the addition of water causes a lowering of its free energy with respect to the surrounding melt - a spherical shape of the critical nucleus is assumed as it would represent the minimum amount of energy needed for the formation of the interface (Dunning, 1969; Landau and Lifshitz, 1980; Hurwitz and Navon, 1994).

Bubbles can nucleate in two different ways: homogeneous nucleation, which occurs completely within the melt and requires higher degrees of volatile supersaturation, and heterogeneous nucleation, nucleation on a crystal surface, which requires lower volatile supersaturations (Blander and Katz, 1975; Gardner, 2007; Hurwitz and Navon, 1994).

For homogeneous nucleation at constant temperature and volume, the Helmholtz free energy (ΔF) required to form a critically sized spherical nucleus is (Equation 1, Hirth et al., 1970; Hurwitz and Navon, 1994; Navon and Lyakhovsky, 1998):

$$\Delta F = \frac{16\pi\sigma^3}{3\Delta p_{sat}{}^2} \quad (1),$$

where σ is the surface energy and Δp_{sat} is the supersaturation pressure. Helmholtz free energy is used instead of Gibbs free energy, as the system is not at constant pressure (Hirth et al., 1970). The critical nucleus size cannot be described in terms of the Gibbs free energy because a reversible constant pressure path can't be constructed, i.e. the final state cannot be achieved from the initial state under constant pressure (for a detailed discussion see Hirth et al., 1970). The supersaturation pressure is the difference between the internal pressure within the bubble (vapour) nucleus and the pressure of the surrounding melt (Hurwitz and Navon, 1994) and is obtained from the Laplace equation (Navon and Lyakhovsky, 1998). The internal bubble pressure is always greater than the melt pressure and the two are related through Henry's constant to the difference between the actual water content of the supersaturated melt and the equilibrium solubility at the melt pressure (Navon and Lyakhovsky, 1998). In reality, the decompression is often equated with the supersaturation pressure for practicality, as during decompression the internal bubble pressure stays the same and the melt pressure decreases (Hurwitz and Navon, 1994).

For heterogeneous nucleation, the energy is (Equations 2-4, Landau and Lifshitz, 1980; Hurwitz and Navon, 1994; Adamson and Gast, 1997; Navon and Lyakhovsky, 1998):

$$\Delta F = \frac{16\pi\sigma_{LV}{}^3}{3\Delta p^2} \times \Phi \quad (2),$$

$$\Phi = \frac{(2-\cos\theta)\times(1+\cos\theta)^2}{4} \quad (3),$$

$$\cos\theta = \frac{\sigma_{SV}-\sigma_{SL}}{\sigma_{LV}} \quad (4),$$

where Φ is a geometrical factor, θ the outer contact angle, σ_{SV} = surface energy between the solid (crystal) and the vapour (bubble), σ_{SL} = surface energy between the solid and the liquid (melt), and σ_{LV} = surface energy between the liquid and the vapour. Since $\Delta F \sim 1/(\Delta p)^2$, a greater degree of supersaturation (greater amount of a volatile compound that becomes available to form bubbles) will reduce the amount of energy needed and thus enable easier nucleation and more bubbles.

Surface tension (or surface energy or interfacial energy or free energy per unit area, Adamson and Gast, 1997) is cubed in Equations 1 and 2 and so it can influence ΔF. The total surface energy of a bubble is smallest as a combination of three surface energies, between melt, gas and crystal surface energies, i.e., when there is a contact line between melt-bubble-crystal (stemming from Young's relation, expanded in Adamson and Gast, 1997). Presence of a crystal-melt interface will cause the needed energy for bubble nucleation to decrease by a geometrical factor Φ (Equation 3) due to a decrease in surface energy (Landau and Lifshitz, 1980). When the geometrical factor is present, regardless of the crystal surface type (i.e., the values of the three surface energies), it follows that heterogeneous bubble nucleation on any surface/crystal will be energetically favourable over homogeneous bubble nucleation.

As heterogeneous bubble nucleation necessitates phase surfaces, an important constraint on the nucleation style is the presence or absence of crystals in the melt. Crystals represent regions of heterogeneity in the magma and crystal features, such as composition, crystal lattice type, morphology, surface energy of their faces and defects in structure (tips, cracks, cavities, impurities or any mechanical damage) are important parameters that could influence their interactions with bubbles. Imperfections on a crystal surface are the most efficient nucleation sites because they are poorly wetted by

the melt and have the greatest tendency to entrap gas (Cole, 1974). Crystal defects promote surface roughness, in turn promoting heterogeneous bubble nucleation (Volmer, 1939; Zanotto and Fokin, 2003). However, not all crystals are alike: some are regarded as efficient nucleation sites and their presence or absence can influence bubble nucleation type, whereas others are commonly regarded as inefficient and hence unfavorable for bubble formation (Hurwitz and Navon, 1994).

Hurwitz and Navon (1994) and Gardner and Denis (2004) have considered the relations between the chemical composition of minerals, their crystal morphology and surface properties, and how these can affect heterogeneous bubble nucleation. Although heterogeneous bubble nucleation is always easier than homogeneous nucleation, crystals of different minerals are not equally efficient as bubble nucleation sites. Each mineral is defined by its composition and geometry of crystal lattice, and thus each has a different surface energy value. The efficiency in bubble nucleation arises from the crystals' ability to be easily wetted by a vapour phase, i.e., to form a large dihedral contact angle (Figure 2.1) between the bubble and itself (the wetting angle, Hurwitz and Navon, 1994). The surface energy value (σ_{SV}) is reflected in the outer contact angle – the lower the surface energy the larger the outer contact angle, and along with crystal morphology is the controlling parameter for a minerals' bubble nucleation efficiency (Hurwitz and Navon, 1994). Due to sparse studies on the subject, the true values of surface energies between crystals and bubbles (σ_{SV}) remain mostly unknown.

The discriminant outer contact angle value was set to 68° by Blander and Katz (1975) based on their formulation of the heterogeneous bubble nucleation rate:

$$J = N^{\frac{2}{3}} S \left[\frac{2\,\sigma_{LV}}{\pi m B F}\right]^{\frac{1}{2}} \exp\left[\frac{-16\pi\sigma_{LV}{}^{3} F}{3kT\,(P_V - P_L)^2}\right] \quad (5),$$

$$S \equiv \frac{1-m}{2} \quad (6),$$

$$F \equiv \frac{2-3m+m^3}{4} \quad (7),$$

$$m = -\cos\theta = \frac{\sigma_{SL} - \sigma_{SV}}{\sigma_{LV}} \quad (8),$$

where J is the bubble nucleation rate, N is the bubble number, S, m and F are geometric factors, B is a factor, k is the Boltzmann constant, T is temperature, σ is the surface energy and θ is the outer bubble-particle contact angle. In Equation 5, the pre-exponential term relates to kinetic factors while the exponential term to thermodynamic factors. In Equations 5 and 7, factor F corresponds to the geometry factor ϕ in Equation 2 from Hurwitz and Navon (1994). Blander and Katz have set their F value for higher heterogeneous bubble nucleation probability as < 77, yielding a θ > 68°, because at these values the exponential term makes up the difference in the preexponential kinetic factors (Blander and Katz, 1975). This leads to the following: if the outer contact angle is < 68°, the crystal is poorly wetted by the bubble and well wetted by the melt, and the reverse if the outer contact angle is > 68° (Blander and Katz, 1975).

Hurwitz and Navon (1994) observed in their experiments that Fe-Ti oxides were the most efficient crystals at heterogeneous bubble nucleation with 50-60% of them having bubbles at decompressions Δp_{dec} = 5 MPa, 70-90% at Δp_{dec} = 5-10 MPa and over 90% at Δp_{dec} = 30 MPa in under 5 seconds. This was attributed to their low σ_{SV} and rough surface with many submicroscopic (not observed) 90º angles. Biotite and zircon crystals were deemed less efficient because the outer contact angles between

them and bubbles (measured in 2D) were > 90º and < 40º, respectively (Hurwitz and Navon, 1994).

In the studies of Hurwitz and Navon (1994) and Gardner and Denis (2004) feldspars and quartz were never wetted (bubbles were not found on their surfaces but in their vicinity). Plagioclase proved to be inefficient at bubble nucleation, even at Δp_{dec} = 150 MPa, due to its very high σ_{SV} (Gardner and Denis, 2004), much higher than for magnetite and hematite, and very low wetting angle < 20º (Hurwitz and Navon, 1994). Gualda and Anderson (2007) were able to measure outer contact angles in 2D at different minerals and confirmed this: for magnetite is $\theta \approx 45° - 50°$, and for plagioclase is $\theta \approx 5° - 25°$.

The inefficiency of silicate crystals was attributed to their compositional similarity to silicate melts. The energy at an interface separating crystals and melt is dependent on the structure and the type of bonding of each phase. If the structure and bonding are similar, as with a silicate mineral in a silicate melt, the ionic charge at their interface is low, hence the interfacial energy is low, and silicates are well wetted by silicate melts. If there is a compositional and bonding difference, as with an oxide mineral in a silicate melt, the ionic charge at the interface is high, the interfacial energy is high, so oxides are poorly wetted by silicate melts (Adamson and Gast, 1997, their Chapter 10). In turn, good wettability of a crystal by a melt leads to poor wettability of the crystal by a bubble, and vice versa.

The literature overview presented above on oxide efficiency at heterogeneous bubble nucleation and inefficiency of silicate crystals was the basis of heterogeneous bubble nucleation studies in the past several decades. Bubbles on silicate crystals have however been reported but not considered significant (e.g. Figure 4 in Hurwitz and

Navon, 1994, shows a biotite completely covered in bubbles with an outer contact angle > 90°). Additionally, as oxides are commonly microlites in experiments, they can nucleate only a small number of bubbles on their surfaces. Thus, although there may be many oxide microlites in silicate magmas (10^7 cm^{-3} vs. $\leq$ 1 cm^{-3} of silicate phenocryst, Mangan and Sisson, 2000) they still do not seem to account for the bubble numbers recorded in samples (Mangan and Sisson, 2000; Mourtada-Bonnefoi and Laporte, 2004), leading to several suggested solutions.

Gardner and Denis (2004) suggested that homogeneous nucleation is only a variety of heterogeneous nucleation but takes place on submicroscopic crystals. This case is hard to argue because these particles cannot be observed directly and so cannot be proven to exist. Mourtada-Bonnefoi and Laporte (2004) suggested that if two populations of bubbles are observed, one could be the result of a homogeneous nucleation event at high supersaturation pressure deep in the conduit, and the other the result of a subsequent heterogeneous nucleation event at a shallower level due to a significant increase in decompression (Δp_{dec}, Jaupart, 1996) or due to extensive (oxide) microlite crystallization (Hurwitz and Navon, 1994 – a sudden increase in favourable bubble nucleation sites was suggested to prompt an additional bubble nucleation event). Navon et al. (1998) previously suggested that the second nucleation event could be homogeneous (independently of the nature of the first one) if the pre-existing bubbles are far away from each other and the magma between them becomes supersaturated. Gardner et al. (1999) however state, that only one nucleation event is possible and that if more than one population of bubbles is observed, it is due to bubble coalescence or inheritance of bubbles from a different system.

A summary of experimental conditions used to obtain the above outlined interpretations is in presented in Table 1.1. These studies have all examined post-process samples and tried to explain the final, observed textures. Bubble textures are very easily overprinted, and their interpretation is challenging as the initial processes can only be inferred.

Table 1.1: Summary of several experimental studies on bubble nucleation. dec. refers to decompression, HEN refers to heterogeneous bubble nucleation. ✓ indicates bubbles present on crystal surfaces, x indicates no bubbles on crystal surfaces, ? indicates not specified.

reference	composition	Δp_{dec} (MPa)	crystal	crystal attribute	bubbles	comment
Fiege et al. (2014)	andesite	70-400	/	/	in melt	homogeneous nucleation
Hurwitz and Navon (1994)	rhyolite	≥ 5	Fe-Ti oxides	present in starting material	✓	
		30	biotite		✓	
			zircon		✓	
			apatite		✓	
		50-134	feldspar		x	bubbles in crystal vicinity
			quartz		x	
Gardner et al. (1999)	rhyolite	< 20	?	?	?	HEN on dissolved crystals
		> 60			in melt	homogeneous nucleation
Gardner et al. (2000)	rhyolite	10-50	oxide microlites	crystallized	on microlites	unspecified on which microlites
			plagioclase microlites			
Mangan and Sisson (2000)	rhyolite	150	/	/	in melt	homogeneous nucleation
		31			fringe bubbles	
Gardner and Denis (2004)	rhyolite	50-70	hematite	crystallized	✓	
		60	plagioclase	crystallized	x	concluded $\sigma_{plag\text{-}bub} >> \sigma_{ox\text{-}bub}$
Mourtada-Bonnefoi and Laporte (2004)	rhyolite	150-200	/	/	in melt	homogeneous nucleation
Mangan et al. (2004)b	rhyolite	< 5	oxides	not specified	✓	
		< 25	cryptic sites		✓	HEN on dissolved crystals
		120-150	/	/	in melt	homogeneous nucleation
Gardner (2007)	rhyolite	20-90	magnetite	crystallized	✓	
			hematite	crystallized	✓	
			plagioclase	crystallized	x	
Cluzel et al. (2008)	rhyolite	> 100	/	/	in melt	homogeneous nucleation
		63-69	hematite	crystallized	✓	
Mangan and Sisson (2005), Mangan et al. (2004)a	dacite	35	feldspar	present in starting material	x	nucleation type not specified
			magnetite		✓	
			pyroxene		?	
Larsen (2008)	K-phonolite	45-50	clinopyroxene	present in starting material	✓	

1.3 Problem: difficulties in correctly interpreting interactions from post-process samples

1.3.1 Change of bubble-crystal contact angle

In the current literature regarding bubble-crystal contact angles within melts, only static contact angle values are reported. This is not surprising, as only post-process textures are available for observation. In contrast, fluid dynamics research of vapour bubbles in contact with particle surfaces within aqueous liquids allows for much easier dynamic observations. One of the results of these observations is that the contact angle is not a static property of a bubble-particle assemblage, but a dynamic one subject to change. Adamson and Gast (1997) already noted that: the contact angle cannot be viewed as simply a static quantity, but the reason for the contact angle change was well summarized by Cattide et al. (2008) with the following equation:

$$V\left(\rho_f - \rho_g\right)g + \frac{\pi D_0^2}{4}\left[p_g - \left(\rho_f g H\right)\right]_p = \pi D_0 \sigma \sin\theta_0 + \int k\, T_{e,l} n\, dS \qquad (9),$$

where V is the bubble volume, ρ is density (suffixes f and g refer to fluid and gas, respectively), g is the gravitational acceleration, D_0 is the diameter of the dry area around the bubble, H is the bubble height, σ is the surface tension, θ_0 is the outer contact angle, k is the unit vector of the z component (perpendicular to the particle's surface), T_e is the Maxwell stress tensor, n is the normal tangent unit vector, S is the area the bubble occupies on a surface.

Equation 9 shows, that in order to keep the buoyancy force, internal bubble overpressure and surface tension forces in balance during bubble growth, the contact angle must change (Cattide et al., 2008). In geological systems it is not yet possible to examine bubble-particle relations in such detail.

1.3.2 Attachment of bubbles to crystals

Bubble – crystal aggregates can form not only through heterogeneous nucleation of bubbles on crystals (or vice versa) but also from their mutual attachment. The driving force of attachment is the same as for heterogeneous nucleation, lowering of the total surface energy. However, certain minerals will form crystals that are more favourable to bubble attachment (Gualda and Ghiorso, 2007). Here I consider the attachment of smaller bubbles to larger crystals, but the same principle should hold for small crystals attaching to a larger bubble (Gualda and Anderson, 2007).

The attachment energy is defined as the total change in surface energy ($\Delta\sigma$) from the fully separated state and the fully attached state of bubbles and crystals (Gualda and Ghiorso, 2007). For attachment to be thermodynamically feasible, the bulk energy of the aggregate (bubble and crystal fully attached) must be lower than when bubble and crystal were fully separated. The total change in surface energy is always ≤ 0, meaning that bubble-crystal attachment is always favoured thermodynamically regardless of the value of the outer contact angle. Once bubbles are attached, the larger the outer contact angle (i.e. the flatter the bubble), the stronger the attachment and the harder it is for them to subsequently detach.

1.3.3 Detachment of bubbles from crystals

The process of bubbles detaching from a surface is readily observable in everyday life (e.g. when water boils in a kettle) and is the focus of many industrial processes. However, bubble detachment is scarcely mentioned in volcanology. Mangan and Sisson (2000) observed detachment of bubbles at very low decompression rates, but from the walls of the experiment capsules, not from crystals. Gualda and Ghiorso

(2007) stated that bubbles would detach once a critical bubble radius is reached. A bubble that nucleated heterogeneously on a crystal grows with time, and as it grows its radius increases and the contact angle could potentially change, due to the changes in free energy if the bubble, melt and crystal are not in equilibrium (Adamson and Gast, 1997). It is inferred from the work of Gualda and Ghiorso (2007) that an increase in outer contact angle value indicates a stronger attachment, whilst a decrease in outer contact angle value means detachment is approaching. However, a change in contact angle is impossible to observe through the study of post-process textures. The potential process of bubbles detaching from a heterogeneous nucleation crystal site is interesting as the site would then be vacated and a new bubble could nucleate. This cycle of repeating bubble nucleation and detachment would lead to a large increase in crystal efficiency at bubble nucleation.

1.3.4 Buoyancy of bubble-crystal pairs

Crystals and bubbles are generally not static in magmas. Bubbles are less dense than the melt and negatively buoyant, so they rise (note that due to the formulation of particle settling velocity of Sparks et al., 1984, positive buoyancy represents sinking and negative buoyancy represents floating; this is adopted throughout the thesis). Most crystals are denser than the melt and sink. Some authors considered the rise of bubbles negligible due to their small size and thus not important in conduits prior to the onset of fragmentation (e.g. Proussevitch and Sahagian, 2005), but Gualda and Anderson (2007) argued that it is precisely bubble migration that causes mass and heat transport. Since thermal convection is the transfer of heat associated with the relocation of matter,

the migration of bubbles along with crystals influences the thermal and compositional history of melts (Gualda and Ghiorso, 2007).

If bubbles and crystals attach, they can slow each other's movements or even become neutrally buoyant. Along with density, the difference in size of bubbles and crystals has a large effect on buoyancy. If a single bubble attaches to a single crystal of the same radius, they would still sink (as water vapour bubbles have a lower density then solid crystals). In order for bubble-crystal aggregates to be neutrally buoyant, $F_{crystal}^{buoyancy}$ and $F_{bubble}^{buoyancy}$ must be of equal but of opposite value. It is critical that bubble-crystal aggregates do not detach before becoming neutrally buoyant. The critical r_{bubble} for detachment is (Equation 10, modified from Gualda and Ghiorso, 2007):

$$r_{bubble}^{critical} = \sqrt[2]{\frac{-3\,\sigma_{VL}}{4\,g\,\Delta\rho}} \times \sin(180° - \theta) \times \sqrt[6]{\frac{4}{2-3\cos(180°-\theta)+cos^3(180°-\theta)}} \quad (10),$$

where g is the gravitational constant, σ_{VL} is the surface tension between a bubble (vapour) and the melt (liquid), $\Delta\rho$ is the density difference between the bubble and the melt and θ is the outer contact angle.

1.4 Hypothesis

The hypotheses explored in this thesis are:

1) Oxides are not the only favourable crystals for heterogeneous bubble nucleation:

    As heterogeneous bubble nucleation is always energetically favoured over homogeneous bubble nucleation, and bubbles are reported in contact with silicate crystals, why are they disregarded as bubble nucleation sites?

2) Bubble walls may act as nucleation sites for crystals:

    Based on energy consideration, the presence of a pre-existing bubble-melt interface could facilitate the crystallization of mineral species.

3) Bubble-crystal contact angles may change with time:

    Bubble growth leads to a change in bubble-crystal contact area, so a change in contact angle could be present as well. If the change in contact angle could be observed (increase or decrease) information on bubble-crystal wetting could be obtained.

The current theories, reviewed in previous subchapters, are too restrictive and due to the ease of bubble displacement and observations conducted in 2D, possibly based on erroneous assumptions, especially for heterogeneous bubble nucleation. A possible reason for such conclusions could be the few measurements of contact angles through which wettability is examined, and the measurement of these contact angles in 2D. A bubble with a small outer contact angle with a crystal (e.g. as is between bubbles and plagioclase crystals) will only be observed in contact with that crystal if the random 2D plane crosses the center of the bubble. A 2D plane of any other orientation will

show such a bubble and crystal not in contact. Thus, examining samples in 3D is much more beneficial and accurate.

Bubbles can grow with time. As a result, in the case of bubbles on crystals, their contact angle could change. The contact angle, representing the bubble-crystal surface energy, is a key parameter by which the bubble's preference for heterogeneous nucleation, attachment and critical size for detachment are examined.

1.5 Objectives

The crystals and bubbles that are present in many magmatic systems have been studied thoroughly, but for the most part separately. Very few papers exist that consider their possible interactions (e.g. Gualda and Ghiorso, 2007; Belien et al., 2010). The specific focus of this research is to bridge this gap by exploring interactions between these important components. Additionally, an andesitic melt composition was chosen to contrast with the existing mostly rhyolitic data (Table 1.1).

The objectives of this research are: 1) to determine if silicates can act as sites for nucleation of water vapour bubbles in andesite magma, 2) to determine if bubble walls can act as nucleation sites for crystals such as oxides, 3) to see how bubble-crystal attachment and detachment could be detected from post-process samples.

1.6 Methodology

In order to study bubbles, crystals and infer their interactions, a volatile-saturated andesitic melt was synthesized in a high pressure – high temperature piston-cylinder apparatus (Boyd and England, 1960). Piston-cylinders allow rapid heating and cooling of the sample, giving reliable results in the temperature and pressure ranges of 800 ºC – 2200 ºC and 100 MPa – 5 GPa, respectively (Hirschmann et al., 2008 and references therein). Bubble nucleation and growth experiments were conducted at high pressure and high temperature conditions within melts (not glasses). After decompressing and quenching the samples to room pressure and temperature, the generated textures were observed in glasses. Bubbles were generated at HPHT by crossing the H_2O pressure-temperature solubility curve through depressurisation. One of the most important aspects of this research is that it generated experimental charges that were imaged first in 3D, and afterwards, if necessary, in 2D, which brought both benefits and restrictions. Although much information on bubble nucleation was obtained from the 3D and 2D images, the early stages of the process were not accessible as the samples are still post-process. To overcome this issue, 4D *in situ* X-ray tomography methods were used to observe bubble nucleation and development during sample heating at ambient pressures.

1.6.1 High pressure and high temperature sample synthesis

The synthesis of experimental samples at high-pressure and high-temperature (HPHT) was conducted in a piston-cylinder apparatus at McGill University. HPHT piston-cylinder experiments were used to synthesize samples for *in situ* heating

experiments and to synthesize samples with macroscopic silicate crystals. For the specific piston-cylinder apparatus and assembly type used, the pressure correction between the nominal and real pressure is 50 MPa, and the friction correction is ± 25 MPa (Baker, 2004).

The pressure and temperature are raised until the sample is undersaturated in volatiles in order to dissolve all the volatiles present in the sample. The samples are held at those conditions for one hour to achieve sample homogenization, after which they are first decompressed at a chosen rate to induce supersaturation and bubble nucleation. After staying at this lower pressure for some time, they are quenched. The exact pressure and temperature parameters of each step of the experiment depend on the sample composition and volatile content. These parameters can be determined using volatile solubility models, such as Papale et al. (2006).

Most of the previous studies on bubble nucleation (Table 1.1), were performed on hydrated rhyolites, with 5 – 11 wt.% H_2O at 50-250 MPa and 750 – 900 ºC (e.g. Hurwitz and Navon, 1994; Gardner et al., 1999; Gardner et al., 2000; Mangan and Sisson, 2000; Gardner and Denis, 2004; Mourtada-Bonnefoi and Laporte, 2004; Mangan et al., 2004a; Gardner, 2007; Cluzel et al., 2008) and a few were conducted on basalt at 150-1000 MPa and 1100 – 1250 ºC (e.g. Bai et al., 2008). My experimental samples consisted of glass made from rock powder of andesitic composition, seed silicate crystals (plagioclase, clinopyroxene and amphibole) and water added in an amount sufficient for volatile supersaturation at chosen HPHT conditions. The main differences between my degassing experiments (Chapter 3) and previous ones (Table 1.1) is the use of starting andesitic glass composition and the addition of crystals into the starting material. This was done to introduce macroscopic crystal surfaces, with the

aim of avoiding the following: complete silicate crystal dissolution, bubbles on cryptic sites meant to be produced by crystal dissolution and silicate microlite crystallization. If silicate crystals crystallized and bubbles nucleated in the same experimental charge, additional difficulties in interpretations would be introduced (which phase nucleated on which, if at all, and when, relatively one to the other).

One restriction of the 3D X-ray tomography that followed each experiment is that X-rays cannot penetrate the metal capsules that contain the samples, so these needed to be taken out of their confining capsules. Due to the bubbles present (an experimental goal), the samples were very fragile and as a rule fractured upon metal capsule removal, leading to uncertainties in original sample orientation.

1.6.2 3D imaging with X-ray tomography

1.6.2.1 Basics of X-ray tomography

The analysis of rock textures consists of measuring the numbers, sizes, shapes and orientations of different objects (Higgins, 2006). X-ray computed tomography is a non-destructive method that provides high-quality results in three dimensions. X-ray tomography is based on the absorption of X-rays when passing through a sample, which is transformed into a 3D image of the linear attenuation coefficient, μ (Baruchel et al., 2000).

The linear attenuation coefficient depends on the composition and density of the sample and the energy of the X-ray beam (Baruchel et al., 2000). However, the linear attenuation coefficient is independent of the mineral's crystallographic orientation, so unless phase contrast mode is used (discussed is subsection 1.6.2.3) X-

ray tomography only produces phase maps – if objects with the same linear attenuation coefficient and cross-section (here crystals of the same composition) are in contact, they cannot be distinguished as individual objects (see Figure 2 in Baker et al., 2012).

After scanning, individual slices are reconstructed from the collected radiographs using appropriate software. The slices are closely spaced grey-scaled images and together they form a 3D volume. The basic unit of a 3D volume is a voxel, the 3D equivalent of a pixel.

There are several X-ray tomography methods, named on the resolution obtained (e.g. micro- or nano-) or the source of X-rays (conventional or synchrotron generated). Conventional X-ray tomography, sometimes referred to as benchtop tomography, is a readily available low-cost method, using a self-contained instrument. However, the X-ray beam is polychromatic, which leads to the production of beam-hardening artifacts (bright rims around objects) stemming from misleading recovery of μ (Baruchel et al., 2000). Synchrotron radiation can give monochromatic X-rays and tomography using this source provides far superior results: it was the primary analytical method used for this research. Nevertheless, I must stress the importance of benchtop tomography, since quickly obtaining lower-resolution 3D volumes in this research ensured that the most promising samples are already preselected for the synchrotron. Several other imaging techniques are implemented during scanning acquisition, such as frame averaging and random movement. The former with the aim to reduce the signal to noise ratio in the collected radiographs and the latter to reduce ring artifacts in the reconstructed images. The values chosen for each represent a compromise between scan quality and acquisition time.

1.6.2.2 Synchrotron radiation X-ray micro-tomography

Several synchrotron radiation properties contribute to its much higher image quality (Mobilio et al., 2015), compared to conventional benchtop tomography: i) near-parallel beam geometry, fast data acquisition, increased number of electrons, ii) a monochromatic beam that significantly reduces beam-hardening artifacts and gives high signal to noise ratio (both the parallel geometry and monochromaticity allow a more precise definition of object geometry), iii) very high beam intensity with X-ray energy higher than that of chemical bonds, and iv) a large sample to detector distance allowing different apparatus to be mounted around the sample, like furnaces (Baker et al., 2012).

The advantages of synchrotron radiation X-ray tomography presented above have allowed the acquisition of high-quality 3D volumes. The examination of these volumes has allowed an increased accuracy in interpreting bubble-crystal textures, as the uncertainties arising from observations from a randomly oriented 2D plane are eliminated. However, these 3D volumes still represent post-process samples from which bubble-crystal interactions need to be inferred.

1.6.2.3 Additional X-ray tomography experiments and methods

In order to overcome the problem of analyzing post-process samples, this research utilized *in situ* real time 4D synchrotron radiation X-ray micro-tomography experiments. Real time here indicates that the scan acquisition speed is faster than the speed of change of the imaged objects. The primary goal was to observe bubble-crystal interactions in real time, most importantly, heterogeneous bubble nucleation. A laser-

heated furnace was placed around the sample and in the path of the X-ray beam to provide localized and controlled heating the heating was achieved by using two class IV lasers and the temperature was measured with a pyrometer (Fife et al., 2012). Entire 3D sample volumes were collected each 0.5 s for 50 s using an ultra-fast continuous data acquisition end-station with a CMOS detector (GigaFRoST, Mokso et al., 2017). This allowed for the direct observation of heterogeneous bubble nucleation and changes in contact angles. The benefits of *in situ* observations cannot be overstated and the temporal resolution of 0.5 s achieved is unprecedented at this time.

The acquisition of 3D volumes has improved accuracy, and 4D experiments provided *in situ* observations, however, the problem of X-ray absorbance remains. The focus of the research are bubble-crystal interactions, and silicate crystals are of interest (especially plagioclase). Thus, it is imperative for them to be visible, which is challenging when they are embedded in a silicate glass, due to the similarities in the X-ray absorbance. To overcome the issue, propagation-based phase contract imaging was used. Usually, in absorption X-ray imaging (described so far) the contrast is generated by the absorption properties of the sample. Propagation-based phase contract imaging is a specific imaging mode, where the contrast is generated additionally by the interference between parts of the wave front that experience different phase shifts (Mobilio et al., 2015). The result is that interfaces of abrupt phase change, such as the surface of a crystal, are more visible. This method already proved very useful for the imaging of feldspar crystals in a glass matrix (Polacci et al., 2010).

During X-ray tomography imaging at the Swiss Light Source, a phase retrieval algorithm was applied to sample reconstruction. It is important to distinguish that phase contrast imaging is an imaging mode, whereas phase retrieval is a set of algorithms

applied when the 3D volume is reconstructed. More specifically, phase retrieval is a method for quantitative phase extraction using a single propagation-induced phase contrast image taken using point-projection X-ray microscopy (Paganin et al., 2002). The main benefit for this research is the additional enhancement of silicate crystal borders.

X-ray tomography and 3D image analysis were used to observe bubble-crystal interactions at sub-second resolutions in 4D experiments and to examine post-process samples (either post-heating or post-decompression) in 3D to aid in correct bubble-crystal relation interpretation. Both HPHT piston-cylinder experiment and 3D imaging and analysis tested all three hypotheses (the role of silicate crystals in bubble nucleation, the nucleation of crystals on bubble walls and the change of bubble-crystal contact angle).

1.6.3 Analysis of reconstructed 3D sample volumes

Once the 3D reconstructed volumes are obtained, there are several steps before textural and morphological characteristics can be quantified. The first step is to select a volume of interest (VOI); a representative subvolume that is large enough to represent samples' complexity and heterogeneity, but small enough not to overload the computer. For this research, the subvolume most commonly contained one crystal and bubbles associated with it, or vice versa. The sizes of subvolumes were not uniform in this research as they partly depend on the volumes of different crystals and bubbles. If the volumes were part of a 4D sequence, the same subvolume must be selected at each time step. Due to sample expansion during heating in 4D experiments, the chosen

subvolume did not maintain the same 3D coordinates in each time step. Bubbles proved easier to segment due to their large attenuation difference from the glass and crystals, but plagioclase crystals were difficult and time-consuming, even in samples where both phase contact imaging and phase retrieval algorithms were applied. Detectability of bubbles or crystals was set to 2 voxel edge lengths.

1.6.4 Scanning electron microscopy (SEM)

Three-dimensional analyses were complemented by more traditional two-dimensional analysis and scanning electron microscopy was used for semi-quantitative compositional measurements using back-scattered electrons. Scanning electron microscopy is a method with which plagioclase-melt interfaces can be readily observed and as such it complements 3D imaging where these interfaces are not easily detected. Additionally, SEM offered a comparison of what a conventional 2D method could provide to 3D XRT observations. This comparison highlighted how interpretations can be influenced by observing in 3D and not just 2D. No hypotheses were directly tested with this method. The scanned 3D volumes still influenced the sample preparation for SEM since the grinding and polishing was constrained to reach specific regions located in 3D volumes.

1.7 Format of the thesis

This doctoral thesis is divided into five chapters and presents a collection of three scientific articles. Two are published in peer-reviewed scientific journals and the third is accepted with major revisions at the moment of the final doctoral thesis submission. The first chapter is an introduction and the fifth is the conclusion. The principal author of all three articles and all thesis chapters is the PhD candidate.

Chapter 1 is an introduction to the entire thesis and contains a short overview of the literature concerning the problem, the hypotheses, the objectives and the methodology.

Chapter 2 contains the first published article, titled *"Dynamic observations of vesiculation reveal the role of silicate crystals in bubble nucleation and growth in andesitic magmas"* published in Lithos in January 2018 (pages 532-546). The article presents the results of a series of 4D (3D + time) X-ray tomography experiments on hydrated andesitic glasses containing seed silicate crystals. The main finding is the real time observations of the location of heterogeneous bubble nucleation and the change in bubble-crystal contact angle. The scientific contribution is the finding that silicate crystals nucleated bubbles on their surfaces during 1 atm heating.

Chapter 3 presents the manuscript for the third article, titled *"Nucleation and growth of bubbles on plagioclase crystals during experimental decompression degassing of andesitic melts"* submitted to the Journal of Volcanology and Geothermal Research in April 2019 and accepted with major revisions in June 2019. The manuscript builds on the findings from the first article (Chapter 2). The main finding is the formation of bubble-plagioclase aggregates in decompression-induced degassing experiments on andesitic glasses. In the scanned 3D volumes, bubble number densities

and size distributions are analyzed and the possibilities of heterogeneous bubble nucleation on plagioclase crystals are discussed.

Chapter 4 presents the second published article, titled *"Production and detachment of oxide crystal shells on bubble walls during experimental vesiculation of andesitic magmas"* published in Contribution to Mineralogy and Petrology in March 2019, volume 174 (pages 1-21). The article focuses on complex bubble-oxide aggregates found within experimentally synthesized and decompressed andesitic glasses. This phenomenon has been observed by others in experimental charges but was frequently disregarded. Here, the aggregates were imaged in 3D by X-ray tomography and their structure and origin discussed. The article indicates potential natural systems where the same kinetics could occur.

Chapter 5 is a summary of the main findings of the overall research presented and the main conclusions drawn from them. The chapter finishes with a suggested direction for future studies.

The three objectives are addressed in Chapters 2 - 4. The hypothesis that silicate crystal surfaces can provide bubble nucleation sites stands. The hypothesis that bubble walls can provide sites for crystal nucleation stands. Detachment and attachment were not directly observed, but new parameters (contact angle change) that could indicate a tendency for bubble detachment were observed.

1.8 Declaration of original contribution

Bubbles and crystals have previously been studied as separate phases in volcanic environments, but only few contributions examined their interactions (e.g., Hurwitz and Navon, 1994; Gualda and Anderson, 2007; Gualda and Ghiorso, 2007; Belien et al., 2010). The principal focus of this thesis is bubble-crystal interaction, such as heterogeneous nucleation, attachment, and detachment.

The samples studied were experimentally synthesized. All experiments and subsequent scans were conducted and/or guided by the PhD candidate. The use of samples of andesitic composition contributes a difference from previous degassing studies that have used samples of rhyolitic or basaltic compositions. A novel aspect is the deliberate incorporation of macroscopic silicate crystals into the experimental charges to better represent natural environments.

This research was partly methodology-driven, as X-ray tomography was always the primary method of sample analysis. 4D *in situ* real time heated experiments were conducted with a 0.5 s per 3D scan acquisition time, presenting an unprecedented temporal resolution. Additionally, a new protocol for the measurement of 3D bubble-crystal contact angles was introduced and implemented.

1.9 Contributions from co-authors

Both published articles and the submitted manuscript contain several co-authors, partly stemming from the time-limited task related to X-ray tomography. Synchrotron time is awarded in continuous time slots: 72 hours at the Swiss Light Source and two times 48 hours at the Advanced Photon Source. As synchrotron time is precious and highly sought after, no time can be wasted and so a 24-hour day is divided into three 8-hour shifts. This leads to a team of minimum two people per allocated period (a single person is possible but not recommended due to the repetitive work of scanning and jetlag associated with the travel to one of the synchrotrons).

For the tomography scanning at the Advanced Photon Source, the teams were once Pia Pleše and Marko Kudrna Prašek and once Pia Pleše and Michael Higgins. Both times the PhD candidate (Pia Pleše) guided the scanning and the accompanying person assisted.

For the 4D tomography experiments at the Swiss Light Source, the team consisted of seven people: the beamline scientist Julie Fife, the PhD candidate Pia Pleše and Don Baker, Lucia Mancini, Francesco Brun, Gabriele Lanzafame and Jake Casselman. The larger group was needed because the minimum number of three people (not two) per 8-hour shift was needed – one person was in charge of sample reconstruction and implementation of phase retrieval algorithms, one person monitored the heating and recorded sample changes, and the third person assisted in other tasks. All the people involved are co-authors in article 1 (Chapter 2).

In article 3 (Chapter 4), co-authors Lucia Mancini and Gabriele Lanzafame helped in optimizing the data analysis parameters, Marko Kudrna Prašek helped with

the piston-cylinder experiments and SEM analysis (same as for article 2), and Shane Rooyakkers collected the natural samples from Krafla (Iceland) and helped interpret their textures.

Detailed co-author contributions are also indicated in subsections 2.7, 3.7 and 4.7.

1.10 References:

Adamson, A. W., Gast, A., 1997. Physical Chemistry of Surfaces, sixth ed. John Wiley and Sons, New York.

Bai, L., Baker, D. R., Rivers, M., 2008. Experimental study of bubble growth in Stromboli basalt melts at 1 atm. *Earth and Planetary Science Letters* 267(3), 533-547.

Baker, D. R., 2004. Piston-cylinder calibration at 400 to 500 MPa: A comparison of using water solubility in albite melt and NaCl melting. *American Mineralogist* 89(10):1553-1556.

Baker, D. R., Mancini, L., Polacci, M., Higgins, M. D., Gualda, G. A. R., Hill, R. J., Rivers, M. L., 2012. An introduction to the application of X-ray microtomography to the three-dimensional study of igneous rocks. *Lithos* 148, 262-276.

Baruchel, J., Maire, E., Merle, P., Peix, G., Buffiere, J.-Y., 2000. X-Ray Tomography in Material Science, General Principles. Hermes Science Publications, Paris.

Belien, I. B., Cashman, K. V., Rempel, A. W., 2010. Gas accumulation in particle-rich suspensions and implications for bubble populations in crystal-rich magma. *Earth and Planetary Science Letters* 297(1–2), 133-140.

Blander, M., Katz, J. L., 1975. Bubble nucleation in liquids. *AIChE Journal* 21(5), 833-848.

Boyd, F. R. England, J. L., 1960. Apparatus for phase-equilibrium measurements at pressures up to 50 kilobars and temperatures up to 1750 °C. *Journal of Geophysical Research* 65, 741–748.

Cattide, A., Celata, G. P., Di Marco, P., Grassi, W., 2008. Experimental study on bubble detachment under variable heat load and the action of electric field. *Fluid Dynamics Research* 40(7-8), 485.

Cichy, S. B., Botcharnikov, R. E., Holtz, F., Behrens, H., 2011. Vesiculation and Microlite Crystallization Induced by Decompression: a Case Study of the 1991-1995 Mt Unzen Eruption (Japan). *Journal of Petrology* 52(7-8):1469-1492. doi:10.1093/petrology/egq072

Clift, R., Grace, J., Weber, M., 1978. Bubbles, Drops and Particles. Academic Press, New York.

Cluzel, N., Laporte, D., Provost, A., Kannewischer, I., 2008. Kinetics of heterogeneous bubble nucleation in rhyolitic melts: implications for the number density of bubbles in volcanic conduits and for pumice textures. *Contributions to Mineralogy and Petrology* 156(6), 745-763.

Cole, R., 1974. Boiling nucleation. *Advances in Heat Transfer* 10, 85-166.

Dunning, W., 1969. General and theoretical introduction. Nucleation, edited by A. C. Zettlemoyer. 1-67. Marcel Dekker, New York.

Fiege, A., Holtz, F., Cichy, S. B., 2014. Bubble formation during decompression of andesitic melts. *American Mineralogist* 99(5-6), 1052-1.

Fife, J. L., Rappaz, M., Pistone, M., Celcer, T., Mikuljan, G., Stampanoni, M., 2012. Development of a laser-based heating system for in situ synchrotron-based X-ray tomographic microscopy. *Journal of Synchrotron Radiation* 19(3), 352-358.

Gardner, J. E., 2007. Heterogeneous bubble nucleation in highly viscous silicate melts during instantaneous decompression from high pressure. *Chemical Geology* 236(1–2), 1-12.

Gardner, J. E., Denis, M.-H., 2004. Heterogeneous bubble nucleation on Fe-Ti oxide crystals in high-silica rhyolitic melts. *Geochimica et Cosmochimica Acta* 68(17), 3587-3597.

Gardner, J. E., Hilton, M., Carroll, M. R., 1999. Experimental constraints on degassing of magma: isothermal bubble growth during continuous decompression from high pressure. *Earth and Planetary Science Letters* 168(1), 201-218.

Gardner, J. E., Hilton, M., Carroll, M. R., 2000. Bubble growth in highly viscous silicate melts during continuous decompression from high pressure. *Geochimica et Cosmochimica Acta* 64(8), 1473-1483.

Giachetti, T., Druitt, T. H., Burgisser, A., Arbaret, L., Galven, C., 2010. Bubble nucleation, growth and coalescence during the 1997 Vulcanian explosions of Soufrière Hills Volcano, Montserrat. *Journal of Volcanology and Geothermal Research* 193(3), 215-231.

Gualda, G. A., Anderson, 2007. Magnetite scavenging and the buoyancy of bubbles in magmas. Part 1: Discovery of a pre-eruptive bubble in Bishop rhyolite. *Contributions to Mineralogy and Petrology* 153(6), 733-742.

Gualda, G. A., Ghiorso, M. S., 2007. Magnetite scavenging and the buoyancy of bubbles in magmas. Part 2: Energetics of crystal-bubble attachment in magmas. *Contributions to Mineralogy and Petrology* 154(4), 479-490.

Higgins, M. D., 2006. Quantitative textural measurements in igneous and metamorphic petrology. Cambridge University Press, 2006.

Hirth, J., Pound, G. M., Pierre, G. R. St., 1970. Bubble nucleation. *Metallurgical Transactions* 1(4), 939-945.

Hirschmann, M. M., Ghiorso, M. S., Davis, F. A., Gordon, S. M., Mukherjee, S., Grove, T. L., Krawczynski, M., Medard, E., Till. C. B., 2008. Library of Experimental Phase Relations (LEPR): A database and Web portal for experimental magmatic phase equilibria data. *Geochemistry, Geophysics, Geosystems* 9(3).

Hurwitz, S., Navon, O., 1994. Bubble nucleation in rhyolitic melts: Experiments at high pressure, temperature, and water content. *Earth and Planetary Science Letters* 122(3–4), 267-280.

Jaupart, C., 1996. Physical models of volcanic eruptions. *Chemical Geology* 128(1), 217-227.

Landau, L., Lifshitz, E., 1980. Statistical Physics, Vol. 1. Oxford: Pergamon 24: 31-57.

Larsen, J. F., 2008. Heterogeneous bubble nucleation and disequilibrium H_2O exsolution in Vesuvius K-phonolite melts. *Journal of Volcanology and Geothermal Research* 175(3), 278-288.

Mangan, M., Sisson, T., 2000. Delayed, disequilibrium degassing in rhyolite magma: decompression experiments and implications for explosive volcanism. *Earth and Planetary Science Letters* 183(3), 441-455.

Mangan, M., Sisson, T., 2005. Evolution of melt-vapor surface tension in silicic volcanic systems: Experiments with hydrous melts. *Journal of Geophysical Research: Solid Earth* 110(B1), B01202.

Mangan, M., Sisson, T. W., Hankins, W. B., 2004a. Decompression experiments identify kinetic controls on explosive silicic eruptions. *Geophysical Research Letters* 31(8), L08605.

Mangan, M., Mastin, L., Sisson, T., 2004b. Gas evolution in eruptive conduits: combining insights from high temperature and pressure decompression experiments with steady-state flow modeling. *Journal of Volcanology and Geothermal Researc*h 129(1-3), 23-36.

Mobilio, S., Boscherini, F., Meneghini, C. (eds.), 2015. Synchrotron Radiation: Basics, Methods and Applications. Springer, New York.

Mokso, R., Schlepütz, C. M., Theidel, G., Billich, H., Schmid, E., Celcer, T., Mikuljan, G., Sala, L., Marone, F., Schlumpf, N., Stampanoni, M., 2017. GigaFRoST: the gigabit fast readout system for tomography. *Journal of Synchrotron Radiation* 24(6), 1250-1259.

Mourtada-Bonnefoi, C. C., Laporte, D., 2004. Kinetics of bubble nucleation in a rhyolitic melt: an experimental study of the effect of ascent rate. *Earth and Planetary Science Letters* 218(3), 521-537.

Navon, O., Chekhmir, A., Lyakhovsky, V., 1998. Bubble growth in highly viscous melts: theory, experiments, and autoexplosivity of dome lavas. *Earth and Planetary Science Letters* 160(3–4), 763-776. doi.org/10.1016/S0012-821X(98)00126-5

Navon, O., Lyakhovsky, V., 1998. Vesiculation processes in silicic magmas. *Geological Society, London, Special Publications* 145(1), 27-50.

Paganin, D., Mayo, S. C., Gureyev, T. E., Wilkins, P. R., Wilkins, S. W., 2002. Simultaneous phase and amplitude extraction from a single defocused image of a homogeneous object. *Journal of Microscopy* 206, 33–40.

Papale, P., Moretti, R., Barbato, D., 2006. The compositional dependence of the saturation surface of H_2O+ CO_2 fluids in silicate melts. *Chemical Geology* 229(1-3), 78-95.

Polacci, M., Mancini, L., Baker, D. R., 2010. The contribution of synchrotron X-ray computed microtomography to understanding volcanic processes. *Journal of Synchrotron Radiation* 17, 215–221.

Proussevitch, A., Sahagian, D., 2005. Bubbledrive-1: A numerical model of volcanic eruption mechanisms driven by disequilibrium magma degassing. *Journal of Volcanology and Geothermal Research* 143(1), 89-111.

Shea, T., 2017. Bubble nucleation in magmas: A dominantly heterogeneous process?. *Journal of Volcanology and Geothermal Research* 343, 155-170.

Shea, T., Houghton, B. F., Gurioli, L., Cashman, K. V., Hammer, J. E., Hobden, B. J., 2010. Textural studies of vesicles in volcanic rocks: an integrated methodology. *Journal of Volcanology and Geothermal Research* 190(3-4), 271-289.

Sparks, R. S. J., Huppert, H. E., Turner, J. S., 1984. The fluid dynamics of evolving magma chambers. *Philosophical Transactions of the Royal Society of London Series A, Mathematical and Physical Sciences* 310 (1514), 511-534.

Volmer, M., 1939. Kinetics of Phase Formation (Kinetik der Phasenbildung). No. F-TS-7068-RE. Foreign Technology Div Wright-Patterson Air Force Base Oh.

Volmer, M., Weber, A., 1926. Keimbildung in übersättigten Gebilden. *Zeitschrift für physikalische Chemie* 119, 277-301.

Zanotto, E. D., Fokin, V. M., 2003. Recent studies of internal and surface nucleation in silicate glasses. *Philosophical Transactions of the Royal Society of London Series A: Mathematical, Physical and Engineering Sciences* 361(1804), 591-613.

CHAPTER 2

Dynamic observations of vesiculation reveal the role of silicate crystals in bubble nucleation and growth in andesitic magmas

Pia Pleše[a], Michael D. Higgins[a], Lucia Mancini[b], Gabriele Lanzafame[b],

Francesco Brun[c], Julie L. Fife[d], Jake Casselman[e] and Don R. Baker[e]

[a] – Département des sciences appliquées, Université du Québec à Chicoutimi (UQAC), 555, boulevard de l'Université, Chicoutimi (Québec), Canada G7H 2B1

[b] – Elettra – Sincrotrone Trieste S.C.p.A. S.S. 14 km 163.5 in Area Science Park, 34149 Basovizza (Trieste), Italy

[c] - National Institute of Nuclear Physics (INFN), Padriciano 99, 34149 Trieste, Italy

[d] - Previously with Swiss Light Source, Paul Scherrer Institut, 5232 Villigen PSI, Switzerland

[e] – Department of Earth and Planetary Sciences (EPS), McGill University, 3450 University Street, Montréal (Québec) Canada, H3A 0E8

Published in

Lithos, Volume 296-299, pages 532-546

January 2018

https://doi.org/10.1016/j.lithos.2017.11.024

RÉSUMÉ

La nucléation et la croissance des bulles contrôlent l'explosivité des éruptions volcaniques et la cinétique de ces processus est généralement déterminée à partir de l'examen d'échantillons naturels et de produits expérimentaux trempés. Cependant, ces échantillons ne fournissent qu'une vue de l'état final, à partir duquel les conditions initiales d'un système magmatique en évolution dans le temps sont ensuite déduites. Les interprétations qui suivent sont inexactes du fait de l'impossibilité de déterminer les conditions exactes de nucléation et du détachement potentiel des bulles de leurs sites de nucléation, une incertitude qui peut masquer leur emplacement de nucléation - de manière homogène dans la fonte ou hétérogène à l'interface entre le cristal et la fonte. Nous présentons les résultats d'une série d'expériences dynamiques de microscopie à rayons X 4D, en temps réel (*in situ*), dans lesquelles nous avons observé le développement de bulles dans des magmas silicatés contenant des cristaux. Verres andésitiques synthétisés expérimentalement avec 0.25 – 0.5 % en poids de H_2O et les cristaux de silicate ont été chauffés à 1 atm pour induire la nucléation des bulles et suivre la croissance et le mouvement des bulles. Contrairement aux études précédentes sur des échantillons naturels et produits expérimentaux, nous avons constaté que les bulles se nucléarisent facilement sur les cristaux de plagioclase et de clinopyroxène, que leur angle de contact changeait au cours de la croissance et qu'elles pouvaient atteindre des tailles plusieurs fois supérieures à celles du silicate à la surface duquel elles provenaient. La nucléation rapide et hétérogène des bulles à faible degré de sursaturation en présence de cristaux de silicate démontre que les silicates peuvent affecter la vésiculation, ce qui influe directement sur le développement subséquent de la perméabilité et la transition expansive vs explosive dans les éruptions volcaniques.

ABSTRACT

Bubble nucleation and growth control the explosivity of volcanic eruptions, and the kinetics of these processes are generally determined from examinations of natural samples and quenched experimental run products. These samples, however, only provide a view of the final state, from which the initial conditions of a time-evolving magmatic system are then inferred. The interpretations that follow are inexact due to the inability of determining the exact conditions of nucleation and the potential detachment of bubbles from their nucleation sites, an uncertainty that can obscure their nucleation location – either homogeneously within the melt or heterogeneously at the interface between crystals and melts. We present results of a series of dynamic, real-time (*in situ*) 4D X-ray microscopy experiments where we observed the development of bubbles in crystal-bearing silicate magmas. Experimentally synthesized andesitic glasses with 0.25 – 0.5 wt. % H_2O and seed silicate crystals were heated at 1 atm to induce bubble nucleation and track bubble growth and movement. In contrast to previous studies on natural and experimentally produced samples, we found that bubbles readily nucleated on plagioclase and clinopyroxene crystals, that their contact angle changes during growth and that they can grow to sizes many times that of the silicate on whose surface they originated. The rapid heterogeneous nucleation of bubbles at low degrees of supersaturation in the presence of silicate crystals demonstrates that silicates can affect when vesiculation ensues, directly influencing subsequent permeability development and the effusive vs. explosive transition in volcanic eruptions.

2.1 Introduction

Volcanic eruptions are commonly driven by the nucleation, expansion (growth) and migration of volatile bubbles (predominantly H_2O and CO_2) following supersaturation of the melt caused by decompression, heating or crystallization (Sparks, 1978). If bubbles nucleate and grow (Figure 2.1) at near-equilibrium conditions quiescent eruptions are probable, whereas if a significant barrier to bubble nucleation and growth is present extreme amounts of volatile supersaturation may be required before explosive nucleation and growth of bubbles leading to violent eruptions. Understanding bubble growth is a longstanding scientific focus (Gardner et al., 1996; Proussevitch and Sahagian, 2005; Giachetti et al., 2010; Sparks, 1978). The "when" of bubble nucleation in silicate melts has also been extensively studied (the reader is referred to the review by Fiege and Cichy, 2015), but "where" nucleation begins has not received equal attention.

The conditions of bubble nucleation, either homogeneously within the melt, or heterogeneously on pre-existing melt-crystal interfaces (Figure 2.1), remain obscure. Due to large density differences between a gas bubble and its surrounding magma (melt + crystals), bubbles can be an easily displaced phase. Their mobility can potentially lead to erroneous assumptions of the bubbles' initial position, based upon observations of the bubbles' final positions in post-process (*ex situ*) samples. Most previous studies of bubble nucleation and growth investigated natural volcanic samples and quenched experimental run products that only provide the final state, from which the initial conditions of a time-evolving magmatic system must then be inferred. Knowledge of all aspects of nucleation and growth of bubbles in magmatic systems is one of the keys to a better understanding of volcanic eruption mechanisms.

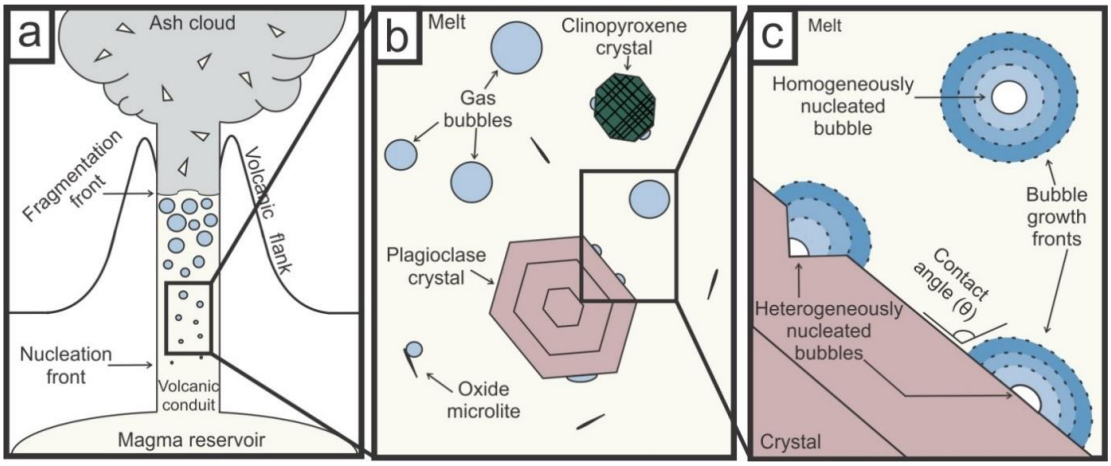

Figure 2.1: Model of bubble formation in silicate melts. a) The nucleation front is marked by the first appearance of bubbles. The fragmentation front marks the transition from a bubbly melt to a gassy spray (Gardner et al., 1996; Proussevitch and Sahagian, 2005; Sparks, 1978). The ash cloud contains particles originating from the volcanic conduit. b) The magma within a conduit can contain crystals of various sizes and compositions. c) Depending on pressure, temperature, and melt composition, bubbles can nucleate homogeneously or heterogeneously. The contact, or wetting, angle (θ) is the angle between the bubble and the crystal measured in the melt (Fiege and Cichy, 2015; Gualda and Ghiorso, 2007).

The nucleation location is influenced by the interfacial energy between the exsolved fluid and molten or solid phases (Hurwitz and Navon, 1994). In a heterogeneous bubble nucleation scenario, a melt-crystal interface already exists prior to bubble nucleation, hence the energy needed to nucleate a bubble is decreased compared to homogeneous bubble nucleation, making the heterogeneous case more favourable and possible at lower volatile supersaturations (Hurwitz and Navon, 1994; Landau and Lifshitz 1980; Navon and Lyakhovsky, 1998). Once a melt becomes supersaturated in a volatile component, the pairing of a bubble and a crystal is always a thermodynamically favoured starting point, achieved either by heterogeneous bubble nucleation or by attachment of existing bubbles to crystals (Gualda and Ghiorso, 2007).

Due to the interfacial energies involved (bubble-crystal, bubble-melt and melt-crystal), the wettability of a crystal by a bubble (where wetting is the ability of the volatile phase to remain in contact with the solid phase, Young, 1805) is considered a representation of the efficiency of a crystal to nucleate a bubble (Hurwitz and Navon, 1994). When comparing different bubble-crystal pairs, various crystal efficiencies at nucleating bubbles are inferred from the values of the contact angle θ between them (Figure 2.1) and the critical value is set to be 68 degrees (Hurwitz and Navon, 1994). Above this value, the crystal is considered efficient at nucleating bubbles, and below this value, the crystal is considered inefficient (Hurwitz and Navon, 1994). Oxides are currently considered favourable bubble nucleation sites (e.g. Gualda and Anderson, 2007; Gualda and Ghiorso, 2007) due to their significant compositional and bonding differences from the encompassing silicate melt (Mysen and Richet, 2005) as well as because of their poor wettability by the melt (Adamson and Gast, 1997).

Most experiments on heterogeneous bubble nucleation (e.g. Gardner et al., 2000; and references in Figure 2.2) were conducted using rhyolitic melts where bubbles were mostly found on oxide microlites, such as titanomagnetite, with very few reported on silicates. However, due to instrumental limitations, bubble-oxide contact angles were rarely measured and not universally found to be greater than 68 ° (Figure 2.2). The data for bubble-silicate crystal contact angles is equally sparse, since silicate crystals are generally excluded from degassing studies (the starting melt is commonly without crystals), but where measured, θ was smaller than seen for oxides (except for biotite; Hurwitz and Navon, 1994). We must stress that all the contact angles reported so far in the literature were measured in 2D, and the plane in question did not necessarily pass through the bubble's maximum cross-section.

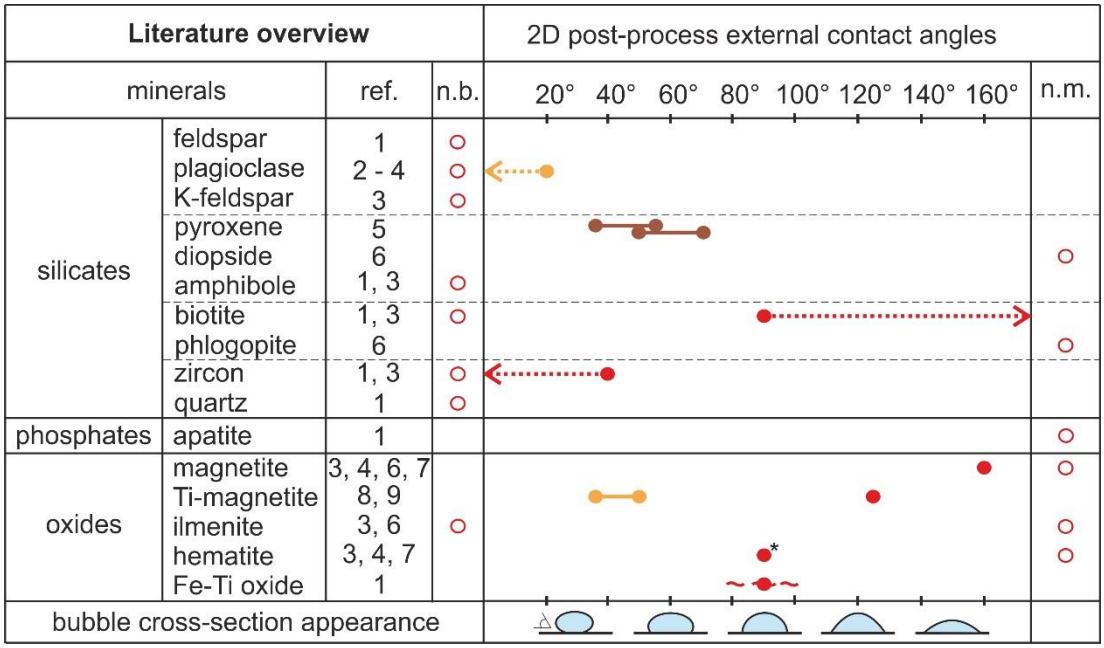

Figure 2.2: Literature compilation of reported bubble-crystal 2D post-process external contact angles. Mineral names are those used in the study. References: 1 = Hurwitz and Navon (1994), 2 = Eichelbert and Hayes (1982), 3 = Cluzel et al. (2008), 4 = Gardner (2007), 5 = Larsen (2008), 6 = Navon and Lyakhovsky (1998), 7 = Gardner and Denis (2004), 8 = Mangan and Sisson (2005), 9 = Mangan et al. (2004). Abbreviations: n.b. = no bubbles present on the crystal surface, n.m. = no measurement of contact angles is reported even though bubbles are present on the crystal surface. Yellow colour represents dacite, red rhyolite and brown K-phonolite. The star sign indicates a calculated, not measured, value. The wavy broken line represents a value around 90°, and dotted arrows represent values reported as lesser or larger than a certain value. The number of measurements was not indicated in any of the studies.

Recently, additional mechanisms of inducing homogeneous bubble nucleation have been hypothesized, such as the passage of seismic waves through a melt (Acocella, 2014; Manga and Brodsky, 2006). If homogeneous nucleation can be achieved more easily than previously thought, and heterogeneous nucleation is always easier to achieve than homogeneous, could silicate crystal surfaces play a role in bubble nucleation? The specific goals of this study were to explore bubble nucleation efficiencies of some silicate crystals based on the following observations:

1) Even though they are seen as inefficient, silicate minerals with attached bubbles have been reported, sometimes even with the same 2D contact angle θ value as measured on oxides (Figure 2.2);

2) The mineral abundance conundrum – iron oxides, not a dominant crystal phase in silicate melts, are considered the most efficient crystals for heterogeneous bubble production (Hurwitz and Navon, 1994). However, it has been questioned whether oxides alone can provide enough nucleation sites to account for the bubble number densities recorded (Mangan and Sisson, 2000; Mourtada-Bonnefoi and Laporte, 2004). If oxides are not found attached to bubbles and silicate crystals (if present) are not considered, then homogeneous nucleation is deemed dominant (e.g. Gualda and Ghiorso, 2007).

3) Bubbles are not stationary in silicate melts and can detach from, or attach to, crystals (Gualda and Ghiorso, 2007), but this process has never been directly observed and hence generally not taken into account, although several authors have considered this possibility (Belien et al., 2010; Blythe et al., 2015; Gualda and Ghiorso, 2007; Mangan and Sisson, 2000).

4) The contact angle θ does not necessarily remain constant throughout a bubble's growth (Gardner and Denis, 2004), so it is difficult to determine from observations of post-process samples the instant when the bubble was ″frozen″ (by natural solidification or experimental quench). Therefore, we do not know if the sample approached kinetic equilibrium and if the measured contact angle is the final one.

In order to examine the first seconds of bubble formation, we employed 4D X-ray tomographic microscopy as a tool to image and record nucleation and growth, therefore building on the pioneering work on *in situ* 2D observations of bubble nucleation and growth (Applegarth et al., 2013; Bagdassarov et al., 1996; Gondé et al., 2006; Gondé et al., 2011; Massotta et al., 2014) with the latest developments in 3D and 4D imaging of geological materials (Bai et al., 2008; Baker et al., 2012a; Pistone et al., 2015a., 2015b).

2.2 Materials and methods

2.2.1 Hydrous glass synthesis

The starting materials for the vesiculation experiments were synthesized using a piston-cylinder apparatus at McGill University (Montréal, Québec, Canada). Rock powder of andesitic composition (AT-29 with 56.8 wt% SiO_2, from Baker and Eggler, 1987) was added to Pt-capsules, along with silicate crystals and 0.25-0.5 wt. % H_2O. An andesitic melt composition was chosen to contrast with existing rhyolitic and dacitic data and because it corresponds to compositions of arc-type volcanos, which are frequently explosive (Sakuyama and Kushiro, 1979; Sigurdsson et al., 2015). The silicate crystals were plagioclase (gem-quality labradorite) and clinopyroxene (augite, from Baker and Eggler, 1987), and both were crushed before being added to the capsule. They were chosen to represent common magma phenocrysts and thus introduce crystal surfaces of minerals thought to be compositionally too similar to the melt to be efficient at nucleating bubbles (Mangan et al., 2004). These minerals contain low concentrations of inclusions (some oxides in the clinopyroxene) and they are nominally anhydrous. The added amount of water was kept low to create melts that would be only slightly supersaturated at 1 atm during the dynamic tomography experiments. The capsules were welded shut and checked for water loss by weighing before and after an hour of heating in a 110 °C furnace.

Three synthesis experiments were performed at 1275°C, 1 GPa to create crystal-bearing hydrous glasses. The durations were chosen to be sufficient for water to homogenize by diffusion in the capsule, but short enough so that the added crystals

did not dissolve. The first run had two capsules, one with AT-29 + clinopyroxene seed crystals (″1a″) and the other with AT-29 + plagioclase (″1b″), both with 0.5 wt. % H_2O and held at pressure and temperature conditions for 1 hour before isobaric quench. The second run also had two capsules, both with AT-29 + clinopyroxene crystals, but with one containing 0.5 wt. % H_2O (″2a″) and the other 0.25 wt. % H_2O (″2b″), both performed for 20 min. The third run was also of 20 min duration and had only one capsule (″3″), containing both AT-29 + clinopyroxene + plagioclase crystals and 0.5 wt. % H_2O. The quenched glass + crystal run products were removed from their Pt-capsules, which resulted into their fragmentation into several pieces.

2.2.2 X-ray computed tomography (CT)

X-ray microtomography (microCT) was used to characterize the synthesis and vesiculation experiments in this study. This technique provides 3D images of specimens and is well-established in the geoscience community (Baker et al., 2012b). In order to fully characterize both the starting materials and the run products of the 4D vesiculation experiments, different X-ray tomography instruments were used. A short overview of the tomography methods applied, the main differences between them, and questions aimed to be answered by them can be found in Table 2.1.

Table 2.1: Summary of different tomography methods used and questions to be answered with them. Conventional refers to stand alone microCT instruments, microCT = micro-scale computed tomography, nanoCT = nano-scale computed tomography, SR = synchrotron radiation. Pixel size refers to 2D image elements. Phase contrast is a technique applied during imaging, and phase retrieval is a set of algorithms applied while reconstructing the imaged radiographs.

Tomography method	**Radiation type**	**Pixel size**	**Phase contrast**	**Phase retrieval**	**Question asked**
microCT	Conventional, *ex situ*	2.59 μm	no	no	1) Did bubbles form? 2) Did clinopyroxene crystals melt during synthesis experiments?
nanoCT	Conventional, *ex situ*	0.22 μm	yes	no	1) Did plagioclase crystals melt during synthesis experiments? 2) Did cracks form at the crystal-glass interface?
4D SR microCT	Synchrotron, *in situ*	3 μm	yes	yes	When do bubbles form and how rapidly?
SR microCT	Synchrotron, *ex situ*	0.65 μm	yes	yes	Where did bubbles form?

2.2.3 Conventional X-ray microtomography (microCT)

Pieces of glass + crystals from several synthesis samples were imaged with a Skyscan 1172 desktop X-ray tomography machine at the MIAM laboratory of McGill University to ascertain if bubbles had formed, and if the silicate crystals had melted, during the synthesis. The scanning conditions were 55 kV, 179 μA, Al filter, camera binning 2x2, source-to-sample distance = 38.68 mm, camera-to-source distance = 345.101 mm, camera pixel size = 11.56 μm, image pixel size = 2.59 μm, exposure time = 0.2065 seconds, rotation step = 0.4 °, projection number = 902 over 360 °, frame averaging = 3, random movement = 10.

A natural sample of basaltic glass from Stromboli volcano was also scanned so that our experimental results could be compared to a natural material. The scanning conditions were 44 kV, 226 μA, Al filter, camera binning 4x4, source-to-sample distance = 36.1 mm, camera-to-source distance = 345.101 mm, camera pixel size = 11.56 μm, image pixel size = 4.84 μm, exposure time = 0.474 seconds, rotation step = 0.68 °, projection number = 531 over 360 °, frame averaging = 4, random movement = 10.

2.2.4 Conventional X-ray nanotomography (nanoCT)

NanoCT was used to obtain 3D scans of specific regions of interest within the glass + crystals starting materials, with the goal of investigating the possible presence of cracks at the crystal-glass interface and the glass and for locating plagioclase in the samples (since both of these features were not clearly visible with the microCT). The 3D scans were performed on the Zeiss Xradia 520 Versa at the Cell Imaging and

Analysis Network of McGill University. The scanning conditions were 70 kV, 85 μA, no filter, camera binning 2x2, camera-to-source distance = 30.24 mm, within which source-to-sample distance = 10.23 mm, optical magnification = 40x, image pixel size = 0.22 μm, exposure time = 25 seconds, rotation step = 0.4 °, projection number = 935 over 360 °. The microCT and nanoCT analysis described above were performed with the aim of learning as much as possible about the synthesized samples without destroying them, in order to recognize the most promising ones for the following *in situ* heating tomography experiments.

2.2.5 4D *in situ* synchrotron X-ray microtomography

Ambient pressure 4D vesiculation experiments were performed at the TOmographic Microscopy and Coherent rAdiology experiments (TOMCAT) beamline of the Swiss Light Source synchrotron at the Paul Scherrer Institut in Villigen, Switzerland (Stampanoni et al., 2006). Approximately 0.5 - 1 mm^3-sized pieces of the synthesized andesitic hydrous glasses + crystals were mounted in a cylindrical, ceramic sample holder and heated using the laser-based heating system at TOMCAT (similar to earlier systems described in Fife et al., 2012). The system incorporates two 150W, class IV diode lasers operating at 980 nm and projecting oval laser spots (4 mm wide by 6 mm high). We worked in propagation-based phase contrast mode setting a sample-to-detector distance of 150 mm. The temperatures were measured with a pyrometer (Fife et al., 2012) that was calibrated using the temperature of the first appearance of bubbles in the sample as measured by a type K thermocouple in a laboratory furnace at McGill. The temperatures are accurate to with ± 20 °C. A

thermal gradient is always present in the laser furnace and we tried to minimize its effect by always placing our sample at the center hot spot of the furnace.

Three pieces from each of the five charges were heated and imaged separately at PSI, giving us the opportunity to verify if the events occurring during heating of a single piece were consistent with events in all other pieces originating from the same charge. The initial heating regime was 2 °C/sec until a chosen temperature was reached that was above the glass transition temperature. At that point the sample was kept at that temperature until the end of the experiment. The goal of rapid heating at 1 bar was to simulate isothermal decompression from the saturation pressure of the sample (dependant on its water content).

Imaging was performed using the GigaFRoST detector (Schlepütz et al., 2017) connected to an optical microscope and incorporating a continuously adjustable magnification tuned to approximately 4x. Polychromatic radiation was filtered to 5% power, and the sample-to-detector distance was set at 280 mm, optimized for phase-contrast imaging of these materials. Each 3D tomographic scan is based upon 501 projections acquired over 180 ° in 0.5 s with a 3 μm pixel size. Real-time radiographs (i.e. the 2D projection images acquired by the camera prior to the tomographic reconstruction) of one piece of each sample were examined to determine the approximate temperature when bubbles first appeared (as in Bai et al., 2008). Subsequent scanning began at a temperature slightly below this temperature in order to capture bubble nucleation. All samples were scanned *continuously* for 50 seconds, and 100 3D datasets (from here on called timesteps, from t_1 at 0.5 sec to t_{100} at 50 sec) were produced for each sample. Tomographic reconstructions were obtained after the application of a phase-retrieval algorithm (Paganin et al., 2002), to the acquired

projections, with the following parameters: X-ray energy = 30 keV, $\delta = 5.1\times10^{-7}$ and $\beta = 5.1\times10^{-9}$ (δ and β are dimensionless real numbers whose ratio is one of the input parameters for phase-retrieval – for more information see Paganin et al., 2002).

2.2.6 High resolution *ex situ* synchrotron X-ray microtomography

To examine more closely some especially interesting features that developed during the *in situ* scanning, selected experiments were re-imaged after their conclusion using high-resolution, monochromatic X-rays and phase-contrast imaging on the TOMCAT beamline. This was critical for determining the post-process position of bubbles with regard to crystal surfaces and cross-referencing the phase contrast scan position of each individual bubble with the *in situ* measurement. The imaging of crystals and bubbles within a silicate matrix by conventional absorption X-ray tomographic microscopy is limited by the contrast in their X-ray absorption. This is especially troublesome for plagioclase crystals, which can be practically indistinguishable from the melt. This lack of phase contrast between plagioclase and glass can prove potentially misleading when bubble nucleation is investigated because it is difficult to determine if the bubble is on the crystal surface. To overcome this issue, propagation-based phase contrast imaging was also utilized for these *ex situ* scans; this method uses the phase information of a material to enhance image contrast (Polacci et al., 2006). An energy of 27 keV was used and a standard optical microscope with 10x magnification was connected to the pco.Edge 4.2 (PCO, Germany) camera, resulting in a 0.65 μm pixel size. The sample-to-detector distance was decreased to 80 mm, and 1501 projections were acquired over 180 ° of continuous rotation,

resulting in a single 3D scan acquired in approximately 20 minutes. A full dataset was reconstructed several times, first without and subsequently with phase retrieval. In the latter case, the δ and β parameters were varied in order to optimize the δ/β ratio by selecting the minimum value for which the fine microstructures were visualized and the phase contrast 'artefacts' were reduced in the resulting slices. The final selected parameters were: $\delta = 5.1\times10^{-7}$ and $\beta = 3.5\times10^{-9}$. The reason why both PSI synchrotron radiation methods applied have a stark difference is due to the different working distances, acquisition times and β parameters chosen.

2.2.7 Volume segmentation

In order to determine the total volume of bubbles generated, the entire sample volume was tracked as it inflated during heating. The initial volume was taken as the one at timestep t_1, and the sample was segmented by binarization (values 90-255 on 8-bit volumes), using Fiji (Schindelin et al., 2012) and Pore3D (Brun et al., 2010). If a crack was present within the sample at t_1, it was not attributed to the sample. The final sample volume was the one at timestep t_{100} and the sample was binarized again (same values). For some samples, the entire sample volume at t_{100} could not be successfully segmented automatically, due to very thin bubble melt/glass films comprising the outer sample outline. In such cases, manual segmentation was used to assign these voxels to the melt, while making certain that the film thickness is preserved. All the segmented volumes were calculated using Pore3D and the difference between the volume at t_{100} and at t_1 was the total bubble volume.

Several bubble-crystal aggregates were chosen for 3D visualization to illustrate bubble-crystal relations. A sample sub-volume that contained the objects of interest was chosen and its voxels were segmented as bubbles and crystals (thresholding values 0-140 for bubbles and 200-255 for clinopyroxene, on 8-bit volumes), and the segmentation was always finished manually. Certain regions of the subvolume were excluded from segmentation to ease the visualization, such as bubbles that nucleated on neighbouring crystals. The segmentation was done by semi-automatic thresholding in 3D for clinopyroxene and bubbles and manually for plagioclase, i.e. simultaneously on 3 sets of 2D slices corresponding to 3 slice orientations (XY, XZ and YZ), using Avizo Fire® (Visualization Sciences Group). The extent of surface smoothing was restricted so that the thin layer of bubbles on the crystal remains visible. Voxels corresponding to melt/glass films between bubbles were assigned to the bubble phase to facilitate 3D visualization. The number of bubbles on individual crystals was determined by applying the watershed algorithm (MorphoLibJ plugin of ImageJ) on the post-process samples imaged at submicron resolution on TOMCAT (Table 2.1), where the resolution and border contrast enhanced their visibility. However, even in this case the melt films proved difficult to segment, either automatically or manually, so the number of bubbles obtained represents a minimum value.

2.2.8 Contact angle measurements in 3D

The 3D contact angle between a bubble and a crystal (Figure 2.3) was defined as the angle whose vertex touches the bubble-crystal-melt contact line, one arm is tangential to the bubble surface (plane YZ in Figure 2.3) and the other lies on the crystal surface (plane XY in Figure 2.3); this angle lies in the same plane as the central axis of the bubble (Figure 2.3) which is defined by the bubble's maximum height. When identified, the 2D slice was then rotated around this axis in order to measure the contact angle at six different places (3 paired values) on the bubble-crystal-melt contact line. Measuring the contact angle through such identification of a specific 2D slice within a 3D volume, is a novel approach that provides improved results over measuring the contact angle on an arbitrary 2D slice. These measurements were repeated for different timesteps of the experiment to track the change in the contact angle for a specific bubble. Only bubbles that were hemispherical caps and had angles on each side differing by less than 5 ° for all timesteps were used for contact angle measurements.

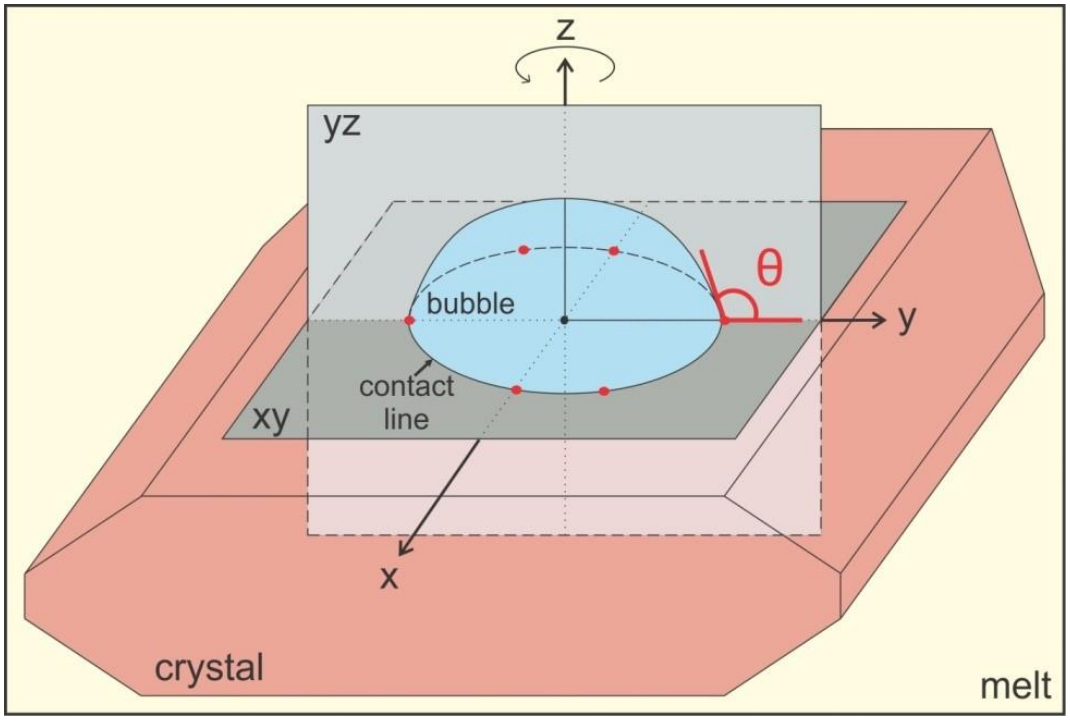

Figure 2.3: Schematic model of the 3D bubble-crystal contact angle measurement. Once planes XY and YZ have been located (in which the two arms of the angle lie) within the 3D volume, the YZ plane was rotated around the Z axis so the contact angle can be measured multiple times along the contact line (measurement location represented by red dots). Each contact angle measurement in a chosen YZ plane was performed twice, on each side of the bubble.

2.2.9 Scanning electron microscopy

To compliment the 3D and 4D data with a well-recognized 2D analysis, and to compare the results, one post-process sample was examined with a Hitachi SU-3500 Variable Pressure -SEM using a BSE detector, at McGill University (Montréal, Canada). One sample was ground down to a target slice identified from the sample's 3D reconstruction. The amount of grinding and polishing was constrained by the fragile nature of the foamy post-process samples.

2.2.10 X-ray tomographic microscopy at APS

The experimental samples produced were also visually compared to a natural andesitic sample from Montserrat, scanned at the GeoSoilEnviroCARS beamline, of the Advanced Photon Source synchrotron (Illinois, U.S.A.). The X-ray beam had an energy of 25keV, the camera magnification was 10x and the image pixel size was 1.24 μm.

2.3 Results

2.3.1 Starting glass + crystals

Pieces of each of the starting materials for the vesiculation experiments were examined with conventional microCT. The scans showed that no bubbles were present. The large clinopyroxene crystals were clearly visible in all relevant samples, as were oxide crystals that grew during synthesis experiments. Plagioclase crystals were not detected with conventional microCT, so a conventional nanoCT scanner was used to check for their presence. The nanoCT scans were too noisy for quantification, but plagioclase crystals were nonetheless successfully detected, as well as cracks within the samples (Figure 2.4). These cracks were most likely formed during isobaric quench at the end of the synthesis, or during the samples' removal from the Pt-capsule. The cracks are not systematically oriented along any crystal boundary, but instead cut through the sample and crystals equally, occasionally following part of the crystal surface.

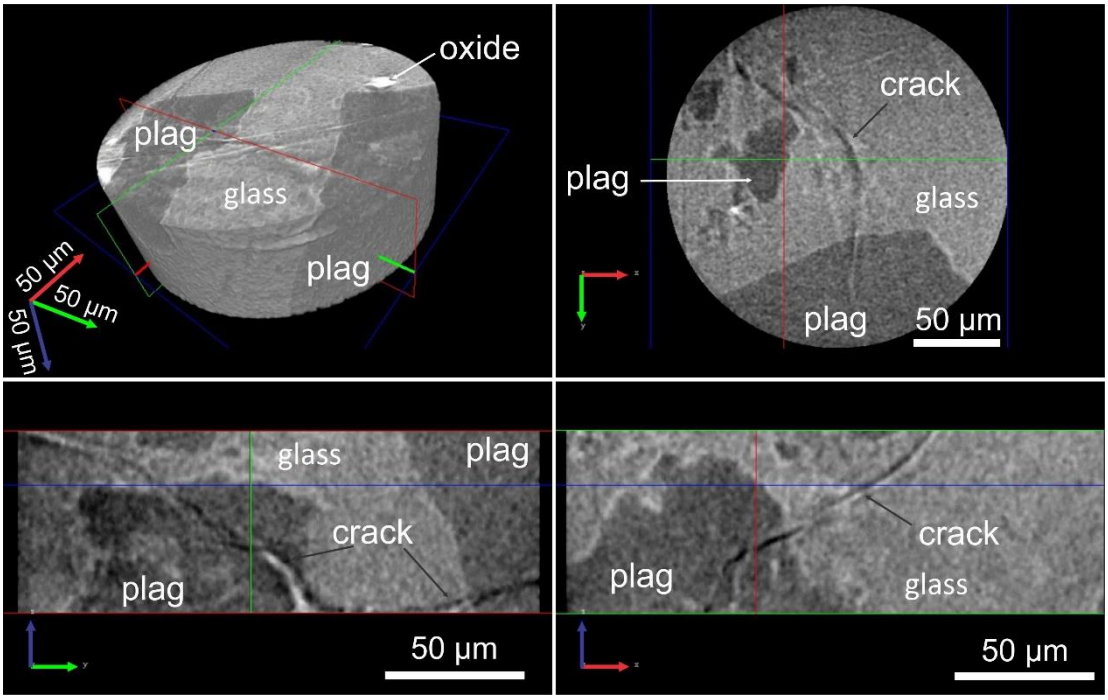

Figure 2.4: 3D visualization and three orthogonal 2D slices of an *ex situ* nanoCT scan of a region of interest within a starting material sample. Plag = plagioclase. In the 3D visualization, the length of each axis of the 3D scale represents 50 µm in its respective direction. Plagioclase crystals, oxide crystals and cracks are clearly visible. The position of the cracks does not follow the plagioclase crystal borders.

2.3.2 *In situ* vesiculation

The determination of the temperature at which bubbles first appeared was performed at PSI in the same manner as the 1 atm furnace at McGill. One piece from each charge was heated and observed only through radiographs (2D projection images). The correction factors obtained are presented in Table 2.2 and henceforth all temperatures discussed are the corrected values. Previous work demonstrated that bubble nucleation begins above the glass transition temperature (Bagdassarov et al., 1996), which for glasses of similar composition and water concentration was determined to be 467 °C (Giordano et al., 2005).

Thermal gradients within experimental charges are always present, but we have made every effort to minimise this effect by positioning the sample close to the laser hotspot. A thermal gradient is nonetheless present, as seen through the number of bubbles that nucleate on different silicate crystal surfaces.

Heterogeneous nucleation always occurs first on the silicate crystals in the furnace hotspot, and in other portions of the sample further away from the hotspot shortly thereafter. There is a 20 second lag time between heterogeneous bubble nucleation on silicate surfaces closer and further away from the hotspot. Heterogeneous nucleation on oxide surfaces or homogeneous nucleation within the melt (in any part of the sample), never occurred before heterogeneous nucleation on silicate surfaces in the coolest part of the sample. Hence, we conclude that the same processes of bubble nucleation were at work throughout the entire sample volume. That is to say, the nucleation events occurred in the same order throughout the sample, but there was a time delay between the ″hotter″ and the ″cooler″ part of the sample.

Thus, if a clinopyroxene in the ″hotter″ part of the sample nucleated more bubbles than a plagioclase in the ″cooler″ part, the clinopyroxene is not more efficient at nucleating bubbles. Hence, to determine the nucleation event timeline we considered only the middle and lower sections of the sample volumes and compared different crystals that were placed at similar heights in the sample, thus comparing nucleation events occurring at similar temperatures.

Four representative samples are presented in detail here, but there are other pieces from the same charges that share their features. A summary of the data obtained can be found in Table 2.2. From timesteps t_1 to t_{100} samples underwent an increase in volume due to bubble nucleation and growth (Figure 2.5). Inspection of 3D volumes for each timestep showed the location, time and temperature of bubble nucleation (Figures 2.6 and 2.7).

Table 2.2: Quantitative data for four representative samples. The sample name corresponds to the piston cylinder run (1, 2, 3), the charge within that run if there were several (a, b) and the experiment number at PSI (6, 7, 8, 11). Plag = plagioclase, cpx = clinopyroxene, n.p. = not present, n.o. = not observed, t_1 = start of acquisition, t_{100} = end of acquisition. The event numbers correspond to those on Figure 2.6. The temperature error is ± 20 °.

Sample name	1b-11	2b-8	3-6	3-7
# of plagioclase crystals in sample	35	n.p.	7	7
# of clinopyroxene crystals in sample	n.p.	29	19	30
# of oxide crystals in sample	9	24	218	7
Sample volume at t_1 (mm^3)	0.256	1.045	0.249	0.167
Temperature correction factor	1.25	1.18	1.3	1.3
Temperature at t_1 (°C)	600	620	540	550
Temperature of heterogeneous bubble nucleation on plagioclase (°C) = event 1	660	n.p.	550	570
Temperature of heterogeneous bubble nucleation on clinopyroxene (°C) = event 2	n.p.	650	560	570
Temperature of homogeneous bubble nucleation within the melt = event 3	690	n.o.	600	590
Temperature of heterogeneous bubble nucleation on oxide (°C) = 4	n.o.	650	670	n.o.
Temperature of sample inflation (°C) = event 5	n.o.	650	615	600
Sample volume at t_{100} (mm^3)	0.289	1.151	0.487	0.590
Percentage of sample volume change (%)	13	10	95	253
Total bubble volume at t_{100} (mm^3)	0.033	0.106	0.237	0.423

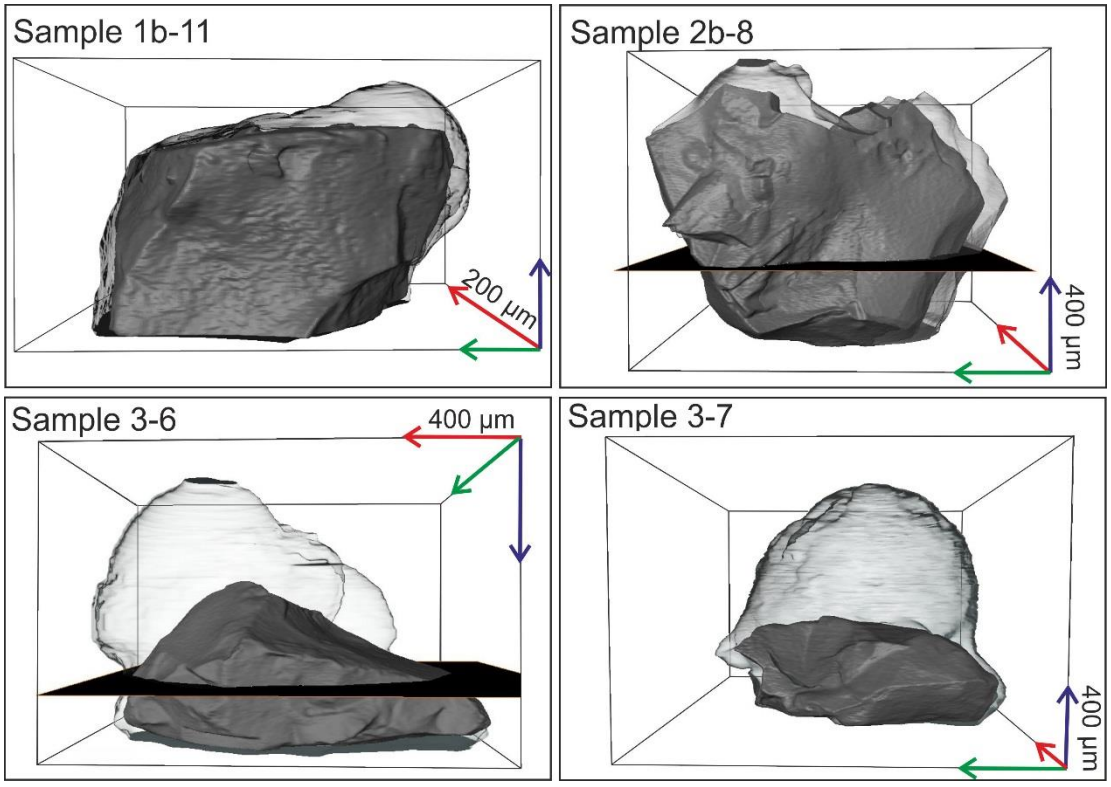

Figure 2.5: 3D representation of 4 representative samples of melt + crystals + bubbles. The smaller, dark grey volume is the unvesiculated sample volume at t_1 (start of the experiment) and the larger, light grey volume is the vesiculated sample volume at t_{100} (experiment's end). The black plane passing through samples 2b-8 and 3-6 represents the locations of 2D slices presented in Figure 2.7. For each sample all three axes of the 3D scale represent the same length, in their respective directions, which is 200 µm for sample 1b-11 and 400 µm for all other samples.

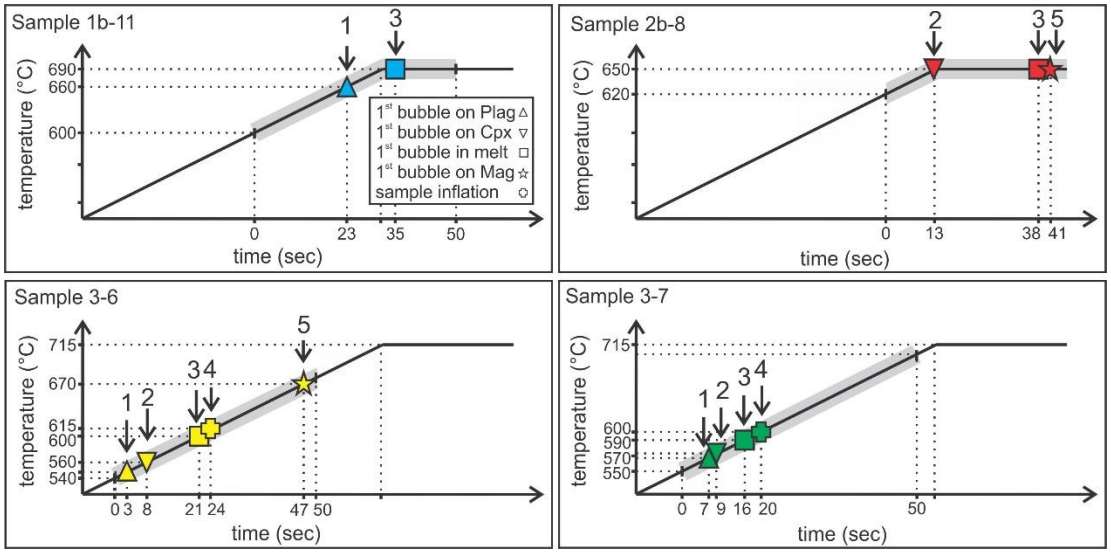

Figure 2.6: Timeline of nucleation events during the *in situ* heating experiments. The x-axis shows time, with the starting value of 0 representing when scanning began (t_1), and the final value 50 when it ended (t_{100}). The y-axis shows temperature. The black line represents the heating regime during each experiment, with the part of it enhanced in grey showing when scanning was performed. The symbols represent the T-t point at which specific events occurred. The order of events (1-5) corresponds to the event order in Table 2.2. Not all samples exhibit all possible events.

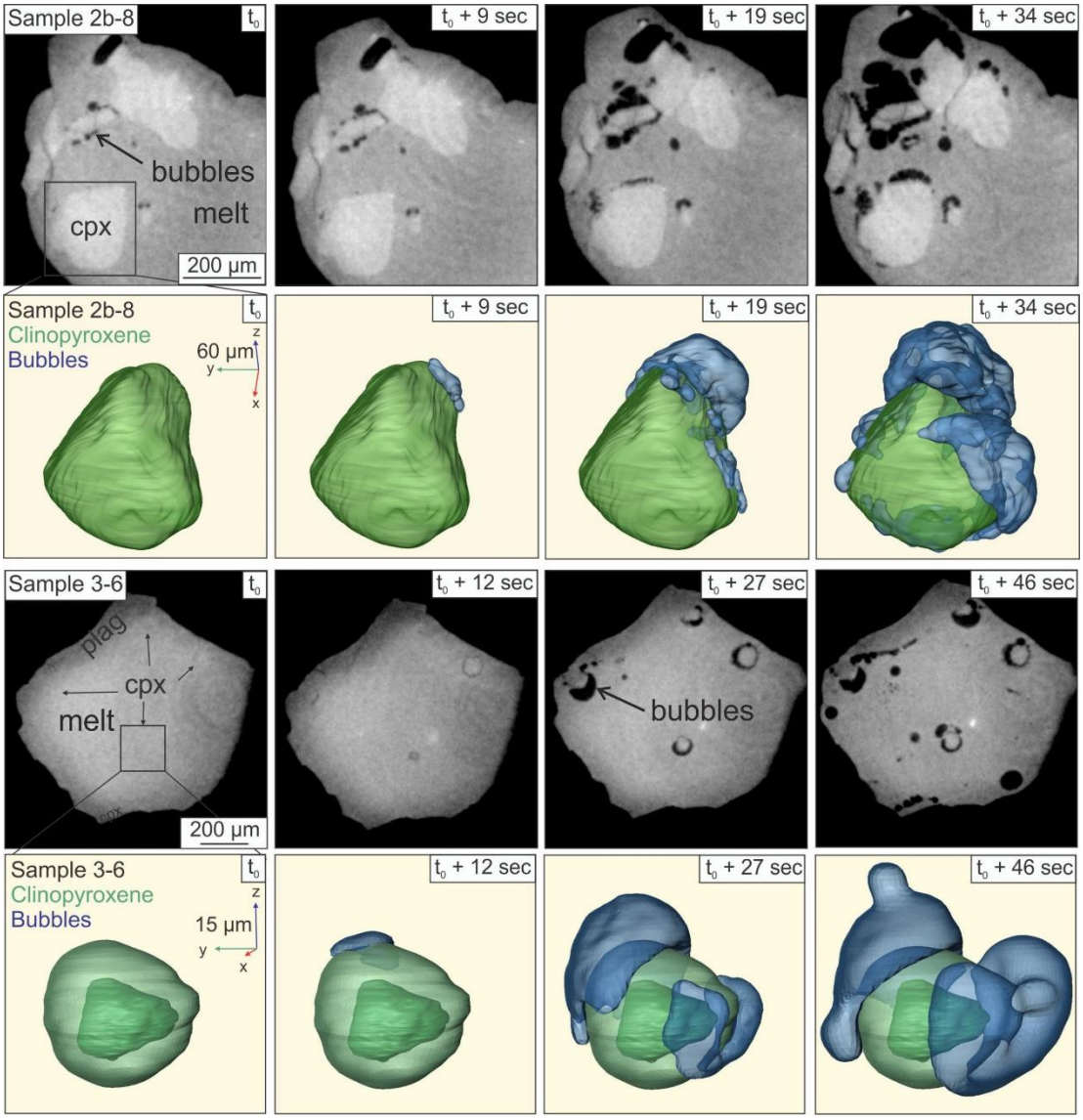

Figure 2.7: 2D and 3D sequences of bubble nucleation and growth on silicate crystals during heating. Sample 2b-8 contains only clinopyroxene (cpx) crystals, while sample 3-6 contains both clinopyroxene and plagioclase (plag) crystals. Note that solitary bubbles apparently within the melt in the 2D sequences are located on crystal surfaces below or above the presented slice. The presented 2D slices are located in the lower part of the cpx and in the middle of the plag, respectively. The locations of the 2D slices within the entire samples are shown on Figure 2.5. All three axes of the 3D scale represent the same length, in their respective directions. The clinopyroxene in sample

2b-8 maintained its original surfaces, while the one in 3-6 has a core and a rim around it. This leads to bubbles appearing to nucleate *in situ* around hollow sphere-like structures. The clinopyroxene core can only be distinguished from *ex situ* PSI scans and has here been incorporated to the *in situ* 3D visualization. The temperature change for both samples can be seen on Figure 2.5.

Large clinopyroxene crystals and oxides were the only crystal phases clearly distinguishable in the *in situ* scans (Figure 2.7), as in the case of the microCT. Observations of the sample during heating showed that the first bubble formation was in part clearly associated with clinopyroxene crystals. The topology of such bubbles was clearly hemispherical on the side facing the melt (outward), and planar on the other side (inward), suggesting nucleation on the surface of an object and not within a melt. Bubbles that nucleated away from the clinopyroxene crystals formed hollow sphere-like structures in 3D volumes (Figure 2.7). Importantly, during these early timesteps, no bubbles nucleated on oxides.

Bubbles initially grew by maintaining their initial topology, until they encountered adjacent bubbles, after which their growth was confined to the hemispherical side. This further confirms that growth on the planar side was impeded by a solid surface. In order to clearly determine whether the other objects around which other bubbles (hollow sphere like ones) nucleated were crystals as well, the *in situ* timesteps were compared with the *ex situ* scans for each sample (Figure 2.8). The phase border enhancement revealed the presence of both plagioclase crystals and small clinopyroxene crystals, both of which had bubbles associated with them, i.e. nucleating on their surfaces. Combining these two tomographic methods allowed us to accurately determine a bubble's starting position and build a nucleation timeline (Figure 2.6).

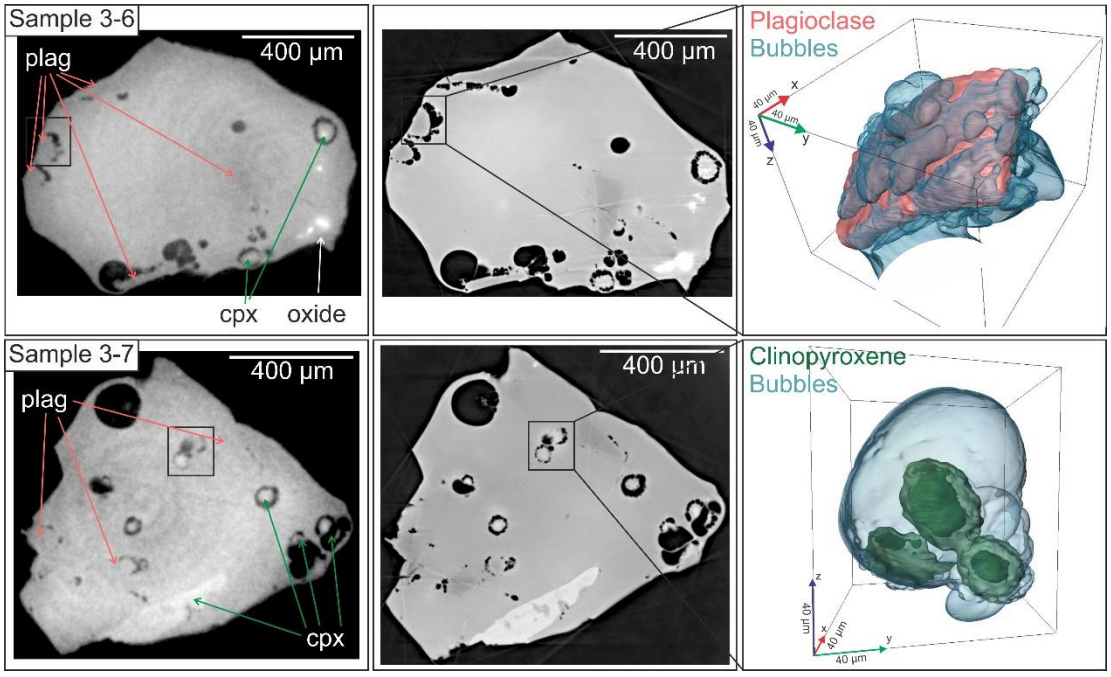

Figure 2.8: A comparison between the *in situ* and the *ex situ* synchrotron radiation imaging. For both samples, the same slice is presented for both methods, followed by a 3D visualization of a clinopyroxene or a plagioclase crystal with their associated bubbles. The *in situ* slice corresponds to timestep t_{100}, and its ex situ counterpart is not completely identical due to a time difference between the end of scanning and quenching. In the ex situ image of sample 3-6 we can see oxides within the melt, that grew during synthesis at high pressure, and have no bubbles on their surfaces. The lowermost bubble in the sample 3-6 plagioclase 3D visualization is faded out because a bubble from another crystal indented it. For sample 3-6 the slice presented here is located 525 µm above the slice presented in Figure 2.7.

Larger clinopyroxene grains were easily distinguishable in tomographic volumes, but smaller crystals proved to be more difficult to discern (Figure 2.7). Clinopyroxene crystals appeared homogeneous without phase contrast in *in situ* scans but turned out zoned in *ex situ* scans. SEM analysis showed that these clinopyroxenes have a core and rim that are compositionally the same, even though the outer part displays a spike-like radial texture. Since neither plagioclase nor clinopyroxene were in exact equilibrium with their surrounding melt during starting material synthesis, we conclude that the smaller clinopyroxene crystals started to melt, but the partially molten part did not have time to mix with the surrounding melt, producing an inner core and outer rim appearance. The reason we see no difference between the core and the outer rim with *in situ* scans is that it is a structural and not a compositional difference. Large clinopyroxene crystals do not exhibit such spike-like radial textures (Figure 2.7).

The clinopyroxene crystals used as seeds are natural augites and they contain inclusions of oxides, which are visible in the scanned volumes. Since the inclusions are randomly distributed within the clinopyroxene, there were also most likely present in the portions of the smaller clinopyroxene crystals that partially melted during starting material synthesis (i.e. in the outer rim). The question then arises if they could have been pushed out to the new outer rim-melt interface, where then they could have acted as bubble nucleation sites during *in situ* vesiculation. We inspected both the *in situ* and the *ex situ* scans for evidence of such oxide placement and found none. We also inspected the larger non-molten clinopyroxene crystal surfaces and found that if an oxide inclusion/impurity was present at the interface it did not act as a bubble nucleation site, whilst the impurity-free, non-molten clinopyroxene surfaces did. If the

oxides within the clinopyroxene were the underlying reason for what appears as heterogeneous nucleation on clinopyroxene surfaces, we would expect the other oxides present within the melt to behave the same, which they do not. Combining these observations with those of inclusions and plagioclases also nucleating bubbles, we see no evidence that oxide impurities within the clinopyroxene crystals were the reason for heterogeneous bubble nucleation on clinopyroxene surfaces.

Several plagioclase-bubble and clinopyroxene-bubble aggregates were isolated from the phase contrast scan of sample 3-7 and divided into sub-volumes to determine the number of bubbles that nucleated on the respective crystals. Bubbles were segmented by combining the watershed and morphological segmentation algorithms of ImageJ. Due to the proximity of some bubbles (Figures 2.7 and 2.8) the values obtained only represent the minimum numbers of bubbles nucleated, and it was often clear with the naked eye that the protocols applied could not discern all the small bubbles present. For plagioclases the minimum number of bubbles was between 110 and 365, while for clinopyroxenes between 20 and 121. To compare, in sample 2b-8, a single oxide crystal out of the 24 present nucleated 2 bubbles, and in sample 3-6 a single oxide out of the 218 present nucleated 6 bubbles.

There is a striking difference in the number of bubbles that nucleated on silicate crystal surfaces compared to those on oxide surfaces in our experiments (2 and 6 on a single oxide vs tens of bubbles on almost all clinopyroxenes, and hundreds on almost all plagioclases), which contrasts with earlier research (e.g. Hurwitz and Navon, 1994; Gualda and Ghiorso, 2007). There is no preferential spatial distribution of silicates or oxides within the samples, i.e. there are oxides, of different sizes, present in both the parts of the sample closer to the hotspot (″hotter″) and in those further away from it (″colder″ part). In many places, we can observe a silicate and an oxide crystal in close proximity, sometimes even an oxide between two silicate crystals, with bubbles nucleating first on the silicates, in every experiment (Figures 2.7 and 2.8, sample 3-6).

A 2D axial slice from the *in situ* imaging that best shows bubble growth with time was selected (Figure 2.7) and subsequently stacked into a time-lapse animation to illustrate the dynamic changes in the three-phase system during the experiments (Appendices 2.1 and 2.2), along with time-lapse animations of bubbles growing on the two different clinopyroxene crystal types in 3D (Appendices 2.3 and 2.4). A complete 3D visualization of PSI *ex situ* scans of samples 2b-8 and 3-6 can be found in Appendices 2.5 and 2.6.

The *in situ* imaging allowed observation of the change in the contact angle during bubble growth, which is a dynamic property not obtainable in static scans. In cases where bubbles did not encounter neighbouring bubbles on the crystal surface, the contact angle between the bubbles and the clinopyroxene changes from a maximum of ~ 140°±5° to a minimum of ~ 50°±5 (measured on 15 bubbles through ~20 timesteps). When two bubbles come into contact their contact angles stopped at 90°. In the latter case, bubbles do not coalesce; instead, they continue to grow outward into

the melt. A thin layer of melt remains between the bubbles, and they do not detach from the clinopyroxene for the duration of the experiment (Figure 2.7).

Bubbles on plagioclase crystals appear as continuous bubble films on the crystal surface and only with close inspection of the *ex situ* scans do the thin melt films between bubbles become visible (Figure 2.8, sample 3-6). This suggests that bubbles nucleated individually on plagioclase surfaces, spread very quickly to occupy the available surface, all occurring below the 3 μm pixel size used in these experiments. In the bubbles that remained solitary on plagioclase crystals, the contact angle changes roughly from 120°±5° to 75°±5° (measured on 15 bubbles through ~20 timesteps).

Bubbles nucleated on oxide surfaces in the very last few timesteps (if at all; Figure 2.6) and had a volume of only several voxels, which prevented the quantification of their contact angle change.

2.4 Discussion

We consider that the simplest explanation of our data is that bubbles nucleate directly on plagioclase and clinopyroxene in an andesitic magma. However, this finding is at odds with many earlier observations; hence we must verify that no other nucleation processes were active in our experiments. First, we discuss the possibility of bubble nucleation on cracks in the glassy sample or crypto-heterogeneities in the melt. Next, we consider the possible role of oxides as bubble nucleation sites in our experiments, and we show that the 2D images used in earlier studies can create the false idea that bubbles nucleate near crystals, rather than on crystal-melt interfaces. If bubbles can nucleate readily on plagioclase and clinopyroxene then are there other aspects of the process that may be important. Asperities and edges play a role in the nucleation of bubbles in some situations, but what was their role here? Finally, we discuss dynamic changes in the contact angle and the role of bubble detachment in magma degassing.

2.4.1 Lack of bubble nucleation on the cracks within the glass and crystals

We must discuss the possibility that bubble nucleation occurred on cracks in the charge (observed with a nanoCT) whilst the material was still a glass. If such cracks were nucleation sites then we would expect to see bubbles forming during *in situ* scanning in linear and planar arrays throughout the sample. This was never observed in these experiments; hence we conclude that bubbles have not nucleated on such cracks. We must also consider the possibility that bubbles could have nucleated on small cracks that formed along the crystal-melt (or glass) boundaries due to the

unequal expansion of crystals and glass during *in situ* heating. Coefficients of thermal expansion ($\alpha_{298\ K}$) are not well known for natural materials and the closest we could find are: 5.8 x 10-6 $°C^{-1}$ for anorthite glass (Arndt and Häberle, 1973) or 4.5 x 10-6 $°C^{-1}$ for aluminosilicate glass (Varshneya, 1994), 1.5 x 10-5 $°C^{-1}$ for plagioclase (five value average for $An_{78}Ab_{22}$ from Tribaudino et al., 2010), 3.33 x 10-5 $°C^{-1}$ for clinopyroxene (diopside, Cameron et al., 1973) and 2.06 x 10-5 $°C^{-1}$ for oxides (magnetite, Skinner, 1966). Based on these values, all the materials expand very similarly, but the smallest difference is between the plagioclase and the glass. Hence, if expansion cracks were the main reason for bubble nucleation, we would expect to see more bubbles nucleating on oxides and/or bubbles nucleating sooner on clinopyroxene than on plagioclase. We did not observe either phenomena and hence reject this hypothesis.

Additionally, the argument that nucleation occurs at expansion cracks implies that when bubbles start nucleating, the material around the crystal is a glass, and not a melt, in which case bubble nucleation and growth would cause further cracking of the glass, which again is never observed in these experiments. From the initial stages of nucleation and throughout their growth all bubbles display hemispherical topologies, indicating that they do not encounter any differential resistance from the surrounding material, which must be a melt. Two additional arguments in favour of melt, rather than glass, surrounding the crystals during bubble nucleation and growth are: 1) the temperatures at which the very first bubble nucleation events occurred (from 550 °C to 660 °C) are above the glass transition temperature for similar composition andesitic glasses (Giordano et al., 2005), 2) as heating commences and before bubble nucleation starts, we observe the annealing of quench cracks within the glass. However, where

these cracks cut across a crystal, they do not anneal and the crystal expands (Figure 2.7, sample 2b-8). No bubbles formed in the intra-crystalline cracks during these experiments. It is easy to distinguish between these textures (un-annealed crystal cracks and the bubbles) because of their different orientation: the former cut through the crystal whereas the latter form along its boundaries. Furthermore, there is a time difference between their formations. When bubbles start to nucleate heterogeneously on silicate crystals that have an un-annealed crack, we do not observe the expansion of this crack along the crystal surface. Based on these arguments we conclude that the bubbles nucleated and grew within a melt and not a glass, and that cracks are not important for bubble nucleation in our experiments.

2.4.2 Lack of nucleation on crypto-heterogeneities in the melt

It has been proposed (Gardner et al., 1999) that nucleation could occur on solid structures within the melt smaller than can be detected with the image resolution used in this study. If this were the case in our experiments, then we would expect to observe two phenomena: First, these crypto-heterogeneities should be randomly present throughout the melt. Crystal melting did not occur or was minimal during the starting material synthesis, and the glass composition is the same both close to and far away from crystals (SEM compositional analysis presented in Appendix 2.7). Hence, we see no reason for localisation of crypto-heterogeneities closer to the crystals rather than further away from them. Second, if bubbles nucleated on crypto-heterogeneities close to the crystal instead on the crystal surface, we would see their shape change from spherical to hemispherical once they encounter the crystal surface. One could argue

that in the first timesteps, where bubbles are identified by only a few voxels, there is not enough information to determine their shape. However, we would then also expect to see bubbles forming on such crypto-heterogeneities sufficiently away from the crystal for us to be able to track their shape, yet, no bubbles are forming away from the crystal at the same time as those that form at the crystal-melt interface. In the volumes imaged *ex situ*, bubble walls were inspected for the presence of small oxides or any other phases that could act as such heterogeneities, unobservable from *in situ* scans alone, and none were found.

2.4.3 Lack of nucleation adjacent to the crystals ("melt films")

Some recent studies have described the presence of bubbles close to silicate crystal surfaces but separated from them by a melt film (e.g., Giachetti et al., 2010; 2011). However, we believe that this observation could be an artefact of observation in 2D. We show a similar situation in Figure 2.9 a-c, where a bubble was imaged by SEM in a section cut from sample 3-7, already imaged in 3D. If the SEM images were the only information at our disposal, we might have concluded that the bubble in question nucleated homogeneously in the melt, close to the crystal surface. However, in the reconstructed 3D volume it becomes clear that the 2D cross-section in question does not contain the bubble's maximum diameter. The maximum diameter plane is in fact located a few micrometers below the SEM cross-section, and there the bubble and plagioclase crystal are in contact. For the sample in question, the SEM cross-section contains other plagioclase crystals with bubbles in contact with their surfaces (Figure

2.9 g-i), but this example shows the importance of 3D (and 4D) imaging in correctly identifying a bubble's position.

For comparative purposes, we imaged two natural samples, one andesitic from Montserrat and the other basaltic from Stromboli (Figure 2.10). The textures produced around silicate crystals present in both those samples are very similar to those in our *in situ* scans, and can also be compared to other published textures (e.g. Hurwitz and Navon, 1994; Giachetti, 2010; 2011). All examples lack a melt film between the plagioclase crystals and the bubbles. Due to our *in situ* observations, the mechanisms that produce such textures can now be explained as bubbles nucleating on the silicate-melt interfaces and growing outward instead of the previous explanation of bubbles nucleating elsewhere in the melt and growing towards the silicate crystals (e.g. Giachetti et al., 2010).

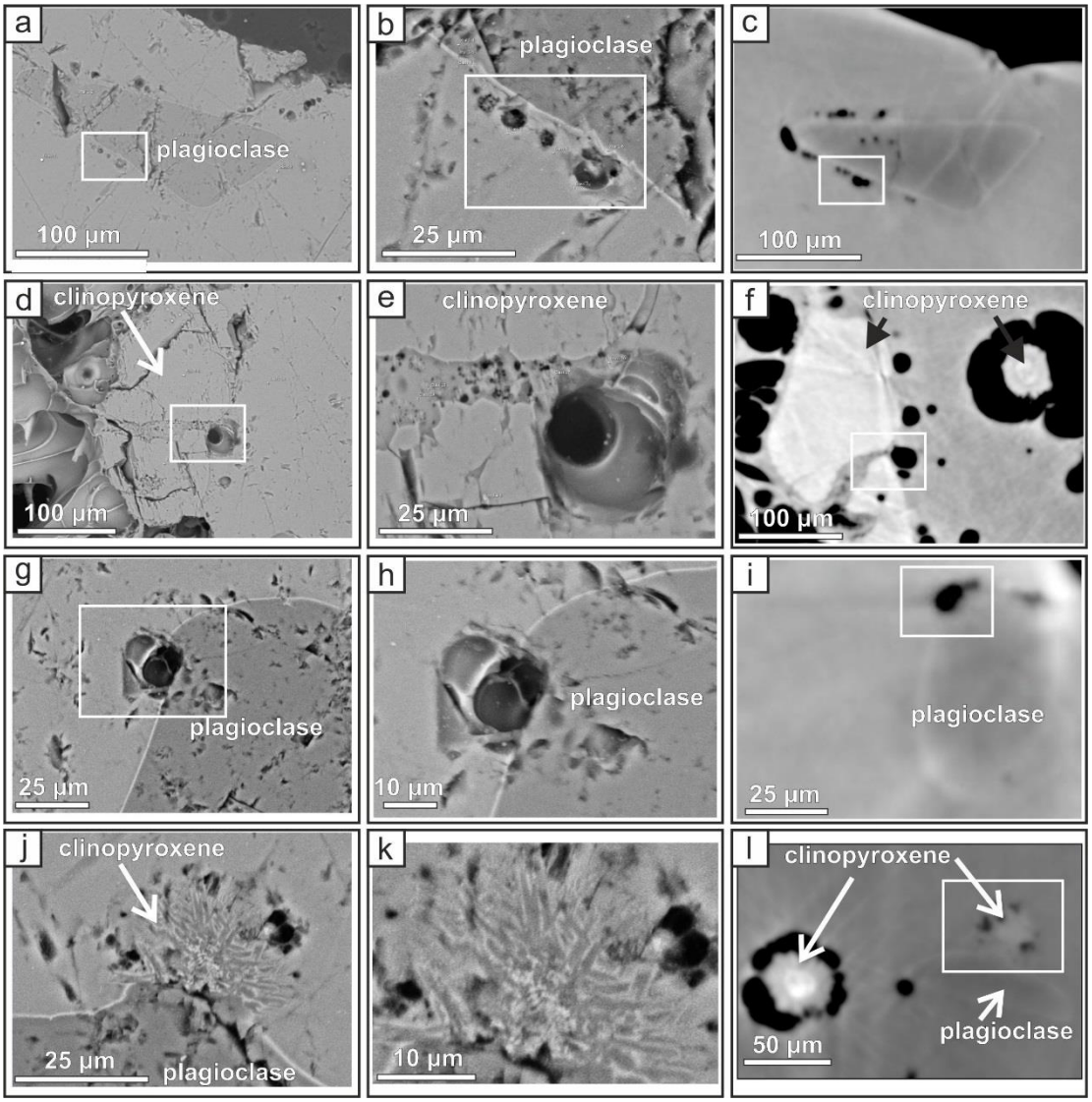

Figure 2.9: Post-process images of sample 3-7, observed with a SEM and with propagation-based phase contrast synchrotron radiation microCT. Each of the 4 rows presents the same feature. There is an angular difference of 15 degrees between the two methods, so the scans are not identical. a, b) Plagioclase crystal imaged with SEM. A series of bubbles can be seen very close to the plagioclase border. Only the one of the furthest right side appears to be in contact with the jagged surface of the plagioclase. c) The same plagioclase crystal, seen with propagation-based imaging. The pale line along the border of the crystal is the x-ray equivalent to the Becke line.

Due to the tilt between the two different planes, image c is 10 μm below images a and b, but on it we see all the bubbles in direct contact with the plagioclases – an example that demonstrates how 2D observations can lead to erroneous assumptions. d, e) Clinopyroxene crystal with bubbles on its surfaces. We see the bubble in direct contact and a part of the crystal that presumably started melting. f) The same clinopyroxene crystal seen from a slightly tilted plane. We see more bubbles on the right-hand side, with a hemispherical topology, due to contact with the crystal. g, h) Plagioclase crystal with a bubble on its surface. The zoomed image shows the absence of any melt film between the bubble and the plagioclase. i) The same bubble on the tilted plane. We see the contact area between the bubble and the plagioclase is now larger and that the curvature of the bubble follows the surface of the plagioclase. j, k) A plagioclase and a clinopyroxene crystal in contact. Only the outer rim of the clinopyroxene is visible, with bubbles around it. We see the outer rim consists of spikes (compositionally the same to the core) and that bubbles are located in between the spikes. l. On the lower magnification propagation-based image we can observe two clinopyroxenes and we see that the one on the left-hand side has larger bubbles on its outer rim, which appear unaffected by its spiked surface.

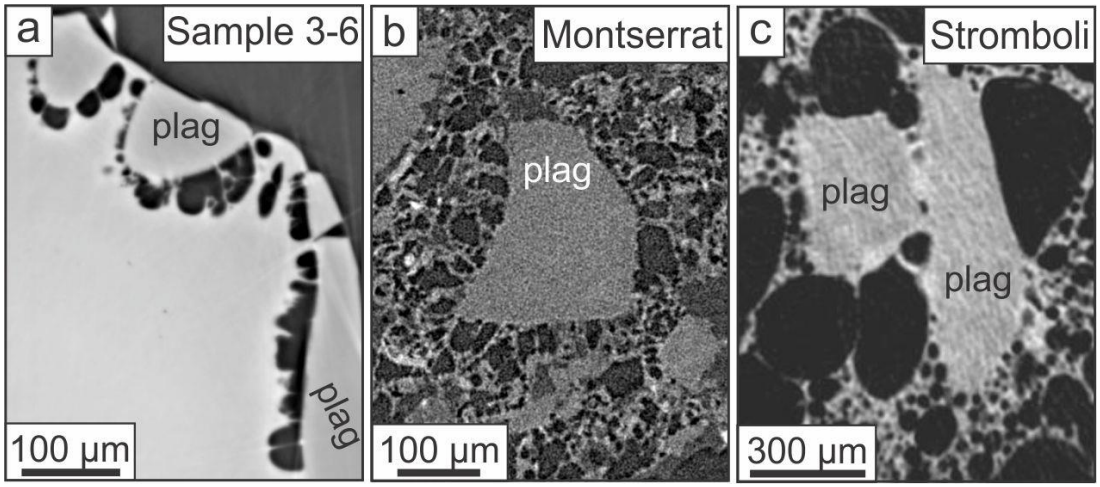

Figure 2.10: Comparison of bubble-crystal textures in experimental charges and natural samples visualized using microtomography. Plag = plagioclase. a. Experimental sample 3-6 of andesitic composition. Three plagioclase crystals are visible on the outer border of the melt, each surrounded by bubbles that nucleated and grew on the crystal surface. b. Natural sample from Monserrat, of andesitic composition. In the center of the image, there is a plagioclase crystal in contact with gas bubbles. The longer axis of the majority of the bubbles appears perpendicular to the plagioclase surface, giving the appearance of an arrangement of bubbles radiating from the crystal outward. c. Natural sample from Stromboli, of basaltic composition, with another plagioclase crystal in contact with bubbles. We see both large and small bubbles, all following the crystal's surface morphology. Cases such as b and c were until now interpreted as bubbles growing towards a crystal (e.g. Giachetti et al., 2010), after nucleating elsewhere.

2.4.4 Bubble nucleation and surface asperities

In many studies in volcanology, material science and fluid dynamics, the surface characteristics of a potential bubble nucleation site are regarded as extremely important (e.g. Atchley and Prosperetti, 1989; Hurwitz and Navon, 1994). It is generally accepted that the rougher parts of an interface are less wetted by the surrounding liquid/melt, and hence have a higher potential for heterogeneous bubble nucleation (Cole, 1974; Blander and Katz, 1975; Atchley and Prosperetti, 1989). At the 3 μm resolution of the *in situ* tomography, the surfaces of clinopyroxene appear smooth and the plagioclase surface is not visible; hence we examined both minerals at higher resolution with phase contrast *ex situ* tomography and scanning electron microscopy (Figure 2.8). The plagioclase crystals have very angular morphologies, consistent with fracture along cleavage planes and show no signs of melting during starting material synthesis. *Ex situ* phase contrast revealed that bubbles are on plagioclase surfaces but give no additional information on the surfaces themselves, as they appear smooth at a resolution of 0.65 μm. Scanning electron microscopy did reveal the presence of some crevices with bubbles (Figure 2.9 a-c). In *ex situ* phase contrast, both the clinopyroxene core and rim surfaces appear smooth, however scanning electron microscopy revealed that the outer rim surface is in fact highly irregular and full of pits (Figure 2.9 j-l) visible at a resolution of 0.65 μm. However, for both plagioclase and clinopyroxene, bubbles have nucleated on both the irregular and the smooth parts of the crystals. Hence, the irregularities present acted as nucleation sites, but there is no evidence to suggest that nucleation occurred more

frequently at asperities than at what appear to be smooth surfaces at the maximum resolution used in this study.

2.4.5 Effect of crystal edges on bubble nucleation and growth

Conventional heterogeneous bubble nucleation theory (Navon and Lyakhovsky, 1998) shows that changes in the surface energies involved in a crystal-bubble-melt assemblage (equations found in Hurwitz and Navon, 1994), would be manifested by a change in the bubble-crystal contact angle. The crystals' contribution to the crystal-melt and the crystal-bubble surface energy would then be dependent on the crystal plane in question, as different crystallographic planes have different surface energies (Eustathopoulus et al., 1999). Furthermore, if a bubble, whilst spreading on a crystal surface were to encounter a change in the crystal plane, such as a crystal edge or corner, the abrupt surface energy change would make it an ideal place for bubble growth to stop or perhaps to induce a rapid change in contact angle that could cause the bubble to detach. If a bubble were to encounter a growth step on the crystal surface, bubble spreading would likely be hindered. The plagioclase crystals and large clinopyroxene crystals in our study exhibit angular morphologies, where cleavage planes intersect (Figure 2.7, sample 2b-8). During the *in situ* scanning, we observed bubbles forming on cleavage plane surfaces and spreading along them. When they encountered a crystal edge, bubbles extended around it and continued to spread on the new crystallographic plane with no change or pause in growth rate. This observation leads us to conclude that either the surface energy differences between crystallographic planes of a single crystal are not different enough to affect the assemblage's combined surface energy,

or that perhaps the assemblage is not so sensitive to surface energy changes. This is also visible for clinopyroxenes with spiked outer rims, where bubbles on the spiked rim have grown to sizes much larger than a single spike, i.e. they are in contact with several spikes, but do not seem to be influenced by such an irregular surface (Figure 2.9 l).

2.4.6 Contact angle changes and possible bubble detachment

The bubble contact angle is an extremely important parameter, yet much existing data have significant limitations. Firstly, in all studies thus far (Figure 2.2), the measurement of the contact angle was done in 2D and the value assumed to be representative of the actual, 3D value. This may not be correct and such data must be viewed with caution. Secondly, contact angles are frequently observed in the final, static state of the sample. We have observed that contact angles changed as bubbles grew and this can only be recognised in dynamic observations. In our study the bubble contact angle on both plagioclase and clinopyroxene surfaces decreased with time, at least until a neighbouring bubble was encountered. A decreasing trend in the contact angle leads us to consider that there is a possibility that it would continue to decrease to zero, if a bubble was solitary, at which point the bubble will detach from the crystal (a zero-degree contact angle implies no contact).

Gualda and Ghiorso (2007) considered that a bubble-silicate crystal pair would tend to detach, contrary to a bubble-oxide pair that would tend to remain attached. Our decreasing contact angles is in agreement with their findings, since it is intuitively clear that detachment of any bubble from any surface would be expressed by an angle

decrease, while attachment would be expressed through a contact angle increase. This process (contact angle change) is well documented and extensively studied in chemistry, material sciences and engineering (e.g. Hirth et al., 1970; Whyman et al., 2008).

Even though we observed a consistent decrease in the contact angle, we did not observe bubble detachment during our experiments. This was anticipated due to the low water content in our samples (0.25-0.5 wt. % H_2O) and the short experimental duration (50 sec). If we were to take for example an andesite with 6 wt. % H_2O and a viscosity of 10 Pa s, and using Stokes' law velocity, it would take a bubble of 100 μm radius 3.3 sec to move 10 μm away from its initial location. In our case, the water content is much lower, hence the viscosity is higher and the bubble velocity is orders of magnitude slower. Since the imaging of bubble development was the primary aim of our experiments, we stopped scanning before any potential detachment could take place. In our experiments, complete detachment would also be difficult to observe due to homogeneous bubble nucleation that takes place as the temperature rises and essentially fills up all the space within the sample. Additionally, our heterogeneously nucleated bubbles are not solitary, but in contact one with the other and thus they interact with one another. This makes it harder for a solitary bubble to detach from the bubble cluster formed on the crystal surface. In a natural system, solitary bubble detachment from a crystal surface would occur when the critical radius of either bubble or crystal is surpassed (i.e. when the detachment force becomes greater than the attachment force; Gualda and Ghiorso, 2007), if at that point, there is space available in the surrounding melt (i.e. homogeneous bubble nucleation has not yet occurred).

We envision two possible mechanisms of bubble cluster detachment: simple cluster detachment and coalescence induced detachment (Figure 2.11). 1) If the bubble cluster does not encompass the crystal's entire surface, at a certain point along the bubble-crystal-melt contact line, melt can protrude between the flank bubble(s) and the crystal, at the point in time when the detachment force surpasses the attachment one (forces defined in Gualda and Ghiorso, 2007). This could lead to a chain reaction, where after the first bubble starts to detach, its immediate neighbours follow suite, preferring to maintain the bubble cluster intact than to remain on the silicate crystal surface. 2) Instead of maintaining individual thin melt films between each neighbouring bubble, in an effort to reduce the bubble cluster's total surface energy, bubble coalescence occurs (either between just two neighbouring bubbles, or more). This coalescence event leads to an abrupt bubble-crystal contact angle change and the total surface energy decreases, provoking bubble detachment. Both hypotheses would be possible if heterogeneous bubble nucleation is the primary nucleation process, and homogeneous nucleation is secondary. In both hypotheses the silicate crystal surface is reactivated for the nucleation of new bubbles. It is this possibility that makes silicate crystals much more interesting than oxide crystals for the study of bubble nucleation and magma degassing.

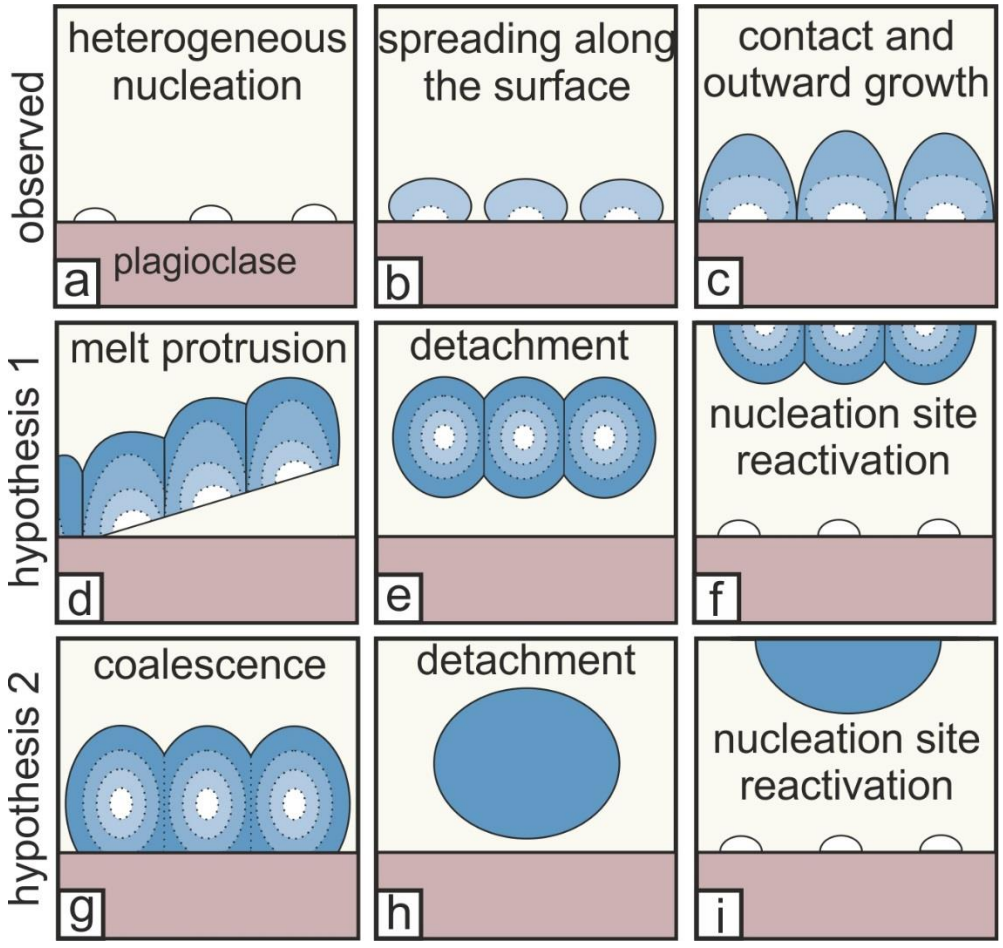

Figure 2.11: Possible bubble-crystal detachment scenarios. a-c) Schematic representation of observed bubble growth during *in situ* experiments. d-f) Hypothesis 1 for bubble detachment from a silicate crystal surface. Here, the flank bubbles start to detach first and the rest follow, preserving a bubble cluster. g-i) Hypothesis 2 for bubble detachment from a silicate crystal surface. Here, bubble coalescence occurs first, and the decrease in bubble surface energy provokes detachment.

2.5 Conclusions

Our findings show that heterogeneous bubble nucleation on silicates can occur in magma and should not be ignored. We also demonstrate a decreasing trend in bubble-crystal contact angles, indicating a tendency for detachment, in accordance with published work on low silicate crystal-bubble affinity (Gualda and Ghiorso, 2007). This indicates that silicate crystals can generate bubbles and subsequently lose them, thereby freeing their surfaces to nucleate bubbles again.

Combining heterogeneous bubble nucleation on silicate crystals with the possibility of detachment could offer an explanation as to why in many natural and experimental systems there are more bubbles found than oxide crystals could be expected to produce (see Shea, 2017). Instead of homogeneously nucleating within the melt, as generally proposed, the excess of bubbles could have been generated on silicate crystal surfaces present in these systems. We show that heterogeneous bubble nucleation on silicates is possible, and that, given the possibilities of 4D imaging and in the light of our findings, the explanations for certain textures in both natural and experimental samples should be reconsidered. We emphasize that observing the contact angle change (increase or decrease) via *in situ* experiments is the best way of determining a bubble's affinity for a crystal surface. We were also able to directly confirm the suggestion of Gardner and Denis (2004): that the contact angle changes during bubble growth and that the post-process angles reported thus far in the literature are unlikely to be true angles.

The minimum number of bubbles that nucleated on minerals in our experiments can be used to demonstrate the relative bubble nucleation efficiencies of their surfaces.

Such a comparison can be safely made within our experimental suite, where in every sample the melt composition, individual mineral species composition and water concentration were constant. In other words, the only changing parameters between different minerals were the crystal-melt and crystal-bubble surface energy, so we can say that the silicate crystals were more efficient than the oxides. It is very tempting to apply this difference in efficiency to other systems with different melt and mineral compositions and water concentrations; however, the authors warn against making direct extensions without further experiments. Nevertheless, our finding that clinopyroxene and plagioclase crystals dominate as sites of bubble nucleation in andesitic melts shows that the possible effect of these crystals on vesiculation and therefore the explosive to effusive transition (Bai et al., 2011) should be taken into account.

If the role of silicate crystals in bubble nucleation is viewed in this light, their importance in bubble nucleation models and eruption prediction models changes considerably, from being an almost neglected parameter to becoming perhaps one of the governing ones – a phenomenon worthy of further research.

2.6 Acknowledgements

We acknowledge the staff at the TOMCAT beamline for their support during the experiments. A portion of this work was performed at GeoSoilEnviroCARS (The University of Chicago, Sector 13), Advanced Photon Source (APS), Argonne National Laboratory. GeoSoilEnviroCARS is supported by the National Science Foundation - Earth Sciences (EAR-1128799) and Department of Energy- GeoSciences (DE-FG02-94ER14466). This research used resources of the Advanced Photon Source, a U.S. Department of Energy (DOE) Office of Science User Facility operated for the DOE Office of Science by Argonne National Laboratory under Contract No. DE-AC02-06CH11357. All authors wish to thank Mark Rivers (APS) for help with acquiring the *ex situ* scan of the natural sample from Montserrat. P.P. wishes to thank Marko Kudrna Prašek for many useful discussions, and all authors wish to thank Fabio Arzilli and Matteo Masotta for their insightful and helpful reviews.

2.7 Author contributions

P.P. (PhD student and principal investigator), D.R.B. (PhD codirector), J.C. (undergraduate student), J.L.F. (beamline scientist at the TOMCAT beamline), L.M., G.L. and F.B. all performed the tomographic microscopy experiments. P.P., M.D.H. (PhD director) and D.R.B. contributed to the ideas developed in the paper. J.C. synthesized the starting materials, J.L.F., L.M. and F.B. performed the fine-tuning of the acquisition and reconstruction parameters at TOMCAT. P.P. performed the volume rendering, manual thresholding, isosurface generation and contact angle measurements. All authors assisted with the manuscript.

2.8 References

Acocella, V., 2014. Structural control on magmatism along divergent and convergent plate boundaries: Overview, model, problems. *Earth-Science Reviews* 136, 226-288.

Adamson, A. W., Gast, A., 1997. Physical Chemistry of Surfaces, sixth ed. John Wiley and Sons, New York.

Applegarth, L. J., Tuffen, H., James, M. R., Pinkerton, H., Cashman, K. V., 2013. Direct observations of degassing-induced crystallization in basalts. *Geology* 41(2), 243-246.

Arndt, J., Häberle, F., 1973. Thermal expansion and glass transition temperatures of synthetic glasses of plagioclase-like compositions. *Contributions to Mineralogy and Petrology* 39(2), 175-183.

Atchley, A. A., Prosperetti, A., 1989. The crevice model of bubble nucleation. *The Journal of the Acoustical Society of America* 86(3), 1065-1084.

Bagdassarov, N. S., Dingwell, D. B., Wilding, M. C., 1996. Rhyolite magma degassing: an experimental study of melt vesiculation. *Bulletin of volcanology* 57(8), 587-601.

Bai, L., Baker, D. R., Polacci, M., Hill, R. J., 2011. In-situ degassing study on crystal-bearing Stromboli basaltic magmas: Implications for Stromboli explosions. *Geophysical Research Letters* 38(17), L17309.

Bai, L., Baker, D. R., Rivers, M., 2008. Experimental study of bubble growth in Stromboli basalt melts at 1 atm. *Earth and Planetary Science Letters* 267(3), 533-547.

Baker, D. R., Eggler, D. H., 1987. Compositions of anhydrous and hydrous melts coexisting with plagioclase, augite, and olivine or low-Ca pyroxene from 1 atm to 8 kbar; application to the Aleutian volcanic center of Atka. *American Mineralogist* 72(1-2), 12-28.

Baker, D. R., Brun, F., O'Shaughnessy, C., Mancini, L., Fife, J. L., Rivers, M., 2012a. A four-dimensional X-ray tomographic microscopy study of bubble growth in basaltic foam. *Nature Communications* 3, 1135.

Baker, D. R., Mancini, L., Polacci, M., Higgins, M. D., Gualda, G. A. R., Hill, R. J., Rivers, M. L., 2012b. An introduction to the application of X-ray microtomography to the three-dimensional study of igneous rocks. *Lithos* 148, 262-276.

Belien, I. B., Cashman, K. V., Rempel, A. W., 2010. Gas accumulation in particle-rich suspensions and implications for bubble populations in crystal-rich magma. *Earth and Planetary Science Letters* 297(1–2), 133-140.

Blander, M., Katz, J. L., 1975. Bubble nucleation in liquids. *AIChE Journal* 21(5), 833-848.

Blythe, L. S., Deegan, F. M., Freda, C., Jolis, E. M., Masotta, M., Misiti, V., Taddeucci, J., Troll, V. R., 2015. CO_2 bubble generation and migration during magma–carbonate interaction. *Contributions to Mineralogy and Petrology* 169(4), 1-16.

Brun, F., Mancini, L., Kasae, P., Favretto, S., Dreossi, D., Tromba, G., 2010. Pore3D: A software library for quantitative analysis of porous media. *Nuclear Instruments and Methods in Physics Research Section A: Accelerators, Spectrometers, Detectors and Associated Equipment* 615(3), 326-332.

Cameron, M., Sueno, S., Prewitt, C. T., Papike, J. J., 1973. High-Temperature Crystal Chemistry of Acmite, Diopside, Hedenbergite, Jadeite, Spodumene, and Ureyite. *American Mineralogist* 58, 594-618.

Cluzel, N., Laporte, D., Provost, A., Kannewischer, I., 2008. Kinetics of heterogeneous bubble nucleation in rhyolitic melts: implications for the number density of bubbles in volcanic conduits and for pumice textures. *Contributions to Mineralogy and Petrology* 156(6), 745-763.

Cole, R., 1974. Boiling nucleation. *Advances in Heat Transfer* 10, 85-166.

Eichelberger, J., Hayes, D., 1982. Magmatic model for the Mount St. Helens blast of May 18, 1980. *Journal of Geophysical Research* 87(B9), 7727-7738.

Eustathopoulos, N., Nicholas, M. G., Drevet, B., 1999. Wettability at high temperatures, Vol. 3. Elsevier, Amsterdam.

Fiege, A., Cichy, S. B., 2015. Experimental constraints on bubble formation and growth during magma ascent: A review. *American Mineralogist* 100(11-12), 2426-2442.

Fife, J. L., Rappaz, M., Pistone, M., Celcer, T., Mikuljan, G., Stampanoni, M., 2012. Development of a laser-based heating system for in situ synchrotron-based X-ray tomographic microscopy. *Journal of Synchrotron Radiation* 19(3), 352-358.

Gardner, J. E., 2007. Heterogeneous bubble nucleation in highly viscous silicate melts during instantaneous decompression from high pressure. *Chemical Geology* 236(1–2), 1-12.

Gardner, J. E., Denis, M.-H., 2004. Heterogeneous bubble nucleation on Fe-Ti oxide crystals in high-silica rhyolitic melts. *Geochimica et Cosmochimica Acta* 68(17), 3587-3597.

Gardner, J. E., Hilton, M., Carroll, M. R., 2000. Bubble growth in highly viscous silicate melts during continuous decompression from high pressure. *Geochimica et Cosmochimica Acta* 64(8), 1473-1483.

Gardner, J. E., Hilton, M., Carroll, M. R., 1999. Experimental constraints on degassing of magma: isothermal bubble growth during continuous decompression from high pressure. *Earth and Planetary Science Letters* 168(1), 201-218.

Gardner, J. E., Thomas, R. M. E., Jaupart, C., Tait, S., 1996. Fragmentation of magma during Plinian volcanic eruptions. *Bulletin of Volcanology* 58(2-3), 144-162.

Giachetti, T., Burgisser, A., Arbaret, L., Druitt, T. H., Kelfoun, K., 2011. Quantitative textural analysis of Vulcanian pyroclasts (Montserrat) using multi-scale X-ray computed microtomography: comparison with results from 2D image analysis. *Bulletin of Volcanology* 73(9), 1295-1309.

Giachetti, T., Druitt, T. H., Burgisser, A., Arbaret, L., Galven, C., 2010. Bubble nucleation, growth and coalescence during the 1997 Vulcanian explosions of Soufrière Hills Volcano, Montserrat. *Journal of Volcanology and Geothermal Research* 193(3), 215-231.

Giordano, D., Nichols, A. R. L., Dingwell, D. B., 2005. Glass transition temperatures of natural hydrous melts: a relationship with shear viscosity and implications for the welding process. *Journal of Volcanology and Geothermal Research* 142(1), 105-118.

Gondé, C., Martel, C., Pichavant, M., Bureau, H., 2011. In situ bubble vesiculation in silicic magmas. *American Mineralogist* 96(1), 111-124.

Gondé, C., Massare, D., Bureau, H., Martel, C., Pichavant, M., Clocchiatti, R., 2006. In situ study of magmatic processes: a new experimental approach. *High Pressure Research* 26(3), 243-250.

Gualda, G. A., Anderson, 2007. Magnetite scavenging and the buoyancy of bubbles in magmas. Part 1: Discovery of a pre-eruptive bubble in Bishop rhyolite. *Contributions to Mineralogy and Petrology* 153(6), 733-742.

Gualda, G. A., Ghiorso, M. S., 2007. Magnetite scavenging and the buoyancy of bubbles in magmas. Part 2: Energetics of crystal-bubble attachment in magmas. *Contributions to Mineralogy and Petrology* 154(4), 479-490.

Hirth, J., Pound, G. M., Pierre, G. R. St., 1970. Bubble nucleation. *Metallurgical Transactions* 1(4), 939-945.

Hurwitz, S., Navon, O., 1994. Bubble nucleation in rhyolitic melts: Experiments at high pressure, temperature, and water content. *Earth and Planetary Science Letters* 122(3–4), 267-280.

Landau, L., Lifshitz, E., 1980. Statistical Physics, Vol. 1. Oxford: Pergamon 24: 31-57.

Larsen, J. F., 2008. Heterogeneous bubble nucleation and disequilibrium H2O exsolution in Vesuvius K-phonolite melts. *Journal of Volcanology and Geothermal Research* 175(3), 278-288.

Manga, M., Brodsky, E., 2006. Seismic triggering of eruptions in the far field: volcanoes and geysers. *Annual Review of Earth and Planetary Sciences* 34, 263-291.

Mangan, M., Sisson, T., 2000. Delayed, disequilibrium degassing in rhyolite magma: decompression experiments and implications for explosive volcanism. *Earth and Planetary Science Letters* 183(3), 441-455.

Mangan, M., Sisson, T., 2005. Evolution of melt-vapor surface tension in silicic volcanic systems: Experiments with hydrous melts. *Journal of Geophysical Research: Solid Earth* 110(B1), B01202.

Mangan, M., Sisson, T. W., Hankins, W. B., 2004. Decompression experiments identify kinetic controls on explosive silicic eruptions. *Geophysical Research Letters* 31(8), L08605.

Masotta, M., Ni, H., Keppler, H., 2014. In situ observations of bubble growth in basaltic, andesitic and rhyodacitic melts. *Contributions to Mineralogy and Petrology* 167(2), 1-14.

Mourtada-Bonnefoi, C. C., Laporte, D., 2004. Kinetics of bubble nucleation in a rhyolitic melt: an experimental study of the effect of ascent rate. *Earth and Planetary Science Letters* 218(3), 521-537.

Mysen, B., Richet, P., 2005. Silicate glasses and melts: properties and structure. Elsevier Science 10: pp. 525.

Navon, O., Lyakhovsky, V., 1998. Vesiculation processes in silicic magmas. *Geological Society, London, Special Publications* 145(1), 27-50.

Paganin, D., Mayo, S. C., Gureyev, T. E., Wilkins, P. R., Wilkins, S. W., 2002. Simultaneous phase and amplitude extraction from a single defocused image of a homogeneous object. *Journal of Microscopy* 206, 33–40.

Pistone, M., Arzilli, F., Dobson, K. J., Cordonnier, B., Reusser, E., Ulmer, P., Marone, F., Whittington, A. G., Mancini, L., Fife, J. L., Blundy, J. D., 2015. Gas-driven filter pressing in magmas: Insights into in-situ melt segregation from crystal mushes. *Geology* 43, 699-702.

Pistone, M., Caricchi, L., Fife, J. L., Mader, K., Ulmer, P., 2015. In situ X-ray tomographic microscopy observations of vesiculation of bubble-free and bubble-bearing magmas. *Bulletin of Volcanology* 77(12), 1-15.

Polacci, M., Baker, D. R., Mancini, L., Tromba, G., Zanini, F., 2006. Three-dimensional investigation of volcanic textures by X-ray microtomography and implications for conduit processes. *Geophysical Research Letters* 33(13), L13312.

Proussevitch, A., Sahagian, D., 2005. Bubbledrive-1: A numerical model of volcanic eruption mechanisms driven by disequilibrium magma degassing. *Journal of Volcanology and Geothermal Research* 143(1), 89-111.

Sakuyama, M., Kushiro, I., 1979. Vesiculation of hydrous andesitic melt and transport of alkalies by separated vapor phase. *Contributions to Mineralogy and Petrology* 71(1), 61-66.

Schindelin, J., Arganda-Carreras, I., Frise, E., Kaynig, V., Longair, M., Pietzsch, T., Preibisch, S., Rueden, C., Saalfeld, S., Schmid, B., Tinevez, J.Y., 2012. Fiji: an open-source platform for biological-image analysis. *Nature methods*, 9(7), 676-682.

Schlepütz, C.M., Mokso, R., Theidel, G., Billich, H., Schmid, E., Celcer, T., Mikuljan, G., Marone, F., Schlumpf, N., Stampanoni, M., 2017. GigaFRoST–a high-speed camera readout system for ultrafast tomography at sustained kHz frame rates. 3rd International Conference on Tomography of Materials and Structures. Lund, Sweden, 26-30 June 2017, ICTMS2017-162.

Shea, T., 2017. Bubble nucleation in magmas: A dominantly heterogeneous process?. *Journal of Volcanology and Geothermal Research* 343, 155-170.

Sigurdsson, H., Houghton, B., McNutt, S., Rymer, H. and Stix, J. eds., 2015. The encyclopedia of volcanoes. Elsevier, Amsterdam.

Skinner, B. J., 1966. Section 6: thermal expansion. *Geological Society of America Memoirs* 97, 75-96.

Sparks, R. S. J., 1978. The dynamics of bubble formation and growth in magmas: A review and analysis. *Journal of Volcanology and Geothermal Research* 3(1-2), 1-37.

Stampanoni, M., Groso, A., Isenegger, A., Mikuljan, G., Chen, Q., Bertrand, A., Henein, S., Betemps, R., Frommherz, U., Böhler, P., Meister, D., Lange, M., Abela, R., 2006. Trends in synchrotron-based tomographic imaging: the SLS experience. Pr*oceedings SPIE, 6318, Developments in X-Ray Tomography V*, 63180M (September 07, 2006).

Tribaudino, M., Angel, R. J., Cámara, F., Nestola, F., Pasqual, D., Margiolaki, I., 2010. Thermal expansion of plagioclase feldspars. *Contributions to Mineralogy and Petrology* 160(6), 899-908.

Varshneya, A. K., 1994. Fundamentals of inorganic glasses, first ed. Academic Press, Inc., San Diego.

Whyman, G., Bormashenko, E., Stein, T., 2008. The rigorous derivation of Young, Cassie–Baxter and Wenzel equations and the analysis of the contact angle hysteresis phenomenon. *Chemical Physics Letters* 450(4), 355-359.

Young, T., 1805. An essay on the cohesion of fluids. *Philosophical Transactions of the Royal Society of London* 95, 65-87.

2.9 Appendices

Appendices 2.1 to 2.6 can be found on a CD-ROM accompanying the thesis.

Appendix 2.1

Time-lapse animation of a 2D axial slice of sample 2b-8, from the *in situ* imaging, complimentary to Figure 2.7. The duration of the sequence is 50 s, starting at 620 °C and ending at 650 °C. The sample contains clinopyroxene silicate crystals, and bubbles are nucleating and growing on its surfaces.

https://www.sciencedirect.com/science/article/pii/S0024493717304097#s0135

Appendix 2.2

Time-lapse animation of a 2D axial slice of sample 3-6, from the *in situ* imaging, complimentary to Figure 2.7. The duration of the sequence is 50 s, starting at 540 °C and ending at 680 °C. The sample contains both clinopyroxene and plagioclase crystals, and bubbles are nucleating and growing on their surfaces.

https://www.sciencedirect.com/science/article/pii/S0024493717304097#s0135

Appendix 2.3

Time-lapse animation of bubbles growing on a clinopyroxene crystal, from sample 2b-8, visualized in 3D. The animation corresponds to Figure 2.7. The clinopyroxene crystal is visualized in green and the bubbles in blue.

https://www.sciencedirect.com/science/article/pii/S0024493717304097#s0135

Appendix 2.4

Time-lapse animation of bubbles growing on a clinopyroxene crystal, from sample 3-6, visualized in 3D. The animation corresponds to Figure 2.7. The clinopyroxene core is visualized in dark green, the outer clinopyroxene rim in light green and the bubbles in blue.

https://www.sciencedirect.com/science/article/pii/S0024493717304097#s0135

Appendix 2.5

3D visualization of sample 2b-8. The video shows the *ex situ* phase contrast scan, with an YZ direction slice passing through it, revealing its inner structure. The sample contains clinopyroxene crystals, oxides and bubbles. The height of the bounding box is 1.16 mm.

https://www.sciencedirect.com/science/article/pii/S0024493717304097#s0135

Appendix 2.6

3D visualization of sample 3-6. The video shows the *ex situ* phase contrast scan, with an YZ direction slice passing through it, revealing its inner structure. The sample contains clinopyroxene and plagioclase crystals, oxides and bubbles. The height of the bounding box is 0.7 mm.

https://www.sciencedirect.com/science/article/pii/S0024493717304097#s0135

Appendix 2.7

Compositional analysis performed with a BSE detector on several points for images presented in Figure 2.9 a–l. Each image is followed by an element spectrum for all points indicated on the image.

https://www.sciencedirect.com/science/article/pii/S0024493717304097#s0135

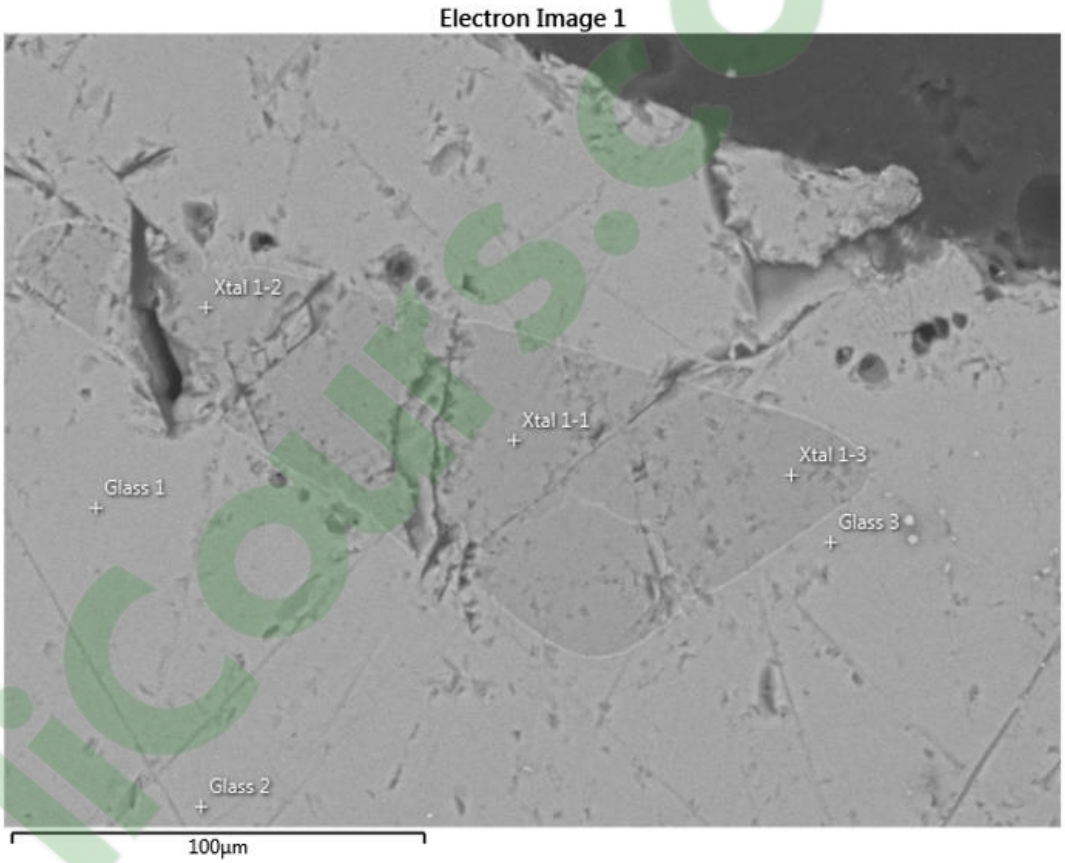

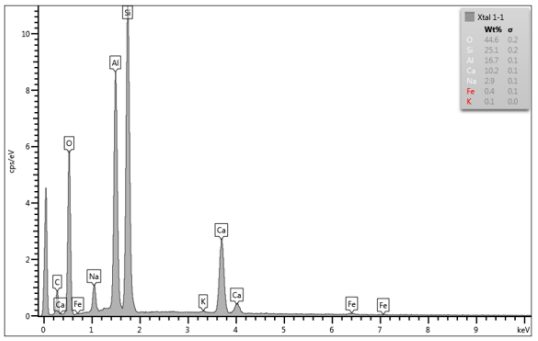
Xtal 1-1
Wt% σ
O 44.6 0.2
Si 25.1 0.2
Al 16.7 0.1
Ca 10.2 0.1
Na 2.9 0.1
Fe 0.4 0.1
K 0.1 0.0
cps/eV
keV

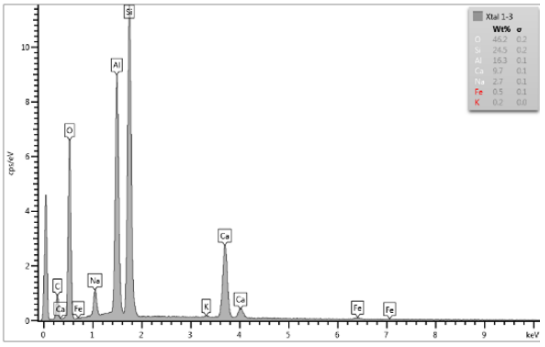
Xtal 1-3
Wt% σ
O 46.2 0.2
Si 24.5 0.2
Al 16.3 0.1
Ca 9.7 0.1
Na 2.7 0.1
Fe 0.5 0.1
K 0.2 0.0
cps/eV
keV

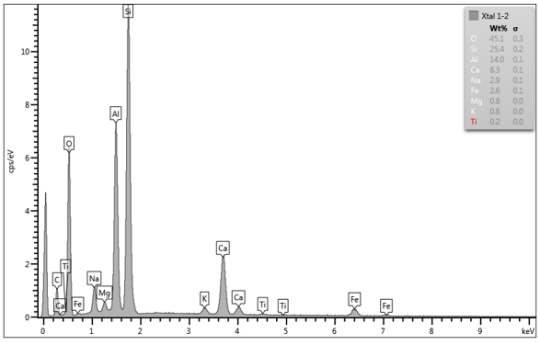
Xtal 1-2
Wt% σ
O 45.1 0.3
Si 25.4 0.2
Al 14.0 0.1
Ca 8.3 0.1
Na 2.9 0.1
Fe 2.6 0.1
Mg 0.8 0.0
K 0.8 0.0
Ti 0.2 0.0
cps/eV
keV

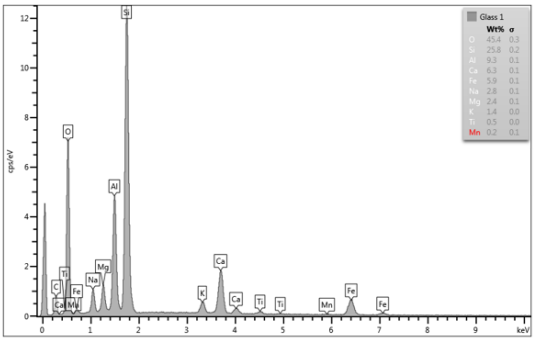
Glass 1
Wt% σ
O 45.4 0.3
Si 25.8 0.2
Al 9.3 0.1
Ca 6.3 0.1
Fe 5.9 0.1
Na 2.8 0.1
Mg 2.4 0.1
K 1.4 0.0
Ti 0.5 0.0
Mn 0.2 0.1
cps/eV
keV

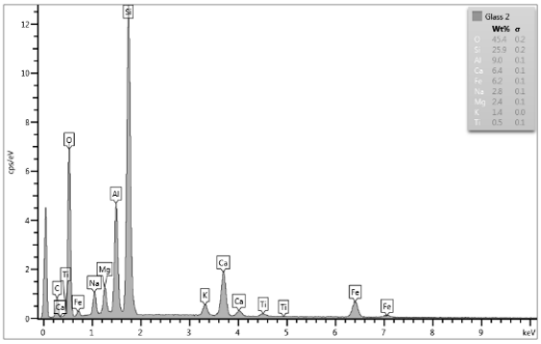
Glass 2
Wt% σ
O 45.4 0.2
Si 25.9 0.2
Al 9.0 0.1
Ca 6.4 0.1
Fe 6.2 0.1
Na 2.8 0.1
Mg 2.4 0.1
K 1.4 0.0
Ti 0.5 0.1
cps/eV
keV

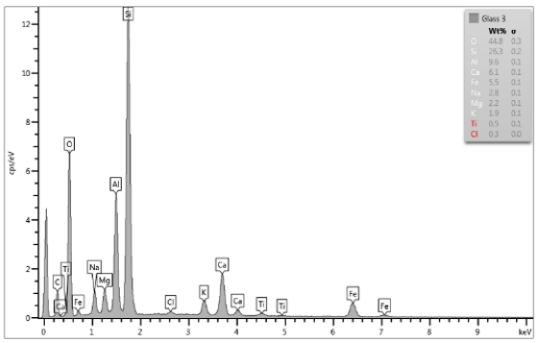
Glass 3
Wt% σ
O 44.8 0.3
Si 26.3 0.2
Al 9.6 0.1
Ca 6.1 0.1
Fe 5.5 0.1
Na 2.8 0.1
Mg 2.2 0.1
K 1.9 0.1
Ti 0.5 0.1
Cl 0.3 0.0
cps/eV
keV

Electron Image 2

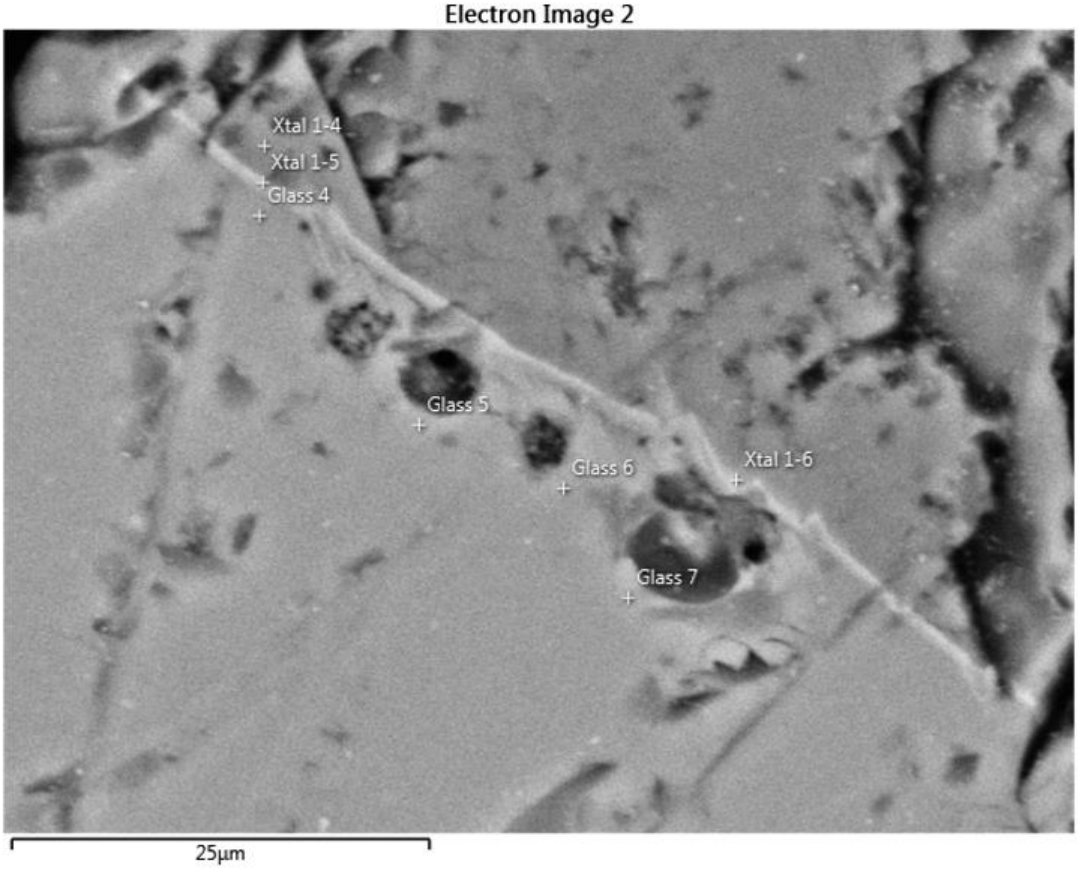

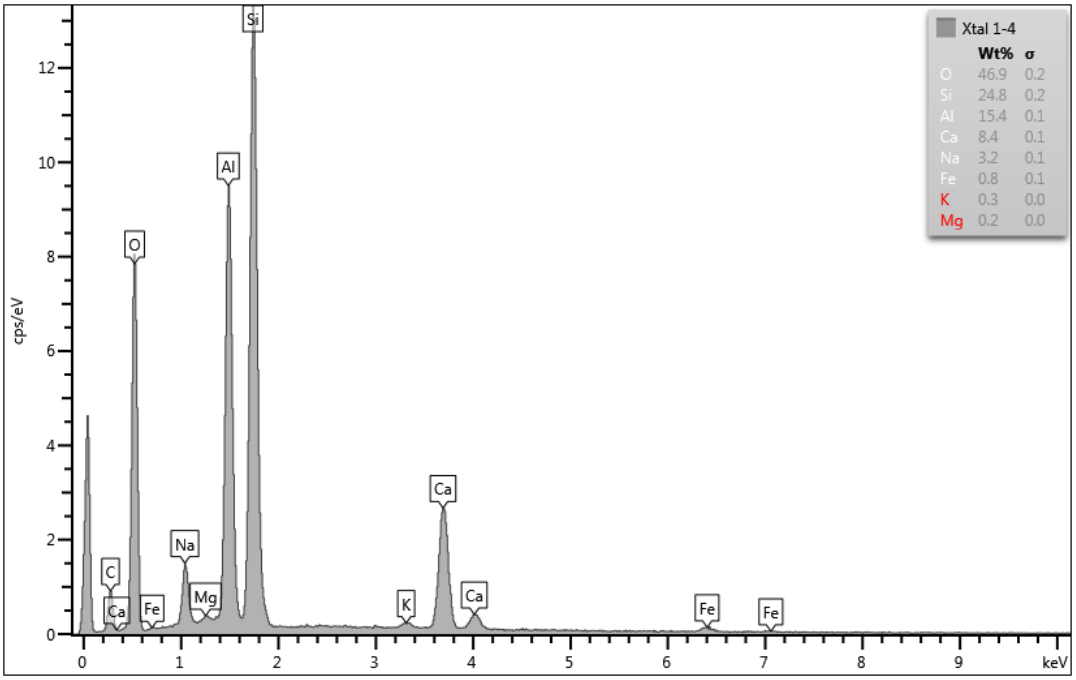

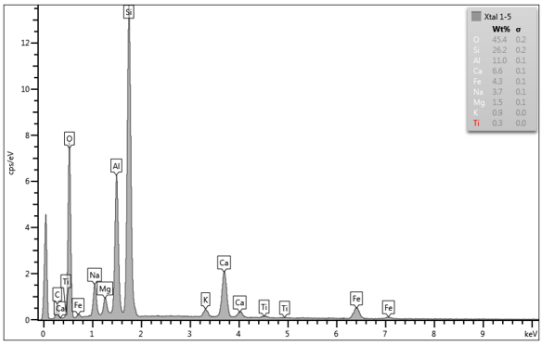
Xtal 1-5
Wt% σ
O 45.4 0.2
Si 26.2 0.2
Al 11.0 0.1
Ca 6.6 0.1
Fe 4.3 0.1
Na 3.7 0.1
Mg 1.5 0.1
K 0.9 0.0
Ti 0.3 0.0
cps/eV
keV

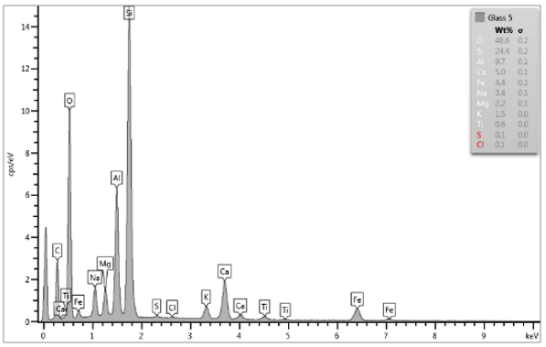
Glass 5
Wt% σ
O 48.6 0.2
Si 24.4 0.2
Al 9.7 0.1
Ca 5.0 0.1
Fe 4.4 0.1
Na 3.4 0.1
Mg 2.2 0.1
K 1.5 0.0
Ti 0.6 0.0
S 0.1 0.0
Cl 0.1 0.0
cps/eV
keV

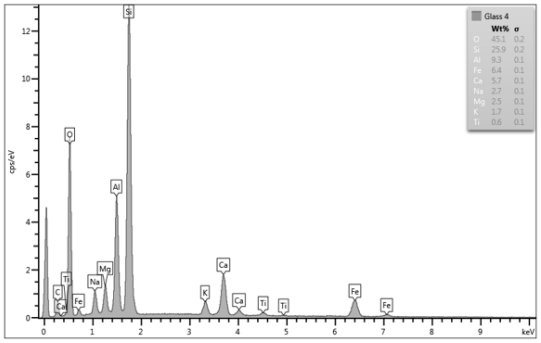
Glass 4
Wt% σ
O 45.1 0.2
Si 25.9 0.2
Al 9.3 0.1
Fe 6.4 0.1
Ca 5.7 0.1
Na 2.7 0.1
Mg 2.5 0.1
K 1.7 0.1
Ti 0.6 0.1
cps/eV
keV

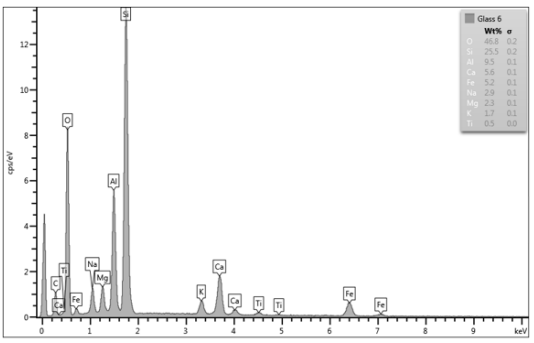
Glass 6
Wt% σ
O 46.8 0.2
Si 25.5 0.2
Al 9.5 0.1
Ca 5.6 0.1
Fe 5.2 0.1
Na 2.9 0.1
Mg 2.3 0.1
K 1.7 0.1
Ti 0.5 0.0
cps/eV
keV

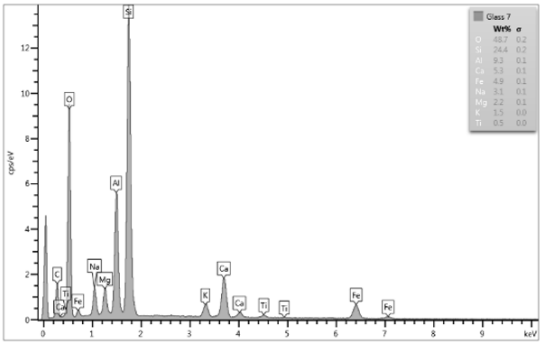
Glass 7
Wt% σ
O 48.7 0.2
Si 24.4 0.2
Al 9.3 0.1
Ca 5.3 0.1
Fe 4.9 0.1
Na 3.1 0.1
Mg 2.2 0.1
K 1.5 0.0
Ti 0.5 0.0
cps/eV
keV

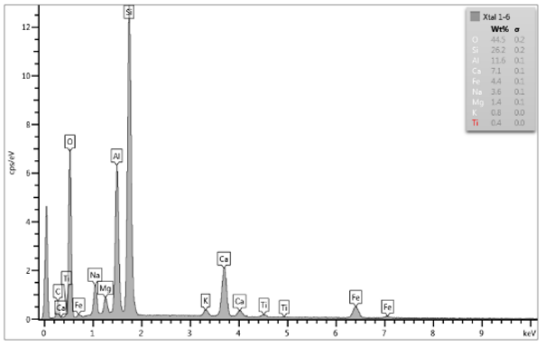
Xtal 1-6
Wt% σ
O 44.5 0.2
Si 26.2 0.2
Al 11.6 0.1
Ca 7.1 0.1
Fe 4.4 0.1
Na 3.6 0.1
Mg 1.4 0.1
K 0.8 0.0
Ti 0.4 0.0
cps/eV
keV

Electron Image 9

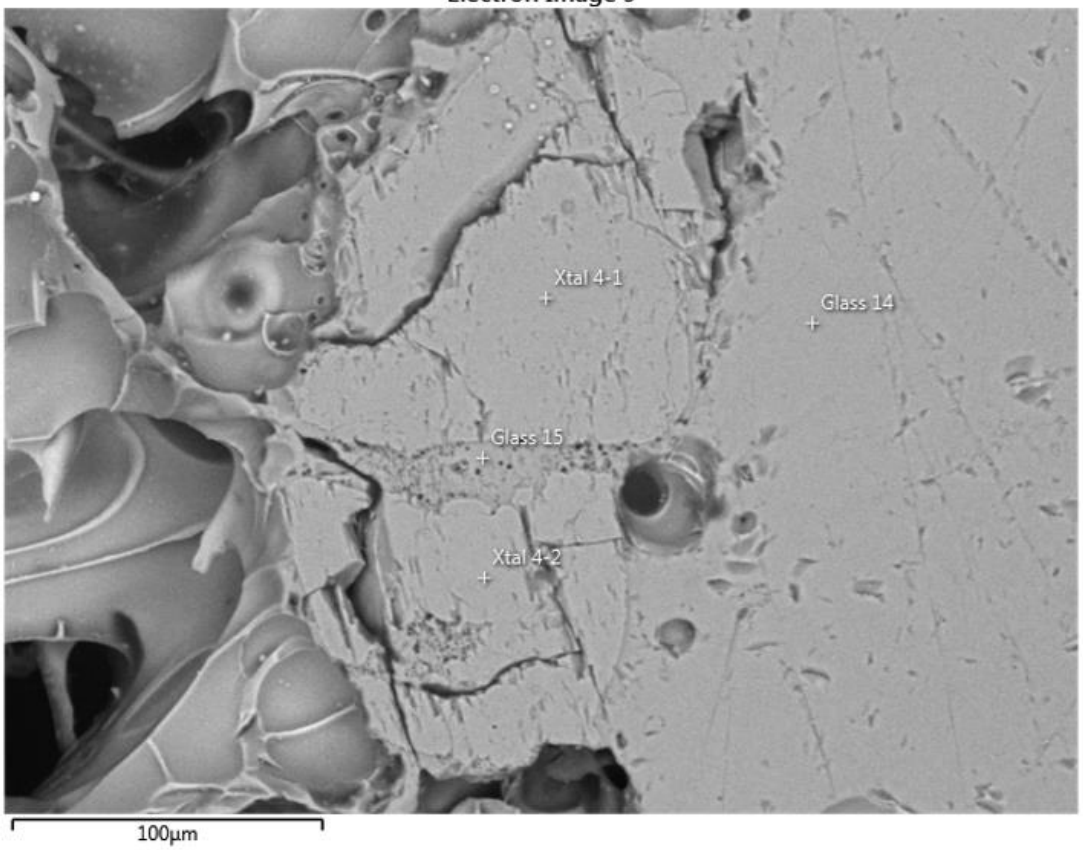

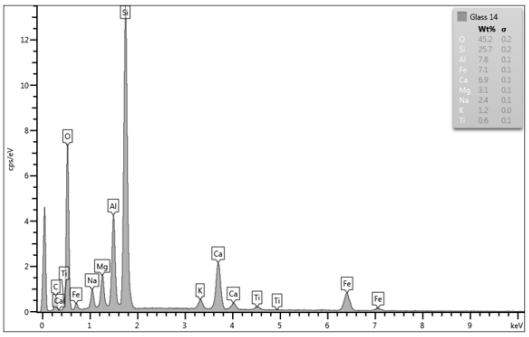

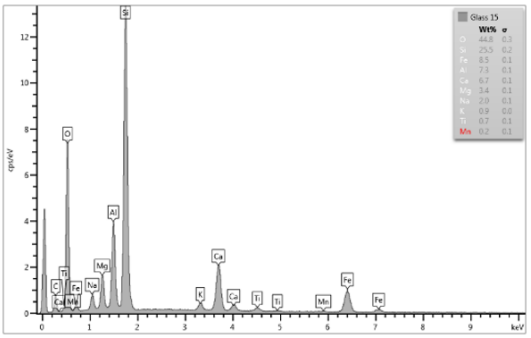

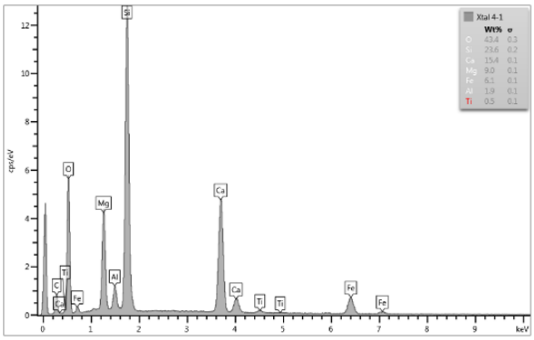

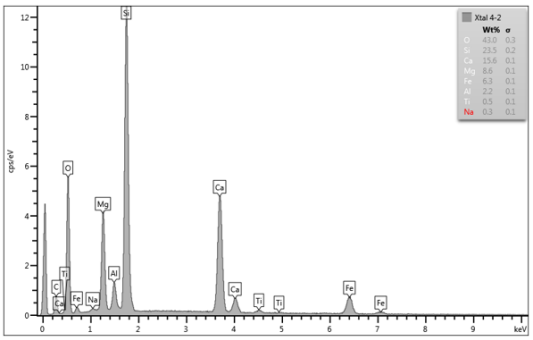

Electron Image 10

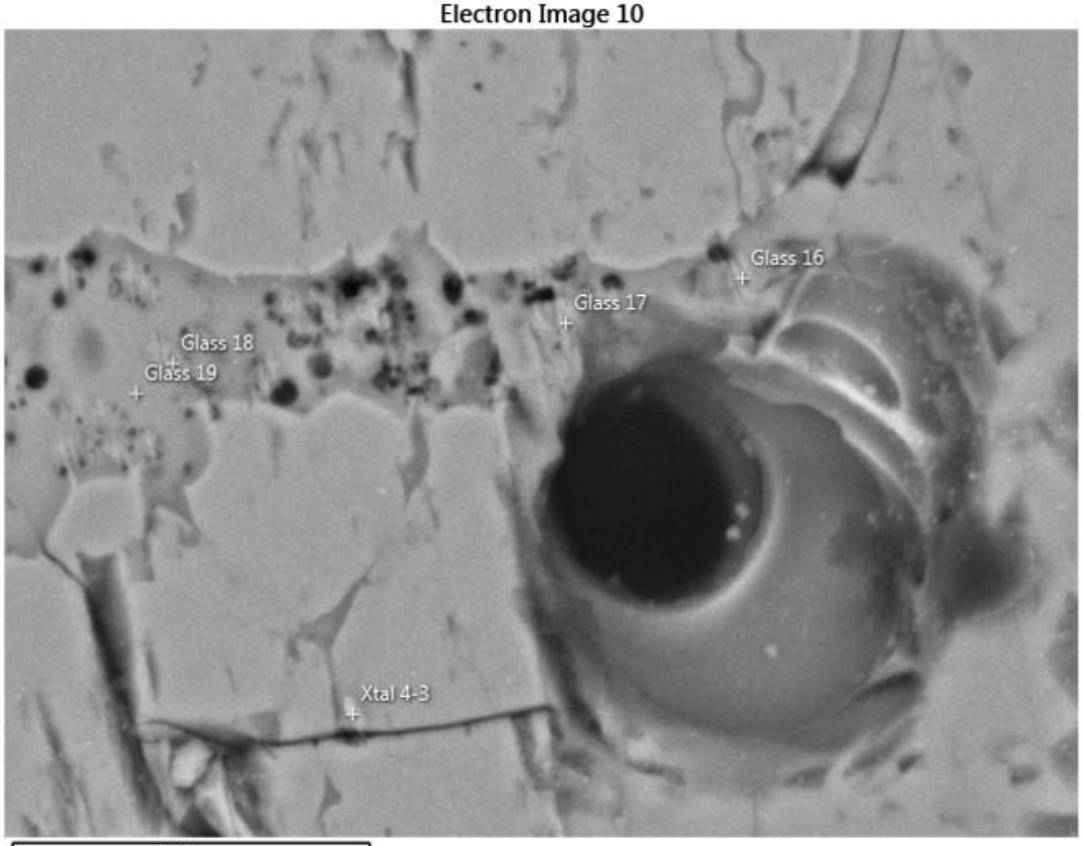

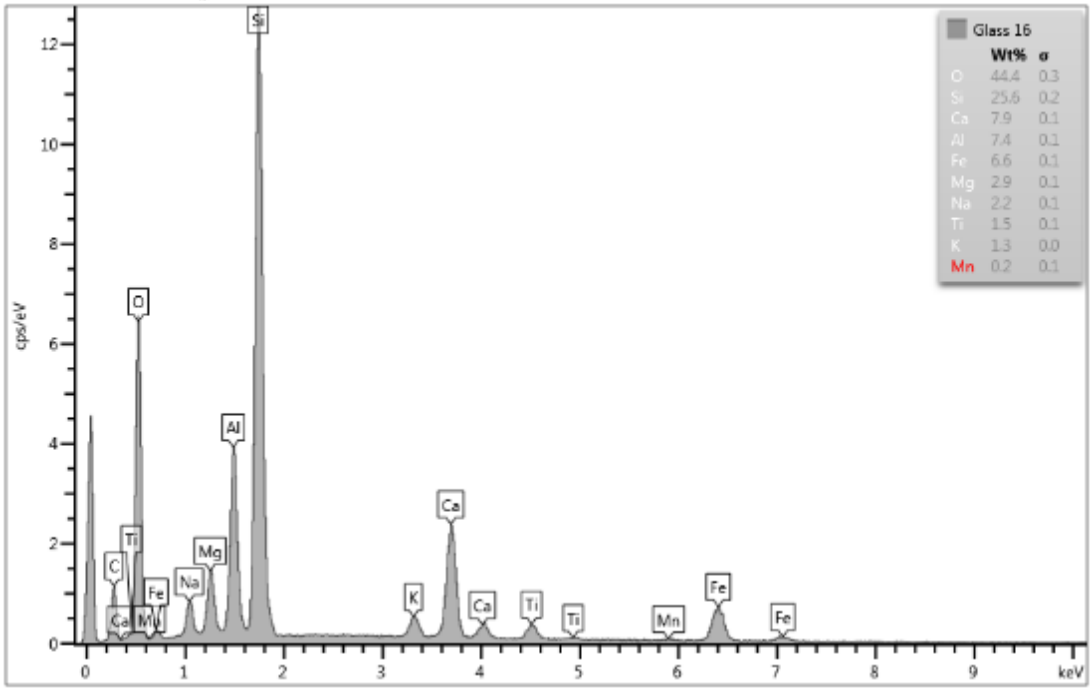

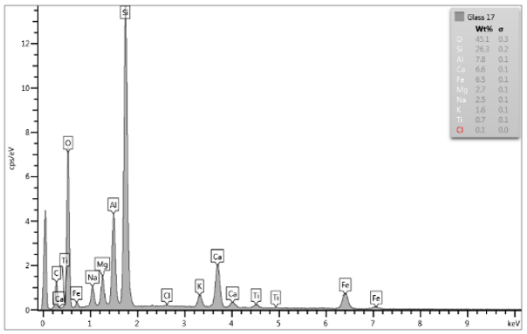
Glass 17
Wt% σ
O 45.1 0.3
Si 26.3 0.2
Al 7.8 0.1
Ca 6.6 0.1
Fe 6.5 0.1
Mg 2.7 0.1
Na 2.5 0.1
K 1.6 0.1
Ti 0.7 0.1
Cl 0.1 0.0
cps/eV
keV

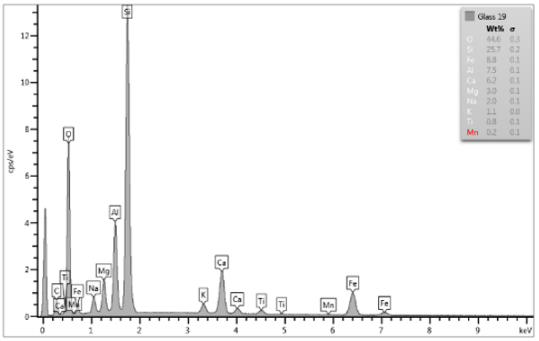
Glass 19
Wt% σ
O 44.6 0.3
Si 25.7 0.2
Fe 8.8 0.1
Al 7.5 0.1
Ca 6.2 0.1
Mg 3.0 0.1
Na 2.0 0.1
K 1.1 0.0
Ti 0.8 0.1
Mn 0.2 0.1
cps/eV
keV

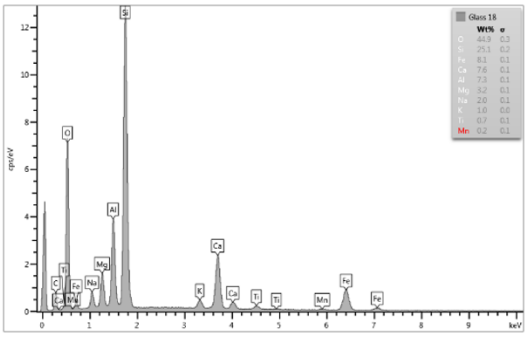
Glass 18
Wt% σ
O 44.9 0.3
Si 25.1 0.2
Fe 8.1 0.1
Ca 7.6 0.1
Al 7.3 0.1
Mg 3.2 0.1
Na 2.0 0.1
K 1.0 0.0
Ti 0.7 0.1
Mn 0.2 0.1
cps/eV
keV

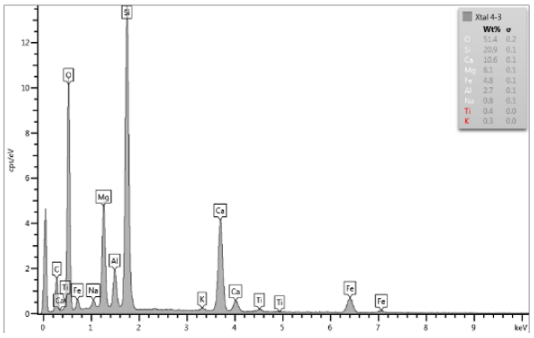
Xtal 4-3
Wt% σ
O 51.4 0.2
Si 20.9 0.1
Ca 10.6 0.1
Mn 8.1 0.1
Fe 4.8 0.1
Al 2.7 0.1
Na 0.8 0.1
Ti 0.4 0.0
K 0.3 0.0
cps/eV
keV

Electron Image 7

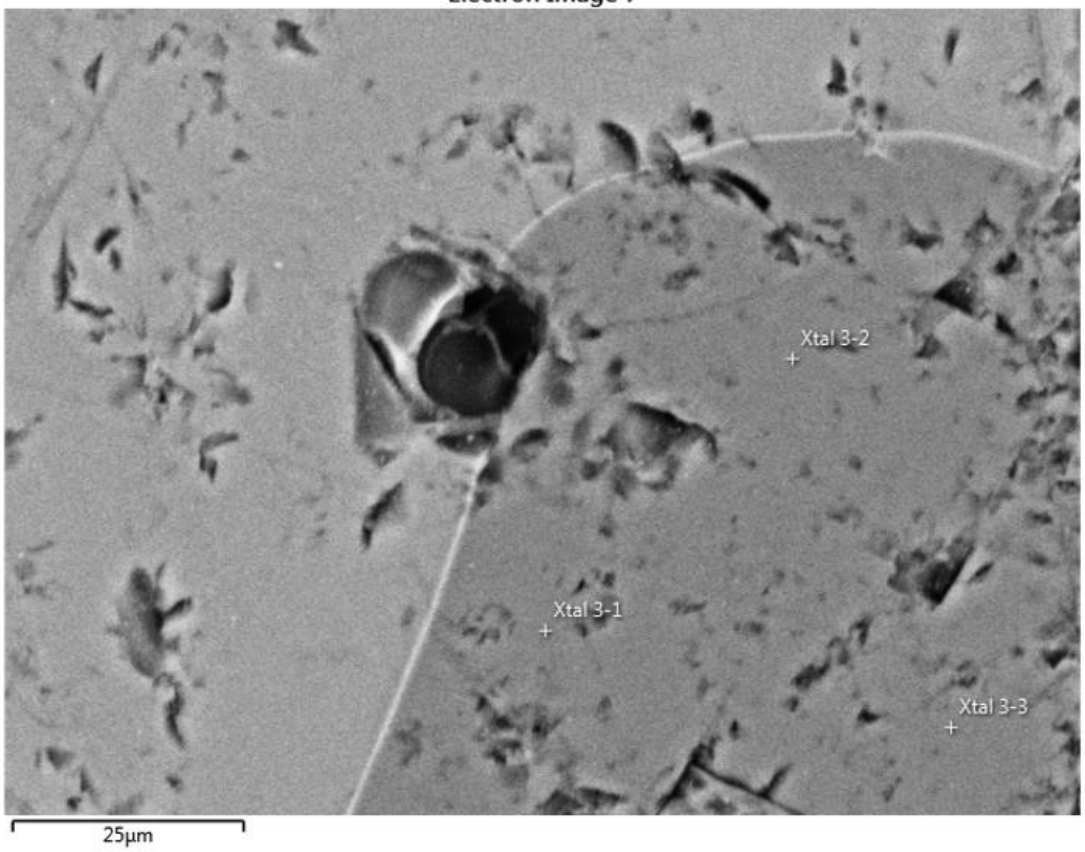

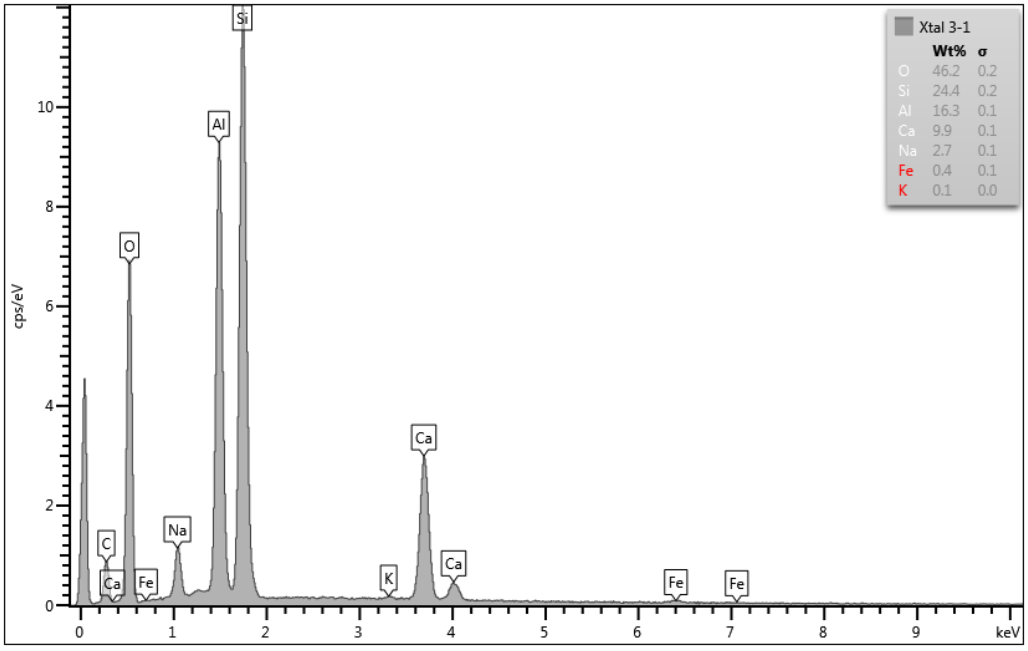

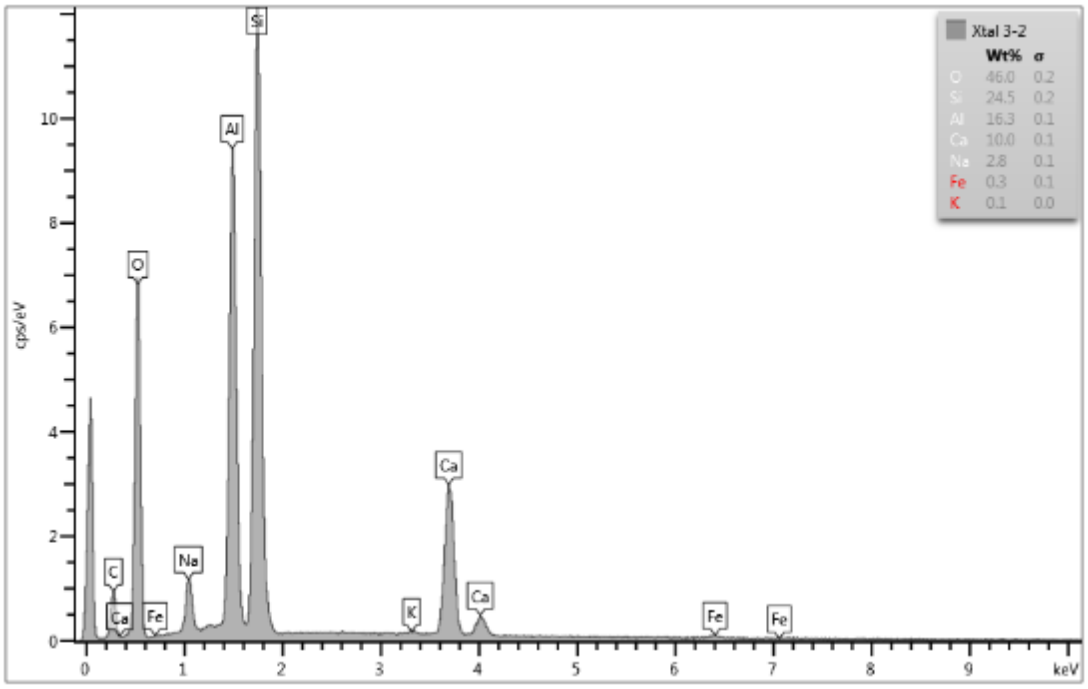
Xtal 3-2
Wt% σ
O 46.0 0.2
Si 24.5 0.2
Al 16.3 0.1
Ca 10.0 0.1
Na 2.8 0.1
Fe 0.3 0.1
K 0.1 0.0
cps/eV
keV
O
Si
Al
C
Ca
Fe
Na
K
Ca
Ca
Fe
Fe

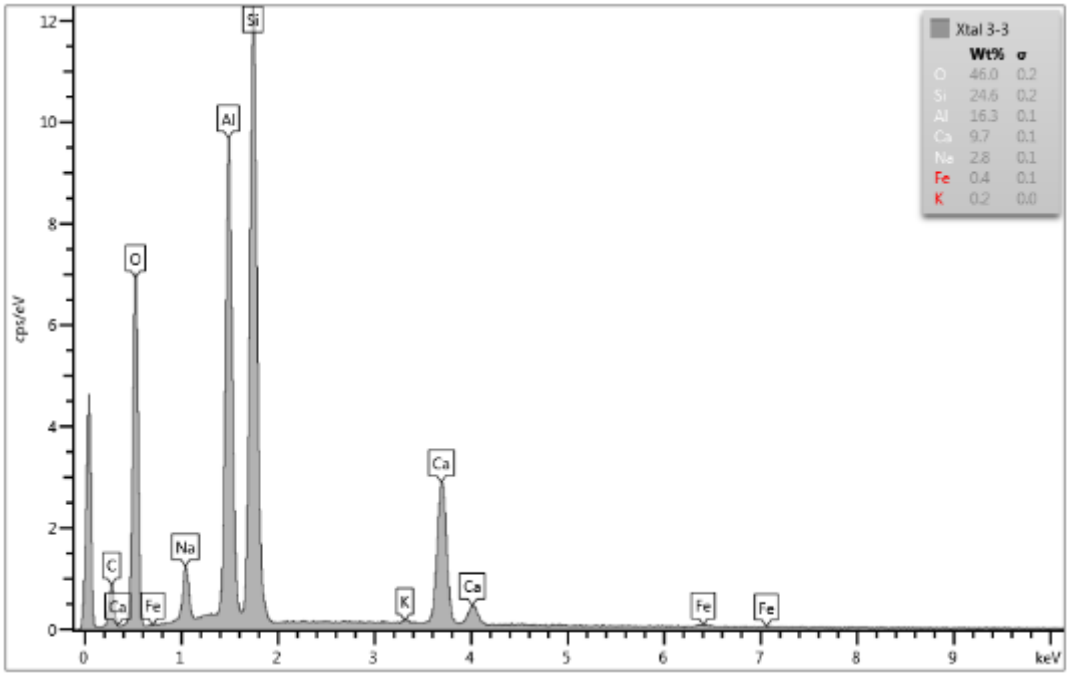
Xtal 3-3
Wt% σ
O 46.0 0.2
Si 24.6 0.2
Al 16.3 0.1
Ca 9.7 0.1
Na 2.8 0.1
Fe 0.4 0.1
K 0.2 0.0
cps/eV
keV
O
Si
Al
C
Ca
Fe
Na
K
Ca
Ca
Fe
Fe

Electron Image 8

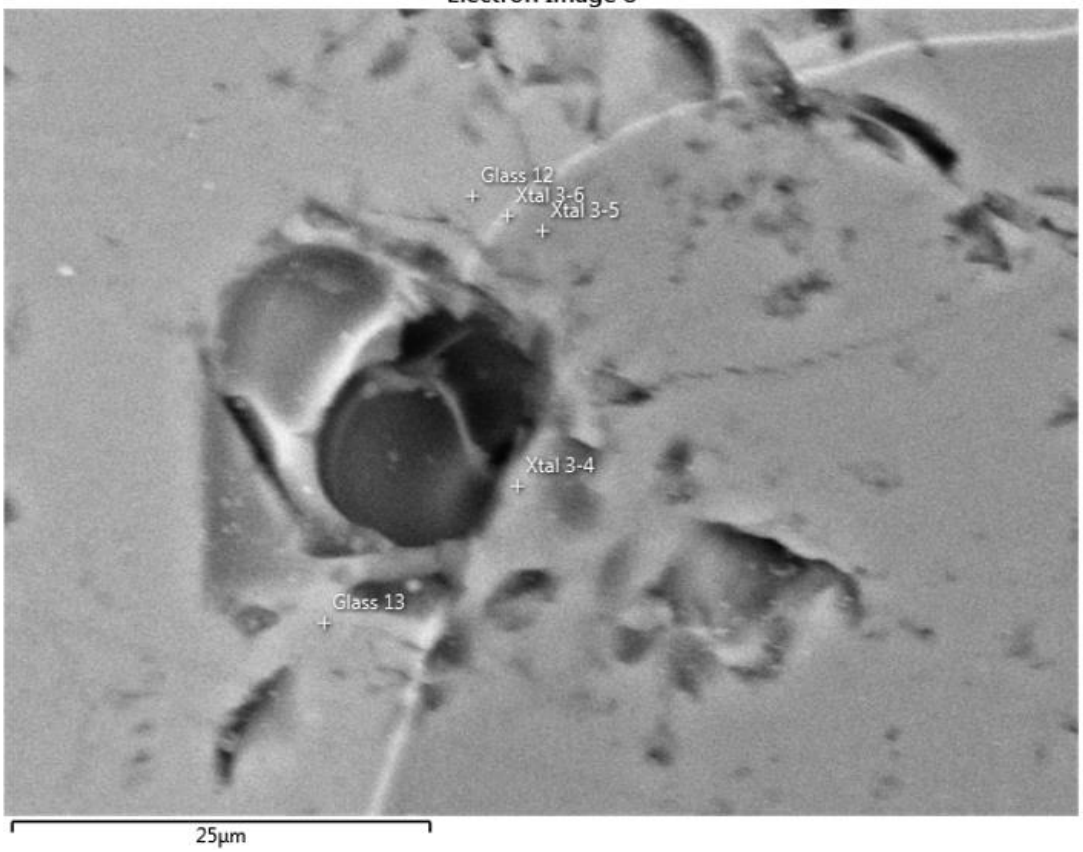

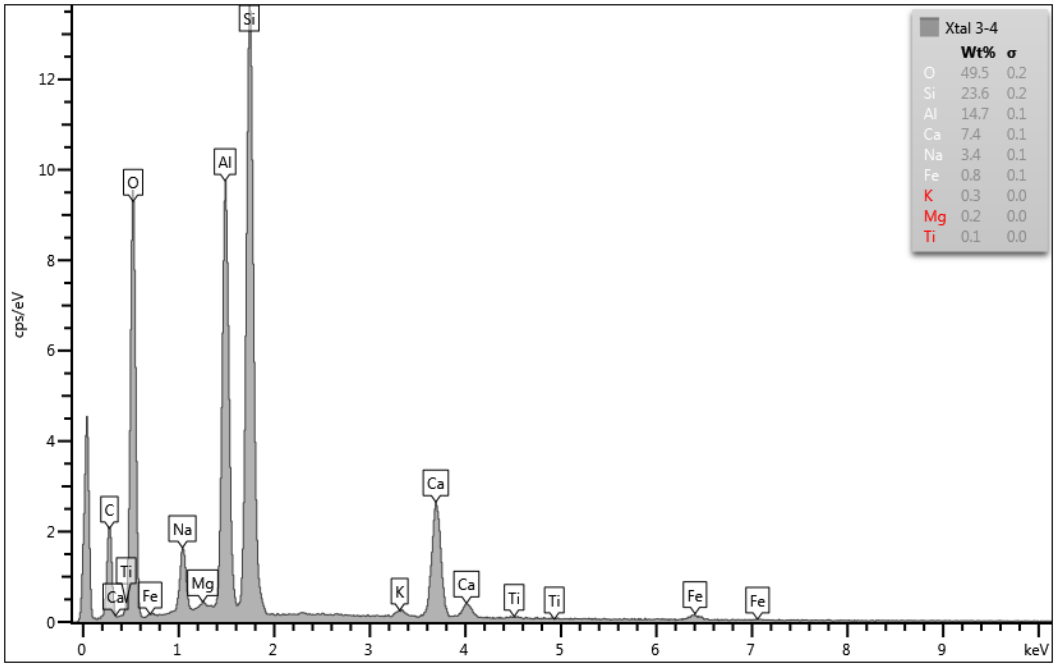

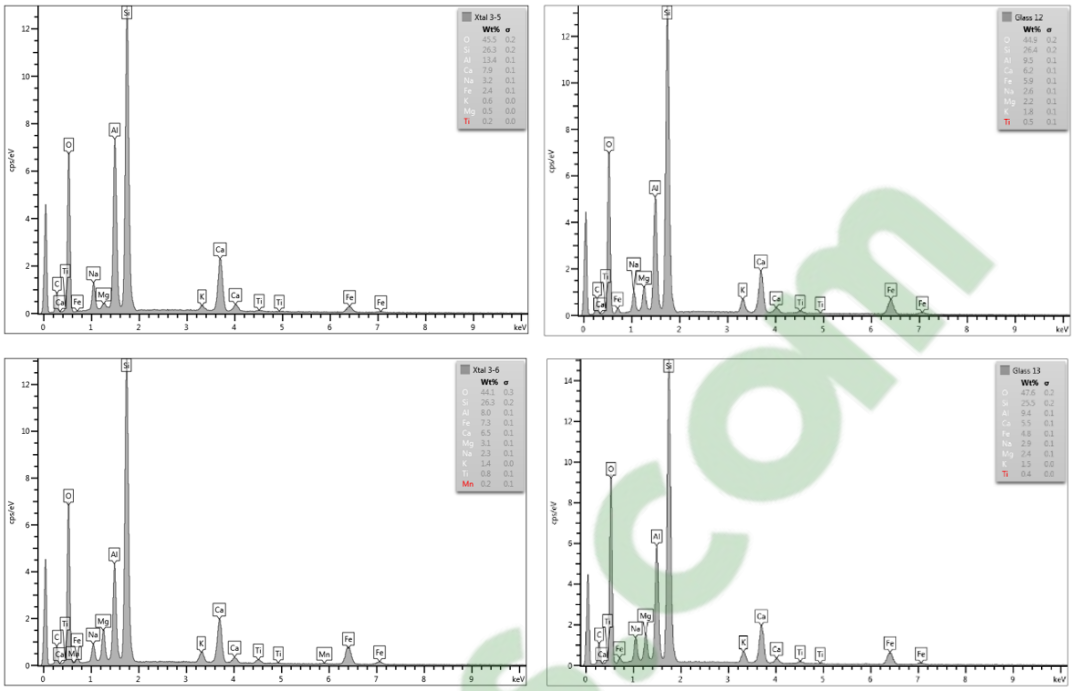

Electron Image 6

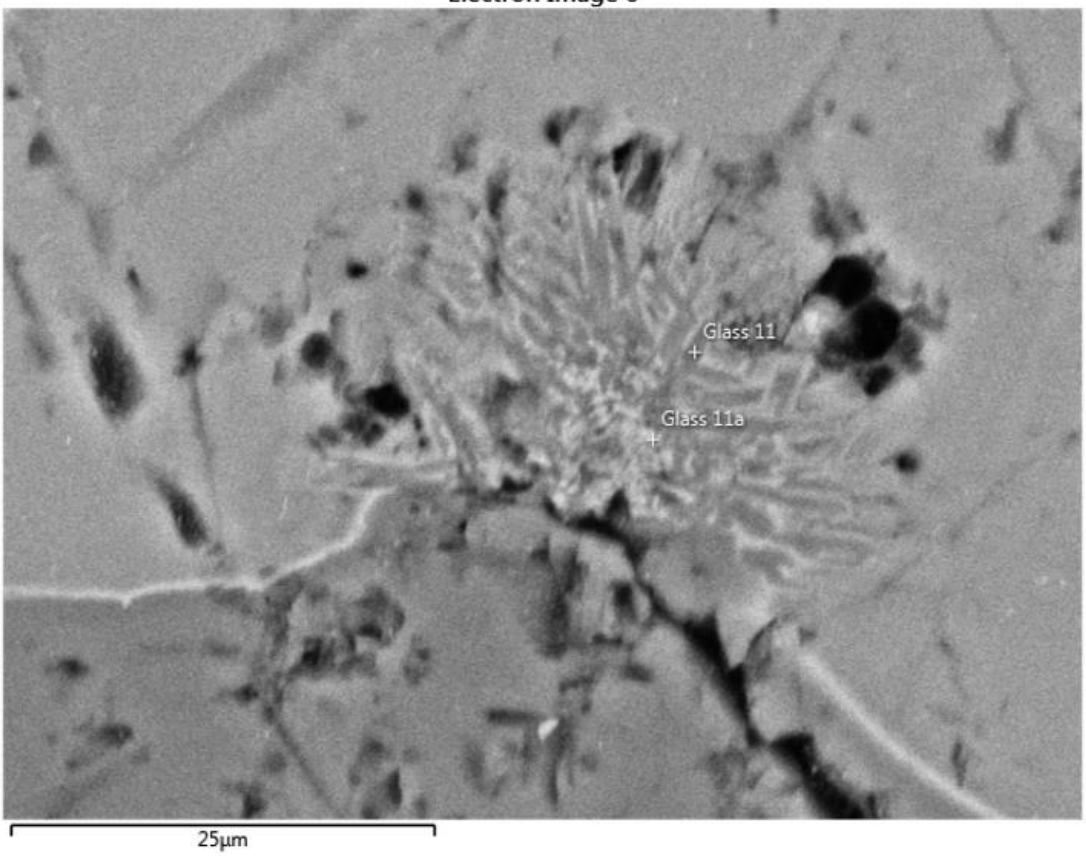

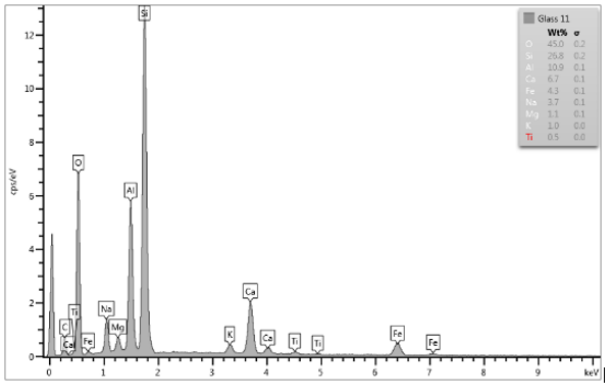

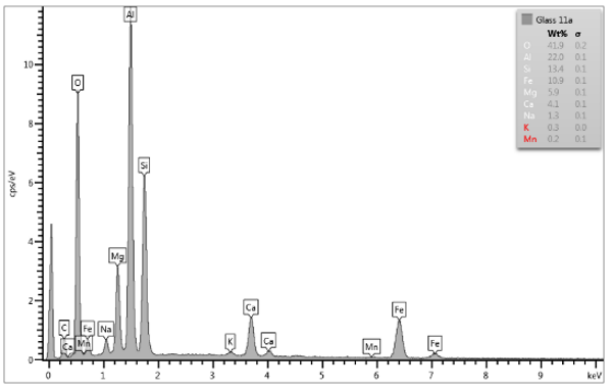

CHAPTER 3

Nucleation and growth of bubbles on plagioclase crystals during experimental decompression degassing of andesitic melts

Pia Pleše[a],

Michael D. Higgins[a], Don R. Baker[b]

and Marko Kudrna Prašek[b],

[a] – Département des sciences appliquées, Université du Québec à Chicoutimi (UQAC), 555, boulevard de l'Université, Chicoutimi (Québec), Canada G7H 2B1

[b] – Department of Earth and Planetary Sciences (EPS), McGill University, 3450 University Street,

Submitted to

Journal of Volcanology and Geothermal Research

April 2019

RÉSUMÉ

La nucléation, la croissance et l'attachement / le détachement des bulles de gaz dans les fondus silicatés est l'un des facteurs clés des éruptions volcaniques et peut grandement influer sur leur explosivité. Auparavant, les oxydes étaient considérés comme les meilleurs candidats pour la nucléation hétérogène de bulles, mais des études récentes ont montré que les cristaux de silicate peuvent également être des sites de nucléation de bulles lors du chauffage à la pression atmosphérique. Cette étude examine si les bulles peuvent se nucléé sur les surfaces cristallines du plagioclase lors du dégazage induit par la décompression, ce qui est une situation naturelle plus courante. Des échantillons expérimentaux ont été synthétisés à partir de poudre de roche andésitique, de H_2O et de plagioclase, puis fondus et décompressés dans un appareil à piston et cylindre. Les produits ont été imagés avec une tomographie 3D à rayons X. En raison de la fusion partielle, les cristaux de plagioclase ont développé des bords de tamis et des interfaces cristal-fonte rugueuses. Tous les cristaux de plagioclase dans tous les échantillons étaient recouverts de bulles. Les comparaisons de la taille des bulles entre les bulles en contact avec le plagioclase et les bulles dans la fonte montrent que les bulles appartiennent à deux populations, générées par deux événements différents, l'un étant la nucléation hétérogène à la surface des cristaux de plagioclase et l'autre, une nucléation homogène dans la fonte. La force d'attachement calculée entre les bulles et la surface du plagioclase est supérieure à la force de détachement. Par conséquent, ces bulles resteraient attachées lors des mouvements cristallins. Dans nos expériences, la flottabilité nette des agrégats était généralement négative, indiquant qu'ils pourraient plonger dans une chambre magmatique. Nos

résultats soulignent la nécessité de reconsidérer le rôle des cristaux de plagioclase dans le dégazage magmatique et montrent des possibilités intéressantes pour le dégazage déclenché par le mélange magmatique.

ABSTRACT

The nucleation, growth and attachment/detachment of gas bubbles in silicate melts is one of the key drivers of volcanic eruptions and can greatly influence their explosivity. Formerly, oxides were considered the best candidates for heterogeneous bubble nucleation, but recent experiments showed that silicate crystals can also be sites for nucleation of bubbles during heating at atmospheric pressure. This study examines whether bubbles can nucleate on plagioclase crystal surfaces during decompression-induced degassing, which is a more common natural situation than 1 atm heating. Experimental samples were synthesised from andesitic rock powder, H_2O and plagioclase seed crystals, and melted and decompressed in a piston-cylinder apparatus. The products were imaged with 3D X-ray computed tomography. Due to partial melting, the plagioclase crystals developed sieve rims and rough crystal-melt interfaces. All plagioclase crystals in all samples were covered with bubbles. Bubble size distribution comparisons between bubbles in contact with plagioclase, and bubbles in the melt, show that bubbles belong to two populations, generated by two different events, one of which is heterogeneous nucleation on plagioclase crystal surfaces and the other is homogeneous nucleation within the melt. The calculated attachment force between the bubbles and the plagioclase surface is stronger than the calculated detachment force, hence such bubbles would remain attached during crystal movements. In our experiments, the net buoyancy of the aggregates indicated that they could sink in an andesitic melt. Our findings highlight the need to reconsider the role of plagioclase crystals in magmatic degassing and shows interesting possibilities for magma mixing-triggered degassing.

3.1 Introduction

The formation of gas bubbles within volcanic conduit magmas is one of the main drivers behind volcanic activity. The study of all aspects of bubble formation and development are of scientific and social importance, whether the focus is the initial conditions of bubble formation or the subsequent potential for outgassing via permeable paths (Sigurdsson et al., 2015), as these can influence eruption explosivity. A sudden new nucleation event that produces many bubbles, which if unable to escape can very rapidly increase the total magma (melt + crystal + bubble) volume and cause violent eruptions (Sigurdsson et al., 2015). Contrastingly, outgassing through permeable paths can sustain calm episodic to long-lasting effusive eruptions (Sigurdsson et al., 2015).

Bubble research is conducted through the observation of natural eruption-produced samples and the creation of bubbles (and crystal microlites) in experimental run products. Both approaches provide (in most cases) samples after completion of bubble formation, which is a product of potentially several different processes. Deciphering such post-process bubble patterns into discrete events is one of the challenges of modern volcanology.

Some of the most important parameters concerning bubble nucleation are the conditions under which bubbles will nucleate (pressure, temperature and location). Bubble nucleation can be homogeneous (within a melt) or heterogeneous (on a crystal surface), and which process will occur depends in part on the availability of favourable bubble nucleation sites, i.e. the presence or lack of suitable crystals (Blander and Katz, 1975, Hurwitz and Navon, 1994). Heterogeneous nucleation occurs at lower supersaturation pressure and is always energetically more favourable then

homogeneous nucleation (Hurwitz and Navon, 1994). The importance of nucleation sites is easily illustrated: the more nucleation sites available (e.g. many favourable crystals or few favourable ones with large surfaces) the more bubbles can form. If the crystallization or assimilation of a favourable crystal is sudden, providing new nucleation sites, heterogeneous bubble nucleation can rapidly follow (provided the volatile-melt saturation threshold is crossed). If there are no crystals, or only unfavourable ones are present, heterogeneous bubble nucleation can become delayed or homogeneous nucleation can ensue (Blander and Katz, 1975). Clearly it is important to understand the role of crystals in bubble nucleation, as is to know which crystals provide favourable bubble nucleation sites. Our primary focus is the bubble nucleation location and not subsequent bubble growth, so we emphasize the role of crystals as opposed to thermodynamic factors controlling the total volume of bubbles.

Heterogeneous nucleation of bubbles on crystals of different minerals can be studied by measuring contact angles between bubbles and crystal surfaces. The contact (or wetting) angle value represents the wettability of a crystal surface (Blander and Katz, 1975; Hurwitz and Navon, 1994). The outer contact angle (θ) is measured within the melt and a value of $\theta > 68\ ^\circ$ represents good wettability of the crystal by the bubble and poor wettability by the melt - the reverse is true for $\theta < 68\ ^\circ$.

Oxides are commonly considered favoured bubble nucleation sites in silicate melts (Hurwitz and Navon, 1994), due to their strongly contrasting chemical and structural differences from the melt (Mysen and Richet 2005, Gualda and Ghiorso, 2007). Consequently, oxides are poorly wetted by silicate melts, compared to silicate crystals that are well wetted by silicate melts, and so poorly wetted by bubbles (Gualda and Ghiorso, 2007). The compositional similarity between plagioclase crystals and

silicate melts is thought to make heterogeneous bubble nucleation on such plagioclase crystals improbable (Mangan et al., 2004). However, recent dynamic experiments have shown that contact angles, on whose values these inferences were made, can change with time (e.g. on plagioclase surfaces, from 120° to 75° in 10 s) leading to difficulty in ascertaining whether a contact angle observed post-process is the final (equilibrium) value (Pleše et al., 2018).

Pleše et al. (2018) demonstrated that oxide surfaces are not the only favourable sites for heterogeneous bubble nucleation in andesitic melts, but that silicate crystals play a role as well. Using dynamic 4D X-ray tomography, while heating previously synthesized hydrous, crystal-bearing, andesitic glasses at 1 atm, they observed *in situ* how plagioclase crystals acted as bubble nucleation sites, along with oxides (but 28-44 s later). Despite the undeniable usefulness of *in situ* observations, technical limitations meant that these experiments were conducted at atmospheric pressure and degassing was induced by heating pre-hydrated melts, so the influence of pressure on the ability of these silicate crystals to provide bubble nucleation sites was not possible to examine.

In this study, we investigate the role of plagioclase in heterogeneous bubble nucleation through depressurization experiments of water-rich andesitic melts. Plagioclase is a silicate crystal commonly present in andesitic melts but was generally excluded from earlier bubble nucleation studies. Recent evidence from Pleše et al. (2018) shows the possible underestimation of its role. In a series of experiments on hydrous plagioclase-bearing andesitic glasses, we have induced degassing by decompression in a piston-cylinder apparatus. The difference between this study and most previous ones is that large plagioclase crystals were introduced to the glass

powder before high-pressure and high-temperature conditions. The goal was to introduce macroscopic plagioclase surfaces, instead of crystallizing plagioclase microlites at high-pressure and high-temperature. We aimed to mimic a process similar to natural magma ascent and volcanic eruptions, assimilation of plagioclase xenocrysts that are in disequilibrium with the surrounding melt, and we examined the final products in 3D. Our earlier *in situ* observations (Pleše et al., 2018), were on the same melt composition with the same plagioclase crystals, hence we hope to enhance the probability of correctly deciphering initial bubble nucleation processes and the behaviour of bubble-crystal aggregates.

3.2 Methodology

3.2.1 Piston-cylinder synthesis of hydrous andesitic glasses

The synthesis of our samples and their subsequent decompression was performed with a piston-cylinder apparatus at McGill University, Canada. The pressure precision is 25 MPa, and the friction correction is 50 MPa (more details on the experimental apparatus are in Baker, 2004). Three components were added to $Au_{75}Pd_{25}$ capsules 3 mm in diameter, 11 mm in length: glass made from rock powder (natural andesite from Baker and Eggler, 1987, with 56.8 wt. % SiO_2, 1 wt. % TiO_2, 16.9 wt. % Al_2O_3, 8.03 wt. % FeO_{TOT}, 0.17 wt. % MnO, 3.09 wt. % MgO, 7.05 wt.% CaO, 3.99 wt., % Na_2O, 2.05 wt. % K_2O, 0.28 wt. % P_2O_5), cleavage fragments of plagioclase crystals (labradorite An_{67}, Stewart et al., 1966) comprising on average 16 wt. % of each charge (from 10.6 to 24.1 wt. %, equivalent on average to ~ 20 vol. % of each capsule), and H_2O (~ 12 wt. % of the starting material, the only volatile added). This plagioclase is of gem-

quality so low concentrations of impurities within its crystal lattice are assumed. The same rock powder, plagioclase crystals and water, but in different proportions, were used in Pleše et al. (2018), which allows us to build on their observations. The water concentrations are such that the water-saturation threshold is crossed during decompression (Papale et al., 2006). The filled capsules were closed by welding in a water bath to minimize water loss and stored in a 110 °C furnace for 1 h. The initial water concentration (wt. % H_2O) was determined by weighing.

All experimental runs were isothermal at 1000 °C and started with a period of 1 hour (t_1) at the maximum pressure (p_1). Table 3.1 summarizes the lower pressures (p_2) to which the runs were decompressed, the decompression duration (t_2), the decompression rate, and finally the duration of the experiments (t_3) at p_2 before isobaric quenching. The sample name consists of the experiment number followed by the number of the capsule within that experimental run (maximum two capsules per run). Our decompression rates (1.55 – 2.56 MPa s^{-1}) correspond to ascent rates of 62 – 102 m s^{-1} (assuming a pressure gradient in the upper crust of 0.025 MPa s^{-1}, Dziewonski and Anderson, 1981) and as such represent well the ascent rates of the 1997 explosive Soufrière Hills eruptions (Druitt et al., 2002). Oxygen fugacity (fO_2) within the charges was NNO+1.5 (Dalpé and Baker, 2000; Liu et al., 2007). Since 3D X-ray scanning was used to analyze the experiments, it was necessary to remove the run products from their metal capsules, during which they fractured and scattered causing their original location and orientation inside the capsule to be unknown.

Table 3.1: Experimental conditions during the piston-cylinder sample synthesis. p_1 is the maximum pressure while p_2 is the lower pressure. t_1 was always 1 h (the homogenization period), t_2 is the decompression time (from p_1 to p_2), t_3 is the rest time at p_2. The decompression rate is $(p_1 - p_2)/t_2$.

experiment #	**sample name**	**T (°C)**	**p_1 (Mpa)**	**p_2 (Mpa)**	**t_2 (s)**	**decompression rate (Mpa s^{-1})**	**t_3 (s)**	**# crystals observed**
15	15-1	1000	650	600	30	1.6	300	1
19	19-1 19-2	1000	650	600	22	2.27	300	1 3
21	21-1	1000	650	300	195	1.8	0	5
22	22-1	1000	850	650	78	2.56	10	1
24	24-1 24-2	1000	650	300	225	1.55	0	0 1
25	25-1 25-2	1000	650	300	222	1.6	0	3 5
26	26-2	1000	650	650	n/a	0	n/a	4
27	27-1 27-2	1000	650	300	212	1.65	5	1 2

3.2.2 X-ray computed microtomography (microCT)

After each experimental run, the largest fragment obtained from a capsule (henceforth called the sample) was first taken to a benchtop tomography machine (Skyscan 1172, at McGill Institute for Advanced Materials, McGill University) to obtain low-resolution scans of ~ 3.8 μm voxel edge length (scanning conditions in the Appendix 3.2, reconstruction done using *NRecon*, Skyscan, 2011). The goal was to ascertain if the plagioclase crystals were retained and if bubbles were generated in order to see if the experimental conditions needed to be changed and to preselect the samples for higher-resolution 3D X-ray imaging. The latter was performed at the GeoSoilEnviroCARS beamline, Advanced Photon Source synchrotron (Illinois, U.S.A.; Rivers et al. 2004; Rivers et al. 2010). The energy of the X-ray beam was 25 keV, with a 10× camera magnification and voxel edge length of 1.32 μm. The reconstruction of samples in 3D was done using *tomoRecon* (Rivers, 2012; http://cars9.uchicago.edu/software/idl/tomography.html). All subsequently presented figures and measurements were done on the synchrotron volumes (at 1.32 μm spatial resolution).

3.2.3 Volume segmentation and measurements in 3D

Our samples contain location specific characteristics, so from each synchrotron-scanned sample volume, two subvolumes were chosen: one containing no plagioclase crystals called the ″melt subvolume″ and one containing an entire plagioclase crystal and surrounding bubbles called the ″crystal subvolume″ (Figure 3.1). Both subvolumes were chosen to be as representative as possible, within very heterogeneous samples.

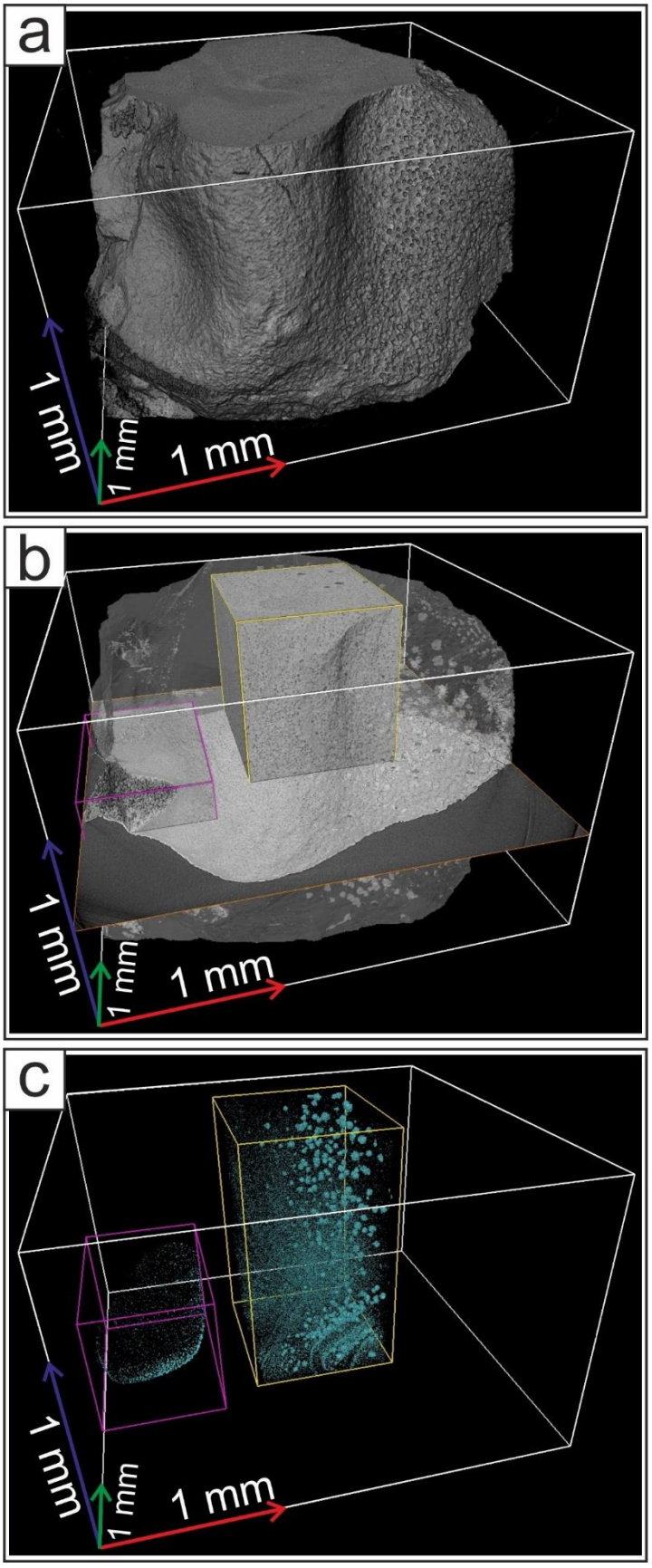
a
1 mm
1 mm
1 mm
b
1 mm
1 mm
1 mm
c
1 mm
1 mm
1 mm

Figure 3.1: 3D visualization of sample 25-1. a) The entire sample volume is rendered; b) the sample volume is transparent so that the locations of two subvolumes seen through it. The melt subvolume is outlined in yellow and the crystal subvolume in purple. The 2D slice cutting through the sample volume is shown in Figure 3.4 a. c) The sample volume is removed and only the bubbles present in both subvolumes are shown in blue.

All the bubbles present in the melt subvolume were segmented in 3D by thresholding (0-103 values on 8-bit volumes) using the image-processing package *Fiji* (Schindelin et al., 2012). Filtering (the removal of objects smaller than a specified size), watershedding (the separation of objects in contact) and quantitative analyses were done with the *Pore3D* software library (Brun et al., 2010: https://github.com/ElettraSciComp/Pore3D) to obtain the number and volume of bubbles, from which bubble number densities and bubble size distributions were calculated.

The same segmentation procedure and calculations were applied to the bubbles in the crystal subvolume, following manual masking. In the microCT volumes, plagioclase crystals do not have a uniform appearance: there are dark patches that we term voids, which are probably newly formed melt pockets. In order to segment only the bubbles on the surface of the plagioclase, we masked bubbles not in contact with the surface as well as melt pockets within the crystal. The latter, immediately below the crystal surface, have a lower sphericity (diameter of maximum inscribed sphere / diameter of equivalent volume sphere) than the bubbles on the crystal surface, and this morphological parameter was used to ensure no melt pockets are erroneously selected as bubbles. All visualizations were performed with *Avizo Fire*® (Visualization Sciences Group).

The segmentation of plagioclase crystals from silicate melts is known to be difficult in X-ray tomographic studies due to their compositional (and hence X-ray absorbance) similarity (Baruchel et al., 2000). In order to compare bubble number density (BND) values, a semi-manual segmentation of plagioclase crystals was performed in 3D to obtain crystal volumes and surface areas. The crystal volumes are

not closed, i.e., part of the crystal is at the sample border (surrounded by air) so their scanned volume is partial. Only the plagioclase crystal in sample 25-1 has a completely closed volume, so its measured volume and surface area are accurate. For other plagioclase crystals, their volume was manually "closed" in 3D (via masking). However, since the manually added surfaces that served to close the plagioclase volume do not contain bubbles, part of the information is lost, leading to approximate plagioclase volumes and surface areas. Thus, the bubble number densities for the entire plagioclase surface area also contain an uncertainty (Table 3.2).

We cannot directly compare bubble number density values for different subvolumes, since BND on the crystal surface is in 2D (mm^{-2}) and BND within the melt in 3D (mm^{-3}) – the 2D BND on the crystal surface needs to be transformed into 3D. To achieve this, first we found the average volume of all bubbles on the total crystal surface. Second, we calculated the average equivalent sphere radius and multiplied it by 2 to obtain the height of the melt (h_{bubble} – measured from the crystal surface) that is occupied by bubbles. Third, the equivalent sphere radius was calculated from plagioclase crystal volumes. The volume of the melt that bubbles occupy is represented by the volume of a spherical shell (Harris and Stöcker, 1998), Equation 11: $V_{spherical\ shell} = \frac{4}{3} \times \pi \times (R^3 - r^3)$ (11),

where r is the plagioclase crystal equivalent sphere radius, and $R = r + h_{bubble}$. To obtain a 3D BND value, the total number of bubbles found on the crystal surface is divided by the spherical shell volume (Table 3.2). We opted to use the average value because if a maximum bubble volume was selected in the first step it would skew the 3D BND results to lower values as the volume of the melt by which the number of bubbles is

divided would be greater. The reverse would hold if the minimum bubble volume was selected. The average value is used instead of the median value due to the large differences in bubble volumes on plagioclase surfaces in different experiments, i.e. average values were used to ease the comparison between 3D BND on plagioclases between experiments.

Measurement of outer contact angles (θ) between bubbles and crystals was performed in 3D following the protocol described in Pleše et al. (2018; Figure 2.3).

Table 3.2. Bubble number densities measured within the melt (mm^{-3}) and on the total crystal surface, the latter converted from 2D to 3D (mm^{-3}), see text for explanation. $V_{spherical\ shell}$ is the volume of the melt that bubbles in contact with the plagioclase surface, occupy, and N_{bubble} is their number. Sample 15-1 had no bubbles within the melt, and sample 24-1 had no plagioclase crystals (designated as n/a).

group	sample name	decompression drop (Mpa)	BND in melt (mm^{-3})	$V_{spherical\ shell}$ (mm^3)	N_{bubble} on crystal surface	3D BND on crystal surface (mm^{-3})
1	26-2	0	6.1×10^5	0.0065	6147	9.4×10^5
2	15-1	50	0	0.0047	18004	3.8×10^6
	19-1	50	3.5×10^5	0.0302	2129	7.0×10^4
	19-2	50	2.2×10^5	0.0032	44155	1.4×10^7
3	22-1	200	3.7×10^4	0.0634	4595	7.2×10^4
4	24-1	350	1.0×10^5	n/a	n/a	n/a
	24-2	350	1.3×10^5	0.0031	180	5.8×10^4
	25-1	350	3.9×10^4	0.0529	3891	7.3×10^4
	25-2	350	7.2×10^3	0.0027	127	4.7×10^4
	27-1	350	7.2×10^4	0.0002	180	8.4×10^5
	27-2	350	5.3×10^4	0.0254	2200	8.7×10^4
	21-1	350	6.8×10^4	0.0299	1360	4.6×10^4

3.2.4 Scanning electron microscope (SEM) analysis

The aim of SEM analysis was to obtain a semi-quantitative chemical composition of the silicate glass and to examine whether there are major element differences close to and away (max 180 μm) from the plagioclase. The scanned and reconstructed 3D sample volume guided grinding to reach a chosen 2D slice in sample 24-2 (Figure 3.2 c). This surface was analyzed using a Hitachi SU-3500 Variable Pressure-SEM at 15 kV and 0.134 mA. Backscattered-electron (BSE) images were obtained as well as semi-quantitative analyses (see Appendix 3.1).

One surface in sample 24-2 was manually outlined from the 2D SEM image (irregular line in Figure 3.2 a) to determine the roughness of plagioclase crystal surfaces. The arithmetic mean roughness value (R_a) was calculated from the profile (sampling length 25 μm) by averaging the absolute values of the amplitudes (distances) of peaks and valleys relative to a median line (Whitehouse, 2004). In order to compare and provide context for the 2D R_a value, the same procedure was applied to the plagioclase surface (sampling length 25 μm) from Pleše et al. (2018; see Figure 2.9 b).

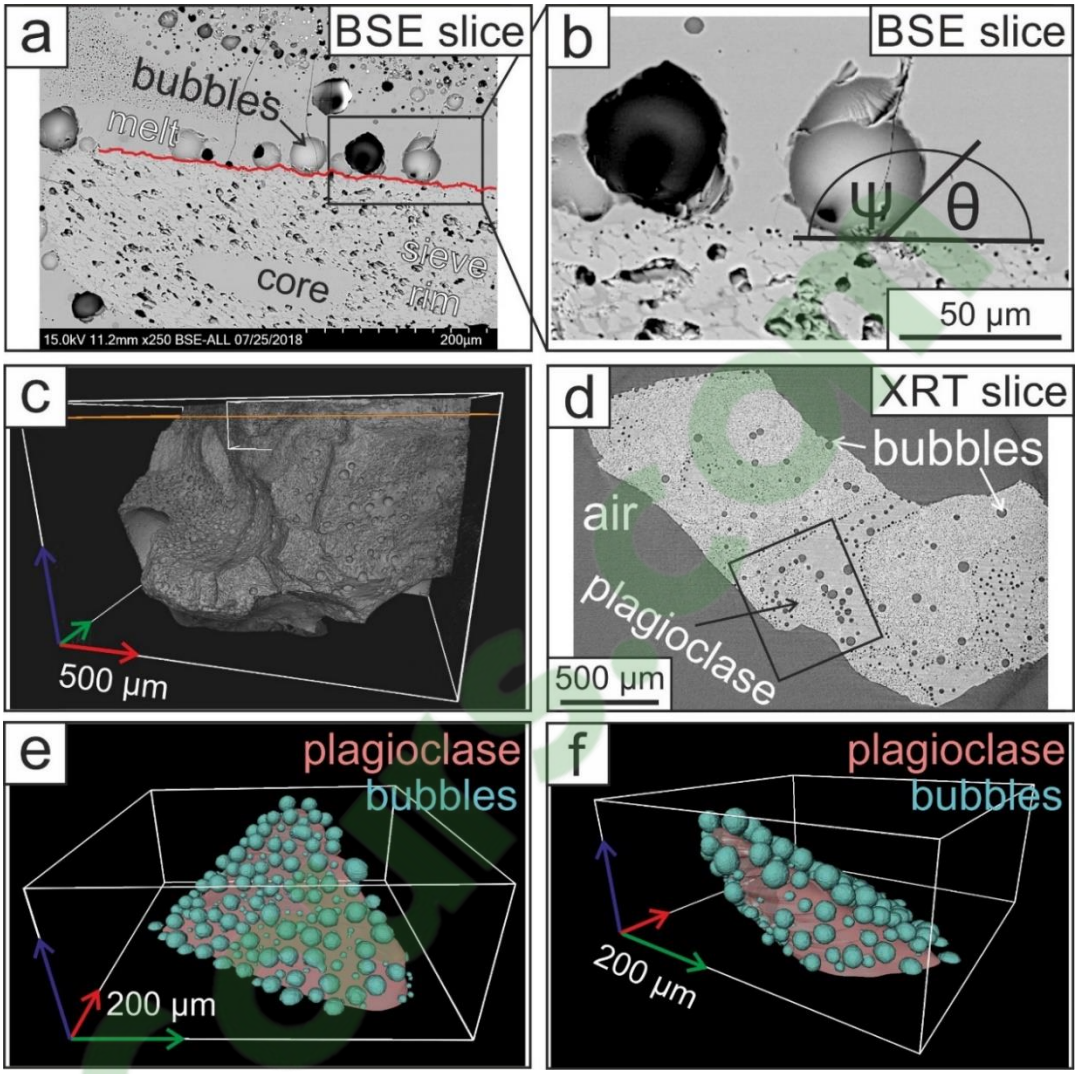

Figure 3.2: Comparison between BSE images and corresponding microCT 2D images, of sample 24-2. a) a BSE image with melt, a plagioclase crystal and bubbles. The irregular line represents the surface outline for the surface roughness measurement (shown in red). b) magnified section of image a, where inner (ψ) and outer (θ) contact angles are indicated (ψ + θ = 180 °), c) a 3D volume rendering of the entire sample, with the 2D slice location corresponding to the BSE image outlined in orange, d) a microCT 2D slice with the plagioclase crystal from panels a and b, e) - f) a 3D volume rendering of the plagioclase crystal and bubbles located on its surface, viewed in two orientations. The length of each arrow in the 3D scale represents 200 µm.

3.3 Results

3.3.1 General sample appearance

The 3D volumes of the different samples are all similar, with a glassy matrix containing plagioclase crystals, bubbles of various sizes and sometimes oxide microlites. Based on the different experimental conditions, the samples are divided into four groups (Table 3.2): 1) no decompression (zero-time) experiment at 650 MPa (sample 26-2), 2) decompression from 850 to 650 MPa (sample 22-1), 3) decompression from 650 to 600 MPa (samples 15-1, 19-1, 19-2), and 4) decompression from 650 to 300 MPa (samples 21-1, 24-1, 24-2, 25-1, 25-2, 27-1, 27-2).

Bubbles within samples are divided, based on their location, into fringe bubbles (formed at the melt/capsule interface), bubbles in contact with plagioclase crystals and bubbles within the melt (no contact with plagioclase crystals). Fringe bubbles are excluded from this study since they are thought to nucleate on imperfections on the capsule wall (Mangan and Sisson, 2000). Oxide microlites are either dispersed within the glass or form complex shells around some (mostly fringe) bubbles. The latter phenomenon was investigated in detail in Pleše et al. (2019; Chapter 4 in this thesis) using four samples of this study (15-1, 24-2, 25-2 and 27-1). Bubbles with oxide shells in these four samples were excluded from this study.

Plagioclase crystals were always clustered in one part of the sample, creating two sample regions, one with crystals, and one without (Figure 3.2 d, Figure 3.3 a, Figure 3.4 a). This division guided our subvolume selection (Figure 3.1 b-c), described

earlier (subsection 3.2.3). Plagioclase crystals are polyhedra with rounded faces, blunt edges and uneven surfaces. Their entire outer surface is densely covered with semi-spherical bubbles (Figures 3.2 and 3.3). These bubbles are within the melt and in contact with the plagioclase-melt interface. No melt film is visible between these bubbles and the crystal surface (Figure 3.2 a, b, d, Figure 3.3 a, b, Figures 3.4 b). All bubbles have discrete volumes and neither shared bubble-bubble interfaces nor coalescence was observed. The 3D outer contact angles (θ) between the plagioclase and the bubbles (Fig. 2 b) are: group 1, 57.3° ± 5° (measured on 3 bubbles); group 2, 49° ± 5° (measured on 4 bubbles); 45° ± 5° (measured on 3 bubbles) and group 4, 42.3° ± 5° (measured on 7 bubbles). The limited amount of measurements stems from the bubble's small sizes, which prevented measurements with low uncertainties.

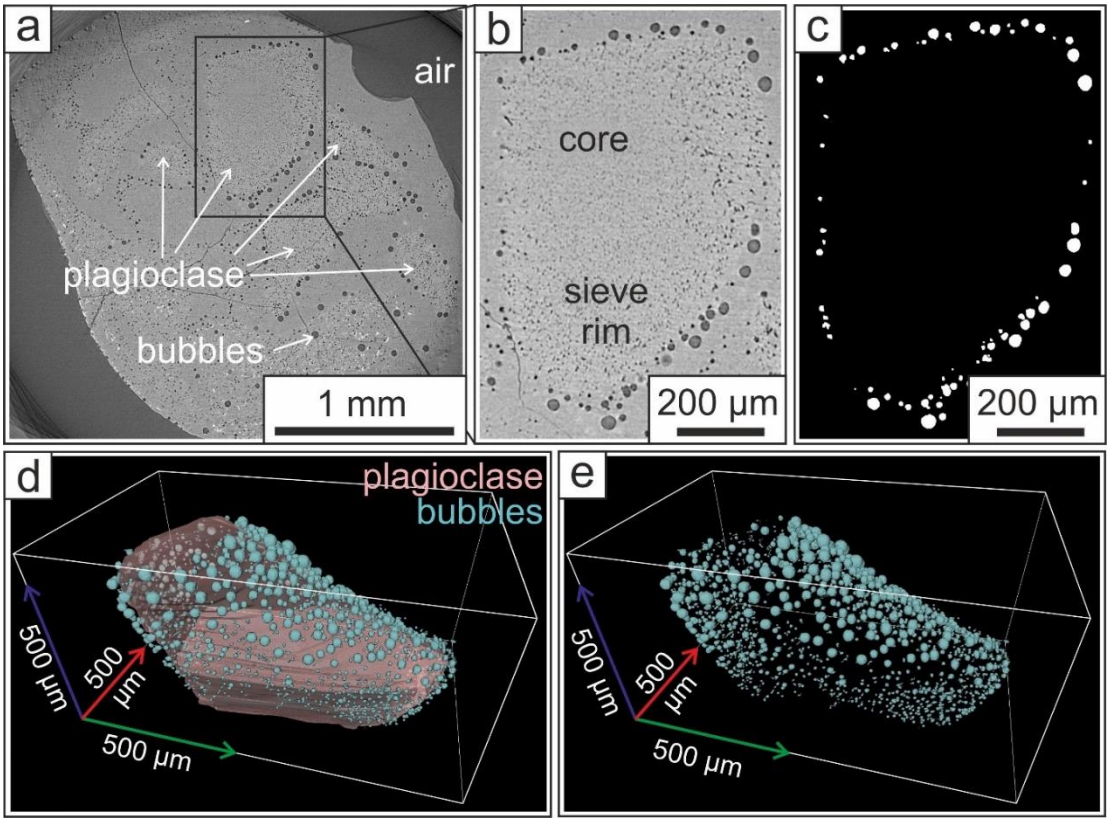

Figure 3.3: X-ray tomography visualizations of sample 21-1 and a plagioclase crystal within it. a) 2D microCT slice with several plagioclase crystals. b) Zoom in on one chosen plagioclase, where the core, rim and outer surface bubbles are visible. c) Segmentation of the bubbles in contact with the plagioclase. d) 3D volume rendering of the bubble-plagioclase aggregate, e) a 3D rendering of only the bubbles that form the aggregate.

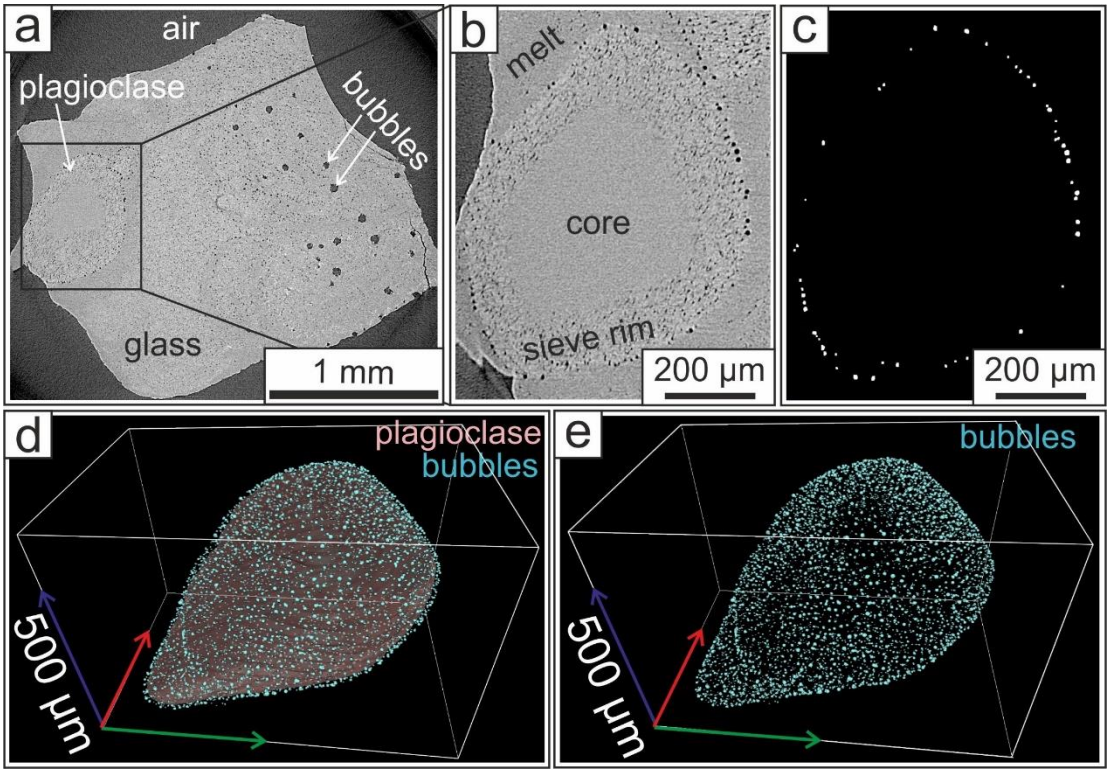

Figure 3.4: X-ray tomography visualizations of sample 25-1 and a plagioclase crystal (the only closed one) within it. a) 2D microCT slice showing two very different regions in the sample. Its location within the sample volume can be seen in Figure 3.1 b. b) Zoom in on the plagioclase, where the core, rim and outer surface bubbles are visible. c) Segmentation of the bubbles in contact with the plagioclase. d) 3D volume rendering of the bubble-plagioclase aggregate, e) a 3D rendering of only the bubbles that coat the plagioclase crystal surface.

Two regions can be distinguished within the crystals, a uniform centre, and an outer rim with elongated darker regions, here termed voids (Figure 3.2 a, d, Figure 3.3 a, Figure 3.4 a, b). The voids are darker as their density is lower than that of their surrounding material (plagioclase crystal in this case) so the X-rays passing through them are less attenuated. The plagioclase's uniform centre (i.e. the innermost region without voids) is here termed core and comprises on average ~15 % of the total crystal volume. The core volume does not have a significant correlation to the experimental decompression drop (Pearson's correlation coefficient is r = - 0.26; Pearson, 1900). The core shape corresponds to the crystal shape. The outer rim contains melt pockets, that could not have existed within the crystal lattice prior to the experiments (their appearance and potential formation mechanisms are discussed in subsection 3.4.1). The outer crystal surface is uneven, or rough - surface roughness (R_a) is better observed with SEM than microCT (Figure 3.2 a-b), due to the small X-ray absorbance difference between the plagioclase crystal and silicate melt. The plagioclase 2D crystal surface roughness in sample 24-2 (Figure 3.2 a) is R_a = 2.9 μm, and there are 10 bubbles on the surface. For comparison, the plagioclase from Pleše et al. (2018) has a 2D R_a = 0.7 μm and 7 bubbles (potential reasons for this surface roughness difference are discussed in subchapter 3.4.1).

The melt in the immediate vicinity of the bubble-lined plagioclase crystals is devoid of bubbles (Figure 3.2 a, b, d, Figure 3.3 a, b, Figure 3.4 a, b). In some cases, this melt region extends further away from the crystal in swirl-like formations (e.g. sample 21-1, Figure 3.3 a). The glass composition in wt. % close to a plagioclase crystal surface is 57.31 SiO_2, 22.22 Al_2O_3, 1.46 K_2O, 8.63 CaO, 0.66 TiO_2, 4.27 FeO_{TOT}, 3.2 Na_2O, 2.26 MgO – calculated as an average of four SEM point analysis

presented in Appendix 3.2, spectrums 242-245, and recalculated to 100%. Bubbles larger than those within the melt sparsely line the border of this bubble-free melt region (Figure 3.2 a, d, Figure 3.3 a).

The plagioclase crystal in sample 26-2 (the zero-time experiment) does not differ in appearance from plagioclase crystals in decompressed samples. However, the bubbles in 26-2 do differ from those in other samples. The bubble population in the melt is dominated by extremely small bubbles (peak at $\log_2[V_{bubble}\ (\mu m^3)] = 2.8$), more than in any other sample (Figure 3.6 a; a $\log_2$ is used to present many very small and similar data values). Due to equipment limitations, the quench in experiment 26 might possibly not have been perfectly isobaric, which could explain the presence of bubbles.

3.3.2 Bubble number densities and bubble size distributions

Bubbles on plagioclase crystals and bubbles within the melt are compared in terms of numbers (Table 3.2, Figure 3.5) and sizes (Figures 3.6 and 3.7). Bubble number densities in 3D are compared for bubbles within the melt and bubbles on the crystal (Figure 3.5) and no consistent difference was found between the two, across the experimental suite (Table 3.2). Additionally, the Pearson's r between the two BND is 0.11 (Pearson, 1900) (Figure 3.5). For the same experimental conditions in different charges, the 3D BND within the melt can differ up to a factor of five (e.g. 38737 mm^{-3} in 25-1 vs. 7193 mm^{-3} in 25-2, Table 3.2), and the 3D BND on the crystal also differs greatly (e.g. 7×10^4 mm^{-3} in 19-1 vs. 1.4×10^7 mm^{-3} in 19-2, and 8.4×10^5 mm^{-3} in 27-1 vs. 8.7×10^5 mm^{-3} in 27-2, Table 3.2).

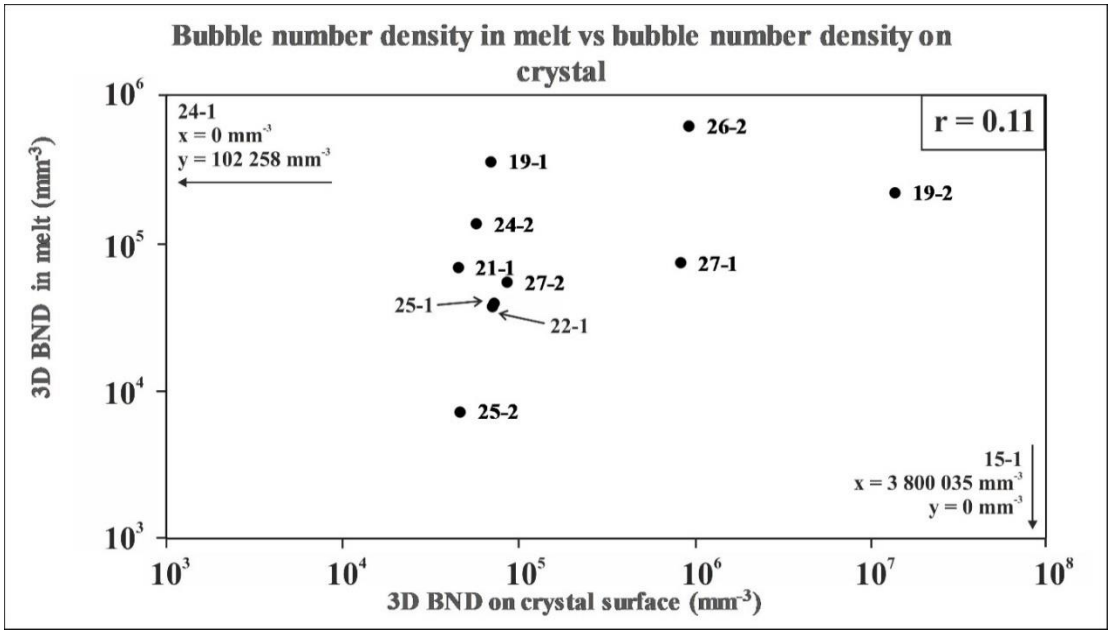

Figure 3.5: Comparison between different bubble number density (BND) measurements from two subvolumes for each sample. The x-axis contains the 3D BND on plagioclase surface (in mm^{-3}) and the y-axis contains the 3D BND within the melt (in mm^{-3}). r refers to Pearson's correlation coefficient. The locations of samples 15-1 (no bubbles in melt) and 24-1 (no crystal) are indicated with arrows and coordinates (the arrow direction stems from $\log_2 0$ = - infinity).

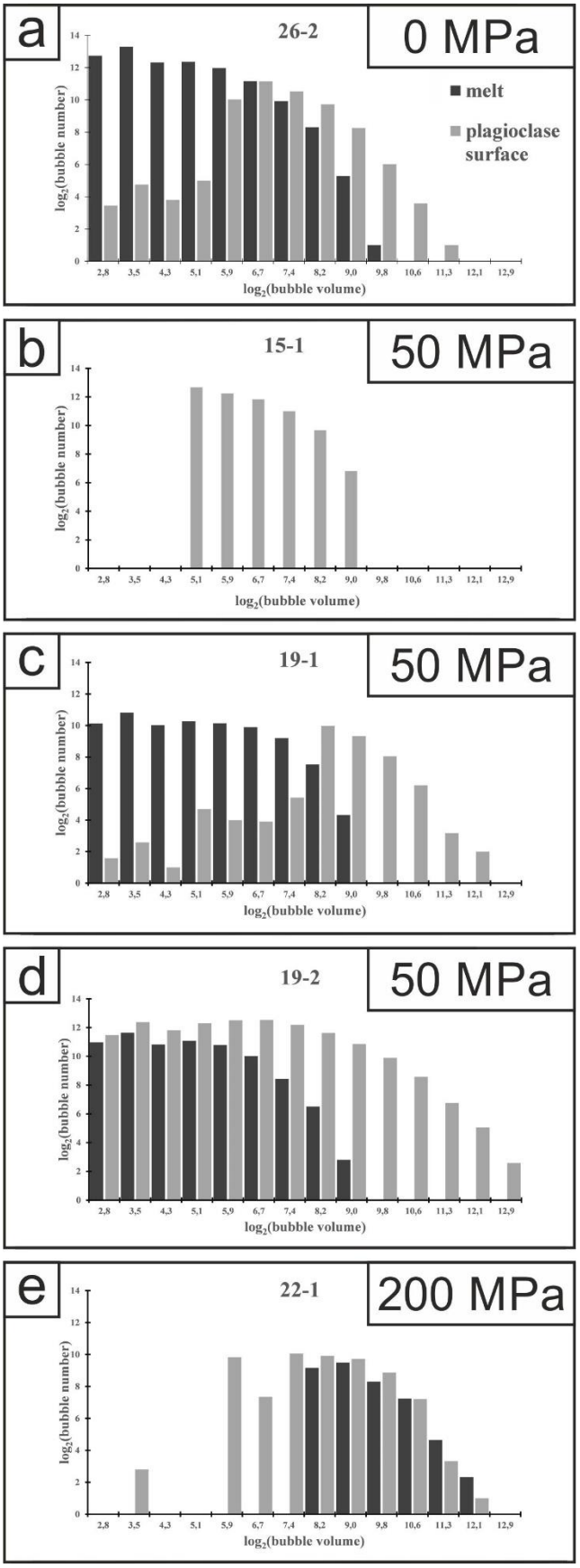
a
26-2
0 MPa
melt
plagioclase surface
log2(bubble number)
log2(bubble volume)
2,8 3,5 4,3 5,1 5,9 6,7 7,4 8,2 9,0 9,8 10,6 11,3 12,1 12,9
b
15-1
50 MPa
c
19-1
50 MPa
d
19-2
50 MPa
e
22-1
200 MPa

Figure 3.6: Bubble size distribution diagrams for bubbles in melt (black) and on crystals (grey) for samples at different decompressions. The x-axis is $\log_2 V_{bubble}$ with volume expressed in μm^3 and the y-axis is $\log_2 N_{bubble}$.

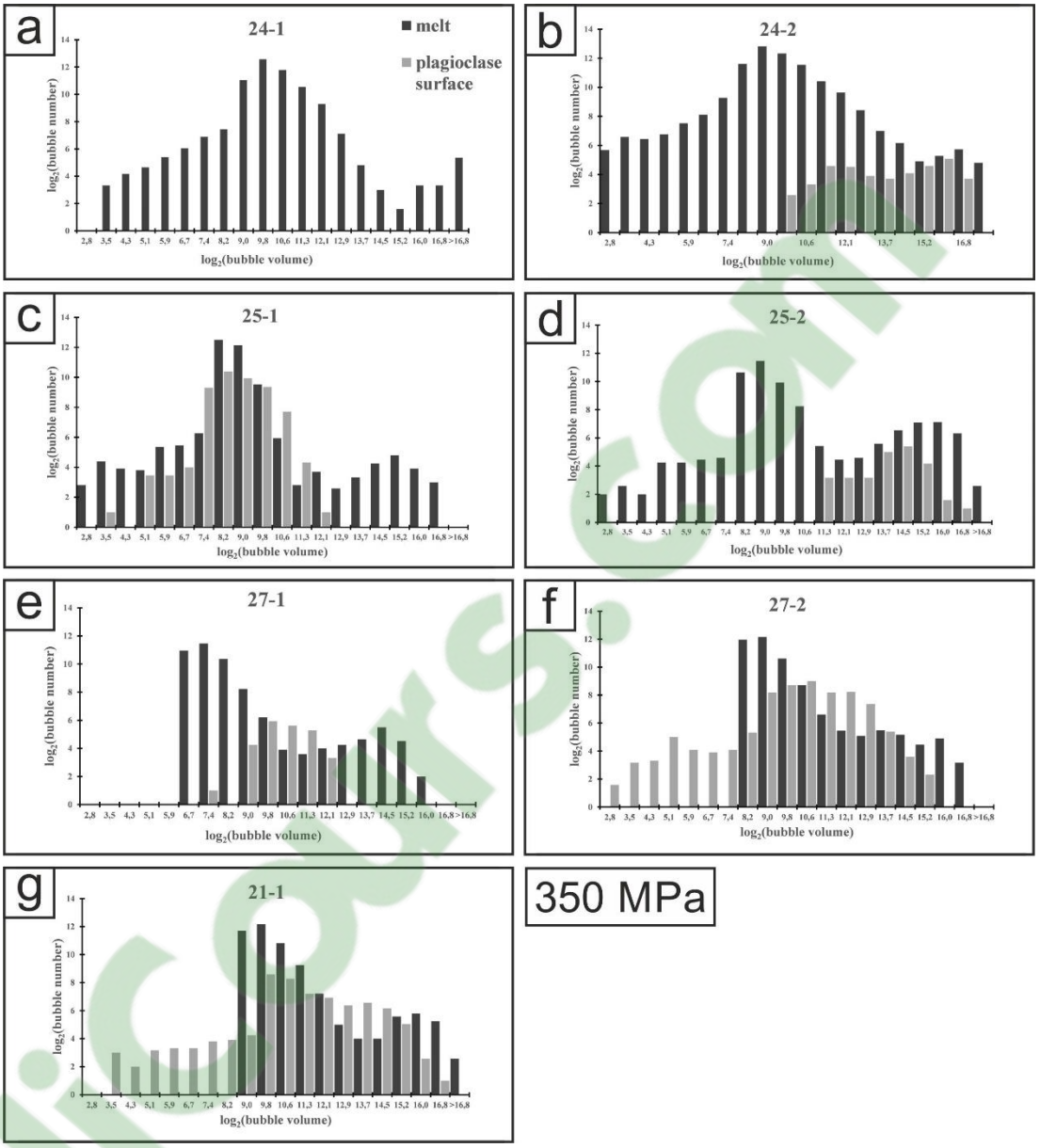

Figure 3.7: Bubble size distribution diagrams for bubbles in melt (black) and on crystals (grey) for samples at 350 MPa decompression. The x-axis is $\log_2 V_{bubble}$ (volume expressed as μm^3) and the y-axis is $\log_2 N_{bubble}$.

Bubble size distributions (BSD) are presented for bubbles within the melt and for bubbles on a single plagioclase crystal surface (Figures 3.6 and 3.7). The values are presented as $\log_2[V_{bubble}\ (\mu m^3)]$ and $\log_2 N_{bubble}$, to simplify the presentation of very small values that exhibit small differences. The bubble size distributions for bubbles within the melt appears to be similar for samples at 0, 50 and 200 MPa decompressions (Figure 3.6); the BSD are wide and flat, there is no pronounced peak value of $\log_2[V_{bubble}\ (\mu m^3)]$ (2.8 to 7.4 - 9.8). Sample 22-1 (decompressed from 850 to 650 MPa, not from 650 MPa) and its BSD differs from others in this group by the lack of small volume bubbles. There were no bubbles in the melt in sample 15-1 (650 to 600 MPa).

Bubbles in contact with the plagioclase surface for 0 MPa (26-2), 50 MPa (15-1, 19-1, 19-2) and 200 MPa (22-1) decompressions (Figure 3.6) exhibit similar BSD for all samples: a unimodal distribution with a peak $\log_2[V_{bubble}\ (\mu m^3)]$ value between 6.7 and 8.2. Only sample 19-2 (650 - 600 MPa) does not have a well-defined peak value.

For larger, 350 MPa, decompressions (samples 21-1, 24-1, 24-2, 25-1, 25-2, 27-1, 27-2), the BSD are again different from other decompressions (Figure 3.7). Bubbles within the melt have a bimodal BSD, with one peak $\log_2[V_{bubble}\ (\mu m^3)] = 8.2$ - 9.8, and another at ~15.2 – 16. Bubbles on the plagioclase surface display a unimodal BSD, but with a variable peak $\log_2[V_{bubble}\ (\mu m^3)]$ value, from 8.2 to 16. In general, for all samples across all decompressions, the BSD for bubbles on the plagioclase surface are very different from those of bubbles within the melt.

3.4 Discussion

The presence of plagioclase crystals in the experimental suite is of particular importance, as they influenced bubble nucleation and bubble size distributions within the samples. The fact that bubbles essentially outline a three-dimensional silhouette of plagioclases (Figure 3.1 c, Figure 3.2 f, Figure 3.3 d, Figure 3.4 d) that would otherwise be invisible by microCT, points to a plagioclase-bubble affinity. First, we discuss the appearance of both plagioclase crystals and bubbles. Second, we address their relationship. Third, we examine what forces act on them as an aggregate and how those forces could influence such an aggregate's fate in a natural melt.

3.4.1 Plagioclase crystals with ″sieve″ rims

Plagioclase crystals in our experiments are rounded with rough surfaces and rims of melt inclusions. Such an appearance has been described in many ways, illustrative (e.g. honeycomb, fingerprint, riddled, spongy, dusty, mantled, sieve; e.g. Nelson and Montana, 1992) or process-implying (e.g. resorbed, disequilibrium; e.g. Tsuchiyama, 1985). We chose ″sieve″ to describe the plagioclase to imply a systematic distribution of similarly sized melt inclusions within the crystal, whose 2D appearance is better described as ellipsoids than as hexagons (a hexagonal shape of multiple melt inclusions would warrant the term "honeycomb"). We infer that these melt pockets were created during high pressure and temperature conditions. Our plagioclases (An_{67}) are more sodic than a plagioclase in equilibrium with the surrounding melt, which would be An_{75} (*Pele*, Boudreau, 1999). Very similar plagioclase textures previously have been produced experimentally (see Tsuchiyama, 1985, Fig. 2 D-E and Fig. 3 B; Johannes,

1989, Fig. 3) and reported in natural volcanic andesites from Hakone (Kuno, 1950), Zao (Tsuchiyama and Takahashi, 1983), Myoko (Tsuchiyama, 1985) and Soufrière Hills volcanos (Murphy et al., 2000), as well as in other andesites and basalts.

One or a combination of the following processes produces sieve plagioclases in nature: magma mixing (Sigurdsson, 1971; Eichelberger, 1978), assimilation of plagioclase xenocrysts (Kuno, 1950; Tsuchiyama, 1985) or rapid decompression during ascent (Nelson and Montana, 1992). In our zero-time experiment (sample 26-2), plagioclase crystals already exhibit sieve rims, so we conclude that they were not produced during decompression but at high pressure and temperature conditions. We know they did not have sieve rims prior to the decompression experiments, since cleavage fragments of the same gem-quality crystals were used in Pleše et al.'s (2018) 1 atm, short duration (50 s) experiments, and no sieve textures were produced.

Both magma mixing and crystal assimilation can trigger the two main processes responsible for sieve texture development: 1) temporary heating events that raise the temperature above the solidus but below the liquidus temperature of plagioclase, causing partial melting (Tsuchiyama and Takahaski, 1983; Murphy et al., 2000), or 2) dissolution of plagioclase into the surrounding plagioclase-undersaturated melt (Lofgren and Norris, 1981; Tsuchiyama, 1985). Following Tsuchiyama (1985), the appearance of our plagioclase crystals corresponds to the appearance of plagioclases that underwent partial melting after assimilation. This process is similar to our experiments in which plagioclase crystals were initially added to the glass, with whose subsequently generated melt they would be in disequilibrium.

Plagioclase partial melting, whether surface-controlled (Johannes, 1989) or controlled by chemical diffusion in the crystal (Tsuchiyama and Takahashi, 1983), is

a process that starts from the crystal surface, potentially leading to a change in chemical composition of the surrounding melt (Tsuchiyama and Takahashi, 1983). We investigated semi-quantitatively the chemical composition of the melt 0-180 μm away from the plagioclase surface and found no systematic compositional differences (see Appendix 3.1). Since we know that plagioclase partial melting occurred at high pressure and temperature, there was an amount of newly generated ″plagioclase-derived melt″ that was incorporated into the surrounding melt. Because we observe no-to-minimal chemical zoning in the melt, we infer that the amount of plagioclase-derived melt was very small.

The characteristics of the plagioclase crystal-melt interface (i.e. the crystal's surface) is of specific interest to us because of the possible effects on heterogeneous bubble nucleation. The original plagioclase crystals were cleavage fragments with almost flat surfaces but became rough during the experiment (R_a = 2.9 μm, Figure 3.2 a), most likely by partial melting. Such a rough surface is thought to be especially favourable for heterogeneous bubble nucleation as the wettability by the melt is lowered (Blander and Katz, 1975). Pleše et al. (2018) demonstrated that smoother-surfaced plagioclase crystals (R_a = 0.7 μm) can nucleate bubbles heterogeneously at 1 atm, so we surmise that the same process occurs on rougher surfaces during decompression. Unfortunately, it is impossible to tell from the present data whether this difference in surface roughness stems from different crystallographically oriented surfaces.

3.4.2 Bubbles in contact with plagioclase crystals

The bubbles present in our samples can be clearly divided into those in contact with plagioclase crystal surfaces and those that are surrounded by the melt. The glass transition temperature for this melt composition and volatile content is between 467 °C (Giordano et al., 2005; who report a ± 2.5 °C uncertainty for the value) and 560 °C (calculated based on Giordano et al., 2008). The experimental temperature is 1000 °C, so we can safely say that all bubble nucleation and growth occurred above the glass transition temperature (the temperature range between a glass and a melt).

Table 3.2 shows that there are bubbles present in sample 26-2 (the zero-time, no decompression experiment) both in the melt and on the plagioclase surface. One explanation would be that the melt was not undersaturated with H_2O at 650 MPa. As the pressure accuracy is 25 MPa it is possible that the pressure was 625 instead of 650 MPa. However, the largest number of the smallest bubbles is found precisely in sample 26-2 (Figures 3.6 and 3.7). For an undersaturated sample that spent 1 hour at 625 MPa we would expect larger bubble sizes. Another possibility is that the quench was not perfectly isobaric, due to slight pressure oscillations when the power is cut off the piston-cylinder to induce quench, that needs to be manually compensated. As there are many very small bubbles instead of fewer larger ones, the sample appears to have been much closer to 650 MPa, and we favour the latter explanation.

The key question is: Do all bubbles, regardless of their final location, belong to the same population and so were formed by a single common process, or do they belong to more than one population, representing several different bubble nucleation processes? The differentiation between different nucleation events could provide clues

into bubble-plagioclase interactions, specifically if attachment or detachment of bubbles occurred.

Silicate crystals are commonly considered unfavourable heterogeneous bubble nucleation locations based on 2D contact angle values (Hurwitz and Navon, 1994; Gualda and Ghiorso, 2007), implying that homogeneous bubble nucleation in the melt would occur rather than nucleation on their surfaces (Blander and Katz, 1975). Our 3D outer contact angle values $\theta = 57 – 42$ °, are more precise than previously reported for plagioclase, ($\theta > 20$ °, Eichelberger and Hayes, 1982, Figure 2.2 in Chapter 2), even though still smaller than 68°. Interestingly, these values correspond to angles reported for bubbles on Ti-magnetites in dacites (Mangan et al., 2004; Mangan and Sisson, 2005). Oxides are favoured bubble nucleation sites based on contact angle measurements, but since we have measured the same angle on plagioclase crystals (considered unfavourable), plagioclase crystals might play a larger role then previously envisioned in heterogeneous bubble nucleation.

We must consider the scenario where bubbles nucleated elsewhere in the experiment and after nucleation encountered the plagioclase surface, either via decompression driven expansion or attachment. If all bubbles nucleated homogeneously within the melt, and then some encountered the plagioclase, the BSD of bubbles on the crystal and bubbles in the melt should be similar. This is not the case and the BSD of bubbles on the crystals are distinctly different from the BSD of those in the melt (Figures 3.6 and 3.7). Additionally, in most samples, the largest bubbles are located within the melt and not on the plagioclase surface. Based on bubble sizes alone we cannot differentiate between heterogeneous bubble nucleation or homogeneous nucleation and subsequent attachment. However, based on the low

wettability of plagioclase by bubbles reported in the literature (due to the plagioclase's compositional similarity to the melt), if bubbles nucleated in the melt and then encountered the plagioclase, we would expect to see a thin melt film between the plagioclase surface and bubbles that encountered it. An indication that there is no melt film present is the morphology of bubbles in contact with the plagioclase surface – they share the morphology of bubbles observed growing on plagioclase crystals in Chapter 2 (before they encountered other bubbles). Additionally, no melt film is observed using SEM-BSE analysis (Figure 3.2 a-b).

The possibility of bubble attachment to plagioclase crystal surfaces can be evaluated through their respective buoyancies. Several physical parameters (changing water content, density, melt viscosity, water diffusivity) for melt and bubbles were calculated for different pressures and are summarized in Table 3.3. Melt viscosity was estimated using Richet et al. (1996), due to the high water concentrations in the melts that are above the calibration range of Giordano et al. (2008). The terminal bubble velocity was calculated from Stokes' law formulation in Sparks et al. (1984) for a bubble with a radius of 0.0065 mm (largest bubble in sample 25-1).

Table 3.3: Physical parameters of the melt and bubbles at different pressures. Wt. % indicates weight percentage, ρ density, μ viscosity, D diffusion and v velocity. Values were calculated based on: [a] Papale et al., 2006; [b] modified Redlich-Kwong equation of state from Holloway, 1987; [c] Lange and Carmichael 1987, and Ochs and Lange 1997; [d] Richet et al., 1996; [e] Zhang and Ni, 2010; [f] Sparks et al., 1984. The negative values for bubble velocity indicate floating.

p (Mpa)	wt. % H_2O in melt [a]	wt. % H_2O in bubble [a]	ρ_{bubble} (g cm^{-3}) [b]	ρ_{melt} (g cm^{-3}) [c]	μ_{melt} (Pa s) [d]	D_{H2O} (μm^2 s^{-1}) [e]	v_{bubble} (μm s^{-1}) [f]
650	12.36	0.00	0.68	2.07	2.26	49.93	-5.67
600	11.34	0.73	0.66	2.09	2.27	47.19	-5.84
500	9.98	2.22	0.60	2.14	2.29	41.53	-6.18
400	8.72	3.59	0.54	2.18	2.30	36.29	-6.59
300	7.44	4.91	0.45	2.23	2.31	30.96	-7.09

If we take the only closed-volume plagioclase (25-1), with a $r_{eqv\ sphere}$ = 0.317 mm ($r_{eqv\ sphere}$ represent the radius of a sphere with a volume equivalent to the plagioclase volume), a plagioclase density of $\rho_{plagioclase}$ = 2.7 g cm^{-3} (Stewart et al., 1966), the gravitational constant g = 9.81 m s^{-2}, the physical melt parameters at 650 MPa (Table 3.3), and insert these values into the Stokes' law formulation (Stokes, 1851; Sparks et al., 1984) for a particle's terminal velocity (v_t in Equation 12):

$$v_t = \frac{2\,(r_{plagioclase})^2\, g\,(\rho_{plagioclase} - \rho_{melt})}{9\mu_{melt}} \quad (12),$$

we obtain a plagioclase velocity of + 0.06 mm s^{-1} (note that a positive value indicates sinking and a negative one floating due to the $\Delta\rho$ formulation, in accordance with Sparks's formulation for settling velocity). If we then take the maximum distance, i.e. the entire length of the Pt-capsule, 11 mm, a plagioclase crystal of that size would need ~ 3 min to sink to the bottom of the capsule. Since the sample stayed at 650 MPa for 60 min and at that pressure the melt is water-undersaturated (Papale et al., 2006), the crystals must have sunk before any bubbles nucleated in the sample.

If we then consider the volume of the largest bubble from sample 25-1 (r = 0.065 mm) and the physical parameters of the melt and bubbles at 300 MPa (Table 3), the bubble's terminal velocity is v_t = - 0.0039 mm s^{-1}. Such a bubble would need 46 min to float across 11 mm and the longest experimental duration at water-saturated conditions ($t_2 + t_3$ in Table 3.1) is ~ 4 min. From this follows: 1) bubbles that are found post-process in the melt further away from the crystal than 1 mm could not have originated on the crystal's surface, detached and floated away, because there was insufficient time, 2) the bubbles found post-process on the crystal's surface equally did not have time to move more than 1 mm through the melt and attach to the crystal,

and 3) the bubbles always float, so they would move away from the crystal (that sunk to the capsule bottom before any bubbles nucleated), not towards the crystal.

Inconsistencies between 3D BND on crystal surface and 3D BND within the melt across different samples at the same experimental conditions (Table 3.2, Figure 3.5) could be due to our subvolume selection or crystal surface heterogeneity. We favour the latter as we observed surface roughness (Figure 3.2 a, b). There is almost a four-fold difference (3.6) in surface roughness (R_a) between the plagioclase in 1 atm experiments (Pleše et al., 2018, Chapter 2 of this thesis) and decompression experiments (this study), that is followed by a small difference in bubble number (10 and 7, respectively). This observation corresponds to heterogeneous bubble nucleation being easier on rough surfaces (Blander and Katz, 1975; Hurwitz and Navon, 1994). Additionally, surface roughness lowers the supersaturation pressure for heterogeneous bubble nucleation (that is already always lower than for homogeneous bubble nucleation, Blander and Katz, 1975; Hurwitz and Navon, 1994). If the plagioclase crystals in our experiments would have remained smooth, i.e. with a surface roughness more like that of plagioclases in Pleše et al. (2018) 1 atm experiments, we would expect to see less bubbles nucleating on smoother surfaces. At present, due to difficulties of imaging plagioclase crystals in andesitic melts using X-ray tomography, it is not possible to easily observe plagioclase surfaces and their heterogeneities, in order to quantify the surface roughness in 3D and compare it with 3D BND. An initial step would be to increase the amount of measurement from 2D crystal-bubble cross-sections obtained by different analytical methods. As this is the first contribution of bubble number comparison to observed (not inferred, as it was in Hurwitz and Navon,

1994) crystal surface parameters, our view is that there is insufficient data to calculate the effect of surface roughness on heterogeneous bubble nucleation.

Another observation supporting heterogeneous bubble nucleation might be the region of melt around bubble-plagioclase aggregates that is free of bubbles. This bubble-free zone is most likely a consequence of water diffusing from that region into pre-existing bubbles. In natural magmas, at small bubble sizes (right above the critical nucleation radius) diffusion of volatiles from the melt into the bubble is very efficient and controls bubble growth (Sparks, 1978, Navon et al., 1998). This would indicate that in our experiments, heterogeneous bubble nucleation on plagioclase surfaces occurred early during decompression, which is consistent with our earlier 1 atm observations (Pleše et al., 2018, Figure 2.5), and these bubbles took up the water from the surrounding melt.

3.4.3 Bubbles not in contact with plagioclase crystals

The BSD of bubbles within the melt are different then the BSD of bubbles on plagioclase surfaces (Figures 3.6 and 3.7). The BSDs of bubbles on plagioclase surfaces are unimodal, pointing to one population generated by a single nucleation event (Gondé et al., 2011), which we argued above is heterogeneous nucleation. We also argued that heterogeneously nucleated bubbles on plagioclase nucleated very early, most probably before other nucleation events. Since the BSDs within the melt do not correspond to BSD on the plagioclases, the bubbles within the melt belong to a different population (Gondé et al., 2011). The BSD in the melt is bimodal, pointing to two populations of bubbles within the melt, and so possibly two nucleation events in

the melt region. Several questions arise: Were both populations of bubbles in the melt produced by homogeneous nucleation? Was one or both populations produced by heterogeneous nucleation, possibly on oxide microlites? Does one population represent bubbles that have nucleated on the plagioclase crystal and detached from it?

Previously we demonstrated that bubbles that nucleated within the melt could not have attached to plagioclase surfaces. Now, we must first consider if bubbles that originated on plagioclase surfaces could have detached, leading them to be found post-process within the melt. Our outer 3D bubble-crystal contact angles are lower than 68 °, so detachment of bubbles from the crystal should be easily achievable, because the lower the outer contact angle value (θ), the easier it is to detach a bubble from a crystal (Gualda and Ghiorso, 2007, but note that their θ and ψ are reversed; $\theta + \psi = 180°$). What was interpreted as the start of bubble detachment from plagioclases was observed *in situ* through bubble-crystal 3D contact angle decrease in Pleše et al. (2018). In our samples, we observe a decrease in the contact angle value with increasing decompression, but since we are observing post-process samples, we cannot know with certainty whether there is any correlation. Additionally, bubbles are still found directly on the plagioclase surface, and we have calculated in subsection 3.4.2 that there was no time for them to detach and float away from plagioclases. Thus, we conclude detachment did not occur, and that the nucleation event(s) that produced bubbles in the melt are separate from heterogeneous nucleation on plagioclase surfaces.

After eliminating plagioclase surfaces as the nucleation sites for bubbles found totally enclosed by melt, we must consider if another crystal phase could have provided bubble nucleation locations. There are oxide microlites present in the melt (Figure 3.3

a), and they are sometimes located on outer surfaces of smaller bubbles. The presence of oxides indicates that for such bubbles we cannot say with certainty whether they nucleated homogeneously within the melt or heterogeneously on oxide crystals. Large bubbles ($\log_2[V_{bubble}\ (\mu m^3)] = > 12.1$) within the melt are only observed in samples at 350 MPa decompressions (Figure 3.7). We see on Figure 3.6 (decompressions smaller than 350 MPa) that no bubble within the melt is larger than $\log_2[V_{bubble}\ (\mu m^3)] = 12.1$. Bubbles within the melt very rarely have oxide microlites on their surfaces. Due to our large initial water concentrations, it is plausible that at decompressions smaller than 350 MPa the supersaturation pressure for homogeneous bubble nucleation may not have been achieved (Hurwitz and Navon, 1994), so we cannot discriminate between heterogeneous and homogeneous nucleation in experiments at 350 MPa decompressions. Pleše et al. (2018) observed that homogeneous nucleation within the melt and heterogeneous nucleation on oxides occurred very close in time, from 3 to 26 s apart. With our decompressions and water contents both heterogeneous nucleation on oxides and homogeneous nucleation within the melt are plausible.

3.4.4 Forces acting on a bubble-crystal aggregate and on a single bubble on a plagioclase surface

Heterogeneous bubble nucleation on a crystal surface will influence the total buoyancy of the aggregate. To determine the bubble(s)-plagioclase aggregate's buoyancy, we followed the calculations developed by Gualda and Ghiorso (2007). We took a plagioclase crystal from each decompression drop (26-2, 19-2, 22-1, 21-1, Table 3.4) and summed the volumes of all bubbles on their respective surfaces. The

uncertainties in the calculations come from crystals without a closed volume, where their volume was manually closed by generating a surface without bubbles.

The aggregate's buoyancy is the net buoyancy (Figure 3.8) from Gualda and Ghiorso (2007):

$$F_{net}^{buoyancy} = F_{plagioclase}^{buoyancy} + F_{\Sigma\, bubbles}^{buoyancy} = -\frac{4}{3}\pi\, g\, [r_{plagioclase}{}^{3} * (\rho_{plagioclase} - \rho_{melt}) + r_{\Sigma\, bubbles}{}^{3} * (\rho_{bubble} - \rho_{melt})] \quad (8).$$

Both radii are derived from equivalent volume spheres, and the appropriate physical melt and bubble parameters for each decompression are taken from Table 3.3. As seen in Table 3.4, the net buoyancy of all but one plagioclase-bubble aggregate indicates sinking.

Table 3.4: Contact angle values (3D) and volumetric parameters used to calculate different forces acting on bubbles located on plagioclase crystal surfaces and on bubble-plagioclase aggregates. The plagioclase equivalent radius was taken as 30.16 μm for all cases. Values are obtained based from the equations of Gualda and Ghiorso (2007), see text for further explanation. Note that a positive value of the net buoyancy force indicates sinking while a negative value indicates floating.

sample name	**26-2**	**19-2**	**22-1**	**21-1**
decompression drop (MPa)	0	50	200	350
outer 3D contact angle θ (°)	57	49	45	42
ρ_{bubble} (kg m^{-3})	679	656	537	450
$r_{max\ bubble}$ (m)	7.49×10^{-6}	2.34×10^{4}	3.62×10^{-5}	2.61×10^{-5}
$V^{measured}_{\Sigma\ bubbles}$ (m^3)	7.85×10^{-13}	5.82×10^{-11}	1.45×10^{-12}	5.46×10^{-12}
$r^{equivalent}_{\Sigma\ bubbles}$ (m)	5.72×10^{-5}	2.40×10^{4}	7.02×10^{-5}	1.09×10^{4}
ρ_{melt} (kg m^{-3})	2070	2094	2181	2228
$F^{buoyancy}_{net}$ (N)	8.14×10^{-7}	-2.8×10^{-8}	6.56×10^{-7}	5.23×10^{-7}
$F^{buoyancy}_{difference}$ (N)	-4.8×10^{-11}	-1.5×10^{-6}	-6.4×10^{-9}	-2.6×10^{-9}
$r^{critical}_{bubble}$ (m)	1.88×10^{-3}	1.62×10^{-3}	1.51×10^{-3}	1.33×10^{-3}
$V^{critical}_{\Sigma\ bubbles}$ (m^3)	2.77×10^{-8}	1.79×10^{-8}	1.45×10^{-8}	9.89×10^{-9}
$F^{attachment}$ (N)	2.53×10^{-6}	6.29×10^{-5}	8.48×10^{-6}	5.44×10^{-6}

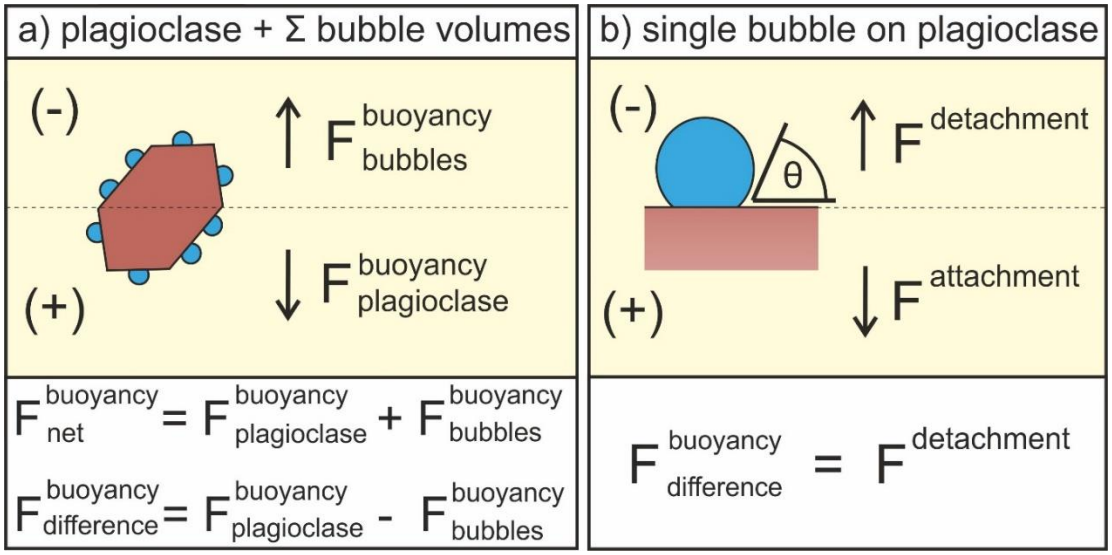

Figure 3.8: Schematic representation of the forces acting on the entire plagioclase-bubble aggregate and on a single bubble on the plagioclase surface. a) If bubbles and the plagioclase crystal were separated, the former would float and latter sink. When they form an aggregate, their net buoyancy determines the aggregate's direction of movement. b) For a single bubble on a plagioclase surface, the outer contact angle is θ. Whether the bubble will remain on the plagioclase surface depends on the attachment and detachment forces acting on it.

The exception is sample 19-2 (650 to 600 MPa), where the plagioclase contains ~ 10 x more bubbles than the plagioclases in the other three samples (44155 vs 1360, sample 21-1, 4595, sample 22-1, and 6147, sample 26-2, respectively). It is unclear why the aggregate from sample 19-2 has more bubbles and whether there is any significant surface roughness difference that could explain it (sample was not observed using SEM). However, it floats one order of magnitude slower than the others sink (Table 3.4). The amount of data available is limited, but it shows that while bubble-plagioclase aggregates would mostly sink, flotation could also be possible.

The net buoyancy calculation only applies while the crystal and bubbles stay attached, and we cannot determine if they will remain attached based on the net buoyancy alone. Gualda and Ghiorso (2007) propose that detachment could occur the moment that the aggregate's net buoyancy is neutral (equals zero). In this moment, bubbles will have a critical radius for detachment ($r_{bubble}^{critical}$, Equation 13):

$$r_{bubble}^{critical} = sin(180° - \theta)\left(\frac{3\sigma_{bubble-melt}}{4g(\rho_{bubble}-\rho_{melt})}\right)^{\frac{1}{2}}\left(\frac{4}{2-3cos(180°-\theta)+cos^3(180°-\theta)}\right)^{\frac{1}{6}} \quad (13),$$

where σ is the surface tension (the original equations are adjusted for our contact angle terminology).

The critical radius term was obtained by equating the difference in buoyancy between crystals and bubbles ($F_{difference}^{buoyancy}$) with the attachment force, as the former acts to separate bubbles and crystals and the latter force keeps them together (Gualda and Ghiorso, 2007):

$$F_{difference}^{buoyancy} = F_{plagioclase}^{buoyancy} - F_{bubble}^{buoyancy} = \frac{8}{3}\pi\, g\, (r_{bubble})^3\, (\rho_{bubble} - \rho_{melt}) \quad (14)$$

($F_{plagioclase}^{buoyancy}$ and $F_{bubble}^{buoyancy}$ are equal in value but of opposite directions in the moment of neutral buoyancy) :

$$F_{difference}^{buoyancy} = F^{attachment} \quad (15),$$

$$F^{attachment} = 2\pi r_{bubble} sin^2(180° - \theta)\sigma_{bubble-melt}\left(\frac{4}{2-3cos(180°-\theta)+cos^3(180°-\theta)}\right)^{\frac{1}{3}}$$

(16)

Note that in the moment of neutral buoyancy, $F_{difference}^{buoyancy}$ can be equated to either the attachment or the detachment force (Gualda and Ghiorso, 2007). If a bubble's radius is larger than $r_{bubble}^{critical}$, the pair will detach, and if a bubble's radius is smaller, the pair will remain attached. In our case, we have multiple bubbles. We summed the volumes of all bubbles on the crystal surfaces (not just from one crystal surface) to obtain $V_{\Sigma\, bubbles}^{measured}$. We the converted $r_{bubble}^{critical}$ to $V_{\Sigma\, bubbles}^{critical}$. Comparing the actual $V_{\Sigma\, bubbles}^{measured}$ to the calculated $V_{\Sigma\, bubbles}^{critical}$ (Table 3.4) we see that the measured volumes are always smaller than the critical ones, indicating that the bubbles will stay attached to the crystal. This is another argument in favour of heterogeneous bubble nucleation on plagioclase being independent of the events producing bubbles within the melt.

The bubbles that coat our plagioclase surfaces are not in contact with one another, so there are no shared bubble-bubble interfaces. This simplifies the situation as we can consider forces acting on a single bubble in order to examine bubble-crystal attachment. Following on the previous paragraph, if we look at the radius of the largest bubble from each decompression group, we see that this radius is always smaller then $r_{bubble}^{critical}$ (Table 3.4), indicating they will stay attached. Another approach is to consider the forces acting on a single bubble; the attachment force will try to keep the bubble

and crystal together, while the detachment force will try to separate them (Gualda and Ghiorso, 2007). Gualda and Ghiorso (2007) have equated $F_{difference}^{buoyancy}$ to $F^{detachment}$, so we only need to compare our calculated attachment force to our calculated buoyancy difference value (Table 3.4). We see the attachment force is larger for all cases, indicating the bubbles will stay attached to the crystal surface.

3.4.5 Magma-mixing triggered heterogeneous bubble nucleation

Our finding of bubbles nucleating heterogeneously on rough surfaces of sieve plagioclase crystals has possible implications for degassing triggered by magma mixing. Plagioclase xenocrysts originating from a less-silicic magma can become incorporated into a more-silicic magma, e.g. with new magma injections in subduction related volcanic environments (Sigurdsson et al., 2015). After magma mixing, plagioclase xenocrysts are in chemical disequilibrium with the surrounding melt and begin to partially melt, leading to sieve rim and rough surface formation (Kuno, 1950, Tsuchiyama, 1985). The observations of such features from natural samples show that plagioclase partial melting is more probable than additional plagioclase crystallization, at least immediately after assimilation. As the plagioclase crystals in our experimental charges only exhibit sieve rims and do not have resorbed rims or regrowth around the sieve rims, we exclude the possibility of additional plagioclase crystallization within the experiment, and so do not extend our observations to natural systems where it could occur. Mixing-triggered compositional melt changes could result in an initially volatile undersaturated melt becoming oversaturated (especially if the injected magma contained volatiles, Sigurdsson et al., 2015). In this scenario, rough surfaced

plagioclase crystals would be immediately available as heterogeneous bubble nucleation sites, possibly leading to early bubble nucleation and volcanic eruptions.

3.5 Conclusions

In this study, we investigated the possibility of heterogeneous bubble nucleation on plagioclase crystal surfaces in an andesitic melt during decompression. The experimental conditions that caused the generation of sieve rims in plagioclases mimic well partial melting due to xenocryst assimilation, one of the natural processes producing plagioclase sieve rims. Thus, the presence and appearance of plagioclases in our samples is applicable to natural conditions. All plagioclase crystals in samples from all decompressions have all their surfaces covered in bubbles, so this observation is not accidental. Comparing bubble size distributions at different decompressions of bubbles on plagioclase surfaces and bubbles away from plagioclase crystals, we show that the two types of bubbles do not belong to the same population. Through Stokes' law calculations we show that bubbles could not have encountered plagioclase crystal surfaces after nucleating elsewhere. Combining these results with recent *in situ* observations (Pleše et al., 2018), where heterogeneous bubble nucleation occurred on smooth plagioclase surfaces prior to any other nucleation event, we conclude that in our samples, the bubbles found on plagioclase surfaces nucleated there. The roughness of plagioclase surfaces in our experiments most likely further contributed to the energetic favourability of such heterogeneous nucleation. The interesting possibility regarding heterogeneous bubble nucleation is that perhaps the presence of a crystal surface is more relevant than the crystal-melt compositional difference.

We considered buoyancy, attachment and detachment forces acting on single bubbles on the plagioclase surface and on the entire bubble-plagioclase aggregate. We found that in a natural environment (i.e. not confined to a small capsule volume), bubbles of sizes comparable to those in our experiments would stay attached to the plagioclase surface and the aggregate would sink. Our findings indicate that plagioclase crystals should not be disregarded when studying magmatic vesiculation.

3.6 Acknowledgements

The authors wish to thank Lucia Mancini from the Elettra Sincrotrone (Trieste, Italy), SYRMEP beamline for her help with Pore3D and *Avizo Fire*® (Visualization Sciences Group). The authors thank Monika Rusiecka for her help with laboratory advice.

3.7 Author contributions

P.P. (PhD student and principal investigator), M.D.H. (PhD director) and D.R.B. (PhD co-director) developed the ideas explored in the manuscript. M.K.P. (graduate student) helped with the sample synthesis and SEM analysis. All authors helped with the writing of the manuscript.

3.8 References

Baker, D. R., Eggler, D., 1987. Composition of melts coexisting with plagioclase, augite and olivine or low-calcium pyroxene at pressures from one atmosphere to 8 kbar, anhydrous and 2 percent H_2O and applications to island arc petrogenesis. *American Mineralogist* 72, 12-28.

Baker, D. R., 2004. Piston-cylinder calibration at 400 to 500 MPa: A comparison of using water solubility in albite melt and NaCl melting. *American Mineralogist* 89 (10), 1553-1556.

Baruchel, J., Maire, E., Merle, P., Peix, G., Buffiere, J.-Y., 2000. X-Ray Tomography in Material Science, General Principles. Hermes Science Publications, Paris.

Blander, M., Katz, J. L., 1975. Bubble nucleation in liquids. *AlChE Journal* 21 (5), 833–848.

Boudreau, A. E., 1999. PELE - a version of the MELTS software program for the PC platform. *Computers & Geosciences* 25, 201-203.

Brun, F., Mancini, L., Kasae, P., Favretto, S., Dreossi, D., Tromba, G., 2010. Pore3D: A software library for quantitative analysis of porous media. *Nuclear Instruments and Methods in Physics Research Section A: Accelerators, Spectrometers, Detectors and Associated Equipment* 615 (3), 326-332.

Dalpé, C., Baker, D. R., 2000. Experimental investigation of large-ion-lithophile-element-, high-field-strength-element-and rare-earth-element-partitioning

between calcic amphibole and basaltic melt: the effects of pressure and oxygen fugacity. *Contributions to Mineralogy and Petrology* 140 (2), 233-250.

Druitt, T. H., Young, S. R., Baptie, B., Bonadonna, C., Calder, E. S., Clarke, A. B., Cole, P. D., Harford, C. L., Herd, R. A., Luckett, R., Ryan, G., Voight, B., 2002. Episodes of cyclic Vulcanian explosive activity with fountain collapse at Soufrière Hills Volcano, Montserrat. *Memoirs of the Geological Society of London* 21, 281-306.

Dziewonski, A. M., Anderson, D. L., 1981. Preliminary reference Earth model. *Physics of Earth and Planetary Interiors* 25, 297-356.

Eichelberger, J. C., 1978. Andesites in island arcs and continental margins: relationship to crustal evolution. *Bulletin Volcanologique* 41 (4), 480-500.

Giordano, D., Nichols, A. R. L., Dingwell, D. B., 2005. Glass transition temperatures of natural hydrous melts: a relationship with shear viscosity and implications for the welding process. *Journal of Volcanology and Geothermal Research* 142 (1), 105–118.

Giordano, D., Russell, J. K., Dingwell, D. B., 2008. Viscosity of magmatic liquids: a model. *Earth and Planetary Science Letters* 271 (1-4), 123-134.

Gondé, C., Martel, C., Pichavant, M., Bureau, H., 2011. In situ bubble vesiculation in silicic magmas. *American Mineralogist* 96 (1), 111-124.

Gualda, G. A., Ghiorso, M. S., 2007. Magnetite scavenging and the buoyancy of bubbles in magmas. Part 2: Energetics of crystal-bubble attachment in magmas. *Contributions to Mineralogy and Petrology* 154(4), 479-490.

Harris, J. W., Stöcker, H., 1998. Handbook of Mathematics and Computational Science. New York: Springer-Verlag, p. 108.

Holloway, J. R., 1987. Igneous fluids. *Reviews in Mineralogy and Geochemistry* 17 (1), 211-233.

Hurwitz, S., Navon, O., 1994. Bubble nucleation in rhyolitic melts: Experiments at high pressure, temperature, and water content. *Earth and Planetary Science Letters* 122(3–4), 267-280.

Johannes, W., 1989. Melting of plagioclase-quartz assemblages at 2 kbar water pressure. *Contributions to Mineralogy and Petrology* 103 (3), 270-276.

Kuno, H., 1950. Petrology of Hakone volcano and the adjacent areas, Japan. *Geological Society of America Bulletin* 61 (9), 957-1020.

Lange, R.A., Carmichael, I.S., 1987. Densities of Na_2O-K_2O-CaO-MgO-FeO-Fe_2O_3-Al_2O_3-TiO_2-SiO_2 liquids: new measurements and derived partial molar properties. *Geochimica et Cosmochimica Acta* 51 (11), 2931-2946.

Liu, Y., Samaha, N. T., Baker, D. R., 2007. Sulfur concentration at sulfide saturation (SCSS) in magmatic silicate melts. *Geochimica et Cosmochimica Acta* 71 (7), 1783-1799.

Lofgren, G. E., Norris, P. N., 1981. Experimental duplication of plagioclase sieve and overgrowth textures. *Geological Society of America Abstract Program* Vol. 498.

Mangan, M., Sisson, T., 2000. Delayed, disequilibrium degassing in rhyolite magma: decompression experiments and implications for explosive volcanism. *Earth and Planetary Science Letters* 183 (3–4), 441–455.

Mangan, M., Sisson, T. W., Hankins, W. B., 2004. Decompression experiments identify kinetic controls on explosive silicic eruptions. *Geophysical Research Letters* 31 (8), L08605.

Murphy, M. D., Sparks, R. S. J., Barclay, J., Carroll, M. R., Brewer, T. S., 2000. Remobilization of Andesite Magma by Intrusion of Mafic Magma at the Soufriére Hills Volcano, Montserrat, West Indies. *Journal of Petrology* 41(1):21–42. https://doi.org/10.1093/petrology/41.1.21.

Mysen, B., Richet, P., 2005. Silicate Glasses and Melts: Properties and Structure. 10. Elsevier Science, Amsterdam. pp. 22-23, 69.

Navon, O., Chekhmir, A., Lyakhovsky, V., 1998. Bubble growth in highly viscous melts: theory, experiments, and autoexplosivity of dome lavas. *Earth and Planetary Science Letters* 160 (3–4), 763-776. doi:http://dx.doi.org/10.1016/S0012-821X(98)00126-5

Nelson, S. T., Montana, A., 1992. Sieve-textured plagioclase in volcanic rocks produced by rapid decompression. *American Mineralogist* 77, 1242-1249.

Ochs III, F. A., Lange, R. A., 1997. The partial molar volume, thermal expansivity, and compressibility of H_2O in $NaAlSi_3O_8$ liquid: new measurements and an internally consistent model. *Contributions to Mineralogy and Petrology* 129 (2-3), 155-165.

Papale, P., Moretti, R., Barbato, D., 2006. The compositional dependence of the saturation surface of H_2O+ CO_2 fluids in silicate melts. *Chemical Geology* 229 (1-3), 78-95.

Pearson, K., 1900. X. On the criterion that a given system of deviations from the probable in the case of a correlated system of variables is such that it can be reasonably supposed to have arisen from random sampling. *The London, Edinburgh, and Dublin Philosophical Magazine and Journal of Science* 50 (302), 157-175.

Pleše, P., Higgins, M. D., Mancini, L., Lanzafame, G., Brun, F., Fife, J. L., Casselman, J., Baker, D. R., 2018. Dynamic observations of vesiculation reveal the role of silicate crystals in bubble nucleation and growth in andesitic magmas. *Lithos* 296, 532-546.

Pleše, P, Higgins, M. D., Baker, D. R., Lanzafame, G., Kudrna Prašek, M., Mancini, L., Rooyakkers, S., 2019. Production and detachment of oxide crystal shells on bubble walls during experimental vesiculation of andesitic magmas. *Contributions to Mineralogy and Petrology* 174 (21).

Richet, P., Lejeune, A. M., Holtz, F., Roux, J., 1996. Water and the viscosity of andesite melts. *Chemical Geology* 128 (1-4), 185-197.

Rivers, M. L., Wang, Y., Uchida, T., 2004. Microtomography at GeoSoilEnviroCARS. *Developments in X-Ray Tomography* IV. Proc. SPIE 5535. doi: 10.1117/12.562556; https://doi.org/10.1117/12.562556

Rivers, M. L., 2012. tomoRecon: High-speed tomography reconstruction on workstations using multi-threading. *Developments in X-Ray Tomography* VIII. Int. Soc. Opt. Photon. 8506:8506U.

Rivers, M. L., Citron, D. T., Wang, Y., 2010. Recent developments in computed tomography at GSECARS. *Developments in X-Ray Tomography* VII. Proc. SPIE 7804:09. doi: 10.1117/12.861393; https://doi.org/10.1117/12.861393

Schindelin, J., Arganda-Carreras, I., Frise, E., Kaynig, V., Longair, M., Pietzsch, T., Preibisch, S., Rueden, C., Saalfeld, S., Schmid, B., Tinevez, J.Y., 2012. Fiji: an open-source platform for biological-image analysis. *Nature Methods* 9 (7), 676.

Sigurdsson, H., 1971. Feldspar relations in a composite magma. *Lithos* 4 (3), 231-238.

Sigurdsson, H., Houghton, B., McNutt, S., Rymer, H., Stix, J. (Eds.), 2015. The Encyclopedia of Volcanoes. Elsevier, Amsterdam. pp. 9, 89, 179.

Skyscan, NV, 2011. NRecon User Manual.

Sparks, R. S. J., 1978. The dynamics of bubble formation and growth in magmas: A review and analysis. *Journal of Volcanology and Geothermal Research* 3 (1-2), 1-37. doi:10.1016/0377-0273(78)90002-1

Sparks, R. S. J., Huppert, H. E., Turner, J. S., 1984. The fluid dynamics of evolving magma chambers. *Philosophical Transactions of the Royal Society of London Series A, Mathematical and Physical Sciences* 310 (1514), 511-534.

Stewart, D. B., Walker, G. W., Wright, T. L., Fahey, J. J., 1966. Physical properties of calcic labradorite from Lake County, Oregon. *American Mineralogist: Journal of Earth and Planetary Materials* 51 (1-2), 177-197.

Stokes, G. G., 1851. On the effect of internal friction of fluids on the motion of pendulums. Transactions of the Cambridge Philosophical Society.

Tsuchiyama, A., Takahashi, E., 1983. Melting kinetics of a plagioclase feldspar. *Contributions to Mineralogy and Petrology* 84 (4), 345-354.

Tsuchiyama, A., 1985. Dissolution kinetics of plagioclase in the melt of the system diopside-albite-anorthite, and origin of dusty plagioclase in andesites. *Contributions to Mineralogy and Petrology* 89 (1), 1-16.

Whitehouse, D.J. 2004. Surfaces and their Measurement. Elsevier, Amsterdam. pp. 51.

Zhang, Y., Ni, H., 2010. Diffusion of H, C, and O components in silicate melts. *Reviews in Mineralogy and Geochemistry* 72 (1), 171-225.

3.9 Appendices

Appendices 3.1 and 3.2 can be found on a CD-ROM accompanying the thesis.

Appendix 3.1

Scanning conditions for imaging with conventional X-ray micro-tomography, using the Skyscan 1172, at MIAM, McGill University, Montréal.

Sample name	Voltage (kV)	Current (µA)	Filtering	Detector binning	SSD (mm)	SDD (mm)	Detector pixel size (µm)
15-1	44	226	Al	4x4	28,40	345,1	11,56
19-1	45	218	Al	4x4	28,36	345,1	11,56
19-2	48	208	Al	4x4	23,23	345,1	11,56
21-1	44	226	Al	4x4	28,36	345,1	11,56
22-1	44	226	Al	4x4	23,23	345,1	11,56
24-1	44	226	Al	4x4	28,36	345,1	11,56
24-2	44	226	Al	4x4	28,40	345,1	11,56
25-1	44	226	Al	4x4	28,36	345,1	11,56
25-2	44	226	Al	4x4	28,40	345,1	11,56
26-2	44	226	Al	4x4	38,68	345,1	11,56
27-1	44	226	Al	4x4	28,40	345,1	11,56
27-2	44	226	Al	4x4	28,36	345,1	11,56

Sample name	isotropic voxel size (µm)	Exposure time/proj. (ms)	Rotation step (°)	# of projections	Frame averaging	random movement
15-1	3,8	474	0,40	902 over 360°	4	10
19-1	3,8	474	0,60	902 over 360°	4	10
19-2	3,1	474	0,40	902 over 360°	4	10
21-1	3,8	474	0,40	902 over 360°	4	10
22-1	3,1	474	0,68	531 over 360°	4	10
24-1	3,8	474	0,68	531 over 360°	4	10
24-2	4,8	474	0,68	531 over 360°	4	10
25-1	3,8	474	0,68	531 over 360°	4	10
25-2	3,8	474	0,68	531 over 360°	4	10
26-2	5,1	474	0,68	531 over 360°	4	10
27-1	2,7	474	0,68	531 over 360°	4	10
27-2	3,8	474	0,68	531 over 360°	4	10

Appendix 3.2

Compositional analysis performed with a BSE detector on several points for sample 24-2, shown in Figure 3.2 a (BSE image).

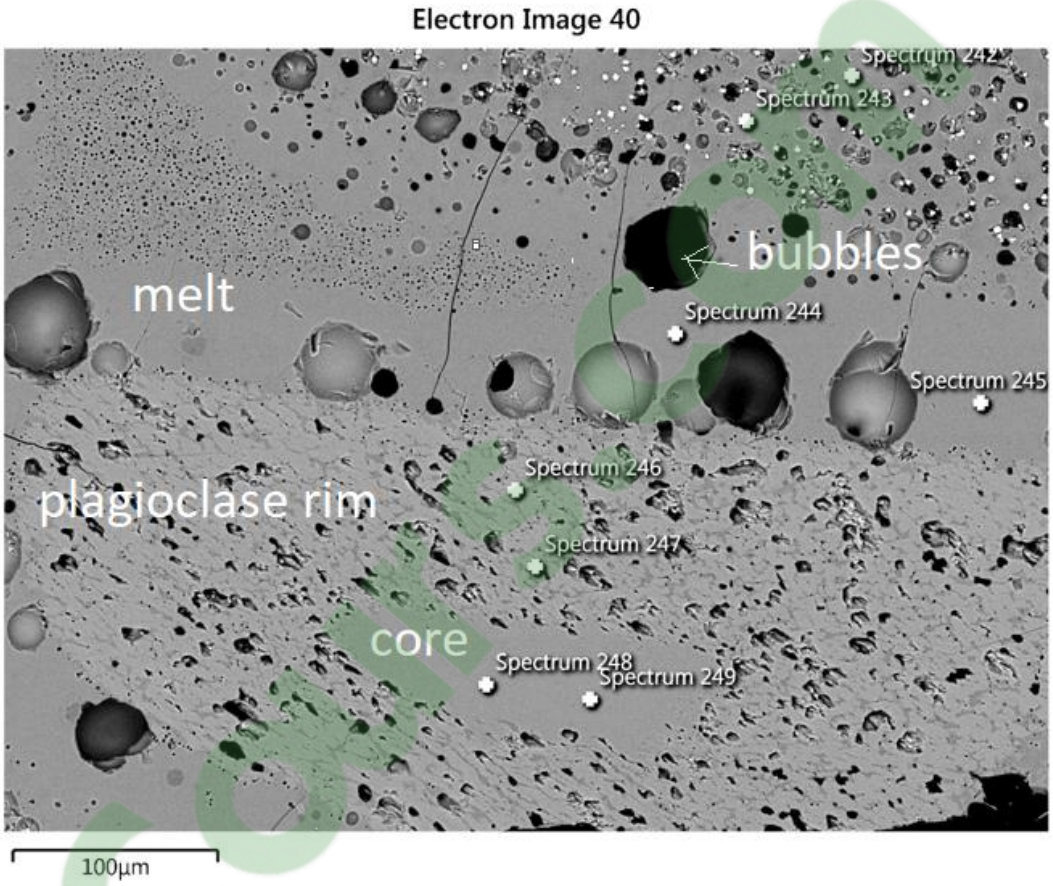

Spectrum Label	Spectrum 242	Spectrum 243	Spectrum 244	Spectrum 245	Spectrum 246	Spectrum 247	Spectrum 248	Spectrum 249
Na_2O	2.8	2.9	2.9	2.9	2.1	1.6	3.7	3.8
MgO	2.0	1.7	2.2	2.2	0.6	0.0	0.0	0.0
Al_2O_3	18.7	19.0	20.6	21.2	31.0	33.4	30.2	30.0
SiO_2	52.5	52.3	49.7	50.6	46.8	45.1	49.6	49.4
K_2O	1.1	1.1	1.5	1.5	0.3	0.0	0.1	0.0
CaO	7.7	7.9	7.5	7.7	14.5	16.3	12.6	12.8
TiO_2	0.7	0.7	0.4	0.6	0.0	0.0	0.0	0.0
$FeO_{(Tot)}$	3.9	3.6	3.9	3.9	1.4	0.4	0.5	0.4
Total	89.4	89.2	88.7	90.7	96.6	96.7	96.8	96.5

Electron Image 41

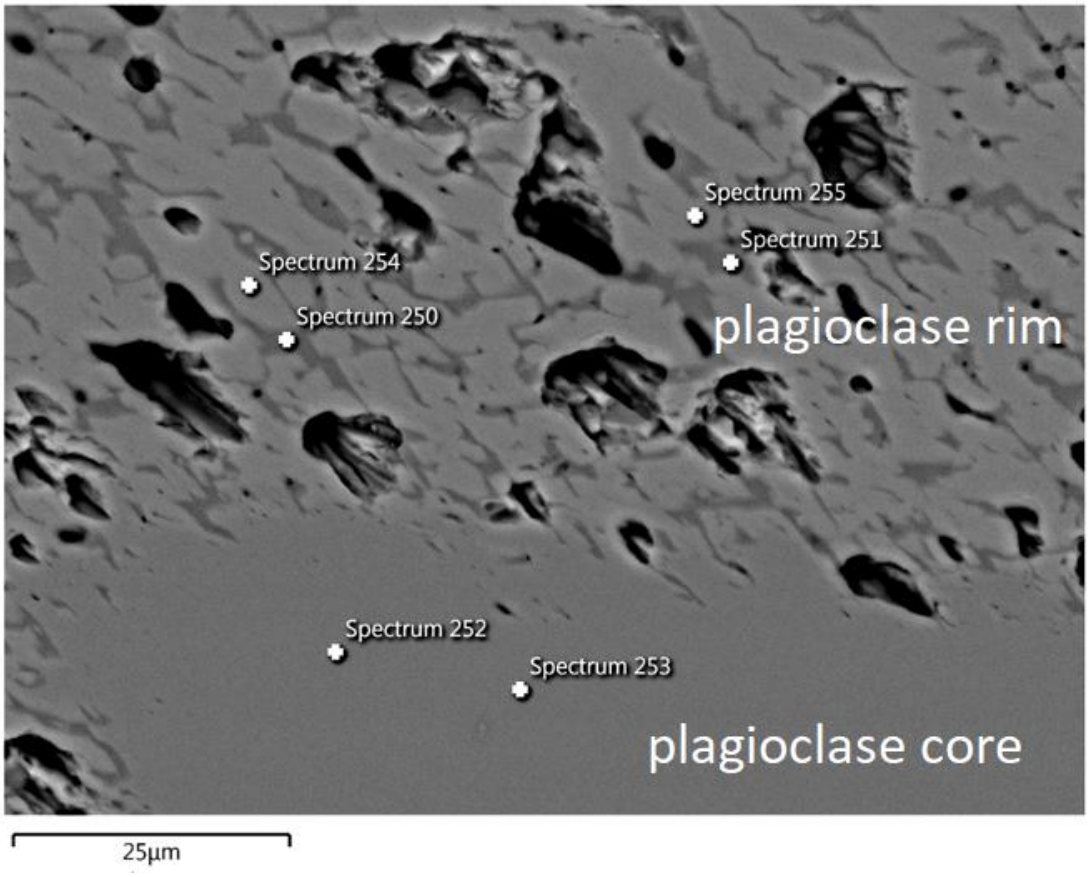

Spectrum Label	Spectrum 250	Spectrum 251	Spectrum 252	Spectrum 253	Spectrum 254	Spectrum 255
Na_2O	2.9	2.9	3.6	3.6	1.4	1.4
MgO	2.7	2.5	0.0	0.0	0.0	0.0
Al_2O_3	19.3	19.4	29.7	29.9	33.5	33.5
SiO_2	55.1	54.0	49.2	49.4	44.0	44.4
K_2O	2.7	2.2	0.0	0.2	0.0	0.0
CaO	4.4	5.4	12.7	12.6	16.6	16.4
TiO_2	0.0	0.2	0.0	0.0	0.0	0.0
MnO	0.0	0.3	0.0	0.0	0.0	0.0
$FeO_{(Tot)}$	3.3	3.4	0.4	0.4	0.0	0.5
Total	90.5	90.4	95.7	96.1	95.5	96.2

CHAPTER 4

Production and detachment of oxide crystal shells on bubble walls during experimental vesiculation of andesitic magmas

Pia Pleše[a],

Michael D. Higgins[a], Don R. Baker[b],

Gabriele Lanzafame[c], Marko Kudrna Prašek[b],

Lucia Mancini[c] and Shane Rooyakkers[b]

[a] – Département des sciences appliquées, Université du Québec à Chicoutimi (UQAC), 555, boulevard de l'Université, Chicoutimi (Québec), Canada G7H 2B1

[b] – Department of Earth and Planetary Sciences (EPS), McGill University, 3450 University Street, Montréal (Québec) Canada, H3A 0E8

[c] - Elettra – Sincrotrone Trieste S.C.p.A. S.S. 14 km 163.5 in Area Science Park, 34149 Basovizza (Trieste), Italy

Published in

Contributions to Mineralogy and Petrology

Volume 174, pages 1-21

January 2019

https://doi.org/10.1007/s00410-019-1556-8

RÉSUMÉ

L’affinité mutuelle entre les bulles et les cristaux d’oxyde (en particulier la magnétite) est bien établie et leur tendance à rester en contact une fois qu’ils se sont connectés (soit par nucléation de l’un sur l’autre, soit par attachement) a conduit à des modèles de transport de l’oxyde par des bulles dans les fondus naturels. Cependant, malgré l’acceptation généralisée de l’association oxyde-bulle, il existe peu de preuves texturales directes de ces processus. Nous présentons les résultats d'une série d'expériences de décompression sur des échantillons des fontes andésitiques, au cours desquelles des agrégats de bulles et d'oxydes se sont formés en raison d'une perte d'hydrogène à travers les parois de la capsule, entraînant une oxydation de la fonte. Les charges expérimentales ont été imagées en utilisant une tomographie 3D à rayons X qui a révélé des agrégats complexes de bulles et d'oxydes, de petits cristaux d'oxydes recouvrant une partie de la surface externe des bulles selon une morphologie analogue à celle d'une coquille. Ces coquilles ont des surfaces intérieures lisses et extérieures rugueuses. Parfois, des coquilles concentriques ou des coquilles partielles peuvent être trouvées autour des bulles, dans le verre entre la paroi de la bulle et une autre coquille. Nous avons quantifié les volumes de bulles et d’oxydes et la composition des oxydes. Nous avons mesuré la surface de contact des bulles et des oxydes, quantifiant ainsi leur interface en 3D, et utilisé ces mesures pour étudier le processus de formation de la coquille d’oxydes. La complexité des textures d'oxydes étudiées en 3D révèle une gamme d'interactions bulle-oxyde, de la génération continue, détachement et à la désintégration. Ces processus ont des implications importantes sur les raisons pour lesquelles ces textures semblent avoir un faible potentiel de conservation dans les

environnements naturels. Néanmoins, nous avons trouvé des échantillons naturels qui ressemblent à nos résultats expérimentaux dans une gamme de compositions de roches de différents environnements géologiques qui auraient pu se former soit par oxydation rapide via la phase fluide, soit par des bulles recueillant différents cristaux.

ABSTRACT

The mutual affinity between bubbles and oxide crystals (especially magnetite) is well established and their tendency to remain in contact once they become connected (either by nucleation of one upon the other, or by attachment) has led to models of oxide transport via bubbles in natural melts. However, despite the widespread acceptance of bubble-oxide association, there is little direct textural evidence for these processes. We present results from a series of decompression experiments on andesitic melts, during which aggregates of bubbles and oxides formed because of hydrogen loss through the capsule walls causing oxidation of the melt. Experimental charges were imaged using 3D X-ray computed tomography that revealed complex bubble + oxide aggregates, with small oxide crystals coating part of the outer bubble surfaces in a shell-like morphology. These shells have smooth inner and rugose outer surfaces. Sometimes additional concentric shells or partial shells can be found around bubbles, in the glass between the bubble wall and another shell. We quantified the volumes of bubbles and oxides and the oxides' compositions. We measured the surface area where the bubbles and oxides are in contact, thus quantifying their interface in 3D, and used these measurements to investigate the process of oxide shell formation. The complexity of the oxide textures when studied in 3D reveals a range of bubble-oxide interactions, from continuous generation, detachment and disintegration. These processes carry important implications on why such textures seem to have a low preservation potential in natural environments. Nevertheless, we have found natural samples that resemble our experimental results in a range of rock compositions from

different geological environments that could have formed either due rapid oxidation via the fluid phase or by bubbles harvesting different crystals.

4.1 Introduction

The major constituents of degassing silicate magmas are melt, crystals and gas bubbles. Each of these constituents individually provides valuable insights into magmatic evolution, such as the rate of nucleation and growth of crystals or bubbles. However, their interactions may be even more informative. Some of these interactions are well-studied, such as the homogeneous nucleation of crystals and bubbles within melt (a crystal-melt and bubble-melt interaction, respectively; e.g., Fenn, 1977; Kirkpatrick, 1977; Gonnermann and Gardner, 2013; Le Gall and Pichavant, 2016; Preuss et al. 2016). Crystal-bubble interactions in magmas have received less attention, yet they may influence a variety of magmatic processes from gas storage at depth, crystal flotation and heterogeneous nucleation (Edmonds, 2015; Shea, 2017; Pleše et al., 2018).

Most studies on crystal-bubble interactions focused on oxides (e.g. Hurwitz and Navon, 1994; Gardner and Denis, 2004). Edmonds et al. (2015) investigated the 2D spatial distributions of bubbles and oxides in basalt and andesite from Soufrière Hills volcano and revealed single point bubble-oxide contacts in the basalt, as well as multiple bubbles on larger oxide crystals, but no bubble-oxide association in the andesite. As bubbles and oxides exhibit a strong attachment force between them, they are considered to remain attached once they become connected, due to their very different chemical composition and bonding type (Mysen and Richet, 2005; Gualda and Ghiorso, 2007). This concept led to a recent model in which bubble-oxide pairs rise through a melt, harvesting more oxides and/or bubbles and facilitating a net transport of oxides towards the surface (Knipping et al., 2015; Edmonds, 2015). Few

observations of similar processes from natural rocks (e.g., Ballhaus et al., 2015) or experimental charges (e.g., Matveev and Ballhaus, 2002) have been put forward. These scenarios of oxide aggregation, concentration and transport have been developed based on several key findings (Knipping et al., 2015; Edmonds, 2015; Ovalle et al., 2018): 1) the existence of a single pre-eruptive bubble - multiple oxide aggregate in a natural sample, consisting of a large bubble with several smaller disconnected magnetite crystals on its surface (Gualda and Anderson, 2007), 2) the affinity of single bubble-oxide pairs in experiments (Shea, 2017; and references therein), and 3) the spatial distribution of sparse bubble-oxide associations in natural samples (e.g. Edmonds et al., 2015). If oxide flotation by bubbles is a viable process of oxide transport, and the attachment force between bubbles and oxides keeps them together, then why are such textures in natural degassing environments so easily overlooked?

One of the biggest obstacles in the study of bubble-crystal interactions is textural overprinting. The initial stages of texture development, and all the intermediate interactions that led to the final textures, are essentially obscured, so the exact processes behind bubble-oxide aggregate formation are not yet recognized in detail. This is especially troublesome for bubbles due to their ease of displacement in melts. Consequently, it is difficult to answer questions such as: will a bubble and a crystal attach? Will one or both change volume while attached? Under what conditions will they detach? Recent studies and advances in 4D in situ experiments have started to bridge the problem of overprinting by enabling observation of the development of a texture in real time (e.g., Bai et al., 2008; Baker et al., 2012; Voltolini et al., 2017; Pleše et al., 2018; Polacci et al., 2018), but there is still need for further research.

The aim of this study is to investigate the interactions between bubbles and oxide crystals in andesitic melts oxidized by hydrogen loss during decompression experiments, including the dynamics of nucleation and crystallization, bubble-oxide attachment and detachment, and aggregation. Our 3D reconstructions of experimentally decompressed melts reveal the early development of oxide-bubble aggregates, which are rarely preserved in natural systems. We compare our experimental observations with a review of natural structures from a range of geological environments and examine if they could have been produced by processes of bubble growth and magnetite crystallization.

4.2 Materials and methods

4.2.1 Hydrous glass synthesis

Hydrous andesitic glasses were synthesized in $Au_{75}Pd_{25}$-capsules in a piston-cylinder apparatus from a natural andesite crystalline rock powder (AT-29, 56.8 wt. % SiO_2; Baker and Eggler, 1987) after the addition of 12 wt. % H_2O (the only fluid added to the starting composition). These water amounts were chosen so that the experiments are water-undersaturated at the maximum pressure and temperature conditions but saturated at lower pressures (calculation based on model in Papale et al., 2006). Five to seven crushed crystal fragments were also added, of either plagioclase (An_{67}; Stewart et al., 1966), clinopyroxene (augite; Baker and Eggler, 1987) or amphibole (magnesio-hornblende; Murphy et al., 2000) of approximately 0.5-1 mm^3 per fragment, comprising on average 16 wt. %, 30 wt. % and 19 wt. % of the charge, respectively. These melt and crystal compositions were chosen to represent subduction related volcanism where andesitic melts carry phenocrysts (their exact chemical compositions can be found in Appendix 4.1). The capsules were welded shut while immersed in water and stored in a 110 °C furnace for 1 h to check for water loss. Only capsules whose weight did not change were used.

Sample synthesis and decompression experiments were performed using a piston-cylinder apparatus at McGill University (Montréal, Canada). The principle behind the piston-cylinder is that force is applied on the larger piston via oil pressure. The larger piston then pushes the smaller one that in turn pressurizes the assembly. The assembly is comprised of a metal capsule in a crushable alumina-pyrex-NaCl solid medium. Due to friction between different parts, from within the assembly to within

the entire apparatus, there is a difference between the nominal and the actual pressure. To perform a friction correction and convert from nominal to actual pressure, a comparison was made between the measured nominal pressure of a selected phase transition (in the piston-cylinder) and the measured actual pressure of the same transition (in another apparatus; Baker, 2004). The friction correction here is 50 MPa, and the pressure accuracy is ± 25 MPa (for more details the reader is referred to Baker, 2004).

Runs contained 2 or 3 capsules, each with a different added mineral phase. Capsules always contained only one mineral phase to avoid any crystal-crystal interactions. All experimental runs were isothermal at 1000 °C, and started at 650 MPa (p_1,) where they were held for 1 hour. The short time was used to prevent significant silicate crystal dissolution, and similar parameters were used in Baker (2004). The runs were then decompressed to a pressure p_2 (ranging from 600-300 MPa) for a duration of t_1 (Table 4.1). Decompression was performed by manually venting the piston-cylinder; there was no delay in decompressing. The decompression rates varied from 1.0 to 1.85 MPa s^{-1}. If we assume an upper crustal pressure gradient of 0.025 MPa m^{-1} (Dziewonski and Anderson, 1981), then our decompression rates correspond to 40-74 m s^{-1}, which falls within the 40-140 m s^{-1} ascent rates of Soufrière Hills late 1997 explosive eruptions (Druitt et al., 2002). Finally, the runs were held at p_2 for a duration t_2 before isobaric quenching. The oxygen fugacity (fO_2) of melts produced using the NaCl-crushable alumina-pyrex piston-cylinder assembly (Baker, 2004) is approximately 1.5 log units above the NNO buffer, NNO + 1.5 (Dalpé and Baker, 2000; Liu et al., 2007).

After quenching, the charges were removed from the capsules. The charges were not cylindrical due to non-uniform compression of the capsule during pressurization. During cooling the charges fractured within their capsules, so upon capsule opening, they scattered. The original orientation of the fragments with respect to the vertical is unknown. The largest fragment (~ 10 mm^3) retrieved from each charge was used for further analysis.

4.2.2 X-ray computed tomography

The largest fragment from each experimental charge (referred to as a sample hereafter) was initially imaged at the MIAM laboratory of McGill University (Montréal, Canada) using a Skyscan 1172 desktop X-ray tomography machine (Bruker, Belgium), with the aim of quickly obtaining medium-resolution 3D volumes (isotropic voxel size ~ 4 μm). The scans were reconstructed in 3D using the *NRecon* software (Skyscan, 2011; http://bruker-microct.com/next/NReconUserGuide.pdf). Two natural samples from Krafla (Iceland), that contained textures similar to our experimental ones, were also scanned by this machine for comparison with the experiments. The scanning conditions for all samples can be found in Appendix 4.2. Samples displaying interesting textural features were selected for high-resolution imaging at the GeoSoilEnviroCARS beamline of the Advanced Photon Source synchrotron (Illinois, U.S.A.; Rivers et al., 2004; Rivers et al., 2010). The X-ray beam was filtered to an energy of 25 keV, with an image pixel size set to 1.32 x 1.32 μm^2. We did not work in phase-contrast mode. The 3D reconstruction was performed with *tomoRecon* and no phase-retrieval algorithms were applied (Rivers, 2012; http://cars9.uchicago.edu/software/idl/tomography.html).

Table 4.1: Summary of experimental conditions during hydrous glass synthesis in a piston-cylinder apparatus. T = 1000 °C, p_1 = 650 MPa in all experiments. Charge # is the arbitrarily assigned number to charges in multiple charge experiments, to differentiate them. p_2 refers to the lower pressure to which the experimental run was decompressed, t_1 refers to how long it took to get from p_1 to p_2, and t_2 refers to how long the run was kept at p_2 before an isobaric quench was performed. Experiment 26 was isobarically quenched directly from p_1.

experiment #	charge #	crystal type	p_1 (MPa)	p_2 (MPa)	t_1 (sec)	decompression rate (MPa s^{-1})	t_2 (sec)
26	1	clinopyroxene	650	650	0	0	0
	3	plagioclase					
14	1	clinopyroxene	650	600	25	1.85	300
15	1	plagioclase	650	600	30	1.6	300
	2	amphibole					
20	1	clinopyroxene	650	600	50	1.0	30
	2	amphibole					
17	1	clinopyroxene	650	300	300	1.22	5
	2	amphibole					
21	2	clinopyroxene	650	300	195	1.8	0
23	2	amphibole	650	300	210	1.62	0
24	2	plagioclase	650	300	220	1.55	0
25	2	plagioclase	650	300	220	1.6	0
27	1	plagioclase	650	300	210	1.65	5

4.2.3 Volume segmentation, visualization and measurements in 3D

All high-resolution scans were examined in detail for bubbles and oxides in contact with one another. Oxides were segmented in 3D by manually adjusting the threshold values (215-255 for oxides) on 8-bit volumes using the image-processing package *Fiji* (Schindelin et al., 2012). The subvolumes of interest had to include the entire bubble and all oxides connected to it. Since each subvolume contained not only oxides in contact with a bubble, but also oxides within silicate crystals (e.g. amphibole) and solitary oxides scattered within the melt, a combination of voxel size filters in the *Pore3D* software library (Brun et al., 2010: https://github.com/ElettraSciComp/Pore3D), manual segmentation and 3D masking were used to segment only oxides in contact with bubbles. Quantitative analyses in *Pore3D* (*Basic* and *Blob Analyses* modules) were then performed to obtain the number and volume of these oxides.

Bubbles in contact with oxides that were located at sample centers (i.e. not at sample borders and so not potentially in contact with the capsule wall), were segmented by an automatic binarization process applied to 8-bit volumes in the *Fiji* software (threshold values of 0-105), since their volume was surrounded by either melt or oxides. Bubbles located at the sample borders were segmented using the same threshold values, however because part of their volume was in contact with the air surrounding the sample during tomographic analysis, their volume had to be manually closed to create a partial bubble volume. For each bubble, the volume of the equivalent sphere was measured by means of *Pore3D* software, from which the bubble radius was calculated. *Avizo Fire*® (Visualization Sciences Group) was used to merge the

segmented oxide and bubble volumes in 3D and visualize them. For border bubbles with a partial volume, a sphere was created by the same software and was then scaled to fit within the real partial bubble volume. This allowed us to obtain ideal bubble volumes and measure their volume and radius, to be used in further geometrical calculations. Ideal bubble volumes were used instead of real partial volumes because we were interested in the morphological relations between bubbles and oxides, not between bubbles and melt.

To determine the surface area of bubbles in contact with oxides, the morphology of the oxides needs to be considered. The oxides form either a spherical cap or a spherical lune (Figure 4.1), where a spherical lune is a sliver of a sphere's surface, defined by two 2D sections passing through the sphere's radius (Harris and Stöcker, 1998). Two different 3D measurements were done, depending on the oxide morphology. The surface area of spherical oxide caps (the most common morphology) was calculated from (Heath, 1987) in Equation 17: $S_{cap\ w/o\ base} = 2 \times \pi \times r_{bubble} \times h$ (17), where r_{bubble} is the bubble radius and h is the height of the spherical cap. r_{bubble} was extracted by *Pore3D* or the fitted sphere volume, and h was measured as the distance between two parallel 2D sections, oriented in 3D by *Avizo Fire*® so that one passes through the base of the spherical cap and the other through its highest point. Where the morphology of the oxides in contact with a bubble more closely resembled a spherical lune, two 2D sections were located in 3D so that both passed through the bubble's (or fitted sphere's) centre and encompassed the oxides. The angle (α) between these 2D sections was measured in the quadrant where the oxides were located and used to calculate the spherical surface area of the lune (S_{lune}, Harris and Stöcker, 1998) using Equation 18: $S_{lune} = 2 \times (r_{bubble})^2 \times \alpha$ (18).

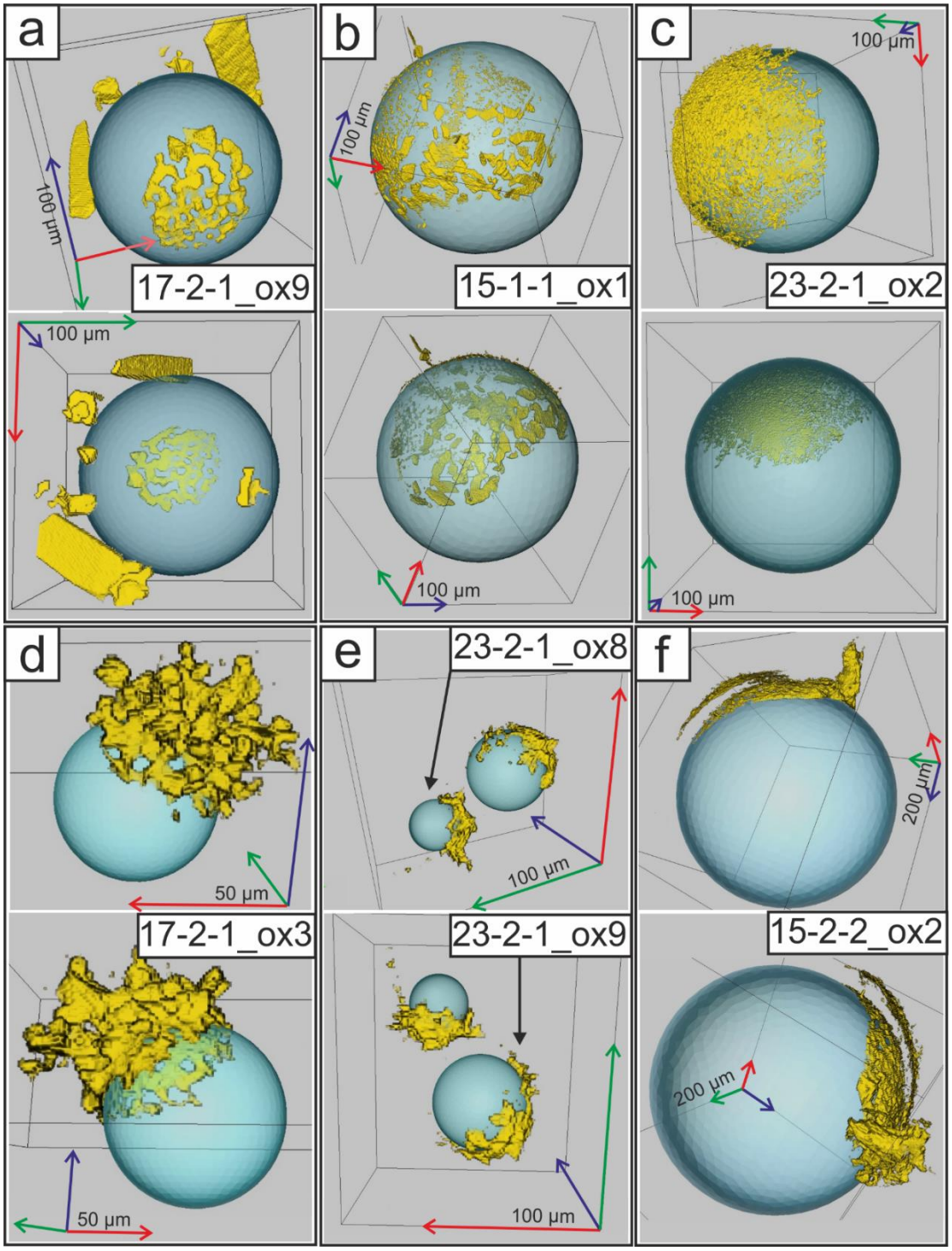

Figure 4.1: 3D visualization of 7 different bubble-oxide aggregates. Bubbles are shown as transparent blue spheres, oxides are shown in yellow, and each aggregate is shown from two different orientations (two images for each aggregate). The arrow

lengths of the 3D scales are the same in all 3 directions. a) A bubble is in single-point contact with 2 tabular and 2 non-tabular oxide crystals, and it also has a small oxide spherical cap. b) A bubble has a spherical cap consisting of small oxides and tabular oxides. c) A bubble has a well-interconnected oxide spherical cap with a pronounced rugose outer surface. d) The bubble has a spherical shell with an extremely rugose outer surface. Oxides spread equally along the bubble's surface and outwards from it. e) Two bubbles have oxide shells facing the same direction. Aggregates 23-2-1_ox9 (larger) and 23-2-1_ox8 (smaller) are shown together due to their proximity in the sample. f) A bubble has two oxide layers in its shell. The layers are positioned one above the other, separated by melt, but in contact at the far-right side of the oxide cap. Both layers have a smooth inner and rugose outer side and they share the bubble's curvature.

4.2.4 Scanning electron microscopy

To obtain high-resolution 2D images and to ascertain the semi-quantitative chemical composition of the oxides in the experimental charges, samples from five experiments with the most interesting features were scanned at McGill University, using a Hitachi SU5000 Scanning electron microscope (SEM) with an Oxford X-MAX80 Energy-Dispersive X-Ray Spectroscopy (EDS) detector and applying an accelerating voltage of 15 kV and 0.134 mA beam current. Special care was taken to grind the sample only to a target slice (known from the 3D reconstructions) where the oxide structures were located. Two natural samples from Krafla that exhibit similar oxide structures to those seen in the experiments were also analyzed for comparison. Semi-quantitative EDS analyses were performed using the *Aztec* 3.3 software (Oxford Instruments).

4.3 Results

4.3.1 Appearance of samples and bubble-oxide aggregates within them

The samples are glassy, with silicate and oxide crystals and bubbles. The silicate crystals are rounded, and exhibit channels filled with glass, due to their partial melting at high pressure and temperature conditions (Figure 4.2 a). Amphibole has the largest number of such channels and they intrude furthest into the amphibole crystals (Figure 4.2 a). Oxide crystals vary in size and location; they occur (in order of increasing relative abundance) dispersed in the glass, as inclusions within silicate crystals (the largest 0.0012 mm^3), on bubble surfaces and along sample borders (ranging from 0.62 x 10^{-7} to ~ 2.78 x 10^{-6} mm^3, Figure 4.2 a). Bubbles also vary in size, with the largest on the sample borders (~ 1 mm^3) and smaller ones within the glass (~ 0.004 mm^3, Figure 4.2 a). Solitary oxide crystals dispersed in the glass did not form part of the quantitative calculations. Bubble-oxide aggregates have been found in both zero-time experiments with no decompression and in experiments with different decompressions (Table 4.1). Here we concentrate solely on bubble-oxide aggregates, so data regarding bubble distribution, overall sample porosity, the relationship between bubbles and silicate crystals, and between bubbles and melt, is discussed in Chapter 3).

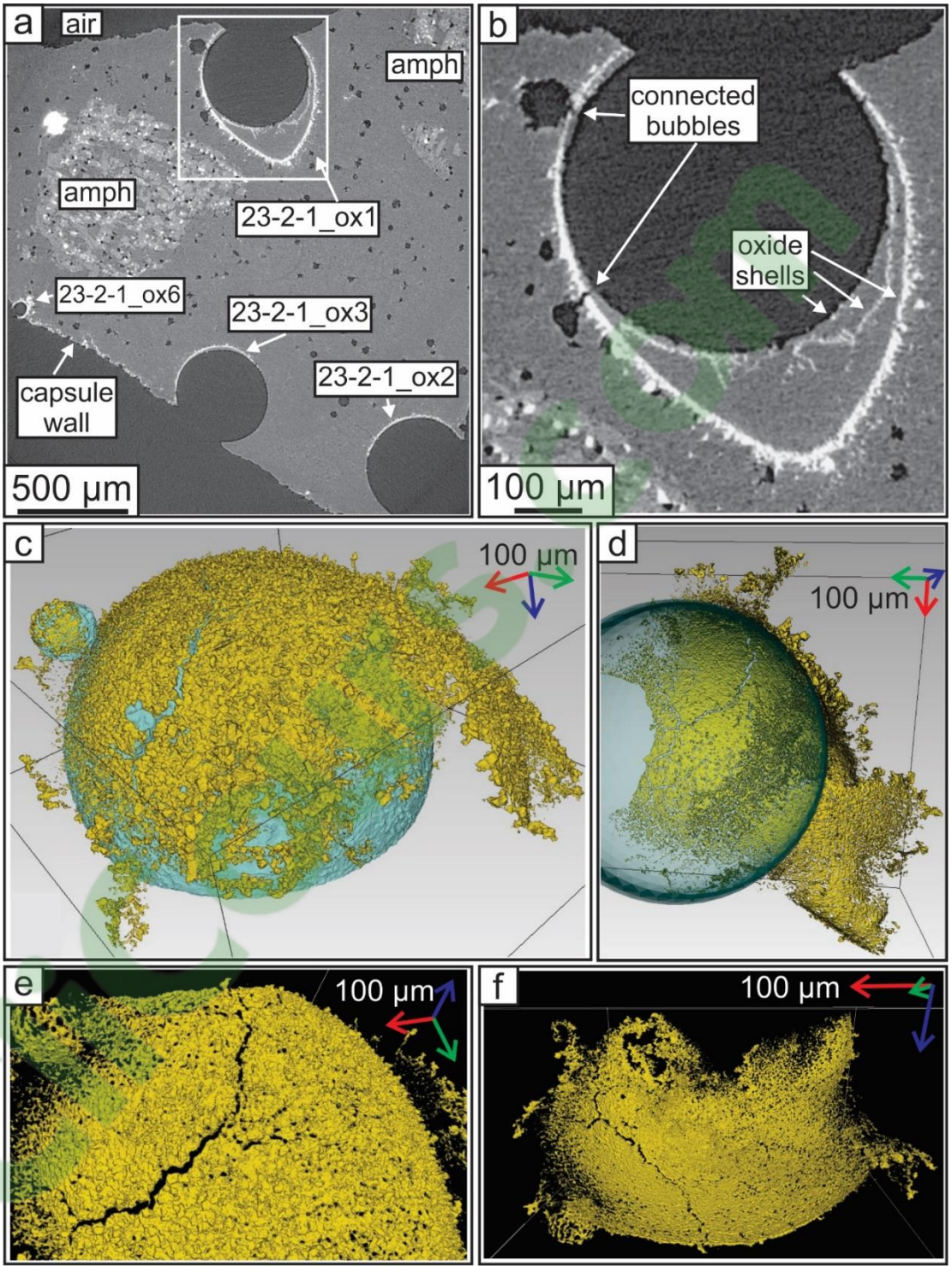

Figure 4.2: 2D and 3D visualization of bubble-oxide aggregate 23-2-1_ox1. a) 2D section from the 3D volume, showing four different bubble-oxide aggregates and 2 amphibole (amph) crystals. Bubbles and air are shown in black, amphiboles in light

grey, silicate glass in dark grey and oxides in white. b) Magnified section of the white rectangle from image a), showing only aggregate 23-2-1_ox1. The largest bubble is connected by narrow necks to two smaller bubbles. Three nested oxide shells are visible. c, d) 3D volume renderings of 23-2-1_ox1, where the bubble is shown in blue and the oxide shell in yellow. The complex morphology of the shell includes a crack, through which the smallest bubble is connected, many apertures, a larger connected bubble, and a tear. In d) the inner smooth surface of the shell is visible, and a large portion of the shell (lower right) is detached from the bubble surface. e, f) 3D volume renderings of the oxide shell against a dark background. Cracks, apertures, the rugose outer surface, smooth inner surface and folding of the shell are all visible.

We define a bubble-oxide aggregate as a single bubble in contact with multiple oxide crystals (Figures 4.1 and 4.2). Bubbles in contact with a single oxide crystal were not considered, since they form a pair and not an aggregate, and accidental contact between bubbles and oxides cannot be excluded in this case. If a bubble with an oxide spherical cap or lune was also in contact with an additional single oxide crystal, then that single-point contact was only qualitatively considered. Ten experiments yielded bubble-oxide aggregates (Table 4.2). In total, 50 bubble-oxide aggregates were examined. Most bubble-oxide aggregates are located at the sample borders (i.e. on the capsule wall), but 20% of the aggregates were completely within the sample (Table 4.2). Bubbles that line the capsule wall are here referred to as ″fringe″ bubbles (see Mangan and Sisson, 2000; Gardner and Ketcham, 2011). Aggregates were named following the convention A-B-C_oxD, where A is the experiment number, B is the capsule within that experiment, C is the identity of the sample piece retained from that capsule, and D is the bubble-oxide aggregate identified within that sample piece. The 50 aggregates identified differ in volume, location, configuration and complexity between and within capsules, but all share the same basic structure of a bubble with an outer surface covered by oxide crystals. The bubbles vary in volume, but they are always larger in volume than their associated oxide shells. Whether the shape of the shell was a cap or a lune is not related to the aggregate's position within the sample.

Table 4.2: Summary of the selected geometrical parameters obtained from 3D measurements of bubble-oxide aggregates. r_{bubble} and V_{bubble} are the bubble radius and volume, respectively. The location of the aggregates is either the interface between the melt and the capsule or the center of the sample. For bubbles on the capsule wall, r_{bubble} is the fitted sphere radius, and V_{bubble} is derived from that radius. Oxide clusters refers to the number of isolated oxide crystal accumulations on the bubble wall. V_{oxide} is the total volume of all oxide crystals on the bubble surface. A_{oxide} is the surface area of the bubble in contact with oxides.

Aggregate name	Bubbles			Oxides		
	r_{bubble} (mm)	V_{bubble} (mm^3)	location	oxide clusters	V_{oxide} (mm^3)	$A_{oxide\ on\ bubble}$ (mm^2)
14-1-1_ox2	0.32000	0.13725	border	1	0.00040	0.22817
14-1-2_ox1	0.34987	0.17939	border	25	0.00053	0.13401
15-1-1_ox1	0.18683	0.02731	border	79	0.00031	0.19266
15-2-1_ox1	0.51288	0.56511	border	1	0.00122	0.32155
15-2-1_ox2	0.47783	0.45699	border	1	0.12857	0.37068
15-2-2_ox1	0.51506	0.57237	border	1	0.00580	0.29155
15-2-2_ox2	0.51264	0.56432	border	1	0.00574	0.42015
17-1-1_ox1	0.62941	1.04446	border	4	0.00153	0.61039
17-2-1_ox1	0.08000	0.00214	center	1	0.00013	0.01676
17-2-1_ox2	0.04811	0.00046	border	13	0.00002	0.00767
17-2-1_ox3	0.03684	0.00020	border	1	0.00008	0.00703
17-2-1_ox4	0.02246	0.00004	center	1	0.00005	0.00258
17-2-1_ox5	0.11496	0.00636	center	12	0.00012	0.03239
17-2-1_ox6	0.56012	0.73610	border	1	0.00224	0.24323
17-2-1_ox7	0.04227	0.00031	border	1	0.00007	0.00980
17-2-1_ox8	0.10431	0.00475	center	8	0.00012	0.00000
17-2-1_ox9	0.09461	0.00354	center	9	0.00016	0.02126
17-2-1_ox10	0.06574	0.00119	center	1	0.00028	0.01767
17-2-2_ox1	0.68163	1.32663	center	1	0.00238	0.23437
17-2-2_ox2	0.36834	0.20934	border	5	0.00560	0.40958
20-1-1_ox1	0.29737	0.11015	border	72	0.00085	0.12106
20-1-1_ox2	0.05158	0.00057	border	1	0.00341	0.00965
20-1-2_ox1	0.09846	0.00399	center	58	0.00031	0.02577
20-2-1_ox1	0.06032	0.00091	border	9	0.00035	0.02690
20-2-1_ox2	0.07582	0.00182	border	1	0.00025	0.01605
20-2-1_ox3	0.53652	0.64692	border	73	0.00966	0.00000
21-2-1_ox1	0.29712	0.10988	border	13	0.00072	0.14514
21-2-1_ox2	0.46128	0.41114	border	350	0.00101	0.31782
23-2-1_ox1	0.33237	0.15380	border	1	0.00659	0.47192
23-2-1_ox2	0.26804	0.08067	border	1	0.00101	0.22562

23-2-1_ox3	0.19677	0.03191	border	1	0.00116	0.18097
23-2-1_ox4	0.02124	0.00004	border	1	0.00005	0.00339
23-2-1_ox5	0.02798	0.00009	border	1	0.00006	0.00571
23-2-1_ox6	0.05969	0.00089	border	3	0.00019	0.02069
23-2-1_ox7	0.03077	0.00012	center	15	0.00001	0.00245
23-2-1_ox8	0.03085	0.00012	border	3	0.00003	0.00379
23-2-1_ox9	0.01753	0.00002	border	14	0.00002	0.00179
23-2-2_ox1	0.05598	0.00073	border	1	0.00028	0.00871
23-2-2_ox2	0.21715	0.04289	border	1	0.00643	0.25968
23-2-2_ox3	0.28562	0.09760	border	10	0.00283	0.20057
23-2-2_ox4	0.10751	0.00520	border	1	0.00016	0.01414
23-2-2_ox5	0,06627	0.00121	border	1	0.00010	0.00799
23-2-2_ox7	0.06278	0.00103	border	6	0.00007	0.00433
23-2-2_ox8	0.04384	0.00035	border	3	0.00004	0.00066
24-2-1_ox1	0.85803	2.64609	border	1	0.00040	0.13463
24-2-1_ox2	0.34059	0.16550	border	1	0.00030	0.12889
25-2-1_ox1	1.15736	6.49369	border	873	0.00280	1.05949
26-1-1_ox1	0.29034	0.10252	border	1	0.00010	0.08451
26-3-1_ox1	0.74853	1.75680	border	1	0.00839	0.43323
27-1-1_ox1	0.01875	0.00002	center	1	0.00002	0.00169

The bubbles and their oxide shells can be in complete or partial contact. We observed three distinct configurations:

1) Complete bubble - oxide shell contact

   In this configuration on average 22 % (ranging from 1.5 to 60%, Figure 4.3 b) of the bubble's outer surface is coated with oxide crystals (Figure 4.1 b-g). The oxide shell is not uniform in thickness and commonly has small apertures (~ 6 μm in diameter). The inner (bubble) side of the shell is smooth and follows the bubble's curvature. The outer (melt) side is uneven and rugose, with features such as small skeletal-like extensions (~ 25 μm in length) projecting into the melt (Fig. 1d). The bubble-shell-melt contact lines are uneven in all aggregates. In some cases (e.g. 14-1-2_ox1 and 17-2-1_ox2), the bubbles had more than one oxide accumulation on their surface (oxide clusters) that were not connected to each other (Figure 4.1 a, Table 4.2).

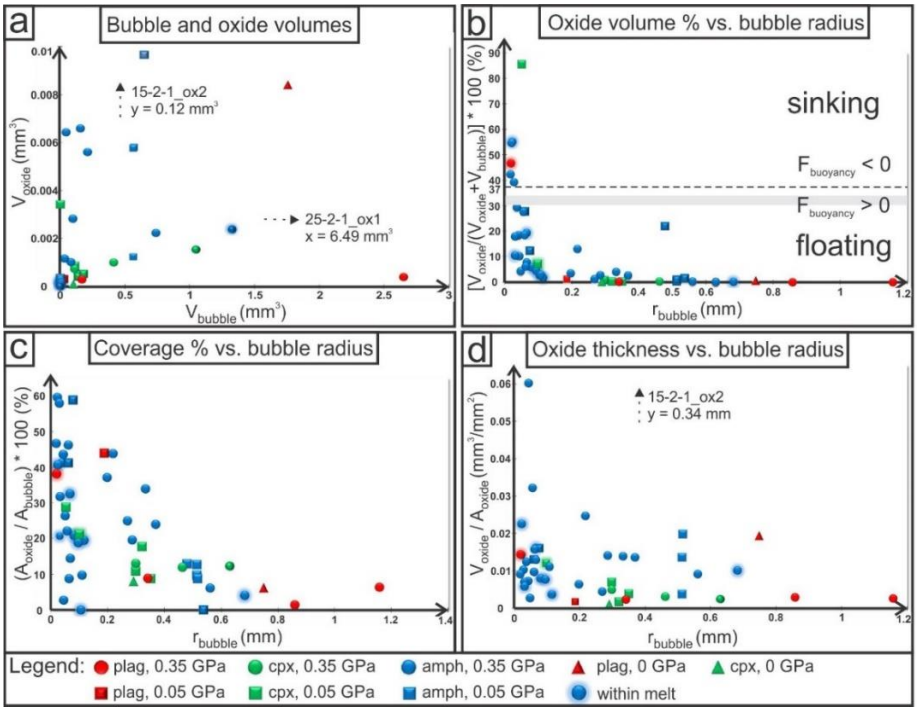

Figure 4.3: Plots of geometrical data for bubble-oxide aggregates. The solid phases in the experimental charge were plagioclase (plag, in red), clinopyroxene (cpx, in green) or amphibole (amph, in blue). Symbols represent different decompression drops: circles for 0.35 GPa, squares for 0.05 GPa and triangles for 0 GPa. A corona around a symbol highlights bubble-oxide aggregates found completely within the melt. No bubbles examined were attached to silicate crystals or were without oxide shells. The direction of an outlier location is indicated with an arrow, along with the aggregate name and the missing coordinate. a) Total volume of all oxides in the shell vs. bubble volume. b) Volume percentage of oxides in an aggregate vs. bubble radius. The neutral buoyancy criteria is located at 37 vol. % oxides (Knipping et al., 2015), and the grey line represents the neutrally buoyant oxide 34 – 30 vol. % range in our samples (at 650 and 300 MPa, respectively). c) Oxide shell coverage of bubbles vs. bubble radius. d) Mean oxide thickness (ratio of the total oxide volume and the area the oxides occupy on the bubble surface) vs. bubble radius.

2) Partial bubble – oxide shell contact

Here, aggregate shells are only partially in contact with the bubble's outer surface (Figure 4.1 f, Figure 2 a-d). The shells exhibit a smooth inner and rugose outer surface morphology as in group 1, both on the parts of the shell in contact with, and away from, the bubble, as well as a range of other features including cracks, tears, folds and swirls (Figure 4.1 f, Figure 4.2 c-f). We here define a crack as an elongated aperture in the oxide shell along which the shell has split but has not separated into separate parts, and a tear as a split where the separation has begun. Regions of the shell that are furthest from the bubble are more strongly swirled and folded and have less interconnected oxide crystals. In four cases (15-2-2_ox2 in Figure 4.1 f, 23-2-1_ox1 in Figure 4.2 a, b, 17-2-1_ox6, 23-2-1_ox6) the space between the bubble surface and the disconnected part of a shell is occupied by a second smaller and thinner oxide shell. Aggregates 15-2-2_ox2, 17-2-1_ox6 and 23-2-1_ox6 contain two such shells. In the case of 23-2-1_ox1, there are three shells in total (Figure 4.2 b), with the inner shells becoming progressively thinner and with less skeletal growths. The outer shell also has larger individual oxide crystals than the inner ones.

3) Additional single-point bubble – oxide crystal contacts.

Some bubbles with oxide shells were also in contact with single oxide crystals (Figure 4.1 a, b). These individual oxide crystals are tabular with different orientations. These configurations were less common and so different from the aggregates that we excluded them from oxide shell volume and bubble-oxide surface coverage calculations.

In some bubble-oxide aggregates (17-2-1_ox2, 23-2-1_ox1, 23-2-1_ox6), smaller bubbles occur in contact with the rugose outer surface of the shell. These bubbles are connected to the larger bubble on the opposite (concave) side of the oxide shell via a thin neck that passes through an aperture in the oxide shell (Figure 4.2 b). The cross-sectional diameter of the neck is the same size as the shell aperture diameter. Some of the more spherical of these bubbles also have an oxide shell of their own (Figure 4.2 c).

4.3.2 Morphological parameters of bubble-oxide aggregates

The volumetric parameters obtained for bubbles and for oxides comprising an aggregate, and the aggregate parameter that takes both into account are presented in Table 4.2. Further morphological aggregate parameters are presented in Figure 4.3.

The morphological data for bubble-oxide aggregates were examined in several different ways (Figure 4.3). Bubble-oxide aggregates are most common in amphibole-bearing charges (70%, or 35 aggregates from 4 samples), less common in clinopyroxene-bearing charges (18%, or 9 aggregates from 5 samples) and least common in plagioclase-bearing ones (12%, 6 aggregates from 5 samples). The aggregates in plagioclase-bearing charges display the greatest variability in their morphology, while those in clinopyroxene-bearing charges are the most uniform. Since most aggregates are from amphibole-bearing charges, their distribution defines the trends in Figure 4.3. One disadvantage of the comparison in Figure 4.3 a is that the data are clustered at small volumes. Hence, we favor the use of the bubble radius as

the independent variable as oxide shell volume and oxide coverage could change with bubble growth (Figure 4.3 b-d).

The volumetric ratio between the bubble and oxides within an aggregate controls the aggregate's buoyancy. The dependence of the volume percentage of oxides in an aggregate on the size of that aggregate's bubble demonstrates that the larger the bubble, the smaller the volume fraction of oxides comprising the aggregate (Figure 4.3 b). The horizontal dashed line at 37 vol. % of oxides in a bubble-oxide aggregate represents the border between positively (< 37 vol. %) and negatively (> 37 vol. %) buoyant aggregates in andesitic melts under similar conditions, using the density values given in Knipping et al. (2015). Equation 19 states:

$$V_{bubble}/V_{magnetite} = (\rho_{magnetite} - \rho_{melt})/(\rho_{melt} - \rho_{bubble}) \quad (19),$$

where $V_{bubble} = 1 - V_{magnetite}$, $\rho_{magnetite} = 5.2$ g cm^{-3}, $\rho_{melt} = 2.27$ g cm^{-3} (Ochs and Lange, 1999) and $\rho_{bubble} = 0.51$ g cm^{-3} for 1000 °C and 200 MPa (Knipping et al. 2015; Pitzer and Sterner, 1995; Driesner, 2007). In our case, $\rho_{magnetite}$ remain the same, but $\rho_{melt} = 2.07$ g cm^{-3} (Lange and Carmichael, 1987; Ochs and Lange, 1997) and $\rho_{bubble} = 0.67$ g cm^{-3} for 1000 °C and 650 MPa, $\rho_{bubble} = 0.45$ g cm^{-3} for 1000 °C and 300 MPa (using the modified Redlich-Kwong equation of state of Holloway, 1987, for 650 and 300 MPa calculations). Our fluid density calculations are lower at a higher pressure, compared to Knipping et al. (2015), probably due to the low estimated concentrations of Fe and Cl in the fluid (cf., Eggler, 1987 in Menzies and Hawkesworth, 1986) which were omitted in our density calculations. For the pressure values of 650 and 300 MPa we obtained 34 and 30 vol. % magnetite, respectively, and the range is shown on Figure 4.3 b with a grey line.

The volume percent of oxides in a bubble-oxide aggregate can be used as a discriminant between the aggregate's floating and sinking because it considers the entire aggregate, not just one phase within it. Additionally, we see that the oxide vol. % required for neutral buoyancy decreases as the pressure decreases. In our experiments only six aggregates have more than 35 vol. % oxides (Figure 4.3 b).

The dependence of oxide coverage (i.e. how much of the bubble's surface is covered in oxides) on the bubble size shows that as the bubble grows the fractional oxide coverage shrinks, i.e. small bubbles are more fully covered by oxides than larger bubbles (Figure 4.3 c). The oxide shell thickness on bubbles ranges between 0.002 and 0.02 mm and does not appear to be correlated with the bubble radius.

4.3.3 SEM analysis of experimental charges and natural samples

Semi-quantitative SEM-EDS (Figure 4.4) was used to determine the chemical composition of silicate glasses and oxides. The amphibole-bearing charges have the highest average FeO_{TOT} content in the glass, 5.34 wt. %, compared to 3.22 wt. % in clinopyroxene-bearing and 3.96 wt. % in plagioclase-bearing charges (Appendix 4.1). Three different oxide groups within the experimental charges: oxides within silicate crystals (mainly amphibole), solitary oxides within melt (glass) and oxides that form shells on bubble walls. The glass remained andesitic and the oxides are Fe-Ti oxides; the semi-quantitative compositions are in Appendix 4.1. The chemical compositions and octahedral morphologies of the oxide crystals imply oxides are magnetites. The three oxide groups are clearly distinguished by their TiO_2 contents: oxide inclusions within amphibole have the highest TiO_2 contents (9.7 to 18.5 wt. %), solitary melt

oxides intermediate (4.7 to 7 wt. %) and the shell oxides the lowest content (2.3 to 4.2 wt. %). When there are several oxide shells around a bubble, their composition is the same.

The glass was analyzed to investigate if there is any difference in major element compositions adjacent to the silicate crystals caused by partial melting of silicate crystals. No evidence for compositional heterogeneity of the melt was observed (compositional data is in Appendix 4.1).

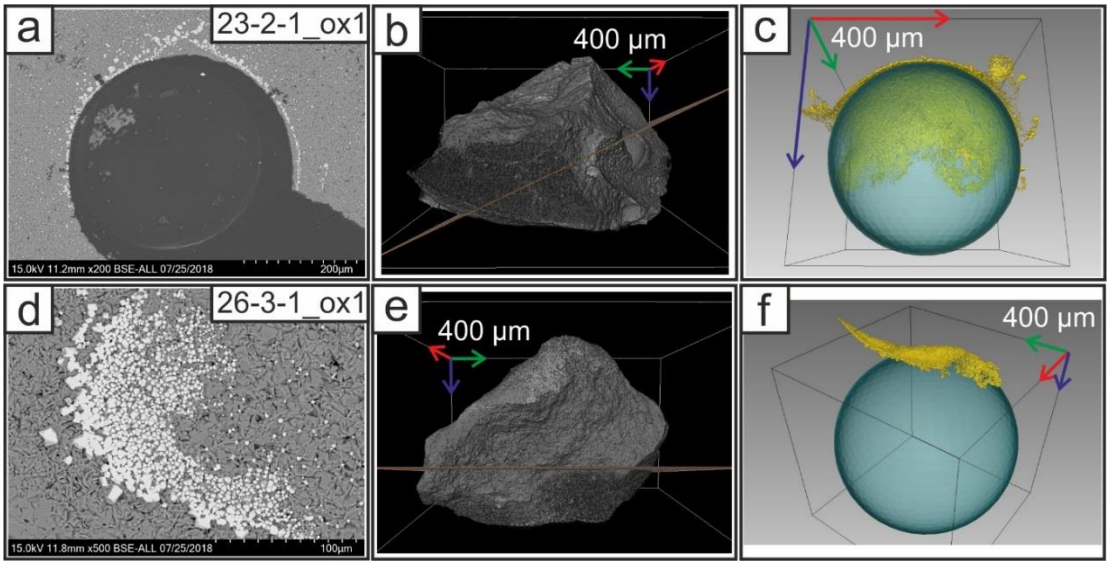

Figure 4.4: Selected SEM (2D) and tomographic (3D) images for two experimental samples. a) SEM image of aggregate 23-2-1_ox1. Oxides are present directly on the bubble surface. b) A 3D visualization of sample 23-2-1, on which the location of the 2D plane on which the SEM analysis was performed, is indicated. The portion of the sample above this plane has been ground away for SEM analysis. c) A 3D visualization of aggregate 23-2-1_ox1. The bubble is shown in blue and the oxide shell in yellow. d) A SEM image of aggregate 26-3-1_ox1. A portion of the oxide shell that detached from the (fringe) bubble is visible, along with the lack of complete oxide crystal cohesion. e) 3D visualization of sample 26-3-1, with the location of the 2D section. f) 3D visualization of the bubble-oxide aggregate. A large portion of the oxide shell has detached from the bubble's surface.

4.4 Discussion

Our experiments clearly show the formation of oxide crystal aggregates on the outer surfaces of bubbles in a hydrous, crystal-bearing andesitic melt. We observed bubble-oxide aggregates in experiments with and without decompression, with no difference in their morphology. We provide evidence supporting recent models invoking the role of bubbles as major oxide carriers (Knipping et al., 2015; Edmonds, 2015; Ovalle et al., 2018) and offer new insights into the association and complex dynamics between bubbles and oxide crystals. Here we discuss: i) How the oxide accumulations formed and what processes could have produced their features, ii) Why these types of bubble-oxide features have not been observed before, and iii) Which natural structures may have formed in a similar way.

4.4.1 Snapshots of dynamic processes from experimental charges frozen in time

4.4.1.1 Potential harvesting of oxides originating from the melt or the amphiboles

Harvesting of oxides by bubbles is considered by many authors to be the main method of oxide accumulation on bubbles and subsequent transport in natural melts (Knipping et al., 2015; Edmonds, 2015; Ovalle et al., 2018), so it is worth examining whether harvesting could have occurred in the experiments. By harvesting, we mean the process of attachment of a pre-existing oxide to a pre-existing outer bubble wall. For oxide harvesting to occur, oxides must be present in the melt and the bubble walls must move with respect to the melt via bubble growth or buoyant rise.

Bubbles with oxide shells in our samples display a range in size (Figure 4.3), thus implying that bubbles were growing during decompression. Since there are solitary oxide crystals within the melt, the bubbles could have harvested them during growth. Sample edges, where the melt was in contact with the capsule, are lined with solitary disconnected oxide crystals and are also the location of the largest bubbles, which likely nucleated heterogeneously on imperfections of the AuPd-capsule wall (Figure 4.2 a). The larger size of the fringe bubbles likely reflects degassing of melt in the interior of the capsule by water diffusion into the fringe bubbles (Mangan and Sisson, 2000). There is no evidence of fringe bubble movement through buoyancy or melt convection. If fringe bubbles moved along the capsule wall, we would expect more oxides on their advancing side (and that would indicate the ″up″ direction). Since we do not observe this, we assume they stayed in place.

Most bubble-oxide aggregates, as well as the largest and most elaborate oxide shells, were found in samples containing amphibole (Figure 4.3) and these samples also contain the highest average FeO_{TOT} wt. %. Amphibole crystals exhibit more melting than the other crystals in our experiments and contain more oxide inclusions (already present in the amphiboles prior to our experiments; Figure 4.2 a) than the plagioclase and clinopyroxene crystals (in their respective charges). The partial melting of amphiboles (at maximum p and T) increased the FeO and MgO content of the melt (to 5.5 and 2.2 wt. %, respectively) compared to the melt in plagioclase and clinopyroxene-bearing charges (to 3.96 wt. % FeO and 0.8 wt. % MgO in plagioclase-bearing, 3.22 wt.% FeO and 0.9 wt.% MgO in clinopyroxene-bearing charges, Appendix 4.1), where crystals melted much less. Consequently, most aggregates are found in amphibole-bearing charges.

During partial melting of the amphiboles, their oxide inclusions could have become incorporated into the melt. Since our 3D imaging took place after the experiments were completed, we cannot rule out that this process was a source of the oxides that were then harvested by growing bubbles. However, firstly, if this was the case, we would expect the melt around the amphiboles to contain some solitary oxides and a greater abundance of bubble-oxide aggregates around the amphibole; we see neither of these features. Secondly, the oxides that remained within the amphibole display a range in size, and some are much larger than the oxides comprising the shells (Figure 4.2 a). Thirdly, if amphibole was the main source of oxides, we would not expect to see bubble-oxide aggregates in samples containing plagioclase or clinopyroxene. Fourthly, there is a difference in Ti content in the oxides within the amphibole, within the melt and on the bubble surface. Fifthly, harvesting would not produce such a smooth inner and rugose outer shell surface, but instead both surfaces would be at least somewhat rugose, due to the random orientation of the harvested oxides towards the bubble surface. We thus conclude that harvesting of oxides originating from the amphiboles or crystallized from the melt was not the main process responsible for the generation of oxide shells.

4.4.1.2 *In situ* crystallization of oxides on bubble walls

If crystal harvesting was not significant, then oxides must have crystallized at the bubble-melt interface. Hence, we must examine the argument for *in situ* oxide crystallization as the dominant mechanism for production of the oxide shells.

Gualda and Anderson (2007) have suggested that crystallization of magnetite on bubble walls could occur in natural melts. At 1000 °C, hydrogen diffuses through the AuPd-capsule wall much faster than oxygen (Jakobsson, 2012). This loss of hydrogen forces the reaction $H_2O \Leftrightarrow H_2 + ½ O_2$ to the right hand-side to preserve equilibrium, thus prompting the dissociation of water molecules within the melt and an increase of oxygen fugacity. Consequently, the melt near the capsule wall becomes locally oxidized, which prompts the precipitation of magnetite. The crystallization of FeTi-oxides in our andesitic samples most likely caused a slight local change in fO_2 by fixing oxygen in their crystal lattice (Lange and Carmichael, 1996), but fO_2 should still be very close to NNO + 1.5 (Dalpé and Baker, 2000; Liu et al., 2007).

The bubble wall represents the interface between the bubble and the melt. As the bubble grows, and H_2O from the melt diffuses through the bubble-melt interface, the melt around it becomes oxidized and supersaturated in magnetite components. This prompts the crystallization of magnetite, more likely on the bubble wall than near it, since heterogeneous nucleation (on a surface) is energetically favored over homogeneous nucleation within the melt (Hurwitz and Navon, 1994). The nucleation of different silicate mineral phases on bubble walls has already been reported (e.g., plagioclase, Applegarth et al., 2013; amphibole and plagioclase, Rooyakkers, et al. 2018), so the process should be applicable to an oxide phase such as magnetite, in both experimental and natural environments.

A further argument for *in situ* crystallization is the morphology of the oxide shells; their smooth side faces the bubble and the rugose side containing skeletal growths faces the melt. The position of the skeletal growths and the detached shell parts points unequivocally to the shell occupying the outer side of the bubble and

originating from the melt. If it were otherwise (on the inner bubble side), the skeletal growths would be facing inward, towards the center of the bubble. The shell itself could then also not detach since that would require the oxides to cross from within the bubble into the melt, breaking the bubble's surface and surpassing its surface tension. This scenario is energetically unfavorable and therefore unlikely.

Figures 4.3 b and 4.3 c show that bubbles with a radius from 0.05 to 0.4 mm have either more voluminous shells, or larger fractional shell coverage compared to larger bubbles. The former could indicate that after an initial spreading of oxides on the bubble surface, oxide outward growth towards the melt becomes more favorable. If the spreading mechanism was harvesting, we would expect a linear dependence between the bubble volume and oxide volume in Figure 4.3 a, or between the bubble radius and oxide thickness in Figure 4.3 d, and that is not the case. Thus, this points to oxide *in situ* crystallization. The fact that the oxide volume percentage decreases as the bubble becomes larger (Figure 4.3 b) could be because oxides form a 2-dimensional shell around a 3-dimensional bubble. This could also explain the lack of correlation between the oxide thickness and bubble radius (Figure 4.3 d). As the mean thickness of the oxide rims remains approximately constant (Figure 4.3 d), the outward growth must mainly occur as narrow skeletal crystals or by the generation of new shells. Both increase the oxide volume without increasing the oxide coverage.

4.4.1.3 Bubble breakup via daughter bubble generation through an oxide shell aperture

The connected bubbles seen in aggregates 23-2-1_ox1 (Figure 4.2 b, c) and 17-2-1_ox2, have not yet been reported in geological environments to our knowledge. We cannot envision a scenario where two bubbles would coalesce by forming a neck through the oxide shell, since creating such a shape would necessitate energy consumption, so we infer that this instead reflects bubble breakup. We see no similarity to spanning clusters of bubbles (Candela, 1991). The larger bubble facing the smooth concave inner oxide shell side is the primary, or "parent", bubble, and the smaller bubble on the rugose, convex, outer side of the shell is the newly generated secondary, or ″daughter″ bubble. Here we chose the term daughter bubble to emphasize the connection between the two bubbles, and so we will refer to this bubble breakup scenario as daughter bubble generation. Bubbles found in contact with the rugose shell side, but with no bubble neck connection to the bubble on the inner side, are not considered daughter bubbles. They are also not former daughter bubbles, since a small bubble volume is expected to remain in the shell aperture after daughter bubble detachment (as seen in Gnyloskurenko et al., 2003). We suggest that daughter bubbles form as a response to decompression-induced bubble expansion coupled with the rigidity of the oxide shell (the rigidity is demonstrated by the cracks). With decreasing pressure, a bubble partially covered with an oxide shell will attempt to expand against its rigid shell. Apertures in the rigid shell may then be exploited as gateways for bubble expansion; the apertures become leakage points. We can envision multiple apertures acting as gateways, but since bubble breakup is energetically unfavorable as more surface is generated, as opposed to less, one aperture could prevail over others. This is

supported by our experiments; where multiple daughter bubbles are present, they have a large volume differences between them (Figure 4.2 b), indicating that for a discrete pressure drop a single aperture is “activated”. We suggest expansion occurs through apertures rather than on the part of the bubble not covered by oxides because circumventing the shell would produce a non-spherical shape, and, in our experiments, because it is prevented by the capsule wall.

The appearance and location of daughter bubbles are evidence that oxide shells are not a quench texture and point to a timeline of events: parent bubble formation, oxide shell formation, daughter bubble formation through apertures, and formation of oxide shells on daughter bubbles (Figure 4.5). If the (parent) oxide shells were a quench texture, we would not see daughter bubbles or their shells. All daughter bubbles have a narrow cylindrical neck, including the one daughter bubble connected through a shell crack. Thus, the crack in the oxide shell must have formed after the daughter bubble, otherwise the neck would not be cylindrical. Since the cracking of the oxide shell was induced by parent bubble expansion, it is also not a quench texture.

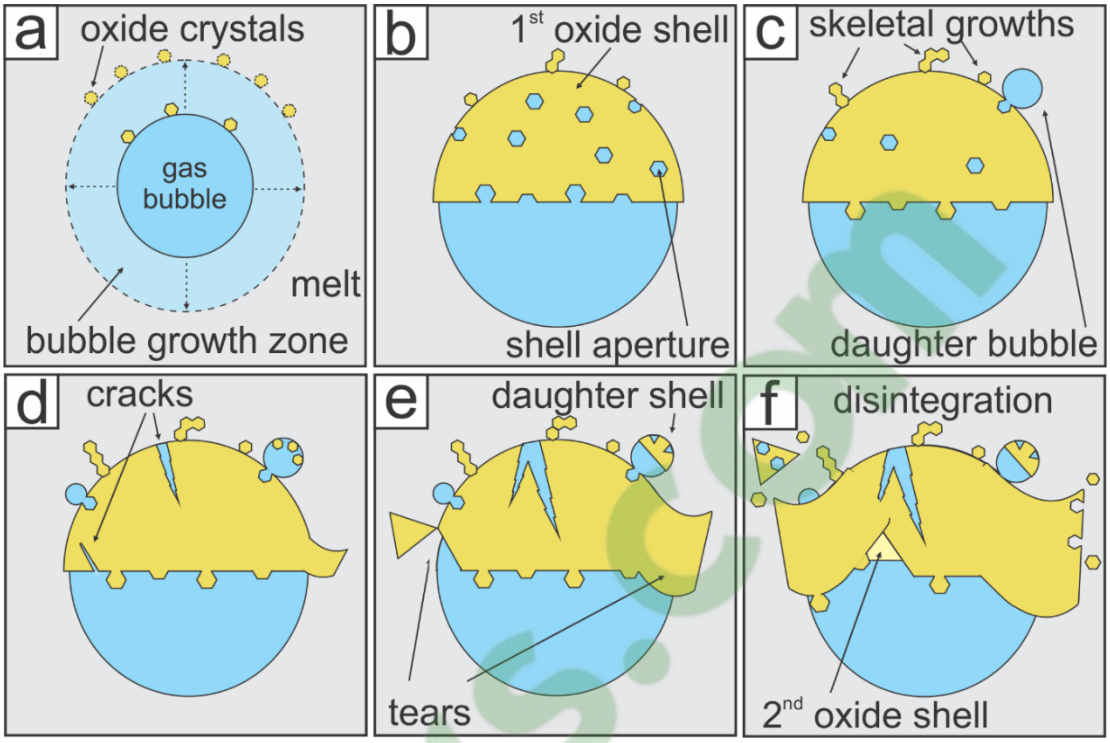

Figure 4.5: Summary of observations of bubble growth and oxide shell development. a) On the surface of a bubble growing within the melt, oxides start to crystallize due to hydrogen diffusion and resultant melt oxidation. b) As the processes continues, oxides become more and more interconnected and create an oxide shell on the bubble wall. c) A complex oxide shell is formed with apertures, an uneven border and skeletal outward growths. Daughter bubbles form by fluid leaking through the apertures. d) Cracks form in the oxide shell, and daughter bubbles may start to develop oxide shells of their own. e) The cracks widen, and some become the starting point of oxide shell tearing. f) After some time, the first oxide shell starts to detach from the bubble and disintegrates, whilst the newly available bubble surface becomes the location for the generation of a new oxide shell.

Daughter bubble generation is a process opposite to bubble coalescence, so it increases the number of bubbles present. Daughter bubble formation is controlled by the decompression rate, the aperture diameter and the volume of the space beneath the aperture (based on Gnyloskurenko et al., 2003, in an aqueous system). The latter is here equivalent to the parent bubble volume. The daughter bubble's volume and shape also depend on the magnitude of decompression, as well as on the wetting conditions and surface properties of the oxides (Gnyloskurenko et al., 2003). In a silicate melt, oxides and bubbles can wet each other's surfaces (Hurwitz and Navon, 1994). In our experiments, the oxide shell's outer surface is very rugose, and the parent bubble's volume is much larger than the aperture diameter. It seems that at our decompression rates, surface phenomena dominate so the wetting conditions at the aperture control the daughter bubble's final volume and shape. Thus, in the case of oxide shell apertures where wetting is favorable, the daughter bubble grows spherically. The daughter bubbles in our samples are mostly spherical and we can clearly see a neck, (Figure 4.2 b), so detachment by neck rupture is expected to follow (Gnyloskurenko et al., 2003). The detachment of a daughter depends on the balance between the buoyancy forces acting upward and the surface tension forces acting downward on the daughter bubble (Gnyloskurenko et al., 2003). The subsequent processes of neck rupture and detachment were not observed in our experimental run products. After detachment, some bubble volume is likely to remain in the aperture (i.e. part of the neck, as seen in Gnyloskurenko et al., 2003), leading to possible continuous generation of multiple daughter bubbles through the same aperture.

4.4.1.4 Stability of bubble-oxide aggregates through attachment and detachment

The ascent of bubbles through a melt is most relevant for the degassing of magmatic systems and the rising or sinking of crystals for the formation of ore deposits (e.g., magnetite, Knipping et al., 2015; Ovalle et al., 2018; or chromite, Matveev and Ballhaus, 2002; Ballhaus et al., 2015). However, if we consider the buoyancy of pairs of different phases (or multi-phased aggregates), here bubbles and crystals, their stability will influence their dynamics. We discuss this stability through interactions, i.e. attachment and detachment forces acting on the aggregate in question (Gualda and Anderson, 2007). Interactions between a bubble and any particle can be divided into three types: collision, attachment and detachment (Phan et al., 2003). In evaluating the stability of our bubble-oxide aggregates, we will only consider attachment and detachment, as collision applies only to harvesting, which we argued above is not occurring in our experiments.

Bubbles and oxides that form pairs or aggregates wet each other's surfaces very well and are held together by surface tension forces. Since the surface energy release is highest when they are joined, once they become attached a large amount of energy (larger than for silicates and bubbles) will need to be spent to detach them (Gualda and Ghiorso, 2007). Gualda and Ghiorso (2007) define the attachment energy between bubbles and oxides as the summation of the adhesion and deformation energy (when a bubble deforms from a sphere to a spherical cap when attaching to a crystal surface). Our oxide shells are much smaller in volume than the bubbles they wet, so bubble deformation is insignificant, and the adhesion energy dominates.

We have found examples of phenomena such as we see in our experiments in the studies of surfaces and mineral processing (e.g., Gnyloskurenko et al., 2003; Phan et al., 2003). We have identified examples similar to our observations and here we apply them to a silicate melt environment. The region of the bubble where bubble and oxides are most strongly attached is the maximum adhesion area (Figure 4.6 b-d) and is defined by the angle θ_1 (< 90°, from the vertical, see Phan et al., 2003) shown in Figure 4.6 b. There the adhesive force between the bubble and the oxides is at a maximum (Phan et al., 2003). Consequently, even though oxides could crystallize anywhere on the bubble wall, they will remain in place only within this area, and oxide shells are most likely to form from these oxides. The configuration of our oxide shells, in a spherical cap morphology, supports this (Figures 4.1, 4.2) and the value of θ_1 in our aggregates varies from 13° to 86°, with a mean and median of 55°, calculated from Equation 20:

$$\cos\theta_1 = (r_{bubble}-h)/r_{bubble} \quad (20),$$

and confirmed by 3D measurements (h is the height of the spherical cap).

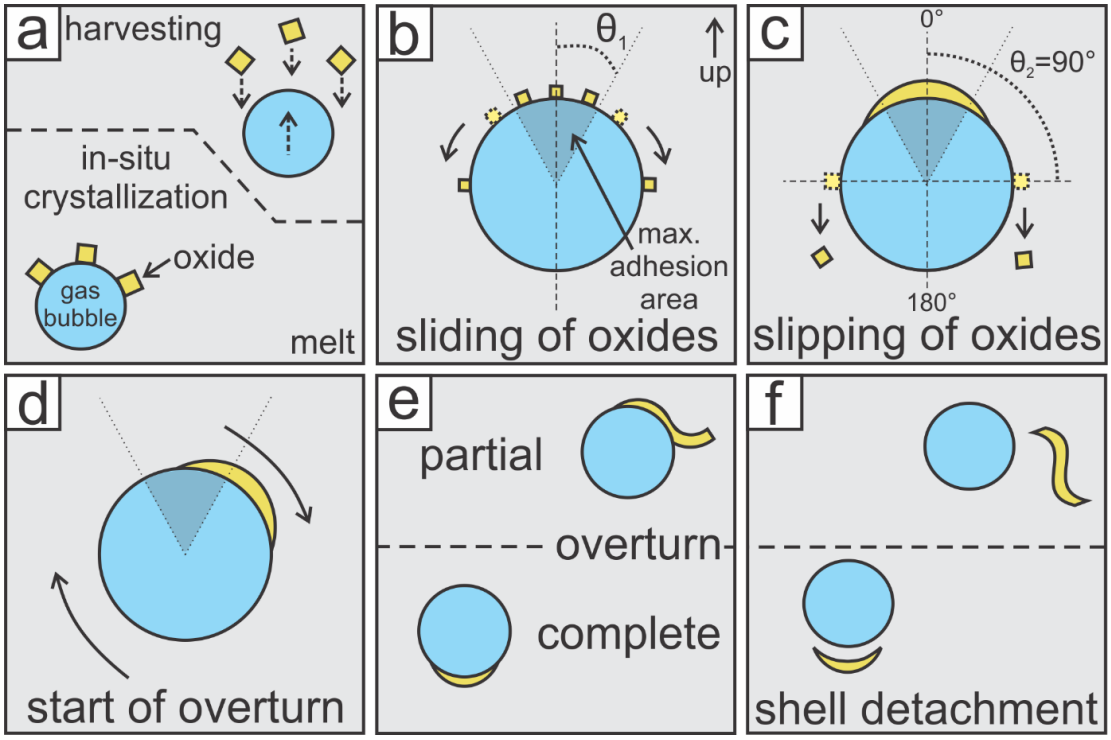

Figure 4.6: Schematic representation of the behavior of bubble-oxide aggregates in relation to the maximum adhesion area. All images are vertical sections with up at the top. a) Bubble-oxide aggregates form, either via *in situ* crystallization on the bubble wall or via harvesting. b) Oxides within the maximum adhesion area are stable, whereas those outside it start to slide downwards on the bubble wall. c) An oxide shell forms within the maximum adhesion area. Due to crystal adhesion, parts of the shell can exceed the adhesion area and become detached. d) Due to the oxide shell's weight, the entire aggregate becomes mechanically unstable and overturns. e) If overturn is faster than detachment, the oxide shell will finish on the opposite side of the bubble. If the overturn is only partial, detachment will start before complete overturn occurs. f) The extent of the overturn governs the style of detachment.

Contrary to attachment, which can be examined when two phases are in contact, detachment is much more difficult to examine in post-process samples, even in 3D. It is difficult to state that two distinct phases have detached if they are not directly observed to transition from an attached to a detached state. We observed several features in 3D that we interpret as the start of oxide shell detachment (Figure 4.2): i) parts of shells not in contact with a bubble surface have smooth inner and rugose outer surfaces and the same concavity as the bubble, ii) several shells may be present on the same bubble, separated by melt, and iii) cracks and tears occur in most oxide shells. We see such detachment features on aggregates that are positively buoyant: 23-2-1_ox1, 23-2-1_ox6, 15-2-2_ox2 and 17-2-1_ox6.

Phan et al. (2003) proposed that the capillary force, the particle's weight and turbulent inertial forces caused by the aggregate's movement govern detachment. We assume the turbulent contribution within the experimental charges as minimal, as we did not observe evidence of fringe bubble displacement. Additionally, detachment is easier for particles outside the maximum adhesion area (Figure 4.6 b, c), which in our aggregates most commonly is $\theta_1 = 55°$. The ease of detachment seems particularly important for our case, since due to crystal adhesion, oxide shells would behave like sheets rather than like individual particles. If one part of the shell extended beyond the maximum adhesion area boundary (Figure 4.6 c), e.g., when sideways oxide growth is faster than bubble growth, detachment could begin, and when part of the shell is detached, the rest starts to peel off (Figure 4.6 e, f). If detachment starts by oxides sliding on the bubble surface, when they reach $\theta_2 = 90°$, they will detach from the bubble wall, rather than continuing on the bubble surface until they reach 180° because the equator is the weakest region, not the bottom of the bubble. Another possibility is

that the oxide shell becomes so thick or envelops so much of the bubble's surface (i.e. outward or sideways oxide growth surpasses bubble growth), that the aggregate overturns (Figure 4.6 d), leaving the uncovered (shell-free) part of the bubble is facing upwards and free to detach by its own buoyancy (Figure 4.6 e, f).

4.4.1.5 Bubble-oxide aggregates with multiple oxide shells

One of the most intriguing structures we observed are multiple oxide shells around a single bubble (Figure 4.2). We envision two possible origins for these. The first possibility is that all shells originate from a single shell that has delaminated, and the second is that all shells originated from the same bubble wall but formed incrementally over time (i.e. the shell furthest away from the bubble is the oldest and the one closest to it is the youngest). We favor the second mechanism because all oxide shells share the same concavity as the adjacent bubble, and have smooth inner sides and rugose, outer sides that could only form if the oxides crystallized against a smooth surface (i.e. a bubble wall). For the latter reason, we also reject the comparison to Liesegang bands, since they exhibit only rugose surfaces (Boudreau, 1995, see his Fig. 8). We therefore regard multiple nested shells around a single bubble as reflecting multiple generations of shells. The different sizes of oxide crystals in separate shells most likely reflect their growth time. The presence of multiple shell generations around a single bubble provides further evidence for detachment. This may occur either as the first (oldest) shell becomes too large and outgrows the maximum adhesion area, or as the bubble's volume or shape oscillates and displaces the rigid shell. In nature, slight pressure changes are constantly occurring in magmatic systems, driven by both

internal (such as localized convection) and external (such as pressure waves passing through the melt) forces, causing bubble volume oscillations or vibrations (e.g. seismic waves; Ichihara et al., 2004). Such slight pressure oscillations are also present in our experiments due to the manually controlled decompression (through slight valve opening). Once detachment from the bubble starts and melt begins to percolate in the newly available space between the detached shell and the bubble, a new shell can form.

4.4.1.6 Preservation potential of oxide shells

The presence of many apertures in our oxide shells indicate that once detached the shells easily disintegrate, as suggested by Edmonds et al. (2015). Away from the bubble wall, the shells can be easily disrupted (e.g. by colliding with other crystals or bubbles, or by movement of the host melt). The disintegration is already visible in Figure 4.2 c-f, in the part of the shell away from the bubble, presumably caused by the lack of a stabilization by the bubble wall. It seems that the unique morphology of the oxide shells enhances their disintegration. Some cohesion must be present between individual oxide crystals within the shell, otherwise they would immediately detach individually from the bubble, but it is present only in two directions since the shells have a sheeted morphology. Forces (e.g., shear, Kushnir et al., 2017) from any direction apart from within the plane of a detached shell could thus be sufficient to cause disintegration. This implies a low preservation potential for detached shells. We infer that this poor preservation potential, coupled with a lack of 3D observations, could be the reason why intact oxide shells have not previously been described in natural or experimental samples.

Despite their low potential for preservation, detached oxide shells need not disintegrate completely into individual crystals. Several crystals that have remained aggregated even after shell disintegration can be seen on Figure 4.2 c-f. Such crystal aggregates could coarsen into larger crystals or crystals clusters and become the precursor for larger oxide accumulations.

4.4.2 Occurrences of analogous structures in geological materials

We have shown that oxide (magnetite) shells can form in experimental charges by crystallization from the silicate liquid at the bubble-melt interface, due to oxidation of the sample by hydrogen loss. Oxidation via hydrogen loss does occurs in magmatic systems (e.g., Vollinger, 2017), and hydrogen loss via diffusion is present in natural systems linked to the surface (e.g., Myers et al., 2019), which leads to the question of whether oxide shells can form around more-oxidized fluid or vapor bubbles in natural magmatic systems.

We hypothesize that the low preservation potential of the oxide shells commonly masks evidence for their formation in nature, either by *in situ* crystallization or by harvesting. Here we review evidence for analogous structures from a range of geological environments that we believe are by nucleation and/or aggregation of crystals on a spherical interface (bubble-melt or melt-melt). Two textural observations are unique to all examples: the possible occurrence of multiple nested shells within the silicate liquid, and the combination of a smooth inner and rugose outer surface of the shells. We also present our own example of natural textures in granophyres from Krafla volcano (Iceland) that we infer were formed by a process of shell formation on

bubble surfaces, similar to our experiments. We will start with natural examples that most resemble our experimental charges and proceed to examples that may be formed by either *in situ* crystallization or harvesting.

4.4.2.1 Krafla granophyres

Natural textures within granophyres from Krafla display some remarkably similar features to our experimental oxide shells. Textures in 2 granophyre xenoliths, KR-7 and KR-19, from Krafla volcano (Iceland) were examined. The samples are derived from shallow felsic intrusions and were ejected in 1724 during the formation of Víti, a small maar crater in the central region of Krafla caldera (Sæmundsson, 1991; Jónasson,1994). Whole-rock compositional data for these samples is not currently available, but similar samples from the Víti crater analyzed by Jónasson (1994; his Table 1) have SiO_2 contents ≥ 73.70 wt. %. The samples have a mineral assemblage of plagioclase + clinopyroxene + magnetite hosted in a granophyric groundmass (intergrown alkali feldspar + quartz).

In 2D sections (SEM and tomographic) the structures of interest appear as linear or curved crystal aggregates (Figure 4.7 a-c). EDS analysis was performed on polished thin sections of the Krafla samples to identify the mineral phases forming the curved structures. The oxides are magnetite, and the silicate phase is clinopyroxene. In reconstructed 3D volumes (Figure 4.7 c, d), we observe shell-like spherical structures with a smooth inner (concave) surface and rugose outer (convex) surface with skeletal projections similar to our experimental oxide shells.

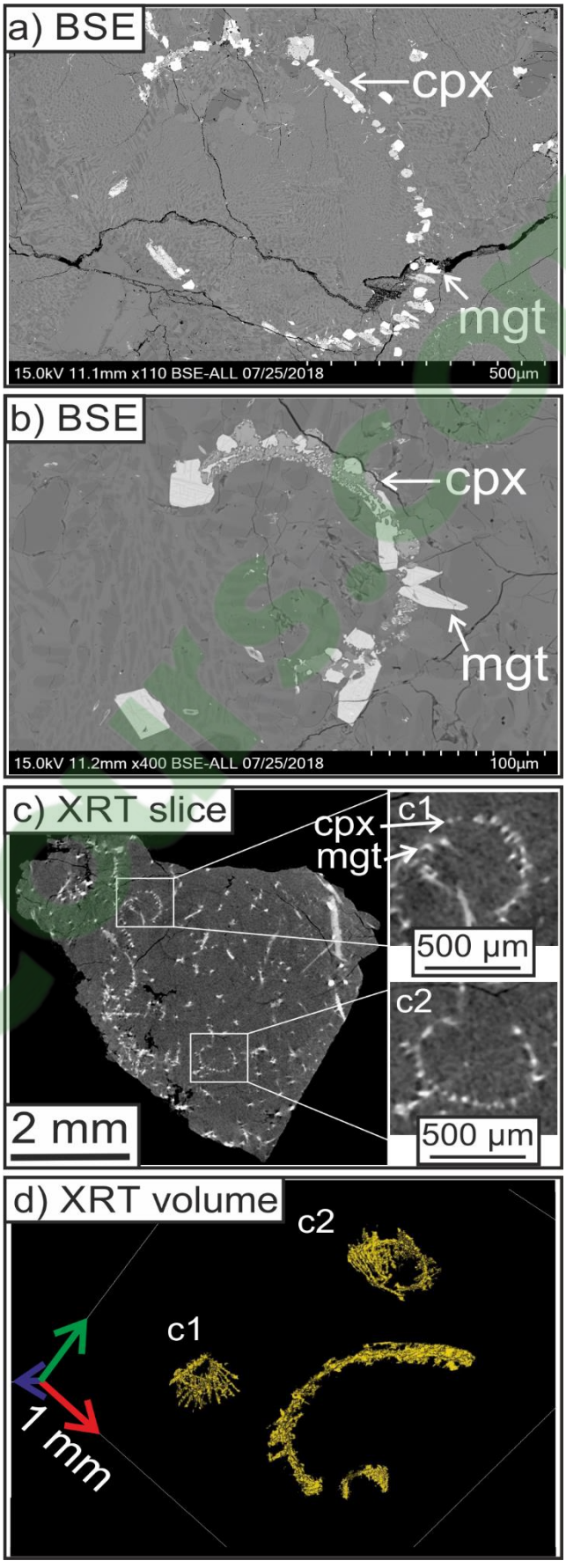
a) BSE
cpx
mgt
15.0kV 11.1mm x110 BSE-ALL 07/25/2018
500µm
b) BSE
cpx
mgt
15.0kV 11.2mm x400 BSE-ALL 07/25/2018
100µm
c) XRT slice
cpx
mgt
c1
500 µm
c2
500 µm
2 mm
d) XRT volume
c2
c1
1 mm

Figure 4.7: SEM and tomographic images for natural sample KR7 from Krafla. a) SEM image of a clinopyroxene (cpx; light grey) and magnetite (mgt; white) aggregate within a granophyric groundmass (mottled light and dark grey). The elliptical structure is ~ 800 μm across. b) SEM image of another accumulation of the same assemblage, with a more pronounced sphericity. It has a smooth inner and rugose outer surface. The relationship between the cpx and mgt crystals is more clearly visible, with skeletal cpx and mgt crystals projecting outward from the convex side. c) 2D section from the 3D tomographic volume of sample KR7. Oxides are the brightest feature in the image, cpx is light grey and the granophyric groundmass is dark grey. Both linear and curved structures are visible, two of which are zoomed in on (insets; c1 and c2). d) A 3D visualization of several curved mgt-cpx structures, manually segmented from the sample volume. Mgt and cpx are not visualized individually to simplify the visualization.

These structures are not observed in association with bubbles, but a process similar to that forming the experimental oxide shells could create spherical structures with such surfaces, due to the proximity to the atmosphere, which could result in rapid oxidation. Rapid growth of crystalline phases without the presence of a bubble would not lead to structures with a smooth inner surface, since they would have nothing to grow against. The smooth inner and rugose outer surfaces of these structures favor *in situ* crystallization of magnetite and clinopyroxene on the outer bubble walls over harvesting. The absence of bubbles in post-process samples could be explained by bubble loss via detachment and buoyant rise, and the subsequent infilling of the space left behind by the melt. We suggest that these ″ghost bubble″ structures were preserved due to the presence of clinopyroxene, which is found between magnetites, and potentially prevented the shell disintegration. The clinopyroxene microlites seem to have also crystallized on the bubble wall, since they exhibit a smooth inner and a jagged outer surface. We see however, some structural relaxation, since some structures are planar and no longer spherical. Since the degree of structural relaxation is unknown, the present circumference and shell sizes do not indicate the original bubble size.

4.4.2.2 Micrometeorites

Shell-like Fe-Ni oxide accumulations (of unspecified mineralogy) have been described on the outer surfaces of gas bubbles in partially molten micrometeorite interiors (Toppani et al., 2001; Taylor et al., 2011). Micrometeorites are interplanetary dust particles recovered from Antarctic ice or deep-sea sediments. The Fe-Ni oxide

shells exhibit a smooth inner and rugose outer surface like the experimentally produced oxide shells (Figure 4.8 a, b), indicating growth from the melt rather than from vapor within the bubble. Crystallization from the melt is also supported by their occurrence in the melt away from the vesicles (see figures in Toppani et al., 2001; and Figures 4b and 8b in Taylor et al., 2011). These textures have an almost identical appearance to our oxide shells and we propose that they may have formed in the same way, by gas loss.

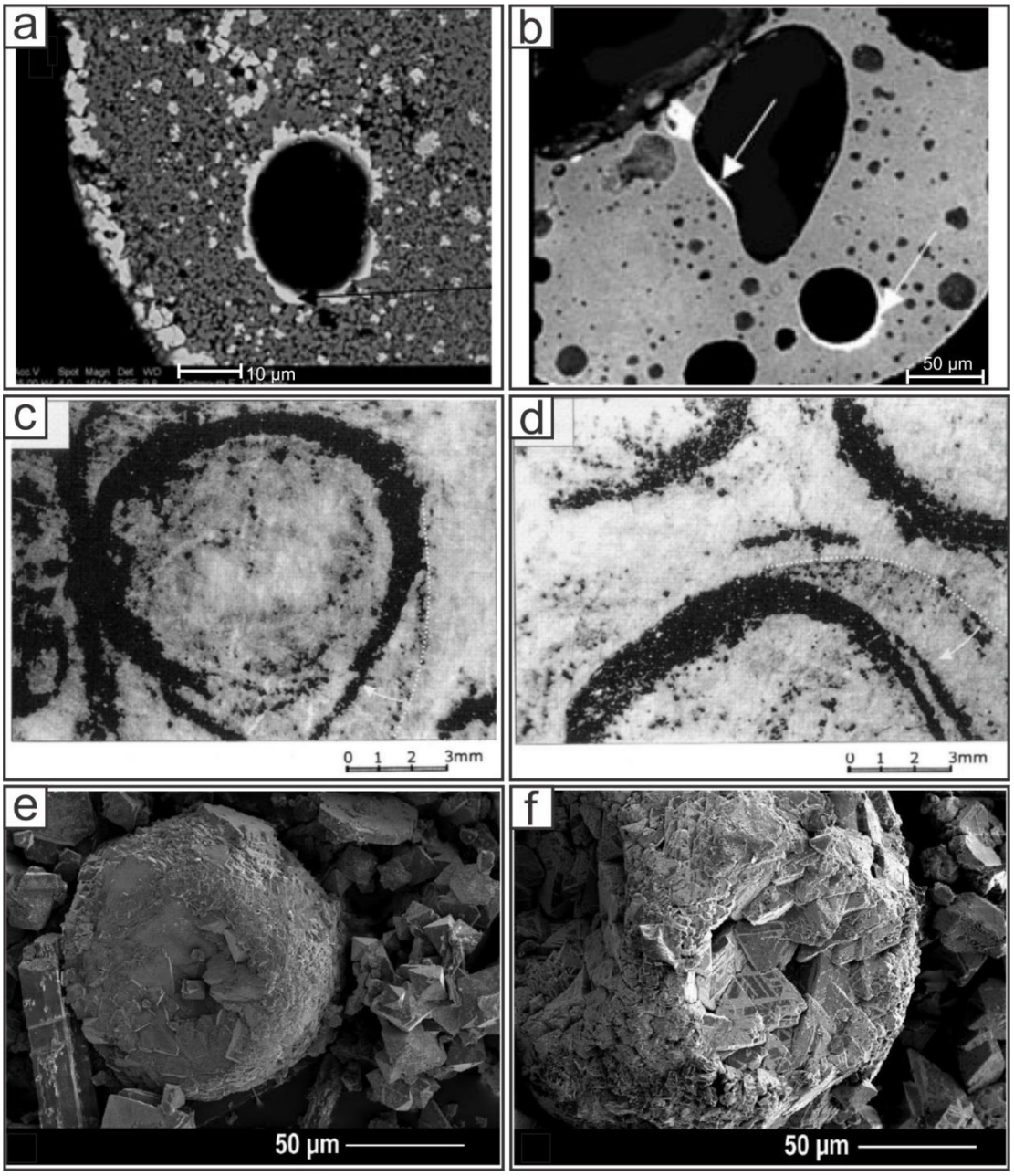

Figure 4.8: A compilation of analogous structures found in literature. a, b) Interior of a micrometeorite (Taylor et al., 2011), SEM images. The bubble in the center of image A is fully covered by a Fe-Ni oxide shell. The shell has a smooth interior and rugose outer surface. There are Fe-Ni oxides lining the micrometeorite border and within the melt. The two bubbles marked with arrows in image B have partial oxide shells. The smaller of the two has a smooth inner and rugose outer shell surface. c, d) Orbicular

chromite in a dunite matrix (Zhou et al., 2001), microscope images. The chromite in image C is highly similar to Figure 4.2 b. The outermost thin chromite shells in both images do not follow the concavity of the inner ones, which the authors interpreted as detachment. e, f) Magnetite spherules from El Laco pyroclastic flow (Nyström et al., 2016), SEM images. The spherules have a hollow center and a densely packed shell of magnetite crystals (a and b from Taylor et al., 2011; c and d from Zhou et al., 2001; e and f from Nyström et al., 2016).

4.4.2.3 Orbicular chromite

Orbicular chromites (Figure 4.8 c, d) consist of a shell of chromite crystals enveloping a roundish dunite (e.g. Greenbaum, 1977) or serpentinite core (e.g. Yamane et al., 1988), in a matrix that is compositionally and texturally the same as the core. Textural features in common with our experimental oxide shells are a smooth inner and rugose outer surface, several partly detached shell layers (Fig. 8 and 9 in Greenbaum, 1977), collapsed shells and shells tracing out ghost cores (Fig. 3i, ii in Zhou et al., 2001). In the formation of orbicular chromites, the nucleation of chromite crystals and their growth could be similar to our oxide shells, i.e. *in situ* crystallization on a bubble or melt droplet (see Greenbaum, 1977; Zhou et al., 2001; Matveev and Ballhaus, 2002; Ballhaus et al., 2015).

4.4.2.4 El Laco magnetite deposit

The processes resulting in the extreme magnetite enrichment in one lava flow from the El Laco volcanic complex (Chile) remain enigmatic (Knipping et al., 2015; Ovalle et al., 2018). We looked for similarities between our oxide shells and the magnetite in this flow but found no explicit evidence of features like ours in published figures or descriptions. Although magnetite spherules found in the friable ore are similar to our observations (Figure 4.1 e, Figure 4.8 e, f), no bubbles were observed at the center of these spherules (Nyström et al., 2016). It has been demonstrated experimentally that crystalline spherulites of $Li_2Si_2O_5$ can form by *in situ* nucleation on bubbles in melts (Davis and Ihinger, 1998). Considering our evidence for the low

preservation potential of oxide shells, we propose that the magnetite spherules may have originated in a similar way to that seen in our experiments, due to the lava flow's contact with the atmosphere. The scenario of bubble-oxide overturn and bubble escape through an upward orientated aperture in the oxide shell (as proposed in Figure 4.6 e) could be the reason why no bubbles were found in the center of El Laco spherules.

4.5 Conclusion

Our experimental results show that bubble-oxide aggregates with complex structures have the potential to form in andesitic magmas. Textural evidence including oxide shell morphology (smooth inner and rugose outer surfaces, skeletal growths), uniform size and low Ti content suggest these features were formed by *in situ* crystallization of oxides on the melt side of the bubble-melt interface. These results provide a glimpse into the events that lead to preferential oxide-bubble spatial distribution within volcanic rocks, suggest a probable mechanism for oxide transport by bubbles that has so far only been theoretically proposed, and answer the question why the initial textures have such a low preservation potential. These features, revealing dynamic mechanisms, could not have been identified through arbitrarily oriented and randomly chosen 2-dimensional sections alone, highlighting the importance of 3-dimensional observations.

We observed evidence for several different dynamic processes in the experiments: i) daughter bubble generation through an oxide shell aperture, ii) detachment of oxide shells from bubble walls, iii) multiple oxide shells around a single

bubble, iv) disintegration of oxide shell after detachment from the bubble. The potential consequences of these processes are the slowing of bubble ascent, continuous production of oxides at different depths and bubble breakup. Our experimentally produced oxide shells are texturally similar to natural textures from a range of geological environments, including magnetite + clinopyroxene structures in Krafla granophyres, Fe-Ni oxide shells around bubbles in micrometeorites, orbicular chromites and El Laco spherules.

The process of *in situ* crystallization at the bubble-melt interface is an alternative to harvesting that can be applied to bubbles of any gas (e.g. H_2O, H_2S, CO_2, …) passing through a magma bearing different elements and providing a surface for either crystal nucleation and growth, or crystal or immiscible melt accumulation. We suggest the same process is behind all the above-mentioned occurrences; a phase (solid, crystal, or liquid, melt droplet) is forming (via different processes, in our case melt oxidation) and/or accumulating on the surfaces of another liquid phase (bubble or melt droplet, via harvesting) and is transported by it. As we have shown in our comparison to natural materials, the same process can occur with different crystals and on different surfaces (bubble-melt or melt-melt) and in different melt compositions.

4.6 Acknowledgements

The authors wish to thank John Stix and Kim Berlo for the use of the Krafla samples, and Chris Ballhaus and three anonymous reviewers for their work, which greatly enhanced the manuscript.

4.7 Author contributions

PP (PhD student and principal investigator), MDH (PhD director) and DRB (PhD co-director) developed the ideas central to the manuscript. LM (beamline scientist) provided access to software and helped with the 3D data treatment, GL (post-graduate scientist) helped with the 3D analyses in Pore3D, MKP (graduate student) helped with the SEM analysis, and SR (graduate student) helped with natural samples. All authors helped with the writing of the manuscript.

4.8 References

Applegarth, L. J., Tuffen, H., James, M. R., Pinkerton, H., Cashman, K. V., 2013. Direct observations of degassing-induced crystallization in basalts. *Geology* 41(2):243-246.

Bai, L., Baker, D. R., Rivers, M., 2008. Experimental study of bubble growth in Stromboli basalt melts at 1 atm. *Earth and Planetary Science Letters* 267(3-4):533-547.

Ballhaus, C., Fonseca, R. O., Münker, C., Kirchenbaur, M., Zirner, A., 2015. Spheroidal textures in igneous rocks–Textural consequences of H_2O saturation in basaltic melts. *Geochimica et Cosmochimica Acta* 167:241-252.

Baker, D. R., 2004. Piston-cylinder calibration at 400 to 500 MPa: A comparison of using water solubility in albite melt and NaCl melting. *American Mineralogist* 89(10):1553-1556.

Baker, D. R., Brun, F., O'Shaughnessy, C., Mancini, L., Fife, J. L., Rivers, M., 2012. A four-dimensional X-ray tomographic microscopy study of bubble growth in basaltic foam. *Nature Communications* 3, 1135.

Baker, D. R., Eggler, D. H., 1987. Compositions of anhydrous and hydrous melts coexisting with plagioclase, augite, and olivine or low-Ca pyroxene from 1 atm to 8 kbar; application to the Aleutian volcanic center of Atka. *American Mineralogist* 72(1-2), 12-28.

Boudreau, A. E., 1995. Crystal aging and the formation of fine-scale igneous layering. *Mineralogy and Petrology* 54(1-2):55-69.

Brun, F., Mancini, L., Kasae, P., Favretto, S., Dreossi, D., Tromba, G., 2010. Pore3D: A software library for quantitative analysis of porous media. *Nuclear Instruments and Methods in Physics Research Section A: Accelerators, Spectrometers, Detectors and Associated Equipment* 615(3), 326-332.

Candela, P. A., 1991. Physics of aqueous phase evolution in plutonic environments. *American Mineralogist* 76.

Dalpé, C., Baker, D. R., 2000. Experimental investigation of large-ion-lithophile-element-, high-field-strength-element-and rare-earth-element-partitioning between calcic amphibole and basaltic melt: the effects of pressure and oxygen fugacity. *Contributions to Mineralogy and Petrology* 140(2):233-250

Davis, M. J., Ihinger, P. D., 1998. Heterogeneous crystal nucleation on bubbles in silicate melt. *American Mineralogist* 83(9-10):1008-1015.

Driesner, T., 2007. The system H_2O–NaCl. Part II: Correlations for molar volume, enthalpy, and isobaric heat capacity from 0 to 1000°C, 1 to 5000 bar, and 0 to 1 XNaCl. *Geochimica et Cosmochimica Acta* 71(20):4902-4919.

Druitt, T. H., Young, S. R., Baptie, B., Bonadonna, C., Calder, E. S., Clarke, A. B., Cole, P. D., Harford, C. L., Herd, R. A., Luckett, R., Ryan, G., Voight, B., 2002. Episodes of cyclic Vulcanian explosive activity with fountain collapse at Soufrière

Hills Volcano, Montserrat. *Memoirs of the Geological Society of London* 21: 281-306.

Dziewonski, A. M., Anderson, D. L., 1981. Preliminary reference Earth model. Phys Earth Planet Int 25: 297-356.

Edmonds, M., 2015. RESEARCH FOCUS: Flotation of magmatic minerals. *Geology* 43(7):655-656.

Edmonds, M., Brett, A., Herd, R. A., Humphreys, M. C. S., Woods, A., 2015. Magnetite-bubble aggregates at mixing interfaces in andesite magma bodies. *Geological Society of London Special Publications* 410(1):95-121.

Eggler, D. H., 1987. Solubility of major and trace elements in mantle metasomatic fluids: experimental constraints. In: Menzies M, Hawkesworth C: Mantle metasomatism.

Fenn, P. M., 1977. The nucleation and growth of alkali feldspars from hydrous melts. *Canadian Mineralogist* 15:135-161.

Gardner, J. E., Denis, M.-H., 2004. Heterogeneous bubble nucleation on Fe-Ti oxide crystals in high-silica rhyolitic melts. *Geochimica et Cosmochimica Acta* 68(17), 3587-3597.

Gardner, J. E., Ketcham, R. A., 2011. Bubble nucleation in rhyolite and dacite melts: temperature dependence of surface tension. *Contributions to Mineralogy and Petrology* 162(5):929-943.

Gnyloskurenko, S. V., Byakova, A. V., Raychenko, O. I., Nakamura, T., 2003. Influence of wetting conditions on bubble formation at orifice in an inviscid liquid. Transformation of bubble shape and size. *Colloids and Surfaces A: Physiocchemical and Engineering Aspects* 218(1-3):73-87.

Gonnermann, H. M., Gardner, J. E., 2013. Homogeneous bubble nucleation in rhyolitic melt: experiments and nonclassical theory. *Geochemistry Geophysics Geosystems* 14:1-16.

Greenbaum, D., 1977. The chromitiferous rocks of the Troodos ophiolite complex, Cyprus. *Economic Geology* 72(7):1175-1194.

Gualda, G. A., Anderson, 2007. Magnetite scavenging and the buoyancy of bubbles in magmas. Part 1: Discovery of a pre-eruptive bubble in Bishop rhyolite. *Contributions to Mineralogy and Petrology* 153(6), 733-742.

Gualda, G. A., Ghiorso, M. S., 2007. Magnetite scavenging and the buoyancy of bubbles in magmas. Part 2: Energetics of crystal-bubble attachment in magmas. *Contributions to Mineralogy and Petrology* 154(4), 479-490.

Harris, J. W., Stöcker, H., 1998. Spherical Wedge. §4.8.6 in Handbook of Mathematics and Computational Science. New York: Springer-Verlag, p. 108.

Heath, T., 1987. The works of Archimedes. Cambridge University Press, Cambridge.

Holloway, J. R., 1987. Igneous fluids. *Reviews in Mineralogy and Geochemistry* 17(1): 211-233.

Hurwitz, S., Navon, O., 1994. Bubble nucleation in rhyolitic melts: Experiments at high pressure, temperature, and water content. *Earth and Planetary Science Letters* 122(3–4), 267-280.

Ichihara, M., Ohkunitani, H., Ida, Y., Kameda, M., 2004. Dynamics of bubble oscillation and wave propagation in viscoelastic liquids. *Journal of Volcanology and Geothermal Research* 129(1-3):37-60.

Jakobsson, S., 2012. Oxygen fugacity control in piston-cylinder experiments. *Contributions to Mineralogy and Petrology* 164(3):397-406.

Jónasson, K., 1994. Rhyolite volcanism in the Krafla central volcano, north-east Iceland. *Bulletin of Volcanology* 56:516-528.

Kirkpatrick, R. J., 1977. Nucleation and growth of plagioclase, Makaopuhi and Alae lava lakes, Kilauea Volcano, Hawaii. *Geological Society of America Bulletin* 88(1):78-84.

Knipping, J. L., Bilenker, L. D., Simon, A. C., Reich, M., Barra, F., Deditius, A. P., Lundstrom, C., Bindeman, I., Munizaga, R., 2015. Giant Kiruna-type deposits form by efficient flotation of magmatic magnetite suspensions. *Geology* 43(7):591-594.

Kushnir, A. R., Martel, C., Champallier, R., Arbaret, L., 2017. In situ confirmation of permeability development in shearing bubble-bearing melts and implications for volcanic outgassing. *Earth and Planetary Science Letters* 458:315-326.

Lange, R. A., Carmichael, I. S., 1987. Densities of Na_2O-K_2O-CaO-MgO-FeO-Fe_2O_3-Al_2O_3-TiO_2-SiO_2 liquids: new measurements and derived partial molar properties. *Geochimica et Cosmochimica Acta* 51(11):2931-2946.

Lange, R. A., Carmichael, I. S., 1996. The Aurora volcanic field, California-Nevada: Oxygen fugacity constraints on the development of andesitic magma. *Contributions to Mineralogy and Petrology* 125(2-3):167-185.

Le Gall, N., Pichavant, M., 2016. Homogeneous bubble nucleation in H_2O- and H_2O-CO_2-bearing basaltic melts: Results of high temperature decompression experiments. *Journal of Volcanology and Geothermal Research* 327:604-621.

Liu, Y., Samaha, N. T., Baker, D. R., 2007. Sulfur concentration at sulfide saturation (SCSS) in magmatic silicate melts. *Geochimica et Cosmochimica Acta* 71(7):1783-1799.

Mangan, M., Sisson, T., 2000. Delayed, disequilibrium degassing in rhyolite magma: decompression experiments and implications for explosive volcanism. *Earth and Planetary Science Letters* 183(3-4):441-455.

Matveev, S., Ballhaus, C., 2002. Role of water in the origin of podiform chromitite deposits. *Earth and Planetary Science Letters* 203(1): 235-243.

Menzies, M., Hawkesworth, C., 1986. Mantle metasomatism. Department of Energy, U.S.A. OSTI ID: 5870369.

Murphy, M. D., Sparks, R. S. J., Barclay, J., Carroll, M. R., Brewer, T. S., 2000. Remobilization of Andesite Magma by Intrusion of Mafic Magma at the

Soufriére Hills Volcano, Montserrat, West Indies. *Journal of Petrology* 41(1):21–42. https://doi.org/10.1093/petrology/41.1.21.

Myers, M. L., Wallace, P. J., Wilson, C. J., 2019. Inferring magma ascent timescales and reconstructing conduit processes in explosive rhyolitic eruptions using diffusive losses of hydrogen from melt inclusions. *Journal of Volcanology and Geothermal Research* 369: 95-112.

Mysen, B., Richet, P., 2005. Silicate glasses and melts: properties and structure. Elsevier Science 10: pp. 525.

Nyström, J. O., Henríquez, F., Naranjo, J. A., Nasuland, H. R., 2016. Magnetite spherules in pyroclastic iron ore at El Laco, Chile. *American Mineralogist* 101(3):587-595.

Ochs III, F. A., Lange, R. A., 1997. The partial molar volume, thermal expansivity, and compressibility of H_2O in $NaAlSi_3O_8$ liquid: new measurements and an internally consistent model. *Contributions to Mineralogy and Petrology* 129(2-3):155-165

Ochs III, F. A., Lange, R. A., 1999. The density of hydrous magmatic liquids. *Science* 283(5406):1314-1317.

Ovalle, J. T., La Cruz, N. L., Reich, M., Barra, F., Simon, A. C., Konecke, B. A., Rodriguez-Mustafa, M. A., Deditius, A. P., Childress, T. M., Morata, D., 2018. Formation of massive iron deposits linked to explosive volcanic eruptions. *Scientific Reports* 8(1):14855.

Papale, P., Moretti, R., Barbato, D., 2006. The compositional dependence of the saturation surface of H_2O+ CO_2 fluids in silicate melts. *Chemical Geology* 229(1-3): 78-95

Phan, C. M., Nguyen, A. V., Miller, J. D., Evans, G. M., Jameson, G. J., 2003. Investigations of bubble–particle interactions. *International Journal of Mineral Processing* 72(1-4):239-254.

Pitzer, K. S., Sterner, S. M., 1995. Equations of state valid continuously from zero to extreme pressures with H_2O and CO_2 as examples. *International Journal of Thermophysics* 16(2):511-518.

Pleše, P., Higgins, M. D., Mancini, L., Lanzafame, G., Brun, F., Fife, J. L., Casselman, J., Baker, D. R., 2018. Dynamic observations of vesiculation reveal the role of silicate crystals in bubble nucleation and growth in andesitic magmas. *Lithos* 296:532-546.

Polacci, M., Arzilli, F., La Spina, G., Le Gall, N., Cai, B., Hartley, M. E., Di Genova, D., Vo, N. T., Nonni, S., Atwood, R. C., Llewellin, E. W., 2018. Crystallisation in basaltic magmas revealed via in situ 4D synchrotron X-ray microtomography. *Scientific Reports* 8.

Preuss, O., Marxer, H., Ulmer, S., Wolf, J., Nowak, M., 2016. Degassing of hydrous trachytic Campi Flegrei and phonolitic Vesuvius melts: Experimental limitations and chances to study homogeneous bubble nucleation. *American Mineralogist* 101(4):859-875.

Rivers, M. L., 2012. tomoRecon: High-speed tomography reconstruction on workstations using multi-threading. *Developments in X-Ray Tomography* VIII. Int Soc Optics Photonics 8506:8506U.

Rivers, M. L., Citron, D. T., Wang, Y., 2010. Recent developments in computed tomography at GSECARS. *Developments in X-Ray Tomography* VII. Proc. SPIE 7804:09. doi: 10.1117/12.861393; https://doi.org/10.1117/12.861393.

Rivers, M. L., Wang, Y., Uchida, T., 2004. Microtomography at GeoSoilEnviroCARS. *Developments in X-Ray Tomography* IV. Proc. SPIE 5535. doi: 10.1117/12.562556; https://doi.org/10.1117/12.562556.

Rooyakkers, S. M., Wilson, C. J. N., Schipper, C. I., Barker, S. J., Allan, A. S. R., 2018. Textural and micro-analytical insights into mafic–felsic interactions during the Oruanui eruption, Taupo. *Contributions to Mineralogy and Petrology* 173(5):35.

Sæmundsson, K., 1991. Geology of the Krafla system. In: Gardarsson A, Einarsson Á (eds) Náttúra Mývatns. Hid Íslenska Náttúrufraedifélag, Reykjavík, pp 25–95 [in Icelandic].

Schindelin, J., Arganda-Carreras, I., Frise, E., Kaynig, V., Longair, M., Pietzsch, T., Preibisch, S., Rueden, C., Saalfeld, S., Schmid, B., Tinevez, J.Y., 2012. Fiji: an open-source platform for biological-image analysis. *Nature Methods*, 9(7), 676-682.

Shea, T., 2017. Bubble nucleation in magmas: A dominantly heterogeneous process?. *Journal of Volcanology and Geothermal Research* 343, 155-170.

Skyscan, NV, 2011. NRecon User Manual.

Stewart, D. B., Walker, G. W., Wright, T. L., Fahey, J. J., 1966. Physical properties of calcic labradorite from Lake County, Oregon. *American Mineralogist* 51(1-2):177-197.

Taylor, S., Jones, K. W., Herzog, G. F., Hornig, C. E., 2011. Tomography: A window on the role of sulfur in the structure of micrometeorites. *Meteoritics & Planetary Sciences* 46(10):1498-1509.

Toppani, A., Libourel, G., Engrand, C., Maurette, M., 2001. Experimental simulation of atmospheric entry of micrometeorites. *Meteoritics & Planetary Sciences* 36(10):1377-1396.

Vollinger, M., 2017. The oxidation state of Hawaiian magmas. Masters Thesis, University of Massachusetts Amherst, 590. https://scholarworks.umass.edu/masters_theses_2/590.

Voltolini, M., Haboub, A., Dou, S., Kwon, T. H., MacDowell, A. A., Parkinson, D. Y., Ajo-Franklin, J., 2017. The emerging role of 4D synchrotron X-ray micro-tomography for climate and fossil energy studies: five experiments showing the present capabilities at beamline 8.3.2 at the Advanced Light Source. *Journal of Synchrotron Radiation* 24(6):1237-1249.

Yamane, M., Bamba, M., Bamba, T., 1988. The first finding of orbicular chromite ore in Japan. *Mining Geology* 38(212):501-508.

Zhou, M. F., Malpas, J., Robinson, P.T., Sun, M., Li, J. W., 2001. Crystallization of podiform chromitites from silicate magmas and the formation of nodular textures. *Resource Geology* 51(1):1-6.

4.9 Appendices

Appendices 4.1 and 4.2 can be found on a CD-ROM accompanying the thesis.

Appendix 4.1

Initial compositions of andesitic rock powder, seed silicate crystals from literature, and compositional analysis performed with a BSE detector of several bubble-oxide aggregates, one natural sample from Krafla and of the standards used.

https://link.springer.com/article/10.1007/s00410-019-1556-8#SupplementaryMaterial

Sample 17-2-1

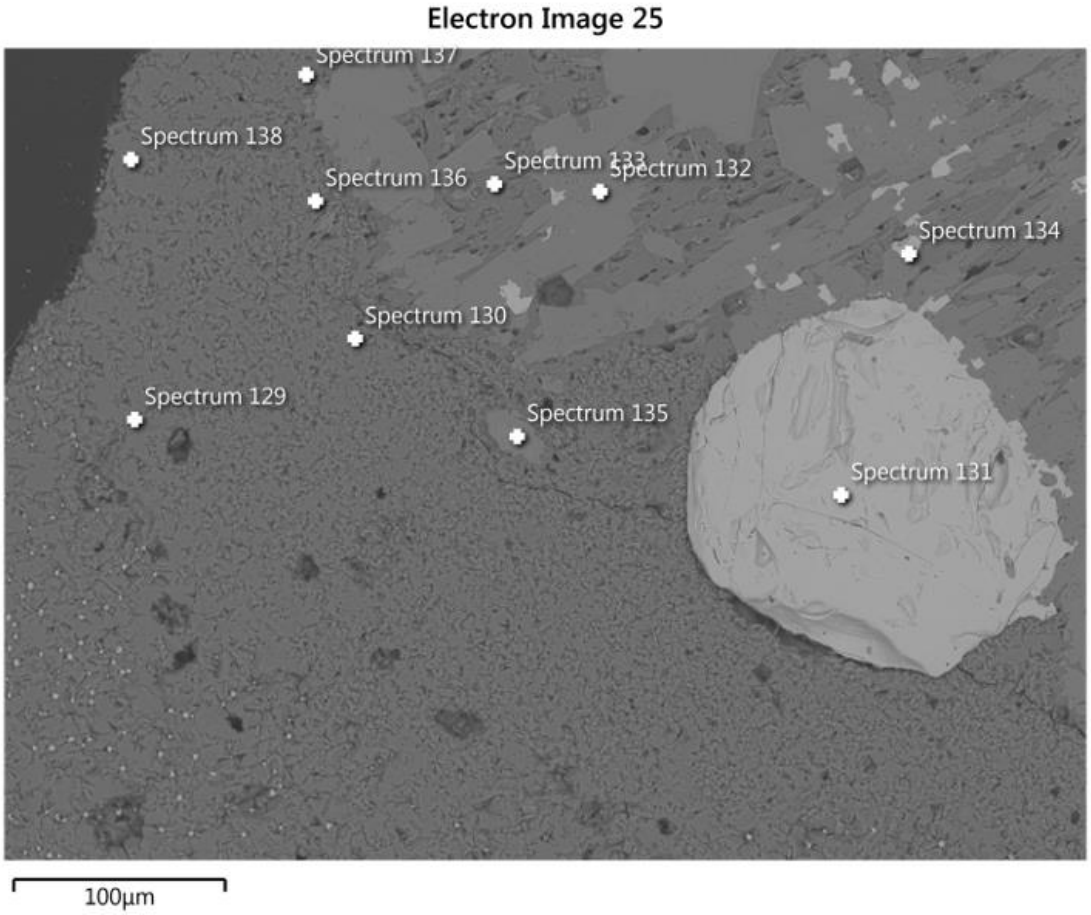

Spectrum Label	Spectrum 129	Spectrum 130	Spectrum 131	Spectrum 132	Spectrum 133	Spectrum 134	Spectrum 135	Spectrum 136	Spectrum 137	Spectrum 138
Na_2O	2.3	2.2			2.2		0.3	2.4	2.6	2.3
MgO	1.2	1.2		16.1	1.8	5.7	17.1	1.3	2.0	3.5
Al_2O_3	15.7	15.4	2.4	3.4	15.6	3.6	1.8	15.7	15.7	15.6
P_2O_5	58.0	58.7		52.3	58.5	0.8	54.4	59.7	59.2	59.0
K_2O		0.2			0.3					
SiO_2	1.1	1.3			1.9			1.7	2.4	3.4
CaO	8.2	7.7		17.3	6.4	0.4	18.7	7.1	6.2	5.5
TiO_2	0.9	0.9	8.1	0.8	1.1	5.0	0.3	0.8	0.8	0.8
VO_2			0.6							
MnO	0.3		0.7	0.5	0.3	0.7	0.5	0.3	0.3	
$FeO_{(TOT)}$	4.6	3.5	81.8	8.8	4.4	77.0	7.0	4.0	3.3	4.6
Total	92.3	91.2	93.6	99.1	92.4	93.3	100.2	93.0	92.5	94.9

Electron Image 26

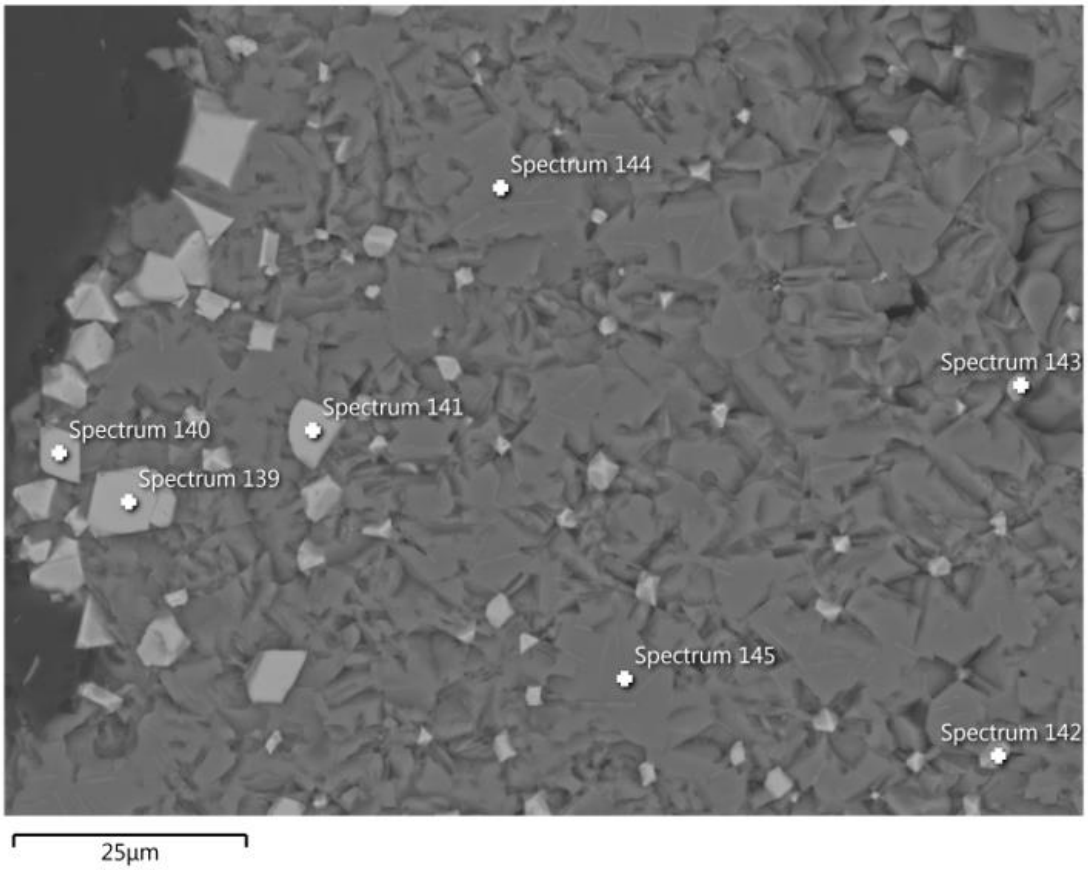

Spectrum Label	Spectrum 139	Spectrum 140	Spectrum 141	Spectrum 142	Spectrum 143	Spectrum 144	Spectrum 145
Na_2O						2.5	2.5
MgO	6.1	6.1	6.0	4.0	6.6	0.8	0.8
Al_2O_3	3.6	3.6	3.8	3.7	4.3	16.0	16.0
SiO_2	0.6	0.5	0.7	2.4	1.7	56.0	55.5
K_2O						0.8	0.7
CaO	0.2	0.2	0.2	0.4	0.3	8.0	7.8
TiO_2	1.6	1.7	1.8	2.4	1.9	0.8	0.7
MnO	0.6	0.5	0.5	0.7	0.6		0.3
$FeO_{(TOT)}$	79.8	79.1	79.2	90.4	70.9	3.9	4.0
Total	92.5	91.8	92.1	104.1	86.2	88.7	88.4

Electron Image 27

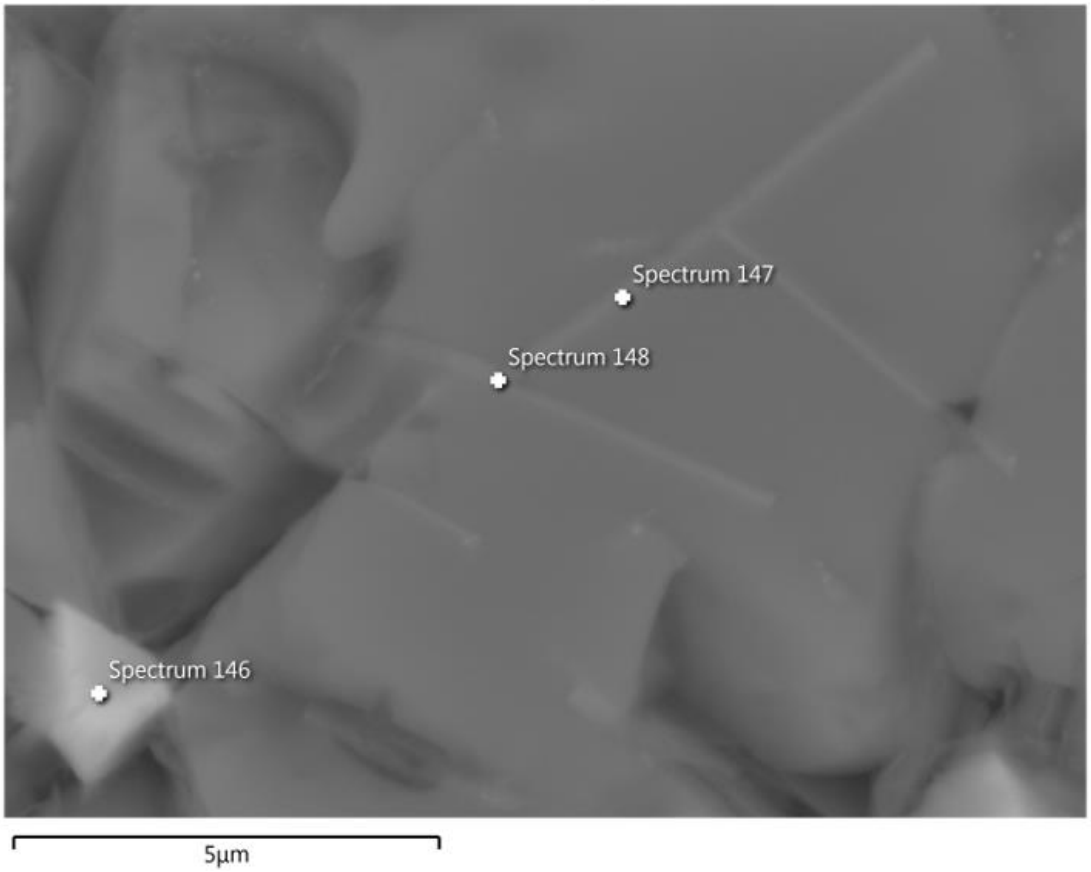

Spectrum Label	Spectrum 148	Spectrum 146	Spectrum 147
Na_2O	2.2		2.5
MgO	5.3	6.3	6.4
Al_2O_3	15.7	4.9	14.9
SiO_2	53.6	5.1	51.2
K_2O	2.4	0.1	2.6
CaO	5.0	0.6	4.5
TiO_2	1.0	1.7	1.1
MnO		0.5	
$FeO_{(TOT)}$	6.9	71.1	6.2
Total	92.2	90.3	89.4

Electron Image 28

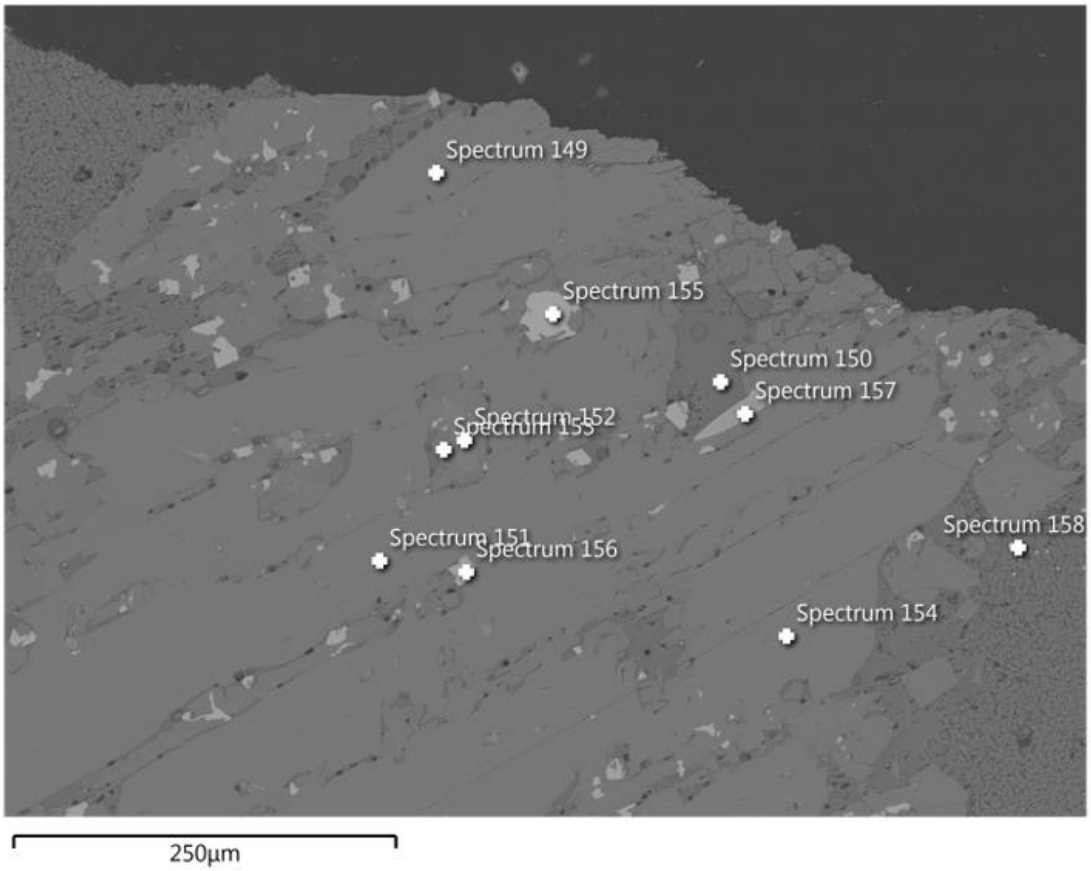

Spectrum Label	Spectrum 149	Spectrum 150	Spectrum 151	Spectrum 152	Spectrum 153	Spectrum 154	Spectrum 155	Spectrum 156	Spectrum 157	Spectrum 158
Na_2O	1.4	2.2	1.4			1.3				
MgO	13.4	4.0	13.7	19.8	17.1	13.4	4.1	5.5	6.9	5.1
Al_2O_3	7.9	14.9	7.7	1.0	2.4	7.6	2.4	3.9	0.6	4.3
SiO_2	46.0	49.8	45.2	49.7	49.6	44.8	0.6	0.8	0.6	0.9
Cl	0.1					0.2				
K_2O	0.2	1.3	0.2			0.2				
CaO	10.3	6.1	10.1	0.9	16.3	10.0	0.2	0.4	0.3	0.2
TiO_2	1.7	1.5	1.4		0.5	1.4	7.7	5.6	39.7	4.3
VO_2							0.5			
MnO	0.6		0.5	1.6	0.7	0.5	0.8		0.6	0.4
$FeO_{(TOT)}$	15.7	6.8	14.9	24.8	9.5	15.1	77.2	76.9	45.7	78.5
Total	97.3	86.6	95.2	97.7	96.2	94.5	93.6	93.0	94.4	93.7

Sample 20-1-1

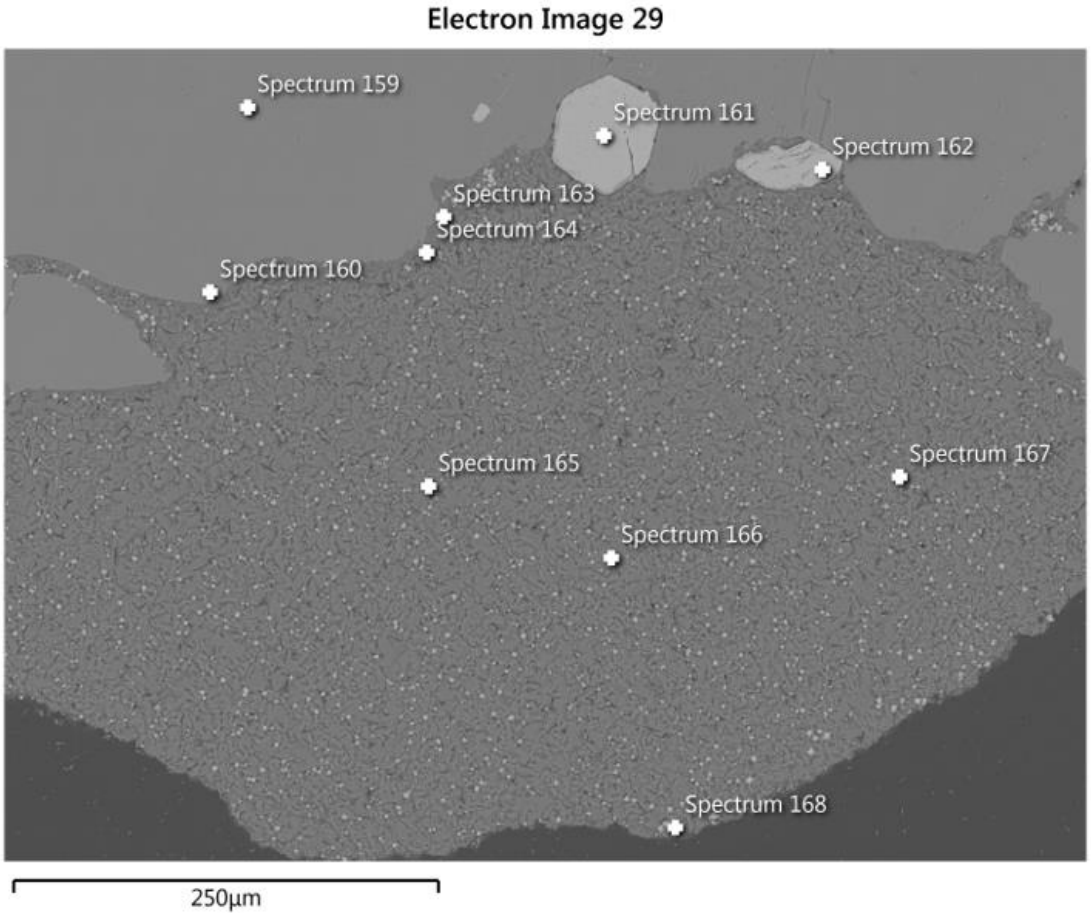

Spectrum Label	Spectrum 159	Spectrum 160	Spectrum 161	Spectrum 162	Spectrum 163	Spectrum 164	Spectrum 165	Spectrum 166	Spectrum 167	Spectrum 168
Na_2O					2.9	2.6	2.2	2.7	2.6	
MgO	14.3	14.4	4.5	5.4	0.6	0.6	1.4	1.4	0.5	5.3
Al_2O_3	4.0	4.0	6.2	6.2	17.6	18.5	16.9	16.2	16.3	4.5
SiO_2	48.1	48.6	1.1	0.7	57.7	62.1	57.4	52.8	55.2	3.4
K_2O					1.4	1.5	1.3	1.3	0.9	
CaO	20.1	21.1	0.3	0.3	5.6	6.8	8.3	7.0	7.8	0.3
TiO_2	0.8	0.8	9.0	6.1	0.5	0.5	0.7	0.6	0.7	1.6
VO_2			0.9	1.0						
Cr_2O_3			0.3	0.5						
MnO			0.3	0.4						0.6
$FeO_{(TOT)}$	8.1	8.1	71.3	74.3	2.5	2.5	4.4	3.2	3.0	74.8
Total	95.5	96.9	93.9	94.9	88.8	95.1	92.7	85.1	87.0	90.5

Electron Image 30

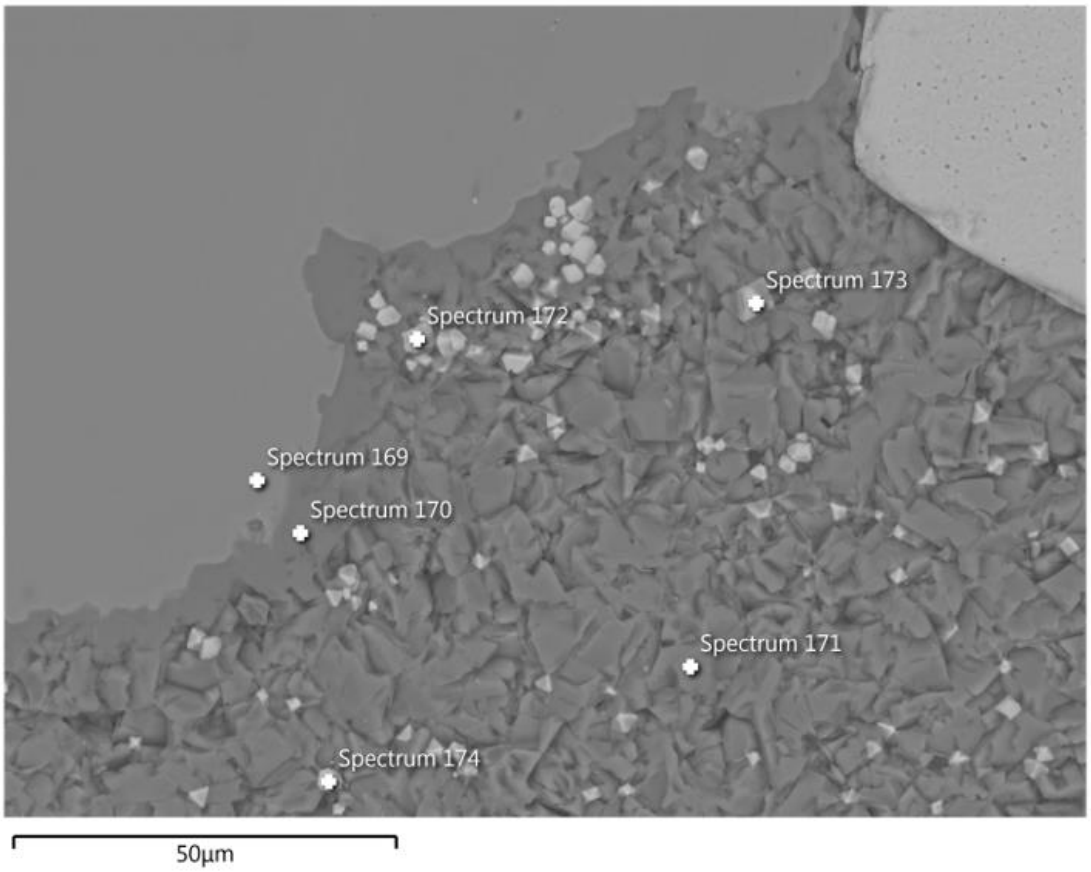

Spectrum Label	Spectrum 169	Spectrum 170	Spectrum 171	Spectrum 172	Spectrum 173	Spectrum 174
Na_2O		2.7	2.4			
MgO	14.4	0.5	0.9	6.0	5.6	5.0
Al_2O_3	3.8	17.8	16.8	3.7	3.9	3.7
SiO_2	48.2	60.2	60.1	1.1	2.5	1.6
K_2O		1.2	1.1			
CaO	20.6	6.3	8.3	0.4	0.5	0.4
TiO_2	0.8	0.5	0.8	1.8	1.9	1.8
MnO				0.5	0.5	0.5
$FeO_{(TOT)}$	8.2	2.5	3.7	75.8	76.1	78.8
Total	96.0	91.8	94.1	89.3	91.0	91.8

Electron Image 31

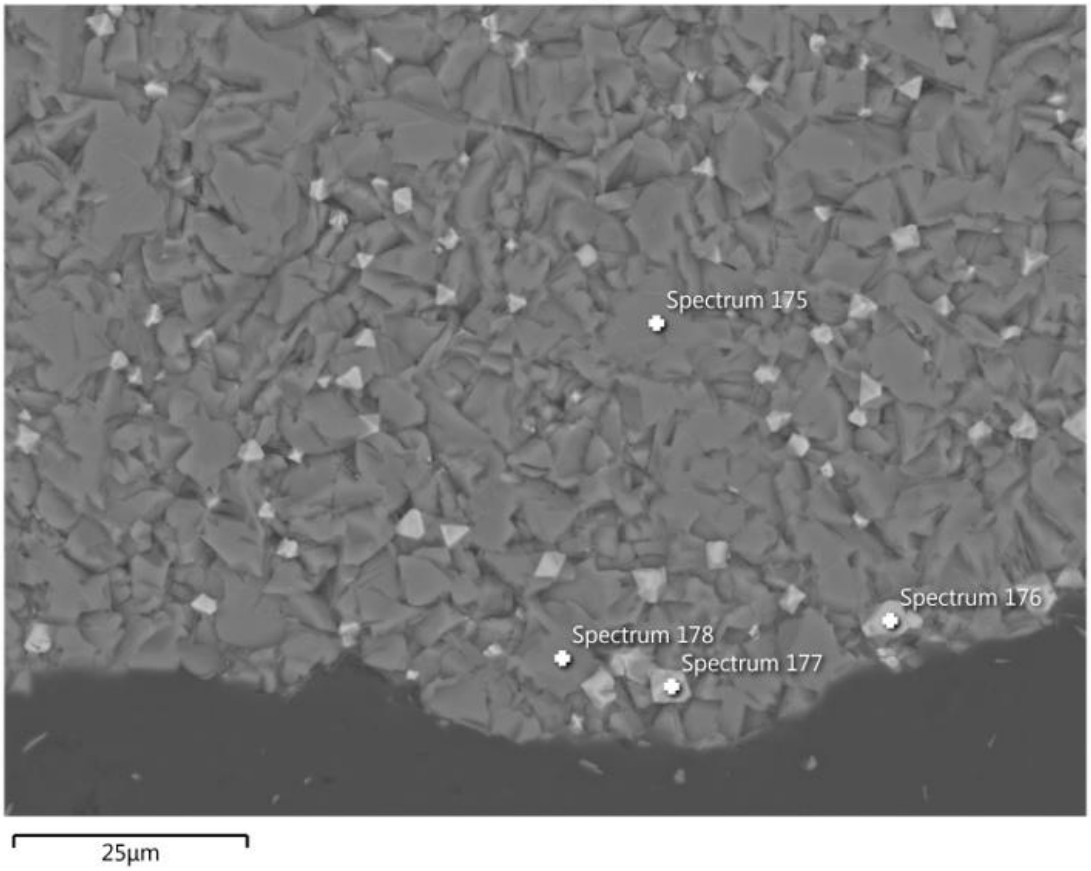

Spectrum Label	Spectrum 175	Spectrum 176	Spectrum 177	Spectrum 178
Na_2O	2.5			2.8
MgO	0.8	5.8	4.2	0.4
Al_2O_3	16.5	3.7	4.2	15.7
SiO_2	56.1	0.8	3.7	51.9
K_2O	0.9			0.9
CaO	7.9	0.2	0.4	6.8
TiO_2	0.7	1.5	1.8	0.6
MnO	0.3		0.4	
$FeO_{(TOT)}$	3.2	78.4	78.3	2.3
Zr				0.6
In			0.3	
W				1.8
Os				1.3

Electron Image 32

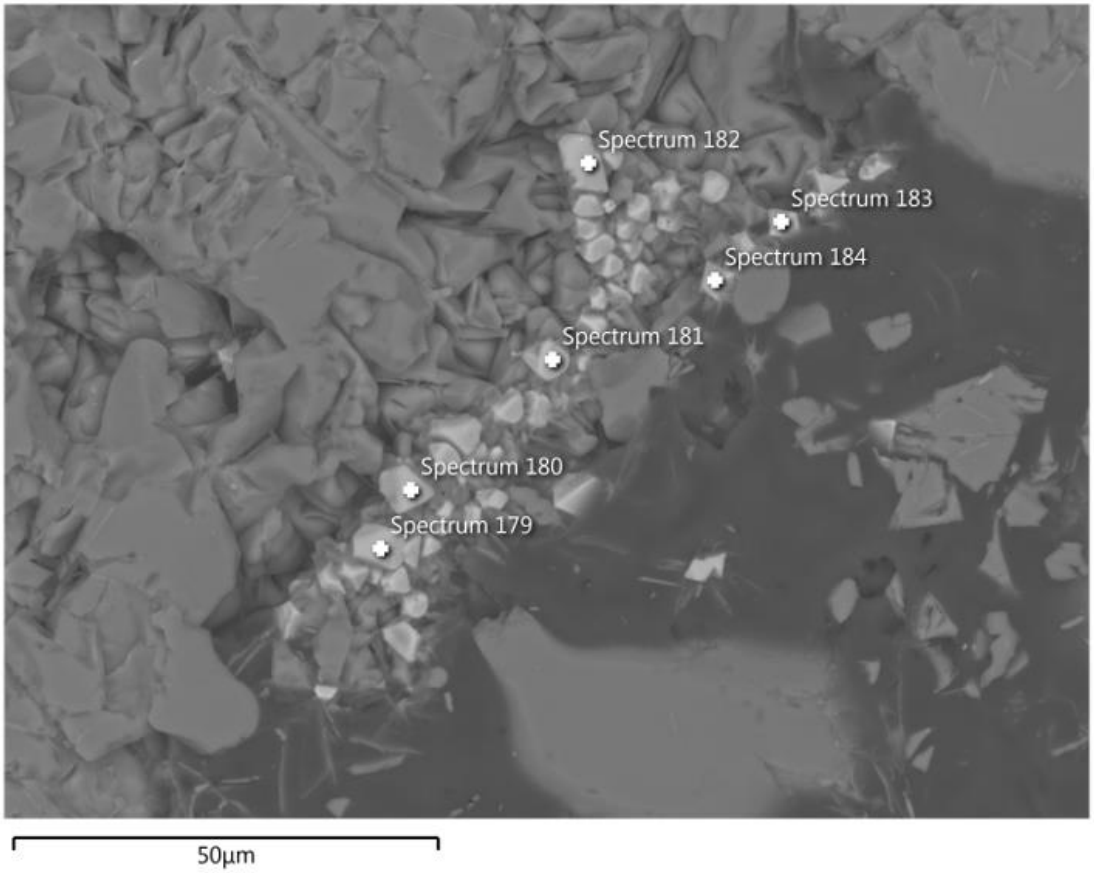

Spectrum Label	Spectrum 179	Spectrum 180	Spectrum 181	Spectrum 182	Spectrum 183	Spectrum 184
MgO	6.1	6.1	4.0	5.3	6.6	7.1
Al_2O_3	3.5	3.6	4.3	3.6	4.3	4.1
SiO_2	0.8	0.7	8.1	1.4	2.7	1.4
K_2O			0.2			
CaO	0.2	0.2	0.6	0.3	0.3	0.2
TiO_2	1.6	1.7	1.8	1.8	1.6	1.5
MnO		0.5	0.5		0.5	
$FeO_{(TOT)}$	80.8	79.4	76.3	83.5	70.1	71.9
Total	93.0	92.2	95.9	95.8	86.0	86.1

Electron Image 33

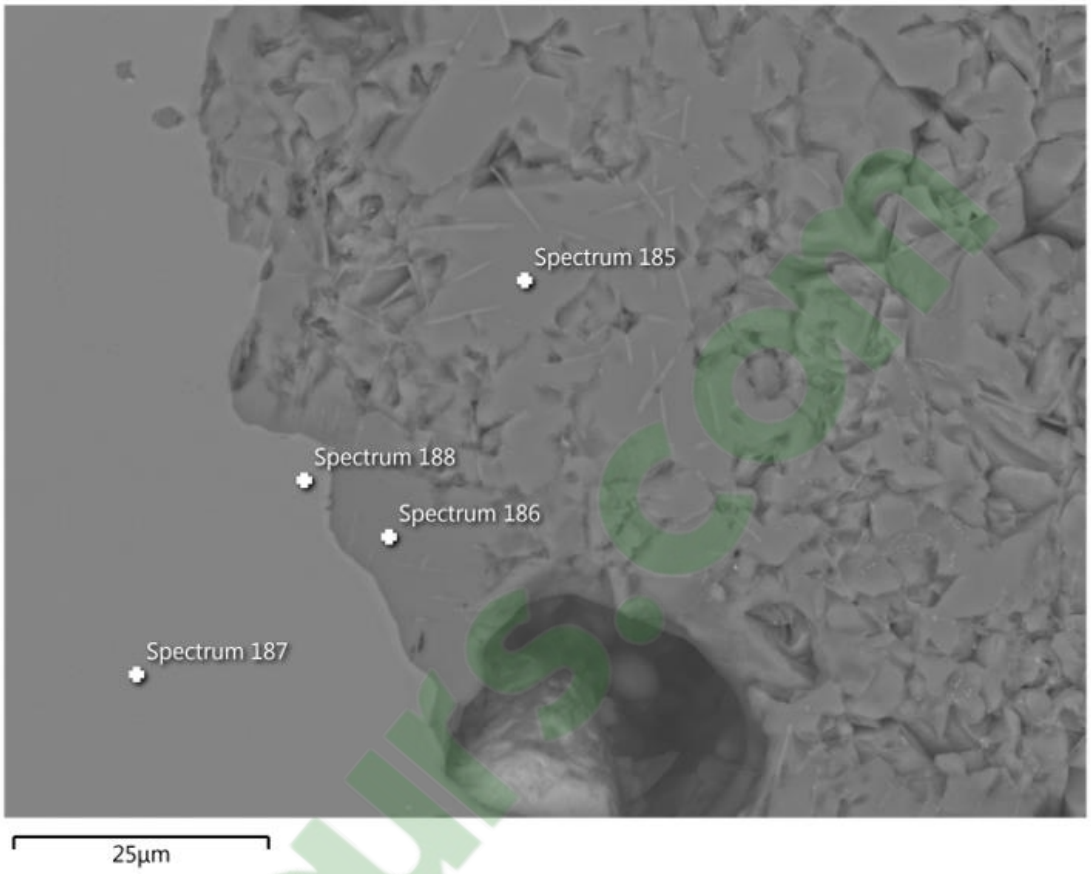

Spectrum Label	Spectrum 185	Spectrum 186	Spectrum 187	Spectrum 188
Na_2O	2.2	2.9	0.4	
MgO	1.6	0.9	14.1	14.1
Al_2O_3	16.1	17.4	4.5	4.6
SiO_2	53.8	53.7	47.6	46.9
K_2O	0.7	0.9		
CaO	7.9	5.5	19.8	19.7
TiO_2	0.9	0.8	0.8	0.8
MnO			0.3	
$FeO_{(TOT)}$	4.3	3.5	8.5	7.8
Total	87.5	85.6	95.9	93.9

Electron Image 34

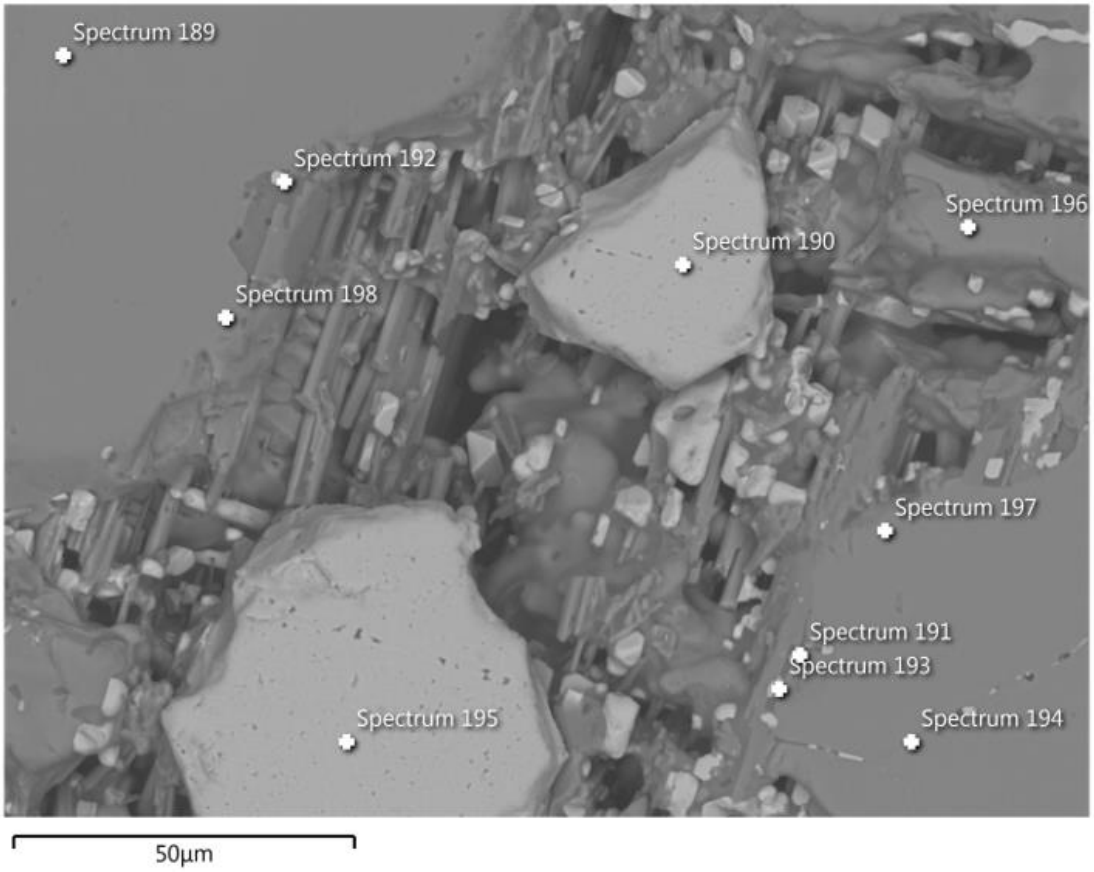

Spectrum Label	Spectrum 189	Spectrum 190	Spectrum 191	Spectrum 192	Spectrum 193	Spectrum 194	Spectrum 195	Spectrum 196	Spectrum 197	Spectrum 198
MgO	14.4	4.8	6.8	5.5	6.4	7.6	3.6	37.3	14.6	14.7
Al_2O_3	4.0	6.2	3.3	2.8	3.0	4.0	4.9		3.9	4.1
SiO_2	47.4	0.6	4.1	1.6	2.2	19.0	0.4	36.7	46.4	48.3
CaO	19.1	0.2	0.5	0.8	0.5	7.1		0.3	18.6	20.7
TiO_2	1.0	5.9	2.2	2.5	2.4	2.0	11.1		0.7	0.8
VO_2		0.9					1.0			
Cr_2O_3		0.4					0.4			
MnO				0.3	0.4			0.4		0.3
$FeO_{(TOT)}$	9.5	74.1	74.8	84.5	77.1	52.9	72.2	23.2	8.0	8.8
Total	95.5	92.9	91.6	98.1	92.0	92.6	93.6	97.9	92.2	97.8

Sample 23-2-1

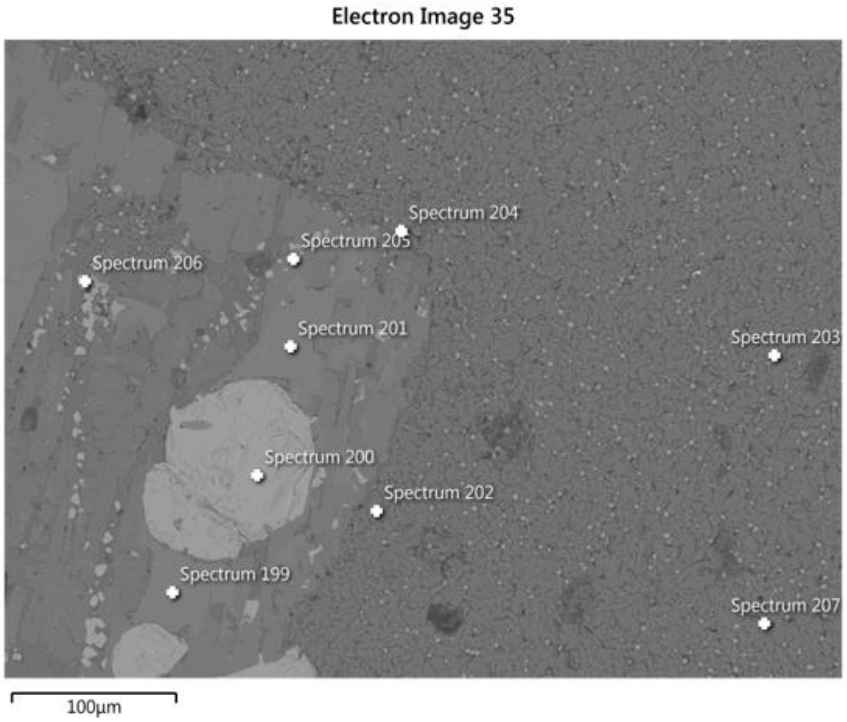

Spectrum Label	Spectrum 199	Spectrum 200	Spectrum 201	Spectrum 202	Spectrum 203	Spectrum 204	Spectrum 205	Spectrum 206	Spectrum 207
Na_2O				2.7	1.8				
MgO	19.1	2.0	19.3	2.2	7.6	5.1	4.8	5.2	4.8
Al_2O_3	0.7	2.0	0.5	15.2	14.6	4.6	2.9	2.6	5.0
SiO_2	50.1	0.4	50.4	53.3	52.0	4.2	1.0	0.9	6.0
P_2O_5				0.5	0.5				
K_2O				1.4	3.6				0.2
CaO	1.0		1.1	6.1	6.2	0.6	0.4	0.3	0.7
TiO_2		5.8		0.8	1.8	3.3	3.4	3.9	2.9
VO_2		0.5							
MnO	1.8	0.7	1.8			0.5	0.7	0.7	0.6
$FeO_{(TOT)}$	25.6	83.1	24.9	4.5	15.4	70.6	80.2	79.3	70.6
Total	98.2	94.5	98.0	86.7	103.5	88.8	93.4	92.9	90.6

Electron Image 36

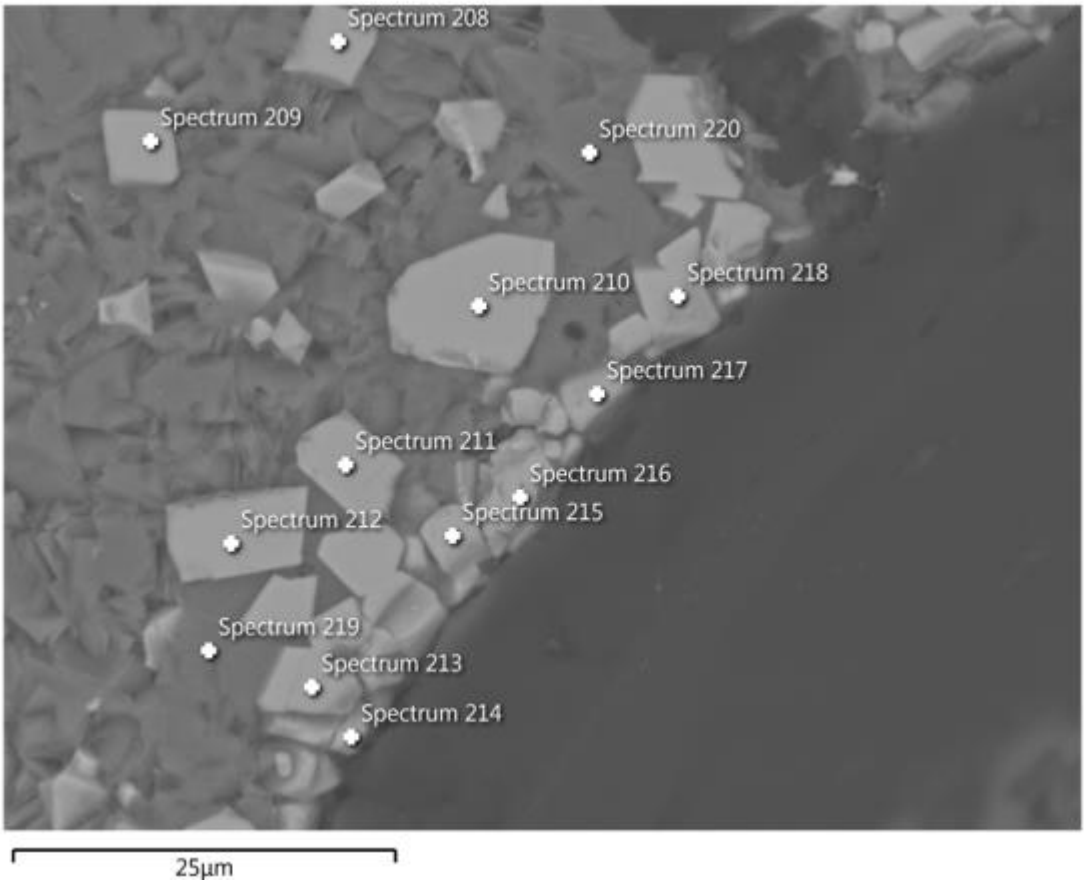

Spectrum Label	Spectrum 208	Spectrum 209	Spectrum 210	Spectrum 211	Spectrum 212	Spectrum 213	Spectrum 214	Spectrum 215	Spectrum 216	Spectrum 217	Spectrum 218	Spectrum 219	Spectrum 220
Na_2O												2.7	2.7
MgO	5.7	5.8	5.5	5.8	5.7	5.6	6.0	5.7	5.6	6.3	3.5	3.1	0.9
Al_2O_3	3.7	3.9	3.8	3.8	3.7	3.7	4.1	3.8	3.6	3.9	2.7	15.3	16.3
SiO_2	0.8	0.8	0.6	0.6	0.7	0.5	1.1	0.4	0.5	0.6	0.6	52.8	57.0
P_2O_5													0.3
K_2O												1.7	1.0
CaO	0.3	0.3	0.2				0.2		0.3		0.2	5.3	7.1
TiO_2	1.9	1.9	1.8	1.9	1.9	2.0	1.9	1.9	1.8	1.8	2.2	0.8	0.4
MnO	0.8	0.5	0.6	0.7	0.7	0.7	0.6	0.7	0.6	0.6	0.8		
$FeO_{(TOT)}$	79.2	78.3	80.4	80.2	80.2	81.5	78.7	80.6	80.6	77.4	93.9	9.7	3.2
CuO									0.9				
CoO											1.4		
Total	92.3	91.4	92.9	93.0	92.9	94.0	92.6	93.1	93.8	90.5	105.4	91.5	89.1

Electron Image 37

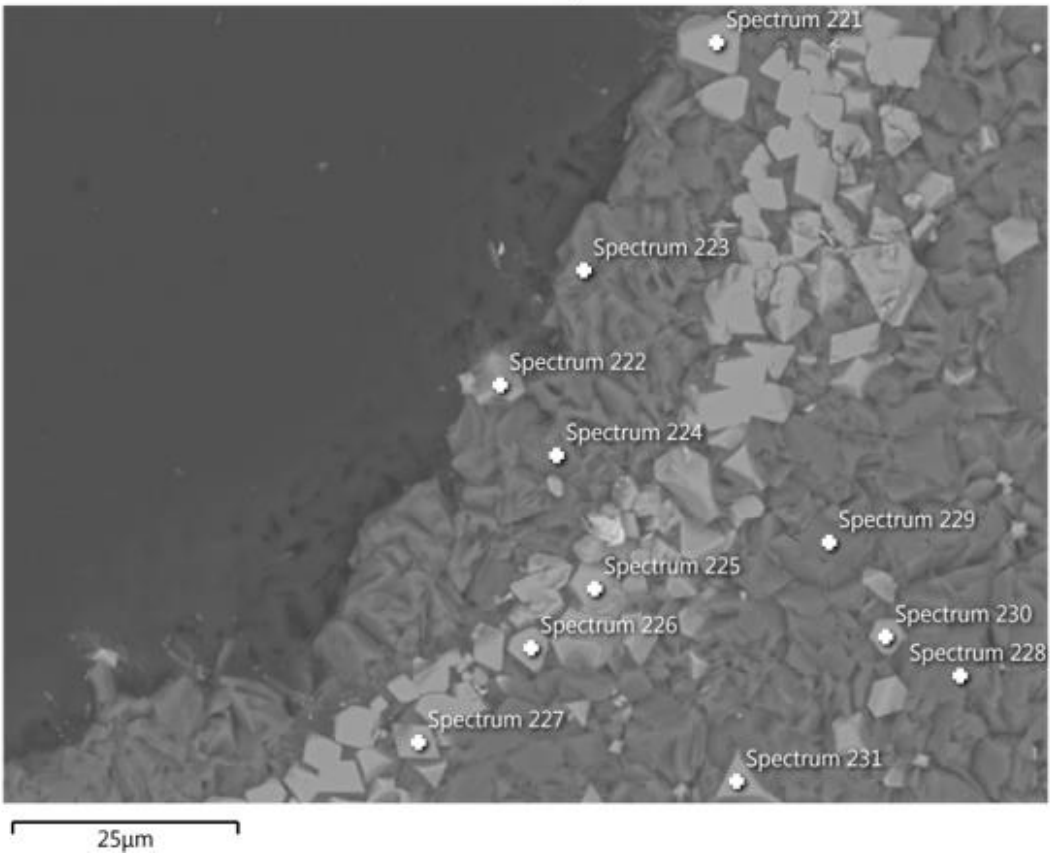

Spectrum Label	Spectrum 221	Spectrum 222	Spectrum 223	Spectrum 224	Spectrum 225	Spectrum 226	Spectrum 227	Spectrum 228	Spectrum 229	Spectrum 230	Spectrum 231
Na_2O			2.2	1.9				2.3	2.8		
MgO	5.8	6.6	2.6	1.8	4.5	5.8	5.7	2.6	1.0	6.0	5.7
Al_2O_3	3.8	4.4	15.3	19.3	3.6	3.9	3.9	16.6	16.1	4.1	4.1
SiO_2	0.6	0.6	55.9	67.7	1.0	0.6	0.6	55.1	54.0	0.9	0.9
K_2O			1.3	1.7				1.7	0.9		
CaO			6.9	10.2	0.2	0.2	0.2	6.9	7.3	0.3	0.3
TiO_2	1.7	1.8	0.7	0.9	2.0	1.9	1.8	0.9	0.6	1.9	1.9
MnO	0.5	0.4			0.6	0.6	0.5			0.6	0.5
$FeO_{(TOT)}$	79.9	72.0	4.5	6.1	87.4	78.3	79.8	5.4	3.7	77.5	78.0
Total	92.3	85.9	89.5	109.5	99.3	91.3	92.5	91.4	86.3	91.1	91.2

Electron Image 38

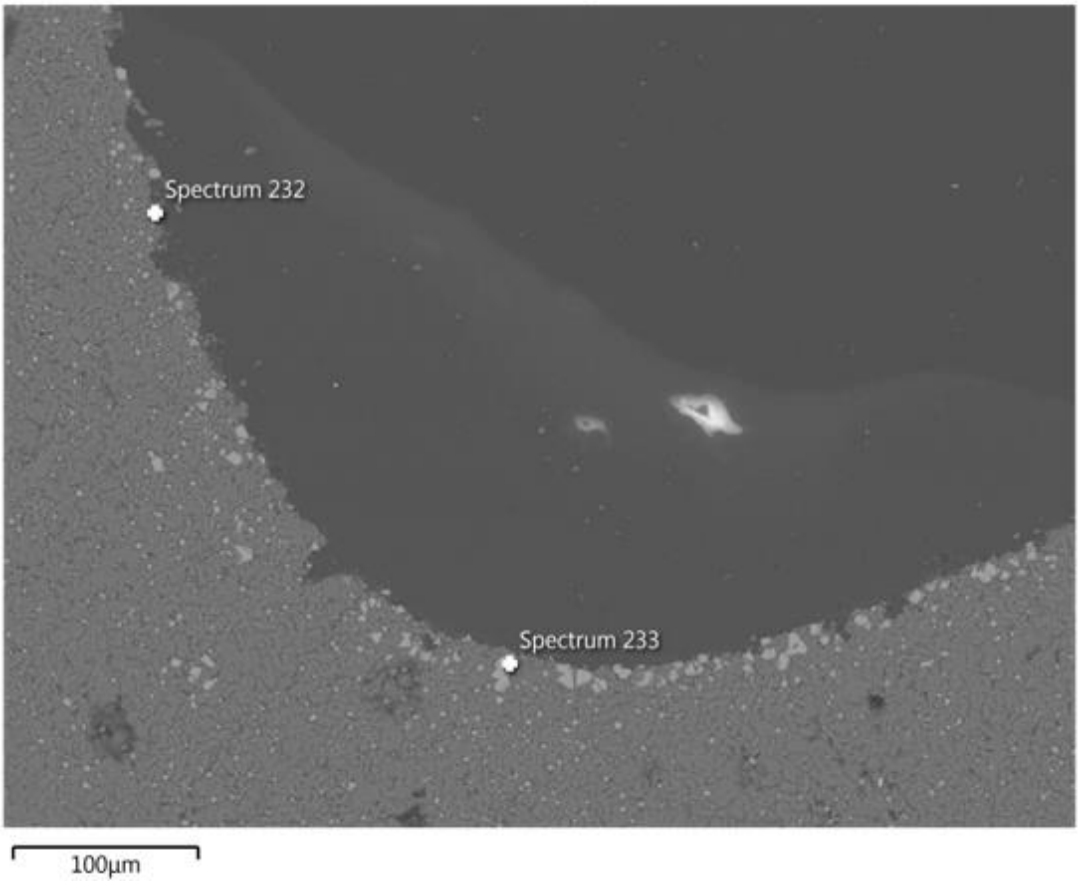

Spectrum Label	Spectrum 232	Spectrum 233
MgO	5.6	6.0
Al_2O_3	3.6	3.7
SiO_2	0.4	0.5
CaO	0.2	
TiO_2	1.9	2.0
MnO	0.6	0.5
$FeO_{(TOT)}$	80.1	79.8
Total	92.6	92.6

Sample 24-2

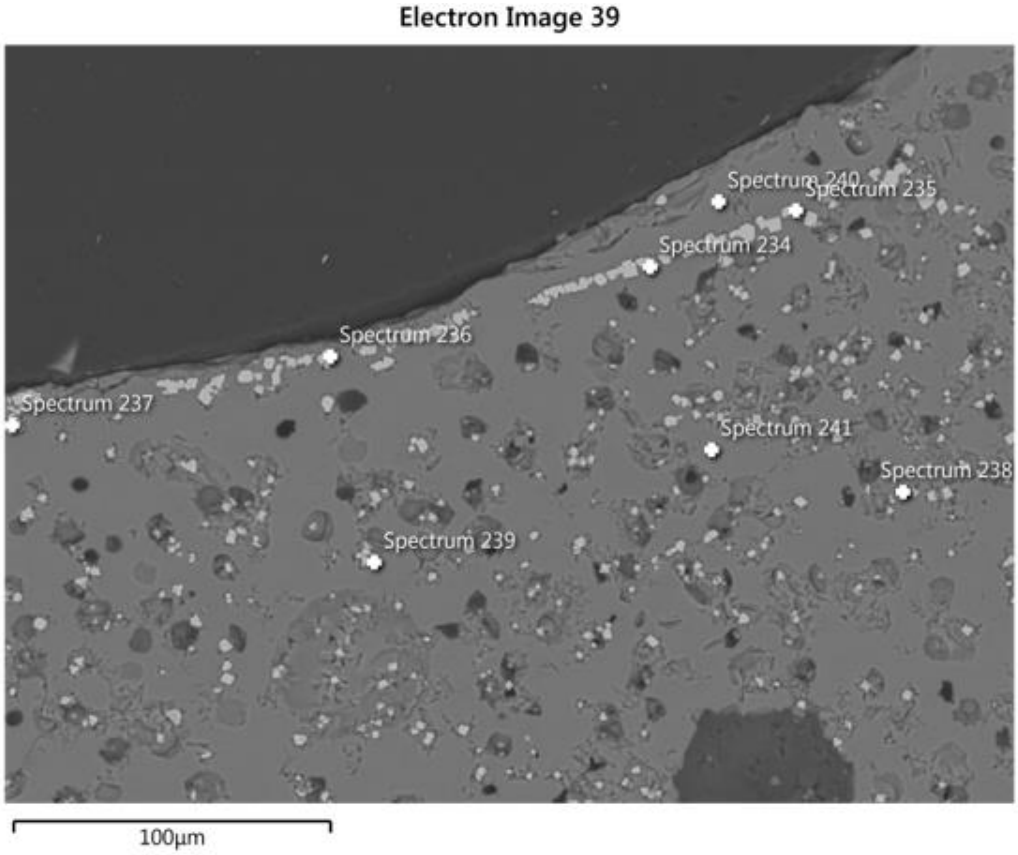

Spectrum Label	Spectrum 234	Spectrum 235	Spectrum 236	Spectrum 237	Spectrum 238	Spectrum 239	Spectrum 240	Spectrum 241
Na_2O	0.0	0.0	0.0	0.0	0.0	0.0	2.7	2.6
MgO	6.5	6.5	6.5	6.7	6.7	6.3	1.9	2.0
Al_2O_3	3.9	4.2	3.8	3.7	4.0	4.1	16.5	17.0
SiO_2	0.6	1.3	0.5	0.4	0.9	1.5	53.9	54.9
K_2O	0.0	0.1	0.0	0.0	0.0	0.0	1.3	1.2
CaO	0.0	0.3	0.2	0.2	0.3	0.3	6.8	7.8
TiO_2	1.2	1.1	1.2	1.1	1.3	1.4	0.8	0.8
MnO	0.8	0.6	0.7	0.6	0.7	0.6	0.0	0.0
$FeO_{(TOT)}$	78.7	77.0	78.0	78.2	76.6	76.9	3.9	4.0
Total	91.7	91.1	90.8	90.9	90.4	91.1	87.8	90.4

Sample 26-3-1

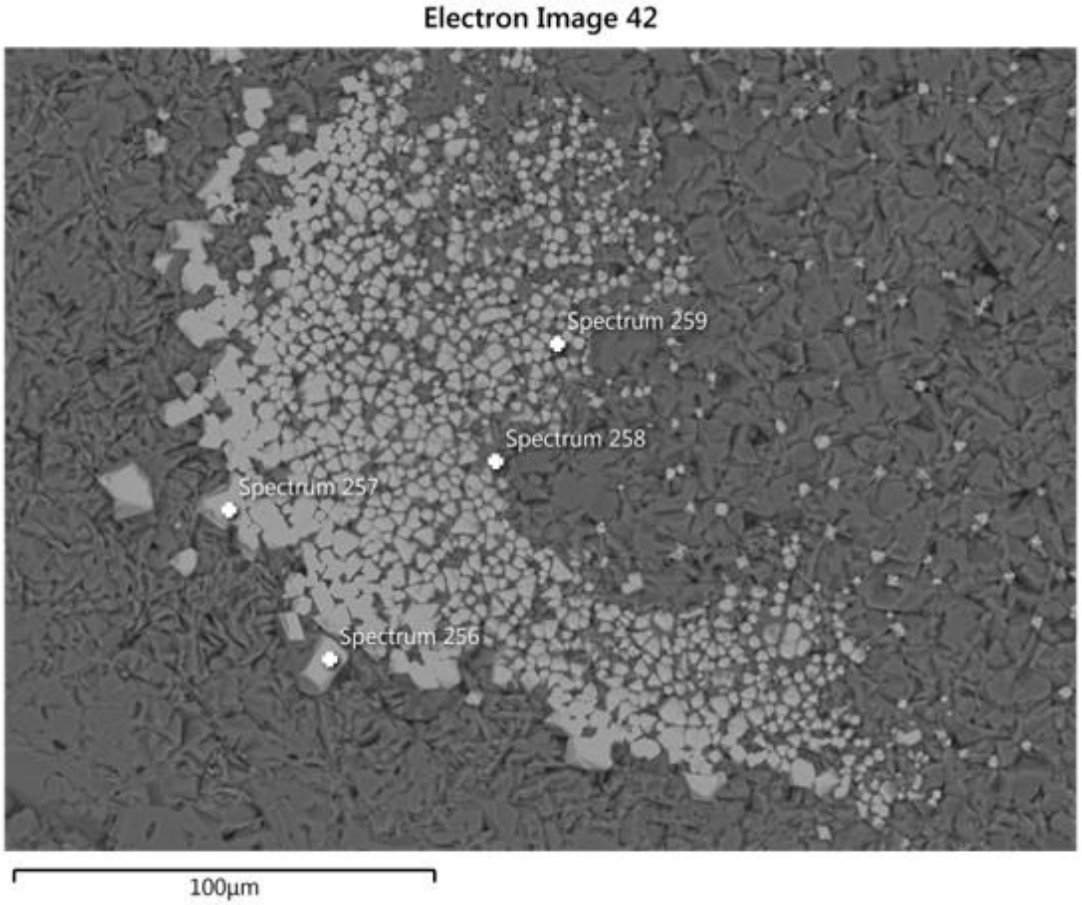

Spectrum Label	Spectrum 256	Spectrum 257	Spectrum 258	Spectrum 259
MgO	5.5	5.5	5.3	4.9
Al_2O_3	3.5	3.6	4.3	4.0
SiO_2	0.6	0.6	2.7	1.7
CaO	0.2	0.2	0.3	0.2
TiO_2	2.4	2.3	2.0	2.2
MnO	0.7	0.5	0.7	0.7
$FeO_{(TOT)}$	80.1	80.6	74.3	79.5
Total	92.9	93.3	89.5	93.2

Sample Krafla KR7

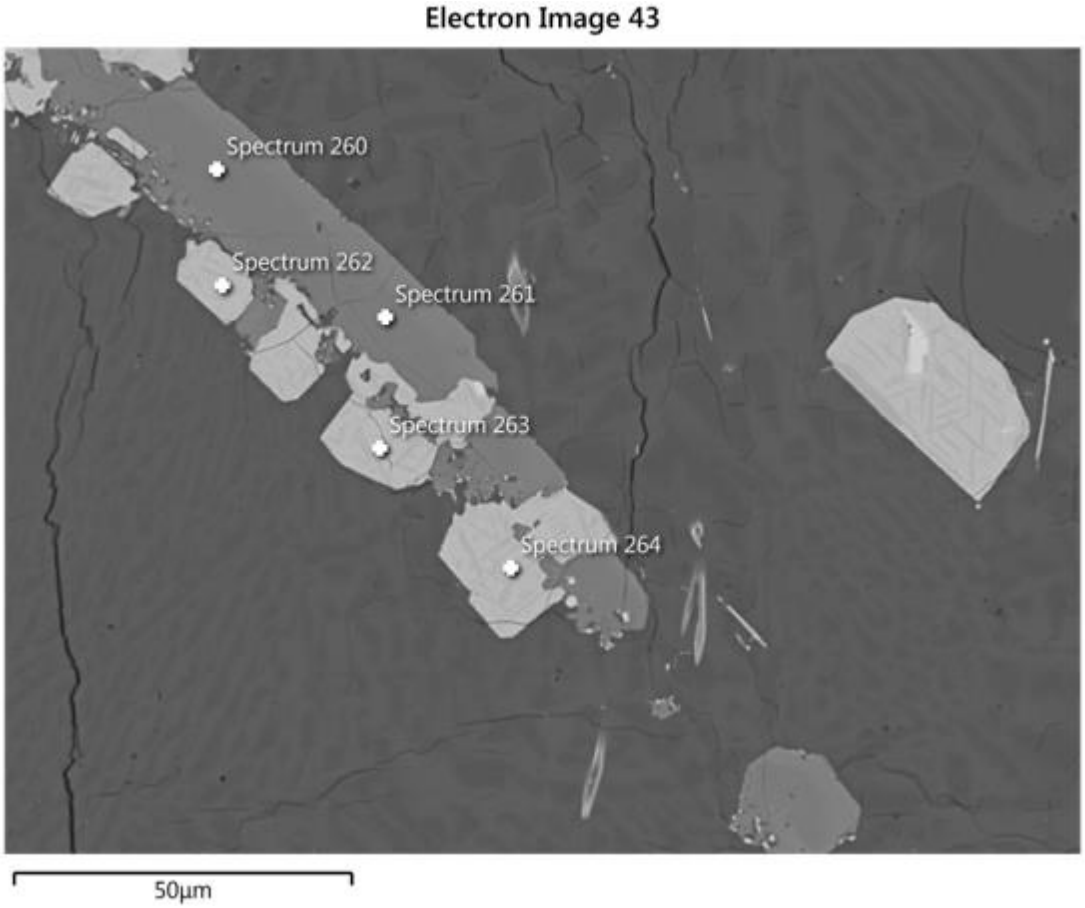

Spectrum Label	Spectrum 260	Spectrum 261	Spectrum 262	Spectrum 263	Spectrum 264
MgO	8.1	8.2			
Al_2O_3	1.8	1.5			
SiO_2	47.8	48.2	1.3	1.2	1.2
CaO	17.8	17.6			
TiO_2	0.8	0.5	14.2	10.0	13.1
MnO	0.6	0.8	0.9	1.0	1.1
$FeO_{(TOT)}$	19.6	19.5	76.2	81.5	78.7
Total	96.5	96.4	92.6	93.8	94.2

Electron Image 44

Spectrum Label	Spectrum 265	Spectrum 266	Spectrum 267	Spectrum 268	Spectrum 269	Spectrum 270	Spectrum 271
Na_2O						2.0	1.7
Al_2O_3			0.5	0.4	0.7	4.1	4.9
SiO_2	1.1	1.4	1.2	1.2	52.1	18.0	51.3
P_2O_5					6.9		1.8
S	37.6			12.2			
Cl					0.5		0.1
K_2O		0.1			0.3	1.0	1.9
CaO					12.7		6.5
TiO_2	0.8	39.7	10.1	6.1		31.1	
MnO		1.5	1.0	0.6		1.1	
$FeO_{(TOT)}$	76.1	52.2	76.2	53.4		36.9	1.8
Total	116.1	94.9	91.0	89.7	89.2	94.2	89.0

Electron Image 45

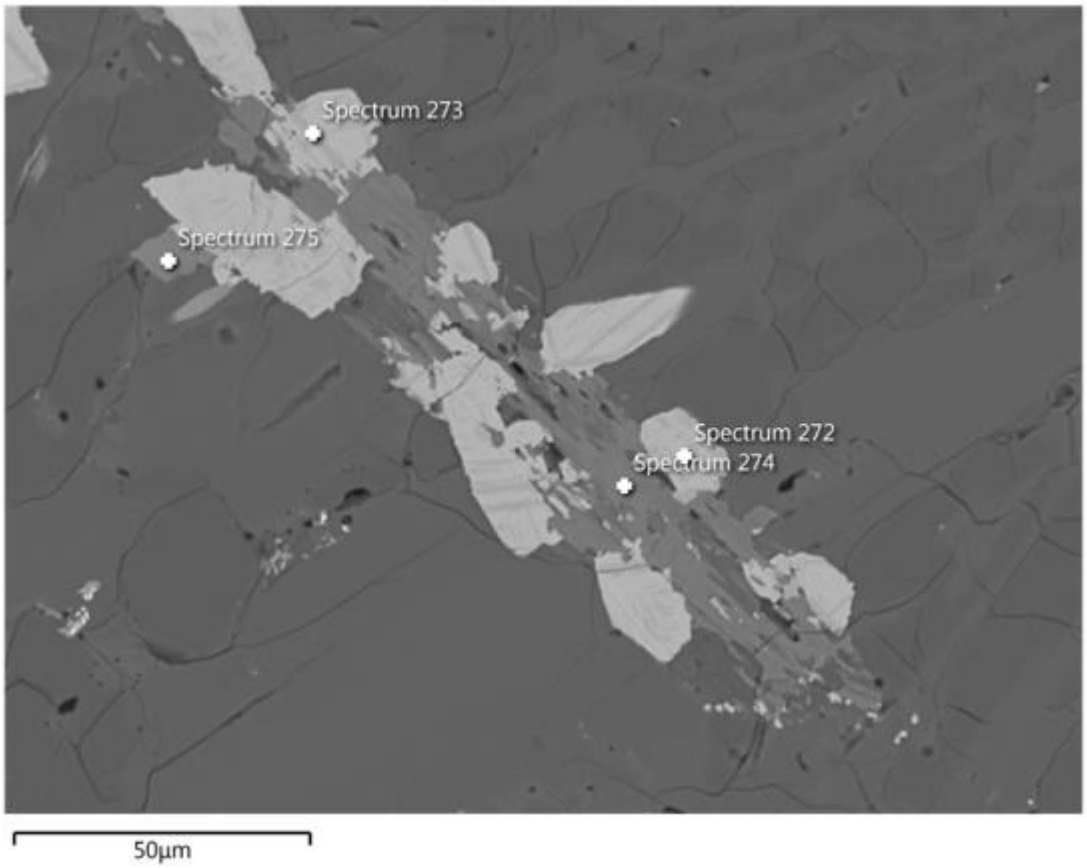

Spectrum Label	Spectrum 272	Spectrum 273	Spectrum 274	Spectrum 275
Na_2O			0.7	0.0
MgO	0.9	1.7	8.7	5.2
Al_2O_3	0.5	0.3	0.7	0.5
SiO_2	1.1	1.0	49.3	48.5
CaO	0.2	0.0	19.8	18.1
TiO_2	9.9	38.3	0.5	0.4
MnO	1.9	2.5	1.9	1.0
$FeO_{(TOT)}$	80.1	50.8	15.5	23.4
Total	94.6	94.6	97.1	97.1

Standards

DRB Hematite	**Average**	**std**
$FeO_{(TOT)}$	91.1	1.0
DRB Magnetite	**Average**	**std**
$FeO_{(TOT)}$	98.3	0.3
Astimex hematite	**Average**	**std**
$FeO_{(TOT)}$	90.0	0.6
Astimex Magnetite	**Average**	**std**
$FeO_{(TOT)}$	92.5	1.4

Appendix 4.2

Scanning conditions for imaging with conventional X-ray micro-tomography, using the Skyscan 1172, at MIAM, McGill University, Montréal.

Sample name	Voltage (kV)	Current (µA)	Filtering	Detector binning	SSD (mm)	SDD (mm)	Detector pixel size (µm)
14-1-1	45	214	Al	4x4	28,4	345,1	11,56
14-1-2	44	226	Al	4x4	28,4	345,1	11,56
15-1-1	44	226	Al	4x4	28,4	345,1	11,56
15-2-1	45	218	Al	4x4	28,4	345,1	11,56
15-2-2	44	226	Al	4x4	28,4	345,1	11,56
17-1-1	44	222	Al	4x4	28,4	345,1	11,56
17-2-1	44	222	Al	4x4	28,4	345,1	11,56
17-2-2	44	226	Al	4x4	28,4	345,1	11,56
20-1-1	44	226	Al	4x4	28,4	345,1	11,56
20-1-2	44	226	Al	4x4	28,4	345,1	11,56
20-2-1	48	208	Al	4x4	28,4	345,1	11,56
21-2-1	44	226	Al	4x4	28,4	345,1	11,56
23-2-1	44	226	Al	4x4	28,4	345,1	11,56
23-2-2	44	226	Al	4x4	28,4	345,1	11,56
24-2-1	44	226	Al	4x4	28,4	345,1	11,56
25-2-1	44	226	Al	4x4	28,4	345,1	11,56
26-1-1	44	226	Al	4x4	28,4	345,1	11,56
26-3-1	44	226	Al	4x4	28,4	345,1	11,56
27-1-1	44	226	Al	4x4	28,4	345,1	11,56
KR7	80	124	Al+Cu	1x1	75,6	228,5	12,06
KR19	100	100	Al+Cu	2x2	257,8	358,5	12,06

Sample name	isotropic voxel size (µm)	Exposure time/proj. (ms)	Rotation step (°)	# of projections	Frame averaging	random movement
14-1-1	3,8	474	0,40	902 over 360°	4	10
14-1-2	3,8	474	0,68	531 over 360°	4	10
15-1-1	3,8	474	0,40	902 over 360°	4	10
15-2-1	3,8	474	0,40	903 over 360°	4	10
15-2-2	3,8	474	0,68	531 over 360°	4	10
17-1-1	4,8	474	0,40	902 over 360°	4	10
17-2-1	3,8	474	0,40	524 over 360°	4	10
17-2-2	3,8	474	0,68	531 over 360°	4	10
20-1-1	3,8	474	0,40	902 over 360°	4	10
20-1-2	3,8	474	0,68	531 over 360°	4	10
20-2-1	4,4	474	0,40	902 over 360°	4	10
21-2-1	4,8	474	0,40	902 over 360°	4	10
23-2-1	3,8	474	0,40	902 over 360°	4	10
23-2-2	3,8	474	0,40	902 over 360°	4	10
24-2-1	4,8	474	0,68	531 over 360°	4	10
25-2-1	3,8	474	0,68	531 over 360°	4	10
26-1-1	3,8	474	0,68	531 over 360°	4	10
26-3-1	3,1	474	0,68	531 over 360°	4	10
27-1-1	2,7	474	0,68	531 over 360°	4	10
KR7	3,9	4123	0,30	682 over 180°	3	10
KR19	17,3	2360	0,40	491 over 180°	1	10

CHAPTER 5

Synthesis and conclusions

This research focuses on three of the most prevalent bubble-crystal interactions: heterogeneous nucleation of bubbles on crystals, heterogeneous nucleation of crystals on bubbles and their mutual detachment or attachment. Several key problems were identified from the existing literature: i) consideration of the crystal efficiency of heterogeneous bubble nucleation lead to the idea that a non-dominant phase (oxide) was thought to be the only one favourable for bubble nucleation (Hurwitz and Navon, 1994; Gardner and Denis, 2004; Gualda and Ghiorso, 2007), ii) the sparsity and discrepancies in contact angle measurements, where overlapping values were reported for silicates and oxides (Mangan et al., 2004, $\theta <$ 65° for quartz and 43° for titanomagnetite) but the former were deemed unfavourable and the later favourable for bubble nucleation, and iii) early processes could not be identified from post-process samples iv) measurements in 2D were unable to capture important information regarding the initial stages of bubble nucleation.

The main differences between our nucleation experiments and previous ones is the use of starting andesitic glass composition and the addition of crystals into the starting material (Table 5.1 – same as Table 1.1 with the addition of the study in Chapter 3).

Table 5.1: Comparison between previous bubble nucleation studies and the study presented in Chapter 3. dec. refers to decompression, HEN refers to heterogeneous bubble nucleation. ✓ indicates bubbles present on crystal surfaces, x indicates no bubbles on crystal surfaces, ? indicates not specified.

reference	composition	ΔP_{dec} (MPa)	crystal	crystal attribute	bubbles	comment
this study	andesite	0	plagioclase	added	✓	±25 MPa
		50			✓	± 25 MPa
		200			✓	850 to 650 MPa (± 25 MPa)
		350			✓	± 25 MPa
Fiege et al. (2014)	andesite	70-400	/	/	in melt	homogeneous nucleation
Hurwitz and Navon (1994)	rhyolite	≥ 5	Fe-Ti oxides	present in starting material	✓	
		30	biotite		✓	
			zircon		✓	
			apatite		✓	
		50-134	feldspar		x	bubbles in crystal vicinity
			quartz		x	
Gardner et al. (1999)	rhyolite	< 20	?	?	?	HEN on dissolved crystals
		> 60			in melt	homogeneous nucleation
Gardner et al. (2000)	rhyolite	10-50	oxide microlites	crystallized	on microlites	unspecified on which microlites
			plagioclase microlites			
Mangan and Sisson (2000)	rhyolite	150	/	/	in melt	homogeneous nucleation
		31			fringe bubbles	
Gardner and Denis (2004)	rhyolite	50-70	hematite	crystallized	✓	
		60	plagioclase	crystallized	x	concluded $\sigma_{plag\text{-}bub} >> \sigma_{ox\text{-}bub}$
Mourtada-Bonnefoi and Laporte (2004)	rhyolite	150-200	/	/	in melt	homogeneous nucleation
Mangan et al. (2004)b	rhyolite	< 5	oxides	not specified	✓	
		< 25	cryptic sites		✓	HEN on dissolved crystals
		120-150	/	/	in melt	homogeneous nucleation
Gardner (2007)	rhyolite	20-90	magnetite	crystallized	✓	
			hematite	crystallized	✓	
			plagioclase	crystallized	x	
Cluzel et al. (2008)	rhyolite	> 100	/	/	in melt	homogeneous nucleation
		63-69	hematite	crystallized	✓	
Mangan and Sisson (2005), Mangan et al. (2004)a	dacite	35	feldspar	present in starting material	x	nucleation type not specified
			magnetite		✓	
			pyroxene		?	
Larsen (2008)	K-phonolite	45-50	clinopyroxene	present in starting material	✓	

5.1 Nucleation and growth of bubbles on silicate crystals

Nucleation and growth of bubbles on silicate crystals was explored in two different sets of experiments: dynamic observations of bubble nucleation by heating at ambient pressure and static, post-process observation of bubbles formed by depressurisation.

In Chapter 2, the presented 4D X-ray tomographic experiments have enabled the observation of exact nucleation location and temperature (Pleše et al., 2018), by looking at bubble formation on plagioclase, clinopyroxene and amphibole crystal fragments during heating at ambient pressure. A combination of several different advanced X-ray tomography techniques provided unprecedented levels of certainty to the observations (especially correlating *in situ* scans with *ex situ* propagation-based phase retrieval scans). The most important finding was that heterogeneous bubble nucleation occurred on silicate crystals first, and only then did it occur on oxides and finally homogeneously in the melt – an observation at odds with the previous bubble nucleation research (see references in Pleše et al., 2018; Shea, 2017).

The dynamic scans clearly showed that previous studies came to erroneous conclusions due to the measurement of post-process contact angles in 2D: such measurements will be in incorrect unless the 2D section in question passes through the bubble's maximum diameter. If an outer contact angle between a bubble and a crystal was measured as < 68°, the crystal was deemed inefficient at bubble nucleation and the bubble considered attached (e.g., Giachetti et al., 2010). Dynamic scans provided the observation of contact angle variations during bubble development from 140° – 120° to 75° – 50°, representing a change from above the 68° discriminant value, to below 68°. This is the first recorded contact angle change in samples representing volcanic environments and it was

determined to represent the beginning of bubble detachment. When only post-process sample were observed, and the later contact angle values recorded, silicate crystals were deemed inefficient at heterogeneous bubble nucleation (Hurwitz and Navon, 1994). However, when the contact angle change is observed through time, it is revealed that the opposite is true – silicate crystals are efficient and show possibilities for bubble detachment. This finding is completely opposite to previously published studies. Additionally, bubble-crystal assemblages proved less sensitive to potential surface tension changes or perhaps the surface tension differences between different crystal planes is not very large. Thus, silicate crystals should no longer be ignored in degassing studies, as they can potentially contribute much more to bubble nucleation than oxide crystals.

Even though strong indications of incipient bubble detachment were observed, due to the limitations of the experimental setup complete detachment was not observed, as the experiments were designed to image the initial seconds of bubble nucleation.

In Chapter 3 research that directly follows the findings from Chapter 2 is presented, but here the emphasis is on bubble nucleation on plagioclase during depressurisation, which is a scenario closer to natural conditions. The research in Chapter 3 is a direct extension of the 4D experimental results, using the same melt and crystal compositions and the interpretation of results regarding bubble nucleation location in Chapter 3 directly use the results from Chapter 2. However, degassing in these two chapters was achieved in different ways. In Chapter 2, heating at 1 atm pressure represents instantaneous decompression from a higher pressure to surface pressure, and bubbles grow by volatile diffusion (as in Bai et al., 2008). In Chapter 3, decompression is not simulated but it is occurring, and bubbles grow by gas expansion. Due to technical limitations at this time, the former can be observed and the latter can't. The primary interest of the research presented is the initial bubble nucleation

when volatile diffusion is the governing parameter for nucleation and growth directly above the critical nucleus size (Volmer and Webber, 1926; Blander and Katz, 1975; Sparks, 1978; Navon et al., 1998). This allows the comparison between these two experiments (two degassing types), even though the experiments followed a different pressure-temperature-time path. Therefore, results from Chapter 3 can be directly compared with those from Chapter 2.

Plagioclase is more similar to andesitic melt (in composition) than clinopyroxene, so based on previous research heterogeneous bubble nucleation should be more difficult on plagioclase. 3D outer contact angles between plagioclase crystal surfaces and bubbles were measured, as they were in Chapter 2, and the results were angles all below 68°. Without the *in situ* observations from Chapter 2, such angles below 68° previously lead to the interpretation of bubbles as attached to the crystal and not as nucleated on the crystal (e.g. Giachetti et al., 2010). To further examine which bubble-crystal interaction took place (nucleation or attachment) we examined whether bubbles present on the plagioclase surfaces belong to the same population as bubbles within the melt. These two bubble groups were found to represent two separate bubble populations, based on 3D bubble number densities and bubble size distributions, formed by two distinct events, i.e. bubbles located on the crystal surface did nucleate on the crystal surface (as observed in Chapter 2). Additionally, the parameter bubble number density on a crystal surface is completely novel.

Growth steps on plagioclase crystal planes, of height comparable to the bubble radius (as seen in Figure 2.9 g-h), seem to have stopped the bubble spreading. Regarding growth steps smaller than the bubble radius (Figure 2.9 b), their influence on bubble spreading is unclear.

Crystal surface roughness and its effect on heterogeneous bubble nucleation was also considered, in a limited manner, by comparing crystals from decompression and 1 atm studies. The very different appearance of plagioclase crystals in these two studies allowed surface roughness comparisons and represent the first quantified relation of bubble numbers and surface properties. The sieve-textured rim plagioclase from decompression experiments mimics particularly well the process of plagioclase xenocryst assimilation common in subduction zone-related volcanism.

The combined observations from Chapters 2 and 3 indicate that perhaps the presence of a (or any) crystal surface is sufficient for heterogeneous bubble nucleation and that the importance of compositional (chemical) difference between the crystals and melt has been overestimated. This can also be seen from Table 5.1, bubbles in this research are found on plagioclase crystals at decompressions lower than observed by previous studies. However, these results do not imply either that homogeneous bubble nucleation is not possible, or that all bubbles, considered to have nucleated homogeneously, have nucleated on silicate crystal surfaces. Instead the conditions needed for homogeneous bubble nucleation could be more restrictive, e.g. at larger and faster pressure drops than currently considered.

Apart from heterogeneous bubble nucleation, attachment and detachment of bubbles was also examined (post-process) since both can influence interpretations of heterogeneous bubble nucleation. Chapter 2 examined how bubble detachment could occur, while chapter 3 discussed why bubble attachment did not occur. Bubble-plagioclase buoyancy considerations additionally showed that bubbles, apart from nucleating on plagioclase surfaces, could remain attached to them, at bubble and crystal sizes comparable to those in the experiments.

5.2 Nucleation and growth of oxide crystals on bubbles

Heterogeneous nucleation refers not only to bubbles nucleating on pre-existing crystals, but also concerns the nucleation of crystals. Chapter 4 (Pleše et al., 2019) examines a case of oxide microlites nucleating on bubble-melt interfaces – hence, the focus has moved from silicate crystals to oxides.

In the presented study, ideal bubble volumes were used instead of real ones. Real (although partial) bubble volumes would need to be used for degassing related studies. We do not see any bubble completely engulfed in oxides, but only partial coverage, so we infer that the difference between the real and ideal bubble volume does not impact the processes of oxide shell formation. The non-spherical shape of fringe bubbles in the experimental charges is due to their emplacement on the Pt-capsule wall. Such a feature is not present in natural environments, yet bubbles nucleate, exhibiting spherical shapes. Thus, the use of ideal bubble volumes instead of partial ones, is favoured for extending our experimental results to natural environments.

Bubble-oxide affinity is extensively researched and used to explain the formation of large-scale ore deposits, where oxides are transported via buoyant bubble rise (Edmonds, 2015; Knipping et al., 2015). However, there is little textural evidence preserved in natural systems. This provoked the question: what was the process involved in bubble-oxide interaction and why are bubble-oxide textures so rarely observed?

The lack of textural observations in natural samples is attributed to textural overprinting, where initial processes and textures are obscured by later ones. Textural overprinting is a difficult issue in all bubble-related studies as bubbles are relatively easily displaced (more easily than crystals). This effect was countered by rapid quench of

decompressed samples and so the fine textures were preserved. The experimental suite is an extension of experiments presented in Chapter 3. The fact that our previous results show that oxides are not favoured bubble nucleation sites, does not mean that there is no bubble-oxide interaction at all, only that it is a considerably different interaction. Instead, our findings highlight the importance of correctly interpreting the interpretations that take place (e.g., nucleation vs. attachment).

Fifty bubble-oxide aggregates were identified, where oxides formed complex and delicate shells on outer bubble surfaces, with features such as several shell generations, skeletal extensions, cracks, tears, folds, swirls. These observations were only made possible by using 3D tomography. The formation of such bubble-oxide aggregates could arise from oxide attachment or heterogeneous nucleation of oxides in situ on bubble surfaces – it is rigorously argued why the latter is more probable.

Several observed textures of bubble-oxide aggregates highlight the complexity of bubble-crystal interactions; crystal-induced bubble breakup (daughter bubble generation), oxide-bubble detachment, continuous heterogeneous oxide nucleation. Daughter bubble generation is opposite to bubble coalescence, and more instead of fewer bubble numbers are generated. It is an entirely new form of bubble-crystal interaction not previously reported in geological environments. Potential daughter bubble detachment and continuous daughter bubble generation could have important degassing implications.

Net buoyancy calculations of bubble-plagioclase aggregates showed that bubbles and plagioclases with sizes as those in our experiments would mostly sink in a natural andesitic magma, but bubble-oxide aggregates would float. The net buoyancy can be related to the type of interaction occurring, as large bubbles will interact with smaller crystals and transport

them upwards, whereas small bubbles in contact with large plagioclase crystals will either stop them from sinking or enhance gas storage in andesitic magmas by sinking with them.

Partial detachment of oxide shells in bubble-oxide aggregates is observed through multiple oxide shell generations and complete detachment via bubble overturn is discussed through surface studies from mineral processing literature where similar phenomena were examined. It is precisely the oxide shell 3D morphology that is responsible for oxide texture disintegration post-detachment, resulting in sparse recognition in natural samples.

The detachment thought to occur between oxide shells and bubbles within experimental charges and Krafla granophyres presented in Chapter 4, should not be equated with the processes of detachment explored in Chapters 2 and 3. The attachment and detachment forces introduced by Gualda and Ghiorso (2007) apply to cases of one bubble on the surface of one crystal. In Chapter 4, the oxide shells represent crystal aggregates, that exhibit a degree of cohesion (whilst on the bubble surface) so the one-on-one scenario is not applicable. The potential detachment of oxide shells is thought to occur due to kinetic instability of the bubble-oxide shell aggregates, and not because of wetting properties. That is why no calculation of detachment force is implemented in Chapter 4.

The oxide shell textures presented in Chapter 4 corroborate the model of Knipping et al. (2015) for volcanic magnetite deposit formation, but also show aspects where the model was oversimplified. In Knipping's model, bubble-magnetite detachment is not envisioned, yet Chapter 4 demonstrates that it is likely to occur. Consequently, as it seems that a single bubble cannot transport its initially associated magnetite crystals all the way to the surface, several bubbles need to be involved. After nucleating on one bubble and detaching, the magnetite crystals (in shell form or individually) need to be harvested by another bubble in a step-like ascent to the surface. This necessitates a steady supply of bubbles that would

promote, transport and aggregate magnetite crystals. It also shows that although oxides can initially nucleate on bubble walls, subsequent oxide harvesting is possible. Although it was not possible to test this step-like scenario in the decompression experiments presented in Chapter 4, it was shown that heterogeneous bubble nucleation on magnetite crystals is not the only pathway to magnetite aggregation and transport (as envisioned in Knipping et al., 2015) but that heterogeneous oxide nucleation on bubbles contributes as well.

5.3 Conclusions and future work

In the research presented in Chapters 2-4, multiple facets of bubble-crystal interactions in andesitic melts are considered that illustrate how correctly identifying interactions can drastically change conclusions. The finding that silicate crystals such as plagioclase and clinopyroxene can nucleate bubbles and potentially lose them has a profound influence on degassing studies that have so far completely disregarded them. The discovery of complex oxide shells forming on bubble walls highlighted how oxide transport via bubbles can start and stop and why it was previously difficult to observe. Our observations encompass continuous bubble generation, continuous oxide generation, oxide detachment and potential bubble detachment. This is the first comprehensive textural analysis that supports models of oxide transport in degassing environment, and an extraordinary example of the complexity and implication of correctly identified bubble-crystal interactions.

The main impact of this research will be on the future determination of the conditions under which bubbles interact with crystals of silicate and oxide minerals within silicate melts, mainly further reconsiderations of silicate crystal efficiency at heterogeneous bubble nucleation and conditions regarding bubble detachment and nucleation site reactivation. By constraining the parameters of heterogeneous bubble nucleation on crystal surfaces and the possible achievement of neutral buoyancy of aggregates, valuable information may be gathered on the formation of long-lived gas reservoirs in magma chambers. The continuous heterogeneous bubble nucleation from surface defects could shed some light on the processes of rapid gas build up in shallow magma chambers and volcanic conduits, which often lead to hazardous eruptions, and thus contribute to their forecast.

5.4. References

Bai, L., Baker, D. R., Rivers, M., 2008. Experimental study of bubble growth in Stromboli basalt melts at 1 atm. Earth and Planetary Science Letters 267(3), 533-547.

Blander, M., Katz, J. L., 1975. Bubble nucleation in liquids. AIChE Journal 21(5), 833-848.

Cluzel, N., Laporte, D., Provost, A., Kannewischer, I., 2008. Kinetics of heterogeneous bubble nucleation in rhyolitic melts: implications for the number density of bubbles in volcanic conduits and for pumice textures. Contributions to Mineralogy and Petrology 156(6), 745-763.

Edmonds, M., 2015. RESEARCH FOCUS: Flotation of magmatic minerals. *Geology* 43(7):655-656.

Fiege, A., Holtz, F., Cichy, S. B., 2014. Bubble formation during decompression of andesitic melts. American Mineralogist 99(5-6), 1052-1.

Gardner, J. E., 2007. Heterogeneous bubble nucleation in highly viscous silicate melts during instantaneous decompression from high pressure. Chemical Geology 236(1–2), 1-12.

Gardner, J. E., Denis, M.-H., 2004. Heterogeneous bubble nucleation on Fe-Ti oxide crystals in high-silica rhyolitic melts. *Geochimica et Cosmochimica Acta* 68(17), 3587-3597.

Gardner, J. E., Hilton, M., Carroll, M. R., 1999. Experimental constraints on degassing of magma: isothermal bubble growth during continuous decompression from high pressure. Earth and Planetary Science Letters 168(1), 201-218.

Gardner, J. E., Hilton, M., Carroll, M. R., 2000. Bubble growth in highly viscous silicate melts during continuous decompression from high pressure. Geochimica et Cosmochimica Acta 64(8), 1473-1483.

Giachetti, T., Druitt, T. H., Burgisser, A., Arbaret, L., Galven, C., 2010. Bubble nucleation, growth and coalescence during the 1997 Vulcanian explosions of Soufrière Hills Volcano, Montserrat. *Journal of Volcanology and Geothermal Research* 193(3), 215-231.

Gualda, G. A., Ghiorso, M. S., 2007. Magnetite scavenging and the buoyancy of bubbles in magmas. Part 2: Energetics of crystal-bubble attachment in magmas. *Contributions to Mineralogy and Petrology* 154(4), 479-490.

Hurwitz, S., Navon, O., 1994. Bubble nucleation in rhyolitic melts: Experiments at high pressure, temperature, and water content. *Earth and Planetary Science Letters* 122(3–4), 267-280.

Knipping, J. L., Bilenker, L. D., Simon, A. C., Reich, M., Barra, F., Deditius, A. P., Lundstrom, C., Bindeman, I., Munizaga, R., 2015. Giant Kiruna-type deposits form by efficient flotation of magmatic magnetite suspensions. *Geology* 43(7):591-594.

Larsen, J. F., 2008. Heterogeneous bubble nucleation and disequilibrium H2O exsolution in Vesuvius K-phonolite melts. Journal of Volcanology and Geothermal Research 175(3), 278-288.

Mangan, M., Sisson, T., 2000. Delayed, disequilibrium degassing in rhyolite magma: decompression experiments and implications for explosive volcanism. Earth and Planetary Science Letters 183(3), 441-455.

Mangan, M., Sisson, T., 2005. Evolution of melt-vapor surface tension in silicic volcanic systems: Experiments with hydrous melts. Journal of Geophysical Research: Solid Earth 110(B1), B01202.

Mangan, M., Sisson, T. W., Hankins, W. B., 2004a. Decompression experiments identify kinetic controls on explosive silicic eruptions. *Geophysical Research Letters* 31(8), L08605.

Mangan, M., Mastin, L., Sisson, T., 2004b. Gas evolution in eruptive conduits: combining insights from high temperature and pressure decompression experiments with steady-state flow modeling. Journal of Volcanology and Geothermal Research 129(1-3), 23-36.

Mourtada-Bonnefoi, C. C., Laporte, D., 2004. Kinetics of bubble nucleation in a rhyolitic melt: an experimental study of the effect of ascent rate. Earth and Planetary Science Letters 218(3), 521-537.

Navon, O., Chekhmir, A., Lyakhovsky, V., 1998. Bubble growth in highly viscous melts: theory, experiments, and autoexplosivity of dome lavas. Earth and Planetary Science Letters 160(3–4), 763-776. doi.org/10.1016/S0012-821X(98)00126-5

Pleše, P., Higgins, M. D., Mancini, L., Lanzafame, G., Brun, F., Fife, J. L., Casselman, J., Baker, D. R., 2018. Dynamic observations of vesiculation reveal the role of silicate crystals in bubble nucleation and growth in andesitic magmas. *Lithos* 296, 532-546.

Pleše, P, Higgins, M. D., Baker, D. R., Lanzafame, G., Kudrna Prašek, M., Mancini, L., Rooyakkers, S., 2019. Production and detachment of oxide crystal shells on bubble walls during experimental vesiculation of andesitic magmas. *Contributions to Mineralogy and Petrology* 174 (21).

Shea, T., 2017. Bubble nucleation in magmas: A dominantly heterogeneous process?. *Journal of Volcanology and Geothermal Research* 343, 155-170.

Sparks, R. S. J., 1978. The dynamics of bubble formation and growth in magmas: A review and analysis. Journal of Volcanology and Geothermal Research 3(1-2), 1-37.

Volmer, M., Weber, A., 1926. Keimbildung in übersättigten Gebilden. Zeitschrift für physikalische Chemie 119, 277-301.